



Universitat Autònoma de Barcelona

ADVERTIMENT. L'accés als continguts d'aquesta tesi queda condicionat a l'acceptació de les condicions d'ús establertes per la següent llicència Creative Commons:  http://cat.creativecommons.org/?page_id=184

ADVERTENCIA. El acceso a los contenidos de esta tesis queda condicionado a la aceptación de las condiciones de uso establecidas por la siguiente licencia Creative Commons:  <http://es.creativecommons.org/blog/licencias/>

WARNING. The access to the contents of this doctoral thesis it is limited to the acceptance of the use conditions set by the following Creative Commons license:  <https://creativecommons.org/licenses/?lang=en>



**Universitat Autònoma
de Barcelona**

**Pd and Co-based (nano)catalysts
for C-C coupling and artificial photosynthesis**

Jonathan De Tovar Villanueva

PhD Thesis

Programa de Doctorat en Química

Dr. Xavier Sala Román & Dr. Jordi García-Antón Aviñó

Departament de Química

Facultat de Ciències

2018

Memòria presentada per aspirar al Grau de Doctor en Química per Jonathan De Tovar Villanueva

Jonathan De Tovar Villanueva

Vist i plau

Dr. Xavier Sala Román

Departament de Química
Facultat de Ciències
Universitat Autònoma de Barcelona

Dr. Jordi García-Antón Aviñó

Departament de Química
Facultat de Ciències
Universitat Autònoma de Barcelona

Bellaterra, 2 de Març de 2018

A mi madre y a mi padre

Acknowledgements

Le 25 septembre 2018, à 23 heures 11 minutes et 32 secondes, la température est de 14°C, le taux d'humidité de 68% et la pression atmosphérique de 1008.1 hectopascals. Aquesta sensació de neguiteig, aquesta sensació estranya, aquesta flaire diferent. Perquè serà? Suposo que és una mescla entre felicitat i records al llarg dels darrers anys. Mai hauria imaginat la magnitud d'aquesta aventura. I és que és gràcies a les mateixes persones m'han acompanyat en aquest viatge les que aquesta etapa esdevingui una realitat. Per començar, voldria agrair de tot cor als meus directors Dr. Xavier Sala i Dr. Jordi García-Antón per acollir-me dins el grup anys enrere i confiar en la meua persona investigadora. Ells són el clar exemple de com ha de ser una formació predoctoral, doncs no tota persona vetlla pels novells amb un somriure i formant un equip. Gràcies de tot cor. D'igual manera agraeixo tot el suport incondicional del Dr. Roger Bofill i Dr. Lluís Escriche que si no hagués estat per ells, la química hauria estat molt més complicada del que s'escriu en un paper. En la mateixa línia, tot i que no hagin estat els meus directors de tesi, voldria agrair tot el suport rebut per part del Dr. Antoni Llobet i la Dra. Carolina Gimbert-Suriñach i els membres del grup doncs no només em van permetre de treballar al mateix sinó que també han estat sempre oberts a ajudar-me en tot problema i dubte. Por supuesto, agradezco a la Dra. Zoraida Freixa y a su grupo Jorge y Ainara por la ayuda prestada durante más de una vez en estos cuatro años. Je ne pourrais jamais si remercier tout ce que j'ai appris en France. D'un coté, à Toulouse grâce à Dr. Karine Philippot, Dr. Catherine Amiens et Dr. Diana Ciuculescu-Pradines doncs je me suis toujours trouvé bien enlevé par elles. D'un autre coté, à Bordeaux par Dr. Nathan McClenaghan and Dr. Sergei Denisov. Moltes gràcies a totes aquelles persones que han treballat en la química d'aquesta tesis, particularment als equips tècnics de la UAB, CNRS-LCC i ICIQ.

Una mención más que evidente no podría faltar para todos mis compañeros y amigos de laboratorio durante estos años; Rosa, Javi, Marcos, Hai Jie, Nacho, Nuria, Lluís, Joan y Jordi C. No se puede pedir más que reír con vosotros día a día. Sempre m'enrecordaré d'aquelles paraules que em vas dir ara fa uns anys: Seràs capaç d'arribar. Gràcies Laia. Aunque igualmente no todo queda en el mismo laboratorio, pues todos los compañeros de planta Merche, João, Anna, Andreu, Alba, Laia, Dani P., Dani H., Quim, Katia, Selene, Jordi B., Jordi M. y Natalia siempre habéis estado dispuestos para todo. Gracias. Això també es trasllada a altres plantes doncs, Anna, Andreu i Imma, vosaltres sempre heu estat per molt més que per la química. Anna, tu ho saps molt bé: Toulouse, one day, one night.

Muy especialmente, quería agradecer a Chuso todas esas llamadas, noches de trabajo y viajes que me han dado la vida i a en Tony per tots aquells cafés (i no tants cafés) que hem pres quan necessitàvem revifar-nos. Iker, gracias por todas las terapias psicológicas que hemos hecho; no hay mayor compañía que la tuya para descubrirse a uno mismo. Abde, pese a conocerme en uno de los peores momentos de mi vida, siempre has velado por mi. Ya sabes que nos toca ahora. ¿No? Poder de 3, Marta i Laura, aquesta aventura sempre l'hem començada units... d'això ja fa 10 anys. Brindo per 10 anys més com aquests al vostre costat. Martí, Ester, Carlota i Vanian, els meus de Girona, gràcies per tots els sopars, fi del món i aquagranny's. Una pel 2018? Javi, ya sabes de sobra que todo lo que has hecho por mi no tiene precio alguno. De verdad te lo digo. Gracias.

Por supuesto no me podría jamás olvidar de aquellas personas que, aunque no compartamos vínculos de sangre, son mi familia. Básicamente hablo de vosotros: los Mihos. ¿Sabéis? Sin esos viajes a Gran Canaria y Mykonos con Hect, sin esos fines de semana de videojuegos, roomscape e intentado salvar el mundo con Mir, sin ésa maravillosa sonrisa con la que siempre me recibes San, sin esos fines de semana en Albons que me dan la vida Lau. Nunca voy a poder agradeceros suficientemente vuestro apoyo incondicional. Os quiero.

Finalmente, a toda mi familia pues ya sabeis que estoy muy orgulloso de vosotros por todo el apoyo e interés que me habéis ofrecido, especialmente a mi hermano Fidel y a mi cuñado Dani. Soys la mejor familia que podría tener, no sólo por estar en todo momento sinó también por enseñarme a ser un luchador. No sé qué haría sin vosotros. Pero no puedo sinó destacar a aquellos que me trajeron al mundo, me han criado, educado, mimado y hecho lo que soy hoy. Los que me han dado todo el amor y más que podría tener. Sí, a vosotros papis: Fidel De Tovar y Montserrat Villanueva.

The work performed in the present doctoral thesis has been possible thanks to the funding of:

Ministerio de Economía y Competitividad. Secretaría de Estado de Investigación, Desarrollo e Innovación through Projects: CTQ2011-26440 and MINECO/FEDER CTQ2015-64261-R.

Finally, I would like to express my gratitude to Universitat Autònoma de Barcelona for the pre-doctoral PIF-UAB grant and to the CTP (Communauté de travail des pyrénées) for the stay fellowship.



(Nano)catalizadores basados en Pd y Co para acoplamiento C-C y fotosíntesis artificial

Visto el esperado incremento por lo que a la demanda global de energía se refiere y las desventajas del uso de energías fósiles (mala distribución, no renovables y altamente contaminantes), la búsqueda de nuevas fuentes de energía renovables libres de carbono se ha convertido en una necesidad para nuestra sociedad. Así pues, una estrategia diferente debe ser considerada para superar estas dificultades. Para ello, los investigadores han sido inspirados por la Naturaleza, en particular por sus procesos fotosintéticos donde la energía solar es almacenada en los enlaces químicos de azúcares y almidones. Los investigadores han intentado mimetizar la Naturaleza almacenando la energía solar en los enlaces químicos de un combustible como por ejemplo el hidrógeno. De aquí, la reacción de división del agua (*Water Splitting reaction*, del inglés) supone una buena alternativa pues la absorción de cuatro fotones provoca la formación de oxígeno e hidrógeno. En este contexto, el uso de catalizadores normalmente basados en metales de transición es necesario para hacer viable estos dos procesos.

En el capítulo I, una introducción general sobre catálisis, nanopartículas, nanocatálisis, acoplamiento C-C y el reto de la fotosíntesis artificial es presentado como motivación del presente trabajo. Una visión general de los catalizadores de oxidación de agua basados en nanopartículas metálicas es discutida reportando los catalizadores mas importantes hasta la fecha.

En el capítulo II se exponen los objetivos del presente trabajo. El objetivo principal de esta tesis es la síntesis y caracterización estructural nanocatalizadores basadas en Co_3O_4 y el posterior estudio de su reactividad en catálisis de oxidación de agua electroquímicamente y fotoquímicamente. El objetivo final es comprender los factores que afectan a su actividad catalítica para ayudar al diseño futuro de catalizadores más eficientes y robustos. Además, el segundo objetivo de la presente tesis es el uso de catalizadores moleculares y coloidales frente a la reacción de Suzuki-Miyaura con el fin de estudiar su diferenciado comportamiento catalítico.

En el Capítulo III, una nueva metodología para la preparación de nanocatalizadores de Co_3O_4 funcionalizados por fotosensibilizadores capaces de captar luz es presentada. Todas las

nanopartículas has sido debidamente caracterizadas por ICP, HREM, XPS, IR y WAXS. Mientras que las nanopartículas de Co_3O_4 han sido caracterizadas electroquímicamente, los sistemas híbridos PS-NP lo han sido fotoquímicamente. Todo ello con el fin de extraer conclusiones sobre su respectiva habilidad para oxidar el agua electroquímicamente y fotoquímicamente.

En el Capítulo IV, sistemas moleculares y coloidales de Pd basados en un líquido iónico o su carbeno N-heterocíclico son usados frente a procesos de acoplamiento C-C. La conversión, rendimiento y diferenciada actividad son discutidas para los cuatro sistemas.

En el Capítulo V se exponen las conclusiones mas importantes del presente trabajo.

Finalmente, el Capítulo VI incluye un anexo que contiene otros trabajos que han sido llevados a cabo y publicados durante esta tesis doctoral.

Pd and Co-based (nano)catalysts for C-C coupling and artificial photosynthesis

Given the expected increase of global energy consumption and the drawbacks of using fossil fuels (ill-distributed, non-renewable and highly CO₂ polluting), it is mandatory to find a new carbon-neutral renewable source of energy for the sustainable development of our society. Hence, a different strategy should be considered to overcome these difficulties. For this purpose and as in many other cases, researchers have obtained inspiration from Nature, particularly from the photosynthetic processes where sunlight energy is stored in the chemical bonds of sugars and starches. Researchers try to mimic Nature storing sunlight energy in the chemical bonds of a fuel such as dihydrogen. From here, the Water Splitting reaction supposes a good candidate since the absorption of four photons provokes the formation of both dioxygen and dihydrogen. Within this context, the use of catalysts usually based in transition metals is necessary to make these two processes viable.

In Chapter I, a general introduction about catalysis, nanoparticles, nanocatalysis, C-C coupling and the challenge of artificial photosynthesis is presented as a motivation for the present work. An overview of water oxidation catalysts based on metal nanoparticles is also discussed exposing the most relevant catalysts reported to date.

Chapter II is focused in the objectives of the present work. The main goal of this PhD thesis is the synthesis and the structural characterization of PS-Co₃O₄-based nanocatalysts for the ulterior study of their reactivity towards electro- and photocatalytic water oxidation. The final objective is to understand the factors that affect their catalytic performance for helping in the future rational design of more efficient and robust catalysts. Additionally, the second goal of this thesis is the testing of molecular and colloidal catalytic systems towards the Suzuki-Miyaura reaction in order to study their dissimilar catalytic behavior.

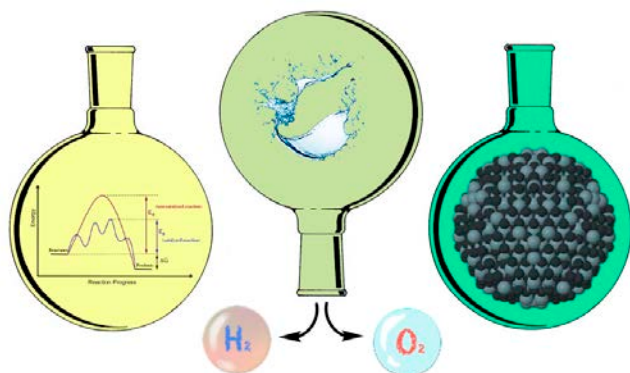
In Chapter III, a novel method for the preparation of a Co₃O₄ nanocatalyst functionalized by light-harvesting photosensitizers is presented. All NPs have been thoroughly characterized by ICP, HREM, XPS, IR and Wide Angle X-ray Scattering, while electrochemical and photophysical studies have been undergone with the bare NPs and the hybrid PS-NP systems, respectively, to extract conclusions with regards to their respective ability to electro- and photo-oxidize water.

In Chapter IV, both molecular and colloidal Pd systems based both on an ionic liquid or its N-heterocyclic carbene (NHC) are tested in C-C coupling processes. The conversion, yield and the different reactivity are discussed for the set of four systems.

In Chapter V, the most relevant conclusions of the present research work are discussed.

Finally, Chapter VI includes an annex containing other works that have been carried out and published during this PhD thesis and that are closely related with the present work.

Chapter I. General Introduction

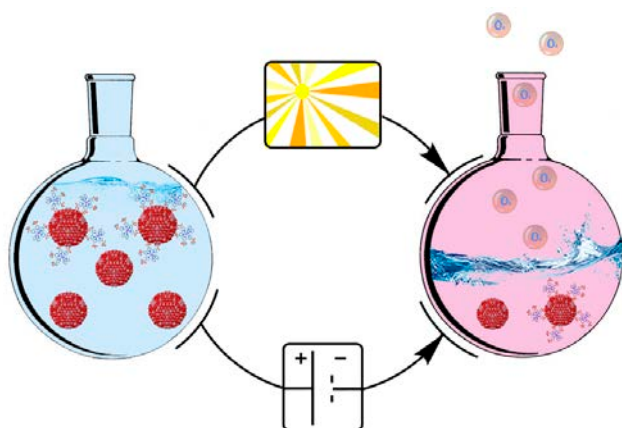


A General introduction about catalysis, nanoparticles, nanocatalysis, C-C coupling and the challenge of artificial photosynthesis is presented in this chapter. An overview of water oxidation catalysts based on metal nanoparticles is also exposed.

Chapter II. Objectives

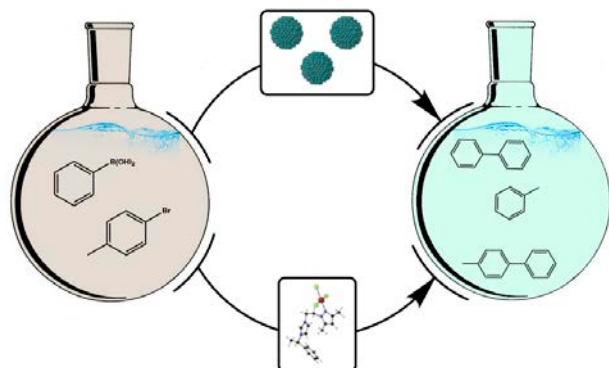


Chapter III. Coordination of photosensitive Ru-polypyridylic complexes at the surface of Co_3O_4 nanoparticles: hybrid dyads for light-driven water oxidation



A novel method for the preparation of Co_3O_4 NPs and a dyad $[\text{Ru}(\text{bpy})_3]^{2+}$ -capped Co_3O_4 nanomaterial is presented. Both systems have been thoroughly characterized by ICP, HRTEM, XPS, IR and WAXS, while electrochemical and photophysical studies have been carried out in order to rationalize their respective ability to electro- and photo-oxidize water.

Chapter IV. Dissimilar Catalytic Behavior of Molecular or Colloidal Palladium Systems with a New NHC Ligand

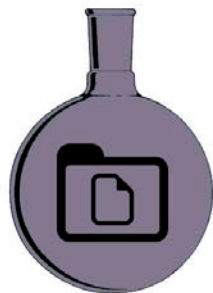


New palladium complexes and nanoparticles based on a N-heterocyclic carbene (NHC) ligand have been tested in the Suzuki-Miyaura coupling. Three different reactions have been observed depending on the nature of catalytic system employed: i) the Suzuki-Miyaura reaction, ii) a secondary reaction, the dehalogenation of the substrate and, iii) the C-C homocoupling between two molecules of bromoarenes..

Chapter V. Summary and Conclusions



Chapter VI. Annexes



Glossary of terms and abbreviations

0D	Zero-dimensional
1D	One-dimensional
2D	Two-dimensional
3D	Three-dimensional
ADP	Adenosine diphosphate
ATP	Adenosine triphosphate
ATR-IR	Attenuated total reflectance infrared
b _{6f}	Cytochrome b _{6f} complex
bda	[2,2'-bipyridine]-6,6'-dicarboxylic acid
Bu	Butyl
BMI-PF ₆	1- <i>n</i> -Butyl-3-methylimidazolium hexafluorophosphate
bpy	2,2'-Bipyridine
BT	4-Methyl-1,1'-biphenyl
CB	Conduction band
CNT	Carbon nanotube
cod	1,5-Cyclooctadiene
CONHSA	2,2'-((2,2'-Bipyridine)-4,4'-dicarbonyl)bis(azanediyl)disuccinic acid
CV	Cyclic voltammetry
DC	Direct current
dcb	[2,2'-Bipyridine]-4,4'-dicarboxylic acid
DFT	Density functional theory
dpbpy	[2,2'-Bipyridine]-4,4'-diylbis(phosphonic acid)
DMA	Dimethylacetamide
DMF	Dimethylformamide
DSPEC	Dye-sensitized photoelectrochemical cell
E _{1/2}	Half wave potential
E _a	Activation energy
ECSA	Electrochemically active surface area
EDX	Energy dispersive X-ray analysis
EPR	Electron paramagnetic resonance
E _q	Equivalent
EXAFS	Extended x-ray absorption fine structure
FAU	Faujasite
FID	Flame ionization detector
FTO	Fluorine doped tin oxide
GC	Glassy carbon
GC-MS	Gas chromatography-mass spectrometry
GC-RDE	Glassy carbon rotating disk electrode
HEC	Hydrogen evolving catalyst
HER	Hydrogen evolution reaction
hcp	Hexagonal close-packed structure
HL-Cl	1-[2-(3,5-Dimethylpyrazol-1-yl)ethyl]-3-((S)-1-phenylethyl)-3H-imidazol-1-ium chloride
HREM	High resolution transmission electron microscopy
I2M	Interaction between two Metal-Oxygen entities
ICP	Inductively coupled plasma

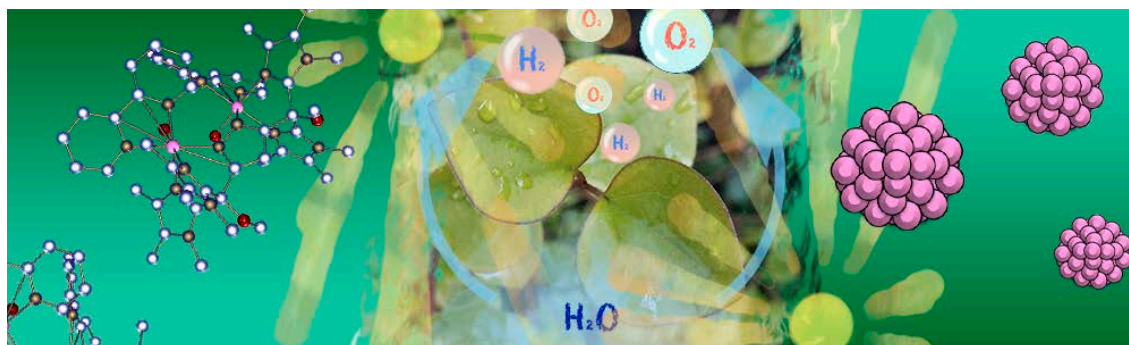
ICP-AES	Inductively coupled plasma atomic emission spectroscopy
ICP-OES	Inductively coupled plasma optical emission spectroscopy
ICP-MS	Inductively coupled plasma mass spectrometry
IPCE	Incident photon-to-current conversion efficiency
IR	Infrared
ITO	Indium tin oxide
K_{eq}	Equilibrium constant of ion-pair complex formation
k_{ET}	Photoinduced unimolecular electron-transfer rate
k_q	Unimolecular quenching constant
k_q'	Bimolecular quenching constant
L	1-[2-(3,5-Dimethylpyrazol-1-yl)ethyl]-3-((S)-1-phenylethyl)-3H-imidazol-2-ylidene
LDH	Layered double hydroxide
M2P	Methylenediphosphonate
Me	Methyl
MHz	Megahertz
MIMS	Membrane-inlet mass spectrometry
MLCT	Metal-to-ligand charge-transfer
MOF	Metal-organic framework
MNP	Metal nanoparticle
ν	Scan rate
nBu	n-butyl
NCNT	N-doped carbon nanotube
NHC	N-heterocyclic carbene
NHE	Standard hydrogen electrode
NMP	N-methyl-2-pyrrolidone
NMR	Nuclear magnetic resonance
NP	Carbon nanotube
NT	Nanotube
OEC	Oxygen evolving complex
OER	Oxygen evolution reaction
OXONE	Potassium peroxydisulfate
PCET	Proton-Coupled Electron-Transfer
PCTA	Partial-charge-transfer-activation
PEC	Photoelectrochemical cell
PEM	Proton exchange membrane
PhMe	Toluene
PLAL	Pulsed laser ablation in liquids
PMMA	Poly(methyl methacrylate)
PS	Photosensitizer
PS0	Tris(bipyridine)ruthenium(II) chloride
PS1	$[\text{Ru}(\text{bpy})_2(4,4'-(\text{PO}_3\text{H}_2)_2\text{bpy})](\text{Cl})_2$
PS2	$[\text{Ru}(\text{bpy})(4,4'-(\text{PO}_3\text{H}_2)_2\text{bpy})_2](\text{Cl})_2$
PSI	Photosystem I
PSII	Photosystem II
PVP	Polyvinylpyrrolidone
RDF	Radial distribution function
RDV	Rotating disk voltammetry

RF	Roughness factor
RHE	Reversible hydrogen electrode
RDE	Rotating disk electrode
RRDE	Rotating ring disk electrode
RuPS	Ruthenium-based photosensitizer
SBA-15	Santa Barbara amorphous type material
SEA	Sacrificial electron acceptor
STEM	Scanning transmission electron microscopy
SV	Stern-Volmer
SWCNT	Single-walled carbon nanotube
τ	Lifetime
τ_{Ar}	Lifetime in the presence of argon
τ_{O_2}	Lifetime in the presence of oxygen
^t Bu	Tert-butyl
TEM	Transmission electron microscopy
THF	Tetrahydrofurane
TOF	Turnover frequency
TON	Turnover number
tppps	3-Sulfonatophenyldiphenylphosphine sodium salt
tppts	Tris(3-sulfophenyl)phosphine trisodium salt
TT	4,4'-Dimethyl-1,1'-biphenyl
TTP-DPAG4	Fourth-generation (G4) phenylazome- thine dendrimers
TW	Terawatt
UV-Vis	Ultraviolet-visible spectrophotometry
VB	Valence band
vs.	Versus
WAXS	Wide-angle X-ray scattering
WNA	Water nucleophilic attack
WOC	Water oxidation catalyst
XPS	X-ray photoelectron spectroscopy
ϕ	Quantum yield
ϕ_{Ar}	Quantum yield in the presence of argon
ϕ_{O_2}	Quantum yield in the presence of oxygen

Table of Contents

Acknowledgments	I
Summary	V
Graphical abstracts	IX
Glossary of terms and abbreviations	XI
Table of contents	XVII
Chapter I. General introduction	1
Chapter II. Objectives	89
Chapter III. Coordination of photosensitive Ru-polypyridylic complexes at the surface of Co ₃ O ₄ nanoparticles: hybrid dyads for light-driven water oxidation	93
Chapter IV. Dissimilar catalytic behavior of molecular or colloidal palladium systems with a new NHC ligand	157
Chapter V. Summary and conclusions	185
Chapter VI. Annexes	191

Chapter I. General introduction



A general introduction about catalysis, nanoparticles, nanocatalysis, C-C coupling and the challenge of artificial photosynthesis is presented. An overview of water oxidation catalysts based on metal nanoparticles is also exposed.

Table of Contents

1.1	Catalysis	5
1.1.1	Parameters in catalysis	6
1.1.1.1	Turnover number (TON).....	6
1.1.1.2	Turnover frequency (TOF).....	6
1.1.1.3	Conversion	6
1.1.1.4	Selectivity.....	7
1.1.2	Homogeneous and heterogeneous catalysis.....	7
1.2	Nanomaterials	9
1.2.1	Properties of nanomaterials.....	10
1.2.1.1	Quantum confinement.....	10
1.2.1.2	Surface-to-volume ratio.....	12
1.2.2	Methodologies for the preparation of nanoparticles.....	14
1.2.2.1	Reduction of transition metal salt precursors.....	16
1.2.2.2	Electrochemical synthesis.....	16
1.2.2.3	Reduction of organic ligands in organometallic precursors (Organometallic approach).....	18
1.2.2.4	Chemical vapor deposition (CVD)	20
1.2.2.5	Thermal, photochemical and sonochemical decomposition.....	21
1.3	Nanocatalysis	23
1.3.1	Suzuki-Miyaura C-C Coupling	28
1.3.2	Leaching in metal nanoparticle catalysis for C-C coupling reactions.....	33
1.4	The energy problem.....	38
1.4.1	Hydrogen production.....	39
1.4.1.1	Steam methane reforming.....	39
1.4.1.2	Gasification of coal.....	40
1.4.1.3	Electrolysis of water	40
1.4.1.4	Biomass	44

1.4.2 Natural photosynthesis	46
1.4.3 Artificial photosynthesis: the water splitting reaction	49
1.4.3.1.1 Mechanistic perspective.....	51
1.4.3.1.2 Evaluation of the catalytic activity of the catalysts.....	52
1.4.3.1.3 Light-driven water oxidation catalysis.....	54
1.4.4 Water Oxidation mediated by Colloidal Cobalt-based nanocatalysts.....	61
1.4.4.1 Scope.....	61
1.4.4.2 Effect of NPs size, shape and composition on the catalytic activity.....	64
1.4.4.3 Catalytic activity dependence on the degree of crystallinity of the NPs and presence/absence of phosphate based ligands	65
1.4.4.4 In situ-formed NPs vs. ex situ-formed NPs.....	65
1.4.4.5 Mechanistic insights	66
1.4.4.6 Supported Systems	72
1.4.4.7 Photocatalytically-triggered systems	74
1.4.4.8 Photoelectrocatalytically-triggered systems.....	75
1.4.4.9 Bimetallic systems.....	76
1.5 References.....	79

1.1 Catalysis

Catalysis is a process in which the rate of approaching the thermodynamic equilibrium of a chemical reaction is accelerated by a compound that is not substantially consumed, named catalyst. It can be described as a cyclic event where the catalyst participates but is recovered in its original form at the end of the cycle. Catalysis has an effect on the kinetics of a reaction but thermodynamics remains unaltered. Nowadays, catalysis is extremely important due to the fact that it is required for the synthesis of many chemical products of paramount importance. Approximately 85-90% of the products of chemical industry are made with at least one catalytic step. Figure 1 shows a potential energy diagram in which both catalytic and non-catalytic reactions are compared. From this, it can be inferred how the catalyst offers an alternative pathway for the reaction, which is more complex, but energetically much more favorable due to a significantly smaller activation energy of the catalytic pathway.[1] Thus, a higher proportion of molecular collisions will possess enough energy to achieve the transition states and overcome the energetic barriers.

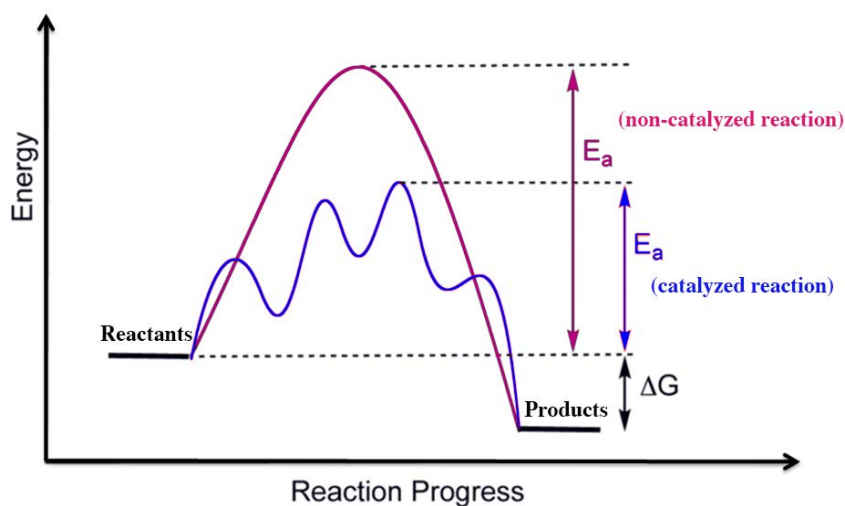


Figure 1. Potential energy diagram for both a non-catalyzed reaction (red) and a catalyzed reaction (blue). (Adapted from reference 1) E_a = Activation energy, ΔG = Free Gibbs energy.

Catalysts can vary from atoms and molecules to large structures such as zeolites or enzymes and their compositions and shapes are of paramount importance. Hence, catalysis falls into two categories, homogeneous and heterogeneous, depending on the relationship between the phase of the catalyst and the involved reactants.[2]

1.1.1 Parameters in catalysis

There are different parameters to characterize the catalyst in a catalytic scenario.

1.1.1.1 Turnover number (TON)

The turnover number is defined as the ratio between the total amount of moles of product and the moles of catalyst used for the reaction (equation 1).[3] It describes the total catalytic cycles performed by the catalyst before the decay of its activity.

$$TON = \frac{\text{moles formed product}}{\text{moles used catalyst}} \quad (1)$$

1.1.1.2 Turnover frequency (TOF)

The turnover frequency, expressed in s^{-1} , is defined as the activity of a particular catalyst in a certain period of time (t , equation 2).[3] It is referred as the number of catalytic reactions occurring per unit of time.

$$TOF = \frac{\text{moles formed product}}{\text{moles used catalyst} \cdot t} \quad (2)$$

1.1.1.3 Conversion

The conversion is the ratio between the moles of reactant consumed and the moles of reactant introduced in the reaction media.[3] To calculate the conversion a mole balance of the reactants is required (equation 3).

$$Conversion = \frac{\text{moles of reactant consumed}}{\text{moles of reactant introduced in the reaction}} \quad (3)$$

1.1.1.4 Selectivity

The selectivity of a reaction is the ratio of substrate converted to the desired product, since in addition to the latter other byproducts can be generated (Equation 4).[3]

$$\text{Selectivity} = \frac{\text{moles of reactant consumed to form the desired product}}{\text{total moles of reactant consumed}} \quad (4)$$

1.1.2 Homogeneous and heterogeneous catalysis

In homogeneous catalysis, both the catalyst and the reactants are in the same phase (i.e. all the molecules are commonly in liquid phase). Examples of homogeneous catalysis are organocatalysis where the catalyst is an organic compound, and the enzymatic catalysis, in which the catalyst is an enzyme. However, coordination or organometallic complexes play the major role as catalysts in homogeneous catalysis. They consist of a central transition metal ion bonded to organic ligands, which usually coordinate the reactant molecules through vacant sites or partial ligand decoordination.[1a,4]

On the other hand, in heterogeneous catalysis, both the catalyst and the reactants are in different phases. The catalysts use to be in solid phase, which catalyze reactions of molecules in gas or solution in their surfaces. Large surface areas, which are needed to produce high proportion of active sites, are essential to increase the rate of the catalytic reaction. Hence, porous materials and nanometer-sized particles use to be good candidates for these catalytic reactions. Briefly, a heterogeneous catalysis starts with the adsorption of the reactant molecules on to the surface of the catalyst, where the catalytic reaction takes place to form the products, and ends with the desorption of the new products.[1a,5]

The major advantages and disadvantages of homogeneous and heterogeneous catalysis are shown in Table 1. In the case of homogeneous catalysis, the recovery of the homogeneous catalysts from the reaction media uses to be difficult since distillation of the reaction products are typically needed in order to re-utilize the homogeneous catalysts and these operations often deactivate the catalysts. However, every single catalytic entity acts as a single active site

yielding high activities and selectivities, and thus, the reaction mechanisms are well-understood. In the case of heterogeneous catalysis, the recovery of the heterogeneous catalysts from the reaction media uses to be easy since the catalysts are in a different phase, which leads to their facile recycling. However, heterogeneous catalysts are formed by multiple active sites that can act differently, leading to low selectivities and complicating the understanding of the reaction mechanism by spectroscopic analyses. Additionally, in the case of heterogeneous catalysis, the diffusion of the reactants towards the catalyst, the adsorption of the reactants and desorption of the products, and the external diffusion should be considered, since these factors are of paramount importance for a good activity.[6]

Table 1. Differences between homogeneous and heterogeneous catalysis. (Adapted from reference 6).

Property	Homogeneous Catalysis	Heterogeneous Catalysis
Typical form	soluble metal complexes, usually mononuclear	metals, usually supported, or metal oxides
Active site	well-defined, discrete molecules	poorly defined
Catalyst phase (normally)	in solution	solid
Diffusion	facile	can be slow
Heat transfer	facile	can be problematic
Product separation	generally problematic	facile
Catalyst recovery	difficult and expensive	easy and cheap
Catalyst modification	easy	difficult
Thermal stability	poor	good
Selectivity	excellent/good – single active site	good/poor – multiple active sites
Activity	good	mutable
Catalyst poisoning	infrequent	easy
Catalyst life	mutable	long
Reaction mechanisms	reasonably well-understood	Poorly understood

1.2 Nanomaterials

Nanomaterials are particles (crystalline or amorphous) of organic or inorganic materials whose size in at least one dimension lays between 1 and 100 nm. From here, different nanomaterials can be classified by means of dimensions (Figure 2). Thus, nanomaterials wherein all the dimensions are measured within the nanoscale (no dimensions, or zero-dimensional) are called nanoparticles. Once one dimension is outside the nanoscale (one-dimensional) nanotubes, nanorods and nanowires are introduced. Finally, nanomaterials where two dimensions are outside the nanoscale (two-dimensional) are called nanofilms or nanolayers.

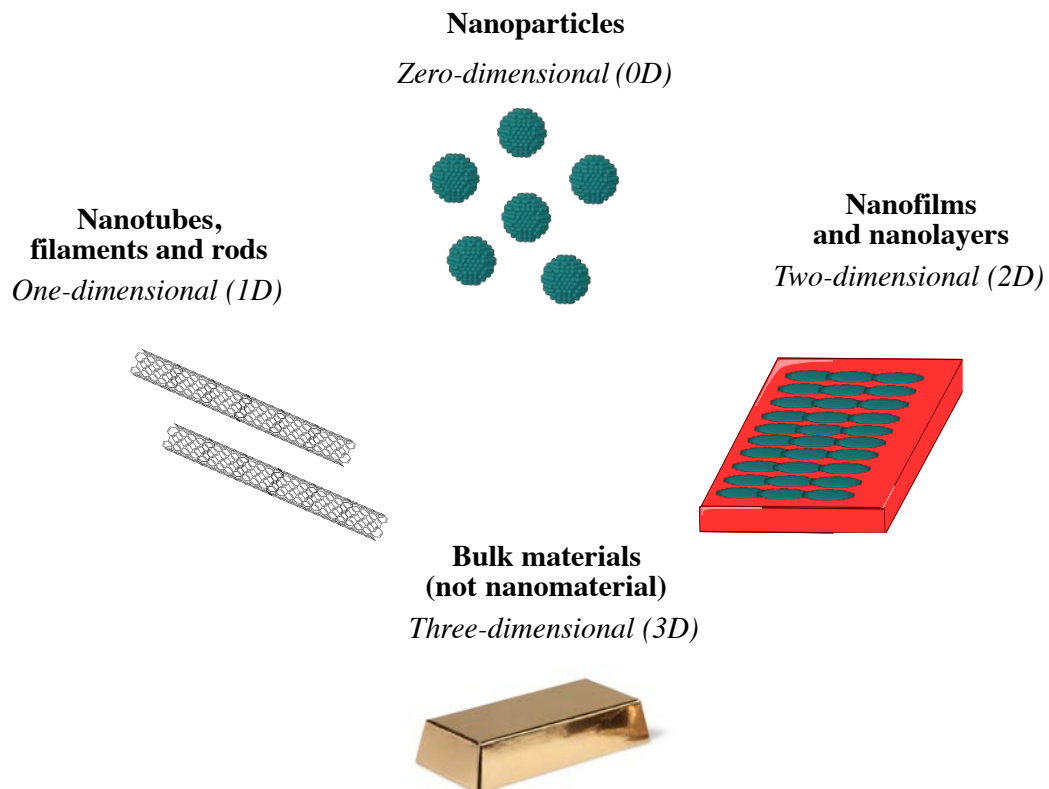


Figure 2. Types of nanomaterials: 0D (zero-dimensional) nanoparticles; 1D (one-dimensional) nanotubes, filaments and rods; 2D (two-dimensional) films and layers; 3D (three-dimensional) bulk materials.

Nanomaterials are a link between bulk materials and atomic or molecular structures (Figure 3) and present differentiated physical and chemical properties. Due to their high surface area to volume ratio, metallic nanoparticles (MNPs) have many applications such as biological and chemical sensor fabrication,[7] information storage[8] and catalysis.[9]

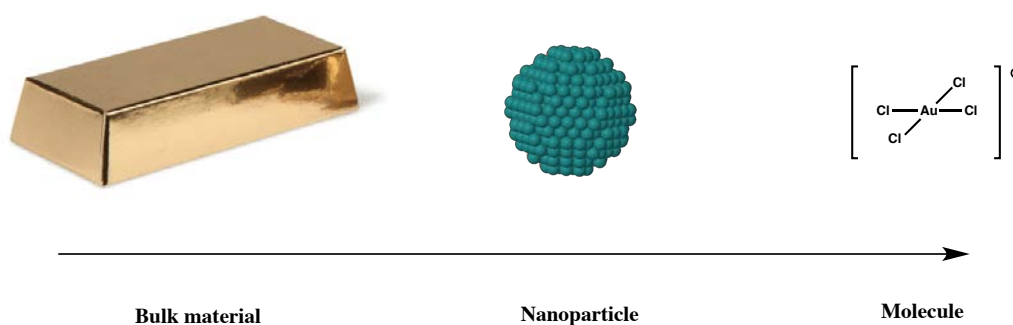


Figure 3. Comparaision among bulk material, nanoparticles and molecular complexes.

1.2.1 Properties of nanomaterials

The nanomaterials have properties (i.e. physical, electrical, optical, mechanical) that are significantly different and considerably improved relative to those of their bulk counterparts. These properties depend on the size of nanomaterials as well as on the large percentage of their atoms in grain boundary environments. Thus, the most popular effects of nanomaterials giving rise to these different properties are the quantum confinement and the surface-to-volume ratio.[10,11]

1.2.1.1 Quantum confinement

The quantum confinement effect is a change of electronic and optical properties when a particular material is of sufficiently small size – typically at the nanoscale. The bandgap increases as the size of the nanostructure decreases. Specifically, the phenomenon results from electrons and holes being squeezed into a dimension that approaches a critical quantum measurement, called the exciton Bohr radius. Thus, in small nanocrystals, the electronic

energy levels are not continuous as in the bulk material but are discrete (finite density of states) as in molecular complexes due to the confinement of the electronic wavefunction to the physical dimensions of the particles (Figure 4). The shape of the surface in nanostructures causes a change in the distribution of the phonon frequencies and creates new modes that are not present neither in bulk materials nor in molecular complexes.[10]

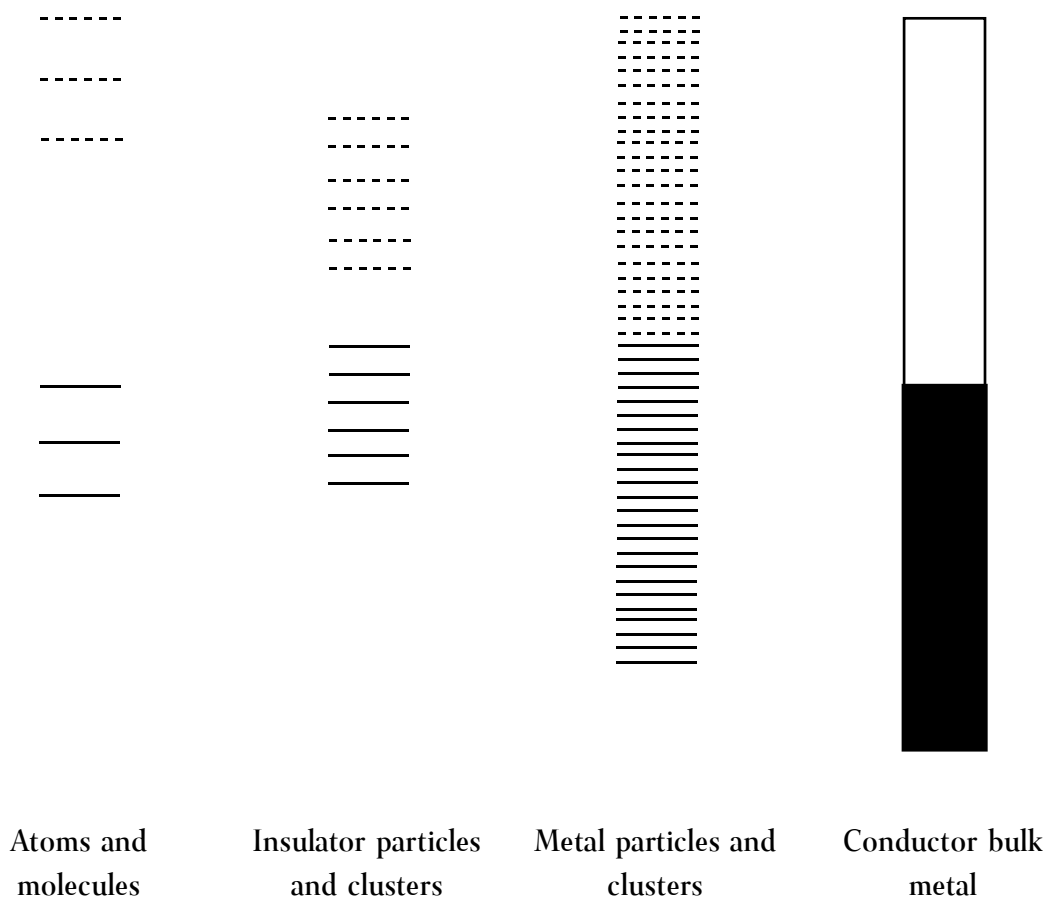


Figure 4. Band gap and density of states as function of the number of atoms for a variety of systems. (Adapted from reference 10b)

1.2.1.2 Surface-to-volume ratio

Many properties of a material depend on the type of motion its electrons can execute, which depends on the available space. Once the physical size of the material is reduced to the nanoscale, the properties change and become sensitive to size and shape. Surface-to-volume ratio constitutes a peculiar aspect of nanomaterials since the structural, thermodynamic, electronic, spectroscopic, electromagnetic and chemical features of these finite systems are size-dependent. To better understand these effects, a face centered cubic nanoparticle is considered where n is the number of layers, G_n is the total number of atoms and S_n is the total surface atoms (equations 5 and 6 and Figure 5).[11]

$$G_n = \frac{10}{3}n^3 + 5n^2 + \frac{11}{3}n + 1; n \geq 0 \quad (5)$$

$$S_n = 10n^2 + 2; n \geq 0 \quad (6)$$

For instance, as seen in Figure 5, once a nanoparticle is formed by 4 layers of atoms (instead of 1) in an fcc structure, its percentage of available atoms on surface dramatically decreases from 92% to 52%.





Number of Layers (n)	Diameter	Number of surface atoms (S_n)	Number of total atoms (G_n)	Percentage of available atoms on surface (S_n/G_n)	Representation
1	3d	12	13	92%	
2	5d	42	55	76%	
3	7d	92	147	63%	
4	9d	162	309	52%	

Figure 5. Magic structural numbers for fcc particles containing n layers where the d diameter in nm is element-dependent. (Adapted from reference 11).

Another way of looking at this phenomenon is to consider a single cube of 1 x 1 x 1 cm with a total surface area of 6 cm², a surface area of 60,000,000 cm² can be achieved if it is cut off into 1 nm-edged cubes (Figure 6). Thus, nanoparticles possess a higher proportion of surface atoms in comparison with bulk materials.

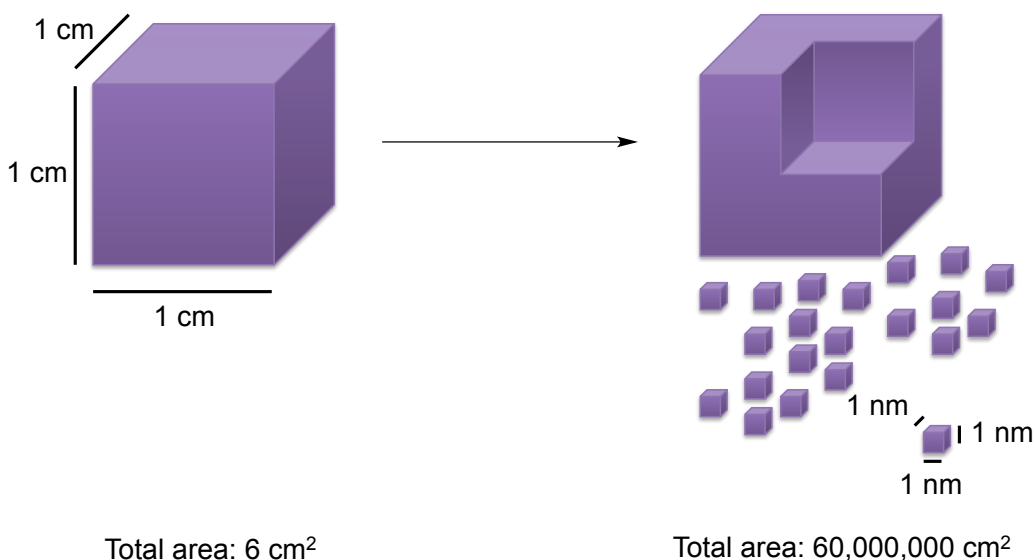


Figure 6. Cutting off a cube of $1 \times 1 \times 1 \text{ cm}$ into cubes of $1 \times 1 \times 1 \text{ nm}$.

1.2.2 Methodologies for the preparation of nanoparticles

Transition-metal nanoparticles are clusters formed by a few tenths to several thousands of metal atoms, stabilized by ligands, surfactants, polymers or dendrimers, preventing their aggregation and protecting their surfaces. The size of these nanoparticles, varying between 1 to 100 nm, allows their dispersion in organic solvents (ethanol, propanol, N,N-dimethylformamide, etc.).[12]

These nanoparticles can be obtained either by consolidating atoms/molecules/clusters or breaking down the bulk material into smaller dimensions. The former is known as the *bottom-up* approach whereas the latter is referred to as the *top-down* approach (Figure 7).[13]

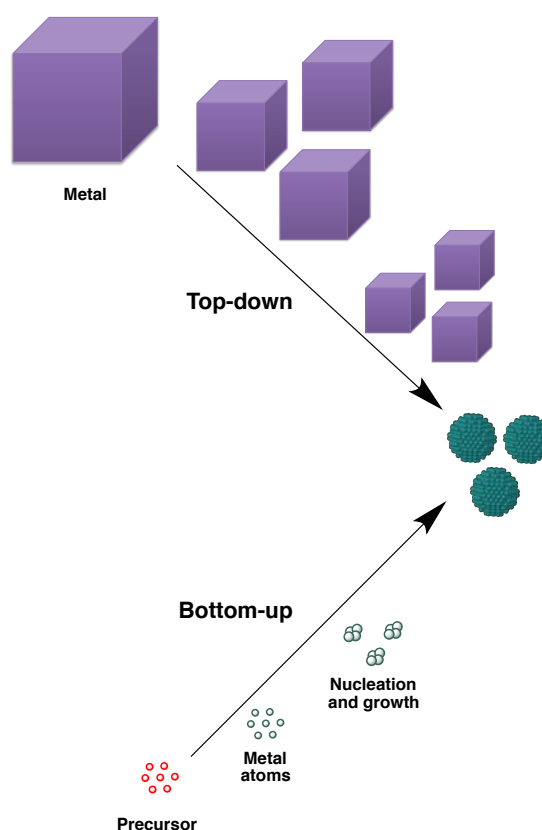


Figure 7. Bottom-up and top-down approaches for nanoparticles construction. (Adapted from reference 13).

In the top-down approach a block of a bulk material is whittled to get the nanosized particles that use to possess impurities and imperfections at the surface and a broad size distribution. This is due to the own methodology including the reagents used.[14] However, this approach comprises well-developed techniques (e.g. ball milling) which are dominant in microfabrication. On the other hand, in the bottom-up approach, individual atoms or molecules are self-assembled precisely to form nanoparticles. This approach is more favorable since it solves the disadvantages of the top-down approach while yielding a good reproducibility.[15]

In catalysis, the main field of this research work, metal nanoparticles are often the chosen catalysts. The different methods for the synthesis of metal nanoparticles have been extensively reviewed by Bönnemann,[16] Schmid,[17] Aiken and Finke,[9f] Roucoux,[9g] Wilcoxon,[18] Philippot and Chaudret[15] and Cushing.[19] In general, these methods can be divided in the five main categories explained next.

1.2.2.1 Reduction of transition metal salt precursors

In this methodology, a reducing agent (e.g. hydrogen, carbon monoxide, alcohols, hydrazine or borohydride) is mixed with the metal salt precursor in the presence of a stabilizing agent (ligand, polymer or surfactant).[9g,20] The former reduces the precursor to free metallic zero-valent atoms that nucleate and grow to form the nanoparticles while the latter prevents their agglomeration and the further formation of the bulk material (Figure 8).[21] The size of the nanoparticles depends on the type of reducing agent, the chosen metal precursor and solvent, the stabilizing agent, the concentration, the temperature and the reaction time.

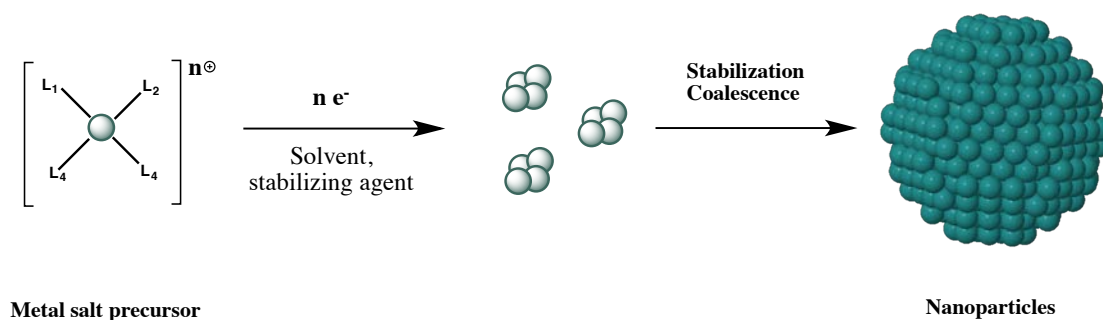


Figure 8. Synthesis of metal nanoparticles by reduction of a transition metal salt precursor. (Adapted from reference 9h)

1.2.2.2 Electrochemical synthesis

This methodology was developed by Reetz and co-workers in the 1990s[22] and consists on the oxidative dissolution of a sacrificial metal bulk anode. Then, the leached metal ions migrate to the cathode where they are reduced to zero-valent metal atoms that nucleate and grow to yield metal nanoparticles (Figure 9). The presence of a stabilizing agent is required in order to avoid the agglomeration and the further formation of the bulk material (e.g. tetraalkylammonium salts). This methodology presents many advantages since the products are easily isolated from the precipitate and it allows an easy size-selection of the particles by tuning the current density or the distance between the electrodes.

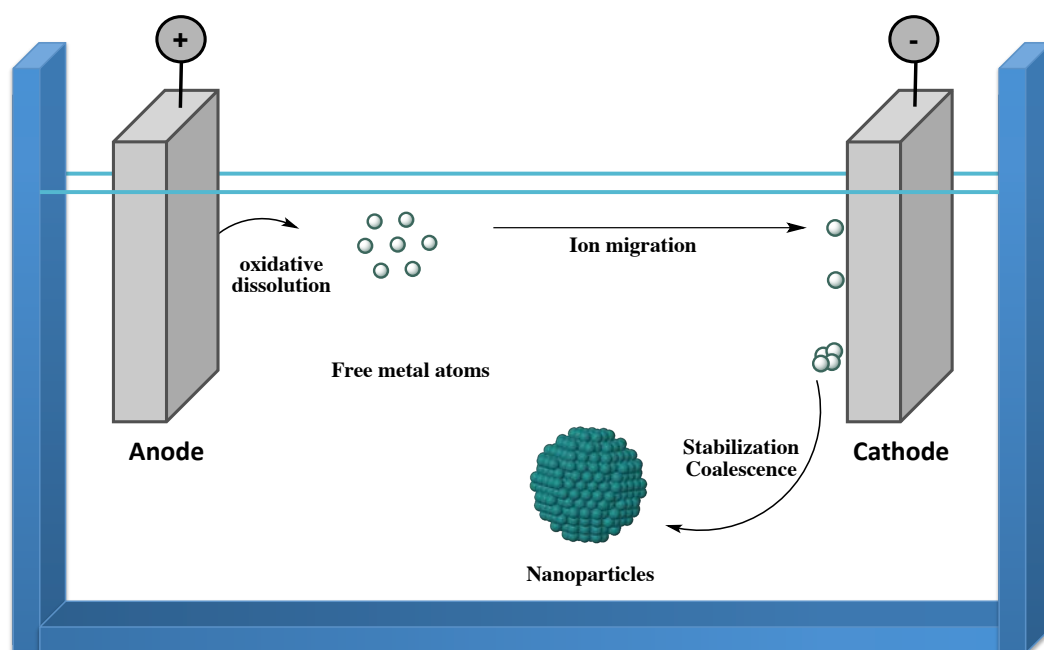


Figure 9. Electrochemical synthesis of metal nanoparticles. (Adapted from reference 9h).

As an example of this methodology, Figure 10 shows Ag NPs prepared by Chen and co-workers by applying a reducing potential to an aqueous phase containing KNO_3 , AgNO_3 and poly(*N*-vinylpyrrolidone) (PVP) under mechanical agitation.[23]

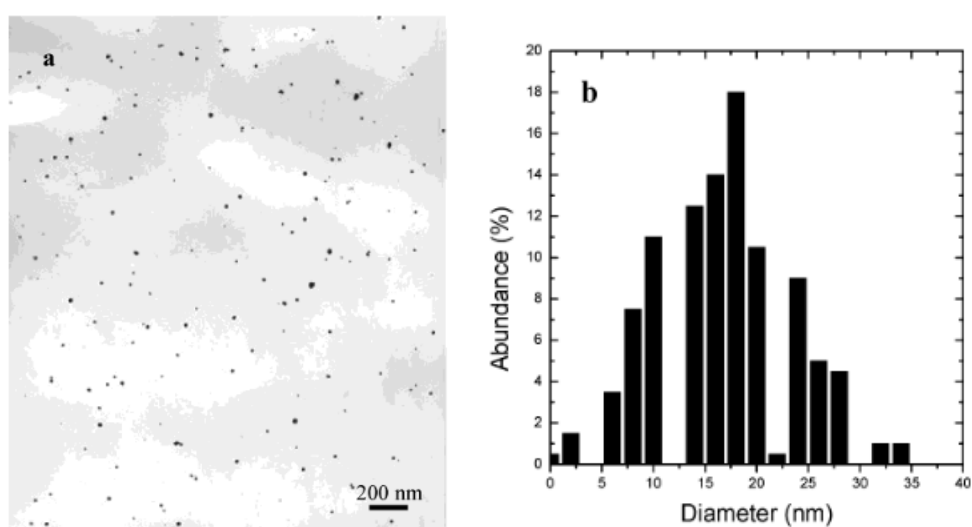


Figure 10. TEM image (a) and particle size distribution (b) of silver nanoparticles electrochemically synthesized in the presence of PVP under mechanical stirring. (Adapted from reference 23).

1.2.2.3 Reduction of organic ligands in organometallic precursors (Organometallic approach)

This methodology was developed by Chaudret and Philippot[24] and starts from low-valency (ideally zero) metal complexes whose ligands are typically reduced by hydrogen. The reduced ligands leave the zero-valent atom centre, allowing the clustering of the metal atoms (Figure 11). This methodology is also known as the organometallic approach.

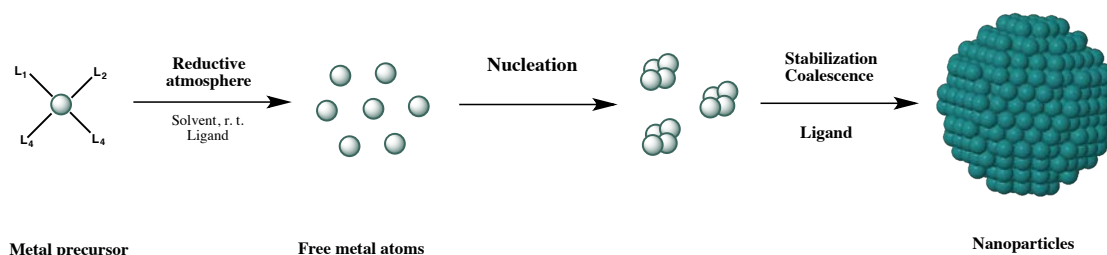
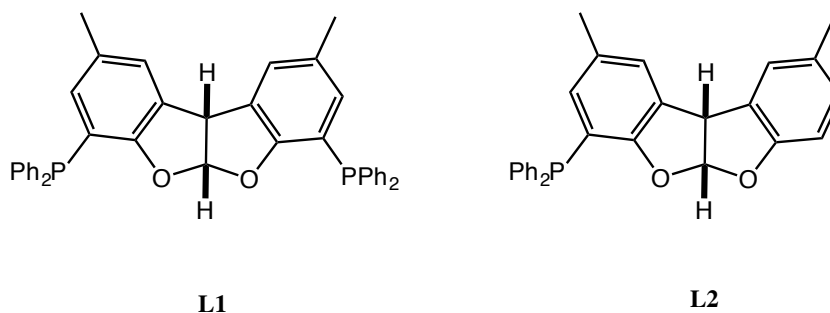


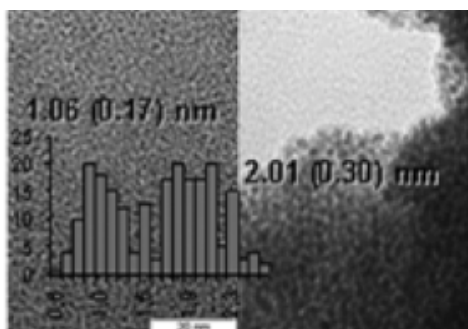
Figure 11. Organometallic approach for the synthesis of metal nanoparticles. (Adapted from reference 24).

The synthesis normally requires an organometallic complex containing an olefinic or polyolefinic ligand able to be hydrogenated for the further releasing of the bare zero-valent metal atoms.[24] The reactions take place in very mild conditions (room temperature or below) in order to achieve a rigorous control of the surface. Additionally, a stabilizing agent (ligand, polymer, solvent, etc.) should be present in the reaction media to properly stabilize the nanoparticles. In this way, the surface of the nanoparticles is well-known since only the solvent and the stabilizing agent are present on it. Ideal candidates are zero-valent complexes such as $[\text{Ni}(\text{cod})_2]$, bis(1,5-cyclooctadiene)nickel(0),[25] $[\text{Ru}(\text{cod})(\text{cot})]$, (1,5-cyclooctadiene)(1,3,5-cyclooctatriene)ruthenium(0)[26] and $[\text{Pd}_2(\text{dba})_3]$, tris(dibenzylideneacetone)dipalladium(0)[27] which decompose under low dihydrogen pressures. Additionally, another type of organometallic complexes containing alkyl, allylic or cyclopentadienyl groups able to easily decompose can be used but in these cases not only is the ligand reduced but also the metal center as for instance, the case of the $[\text{Rh}(\text{C}_3\text{H}_5)_3]$, tris(allyl)rhodium(III)[28] and $[\text{Co}(\text{coe})(\text{cod})]$, (1,5-cyclooctadiene)(cyclooctadienyl)cobalt(I).[29]

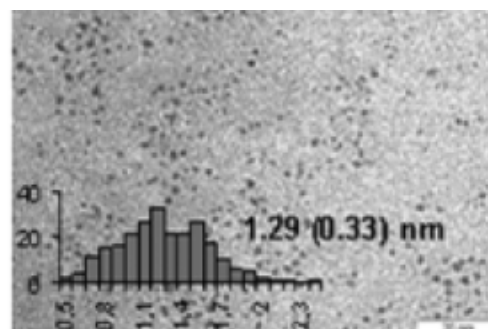
For instance, Chaudret, Van Leeuwen and co-workers prepared different mono- or diphosphine stabilized Ru NPs by decomposition of a THF solution of the organometallic precursor [Ru(cod)(cot)] in the presence of 0.1 or 0.2 equivalents of the corresponding phosphine under 3 bar of dihydrogen (Figure 12).[30]



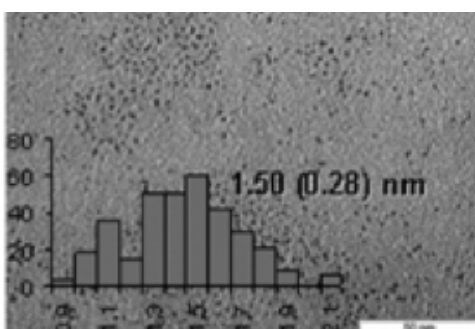
a)



b)



c)



d)

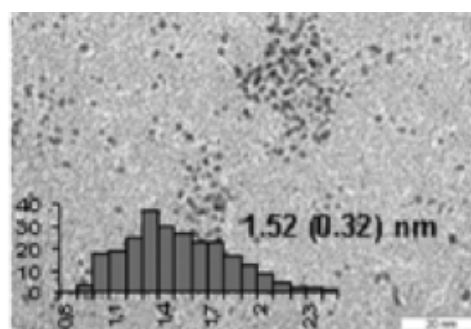


Figure 12. TEM images of Ru NPs and their size distribution for (a) 0.1 equivalents of L1, (b) 0.2 equivalents of L1, (c) 0.1 equivalents of L2, (d) 0.2 equivalents of L2. (Adapted from reference 30).

1.2.2.4 Chemical vapor deposition (CVD)

This methodology consists in the vaporization of metal precursors and their decomposition onto a surface to form nanoparticles.[31] This reaction requires an activation energy to vaporize the precursor, which can be provided thermally, by plasma and by laser. Thus, the precursors in gas phase react with a substrate (surface) where their atoms are deposited.

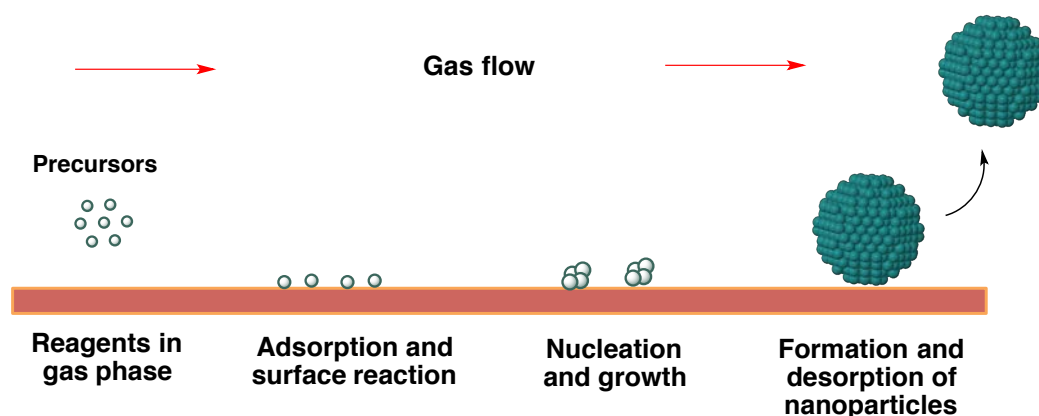


Figure 13. General chemical vapor deposition mechanism for the formation of supported nanoparticles. (Adapted from reference 31).

1.2.2.5 Thermal, photochemical and sonochemical decomposition

These methodologies consist on the decomposition of organometallic complexes by heat,[32] light[33] (Figure 14) or acoustic phenomena[34] to release the zero-valent atoms to form metal nanoparticles in the presence of a stabilizer.

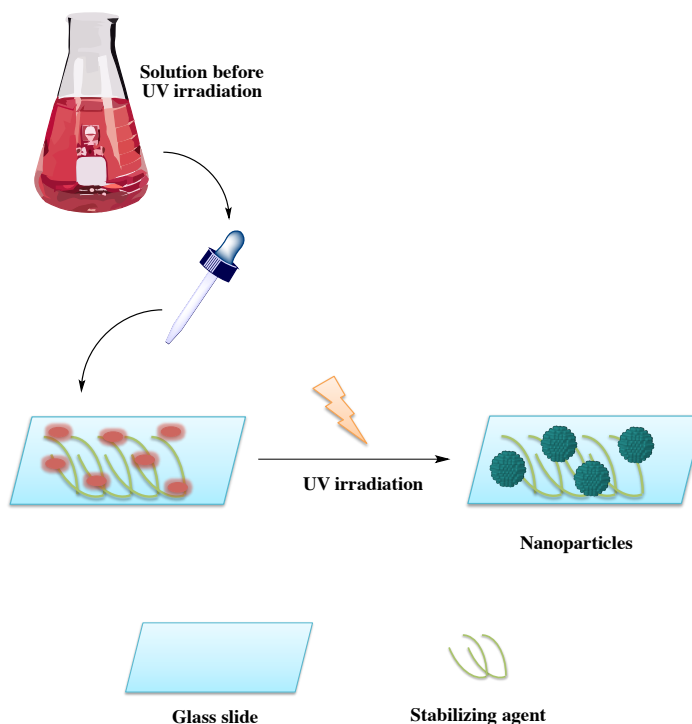
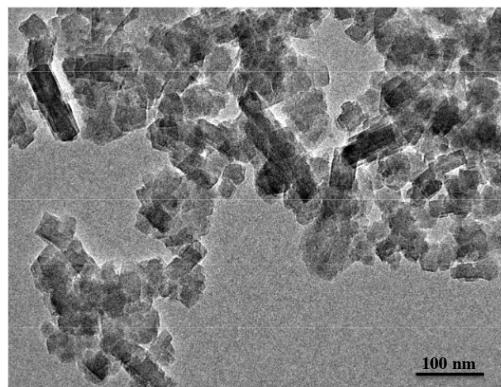


Figure 14. Photochemical decomposition for the formation of metal nanoparticles. (Adapted from reference 33c).

For instance, Mintova *et al.* prepared Ag NPs by photochemically irradiating UV light to both a suspension of AgNO_3 and a suspension of AgNO_3 containing faujasite type (FAU) zeolites in the presence of 2-hydroxy-2-methylpropiophenone. The authors studied the stabilizing role of FAU zeolites in the synthesis evidencing that these structures act as good NPs stabilizers, since their suspensions are maintained through the time as evidenced from their surface plasmon band resonance (Figure 15).[35]

(1)



(2)

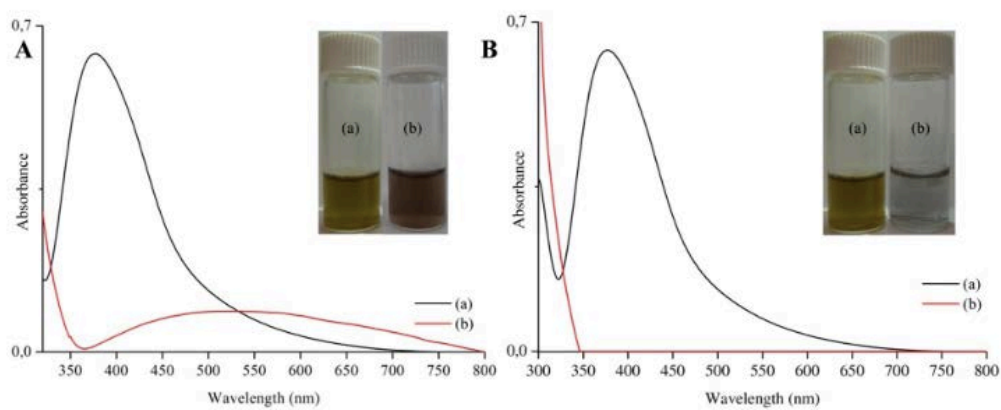


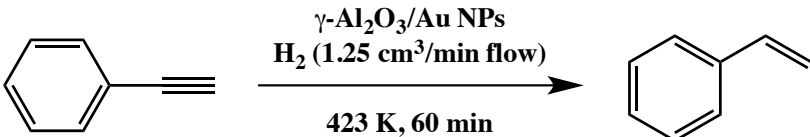
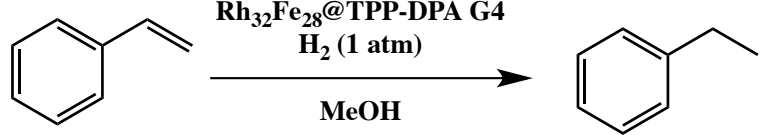
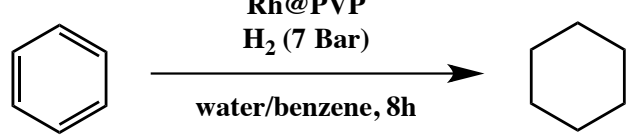
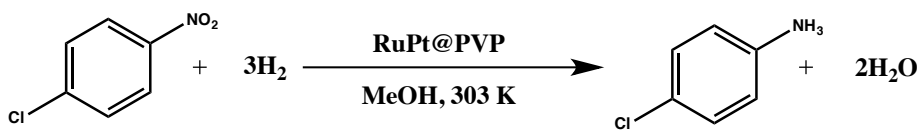
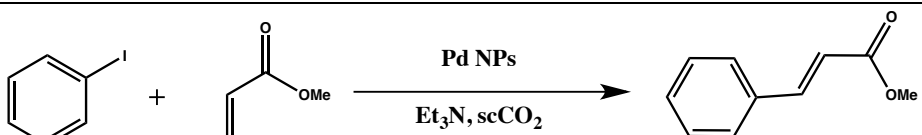
Figure 15. (1) TEM picture of FAU-Ag sample. (2) (A) Plasmon band of Ag NPs in (a) a FAU-Ag⁺ suspension and (b) pure Ag NPs in water. (B) Evolution of the plasmon band for (a) FAU-Ag and (b) pure Ag in water after 60 min. (Adapted from reference 35).

1.3 Nanocatalysis

As mentioned above, heterogeneous catalysts possess some advantages in front of their homogeneous counterparts such as the easy removal/recovery of the catalyst from the reaction media and its potential operation at high temperatures with certain stability. However, heterogeneous catalysts usually tend to be less selective due to the presence of multiple (and diverse) active sites, difficult to tune and difficult to understand from a mechanistic perspective.[1d] Transition-metal nanoparticles (MNPs), at the interface between homogeneous and heterogeneous systems, merge some of the good points of both worlds, being easy to recover from the reaction media, showing distinctive selectivity and high catalytic activity due to their dimensions and being usually stable at high temperatures. Therefore, the interest on their preparation and catalytic application has exponentially risen in the last two decades.[9d]

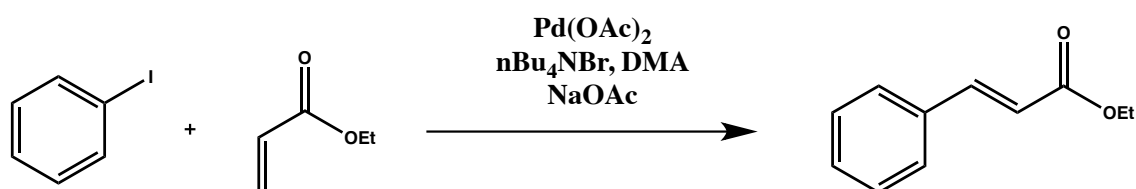
The finding of these new catalysts has prompted researchers to test nanoparticles in many catalytic reactions obtaining good efficiencies as shown in the selected examples shown in Table 2.

Table 2. Selected examples of chemical reactions in which nanoparticles has been tested as catalysts. ^a Rh-Fe bimetallic nanoparticles stabilized by the dendrimer TPP-DPAG4 = fourth-generation (G4) dendrimer. ^b PVP = polyvinylpyrrolidone

Type of reaction	Chemical reaction	Results	Reference
Hydrogenation of alkynes		Selectivity = 100% Conversion = 100 %	[36]
Hydrogenation of styrene ^a		TON = 500 Yield = 100%	[37]
Hydrogenation of aromatic compounds ^b		Yield = 100%	[38]
Hydrogenation of aromatic nitro compounds		Selectivity = 100% Conversion = 100%	[39]
Heck arylation		Selectivity = 100% Conversion = 70%	[40]

It is well-known the excellent performance of molecular homogeneous catalysts in a myriad of catalytic reactions. [2a,4] However, in some particular cases, they have been called into question, since they proved to be in fact colloidal catalysts formed *in situ* under turnover conditions.[9i, 41] For instance, Reetz and co-workers studied the Heck reaction of iodobenzene with ethyl acrylate in *N*-methylpyrrolidinone (NMP), using Pd(OAc)₂ as catalyst, evidencing then the formation of palladium nanoparticles as the true catalyst of the reaction (Figure 16).[42]

a)



b)

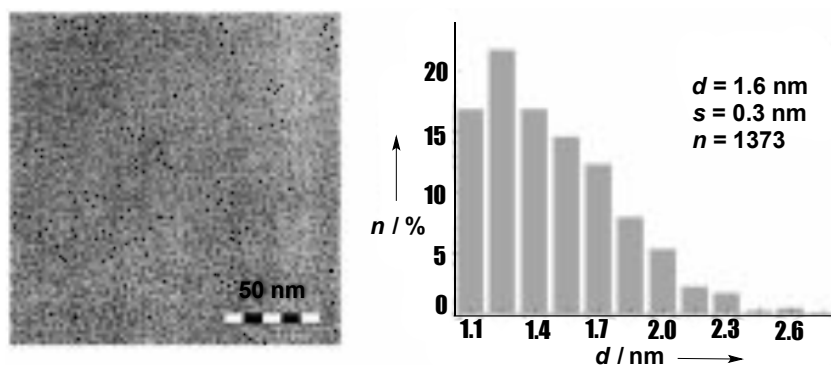
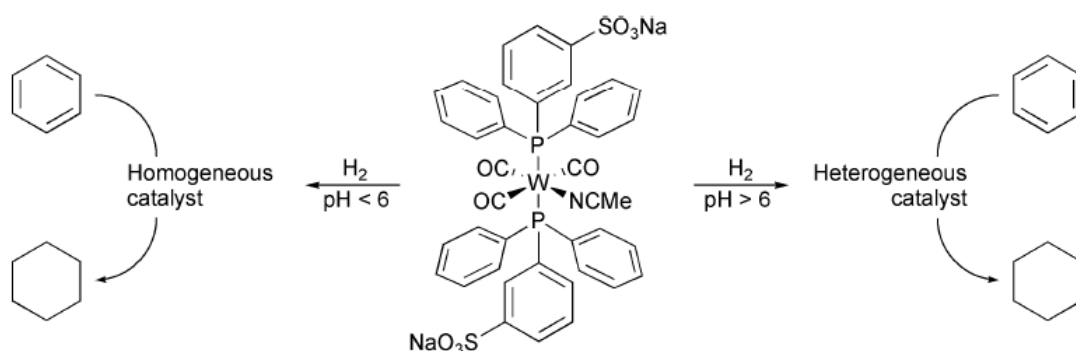


Figure 16. a) Heck reaction of ethyl acrylate with iodobenzene and b) TEM image of the Pd nanoparticles formed in the reaction together with size histogram. d = average diameter; s = standard deviation; n = number of particles. (Adapted from reference 42).

Also, since it is known that a solution of [Pd(PPh₃)₄] spontaneously forms nanoparticles within 1 day even at room temperature,[43] several authors tested palladium phosphine and NHC complexes in the Heck reaction at temperatures above 120 °C observing their instability and thus, their decomposition towards the formation of nanoparticles.[44]

Arene hydrogenation is an important reaction for industrial processes, for example the synthesis of cyclohexene (a precursor of adipic acid used to produce nylon®).[45] Nanoparticles are able to catalyze this reaction.[46] Dyson studied the mechanism for the arene hydrogenation catalysis finding that many catalysts commence as homogeneous but rapidly decompose to give heterogeneous catalysts.[47] For instance, the tungsten compound $[W(CO)_3(MeCN)(tppms)_2]$ ($tppms = 3\text{-sulfonatophenyldiphenylphosphine sodium salt}$) catalyzes benzene hydrogenation in aqueous solution, and the nature of the catalyst varies with pH (Scheme 1).[48]



Scheme 1. pH-dependent homogeneous/heterogeneous hybrid catalysis resulting from the pre-catalyst $[W(CO)_3(MeCN)(tppms)_2]$. (Reproduced from reference 47)

At or below pH 6.0, the activity exhibited is totally suppressed by addition of mercury, indicative of a heterogeneous catalysis. However, under alkaline conditions, both, the appearance of the catalytic solution and the turnover frequency for the hydrogenation of benzene differ. Significantly, addition of mercury to the basic reaction does not cause a reduction in turnover frequency, indicating a homogeneous process. It is important to highlight that turnover frequency for heterogeneous catalysis is much higher than for the homogeneous counterpart, indicating that benzene is hydrogenated by being η^6 coordinated to different metal atoms (at the surface of nanoparticles) as depicted in Figure 17.

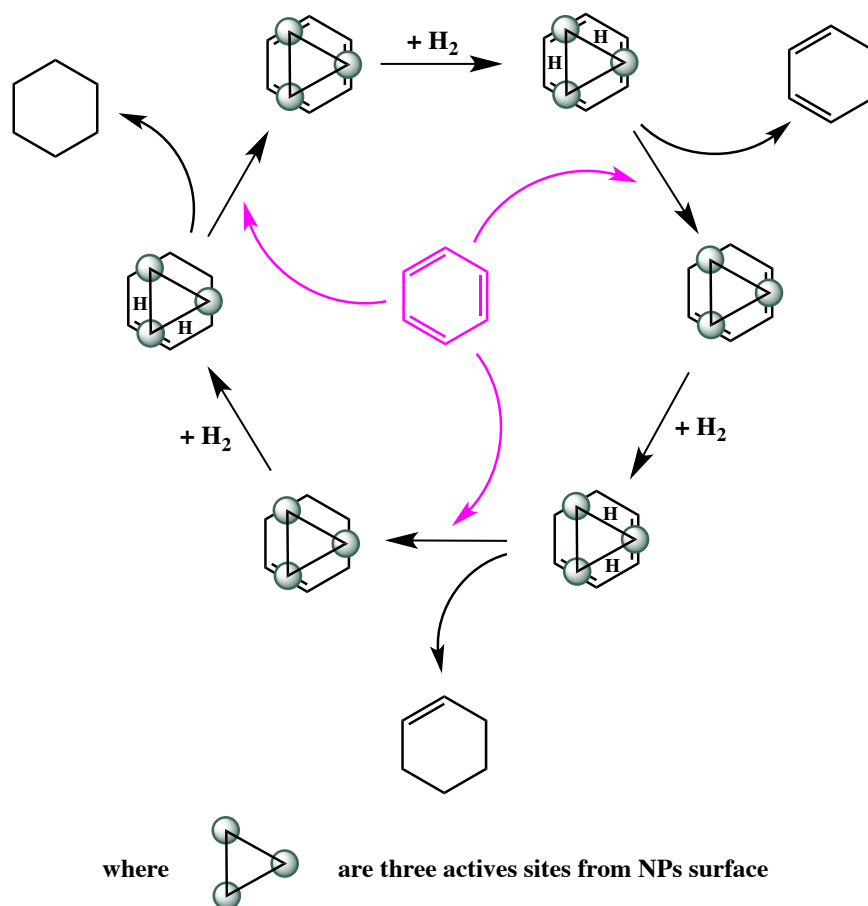


Figure 17. Proposed arene hydrogenation mechanism for heterogeneous catalysts. (Adapted from reference 47).

1.3.1 Suzuki-Miyaura C-C Coupling

Organic molecules serve for the preparation of different active pharmaceutical ingredients, agricultural chemicals or other compounds of current interest.[49] In many cases, an aromatic C-C coupling reaction is required in their syntheses such as Heck, Suzuki-Miyaura, Sonogashira, Stille and Negishi reactions (Figure 18), where two hydrocarbon fragments link to form a new molecule through a carbon-carbon bond. Although there are different catalysts that can catalyze these reactions, palladium-based complexes and nanoparticles are the main used systems due to the fact that extremely small amounts of these catalysts can be sufficient to achieve high TON and TOF values.[50]

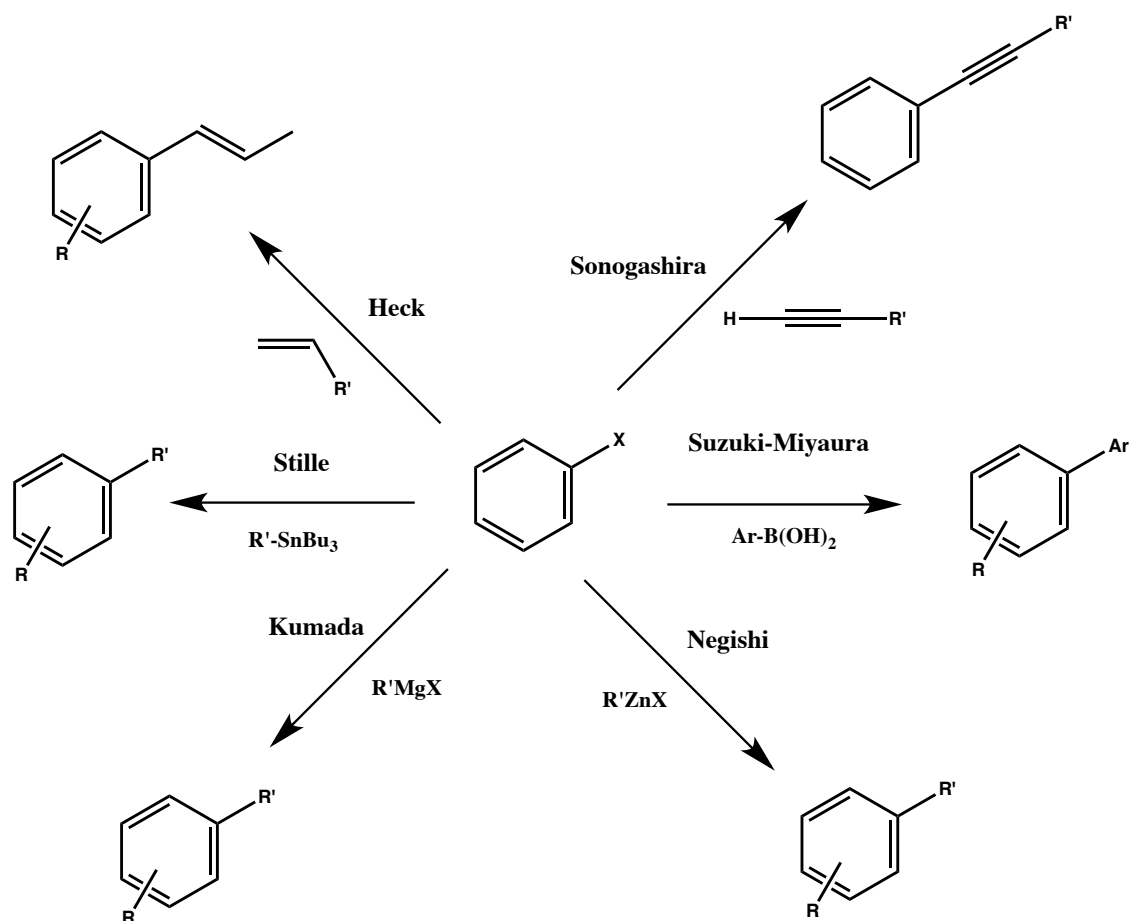
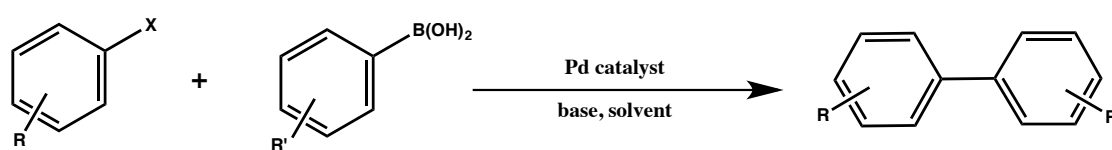


Figure 18. Pd-catalyzed aromatic substitution reactions where X = halide or other suitable leaving group.

As mentioned above, different C-C coupling reactions can be used for the preparation of different products, but the Suzuki-Miyaura is one of paramount importance due to the large scope of organoboronic-based acids, the feasible purification of the products as well as the mild conditions required.[41,51] In this reaction, typically an arylhalide and an arylboronic acid are coupled in a reaction catalyzed by a palladium complex in the presence of a base (Figure 19) although it has been also reported to work with vinyl, alkenyl and allyl halides.



X = Cl, Br, I

R = aryl, vinyl, alkenyl, allyl

Figure 19. Suzuki-Miyaura reaction.

Moreover, the organoboronic acid can also be replaced by boronic esters.[52] As an example, Buchwald and co-workers prepared a palladium complex containing the 2-(2',6'-dimethoxybiphenyl)dicyclohexylphosphine ligand (Figure 20), which is able to perform the Suzuki-Miyaura coupling of heterocyclic boronic acids with a wide variety of aryl- and bromides and chlorides with excellent yields, at extremely low amounts of Pd catalyst.[53]

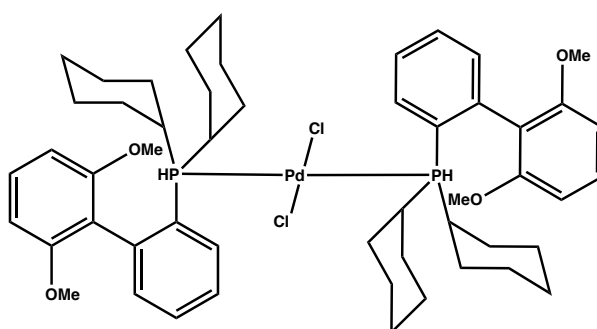
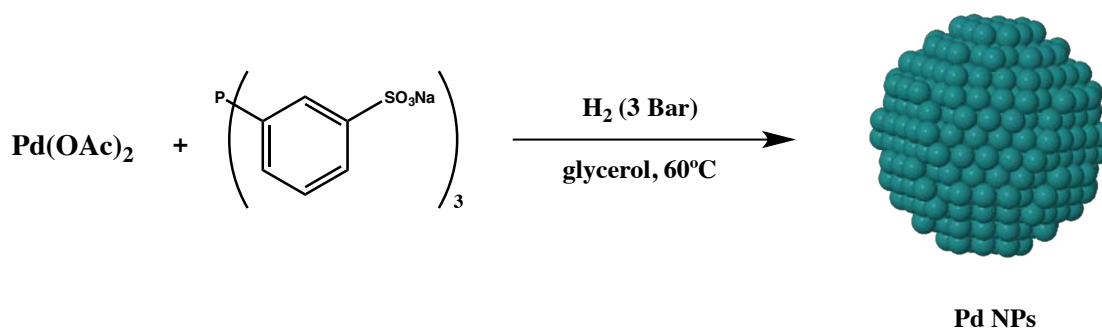


Figure 20. Chemical structure of the palladium catalyst containing the 2-(2',6'-dimethoxybiphenyl)dicyclohexylphosphine ligand.

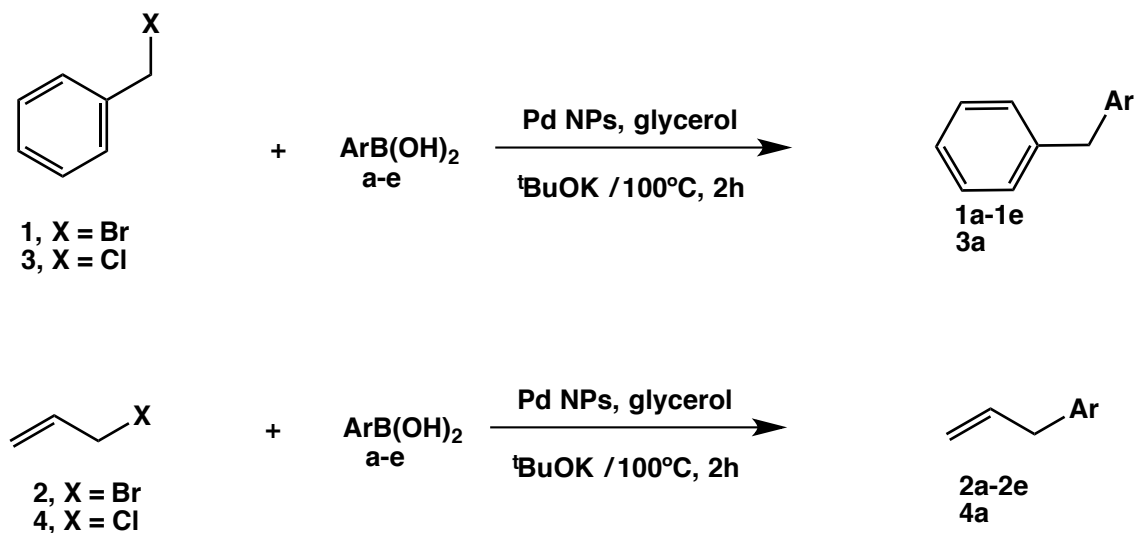
Since Manfred, Reetz and co-workers reported the first palladium nanoparticles for the Suzuki-Miyaura reaction,[54] several authors have synthesized different palladium nanoparticles and studied the different parameters that affect their capacity as catalysts for this reaction. [55]

For example, Gómez and co-workers have prepared palladium nanoparticles using Pd(OAc)₂ as precursor and tris(3-sulfohenyl)phosphine trisodium salt (TPPTS) as stabilizing agent in neat glycerol (scheme 2) and obtained excellent yields and selectivities for the Suzuki-Miyaura reaction (Table 3).[56]



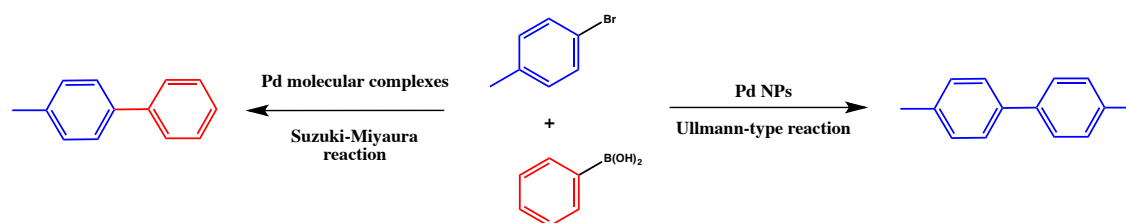
Scheme 2. Synthesis of palladium nanoparticles in glycerol using TPPTS.

Table 3. C_{sp3}-C_{sp2} bond formation by Suzuki-Miyaura cross-coupling reaction using Pd NPs as catalyst. Reaction conditions: 1 mmol of substrate, tBuOK / ArB(OH)₂ / Substrate = 2 / 1.5 / 1; in glycerol (1 mL, 13.6 mmol).^a Isolated yields after column chromatography. ^b Reaction time: 12 h. (Adapted from reference 56 with permission of *Adv. Synth. Catal.*).



Entry	X	ArB(OH) ₂	Product	Yield (%) ^a
1	1	a (Ar = Ph)	1a	>99
2	1	b (Ar = 2-Me-C ₆ H ₄)	1b	92
3	1	c (Ar = 2,6-Me ₂ -C ₆ H ₃)	1c	93
4	1	d (Ar = 1-C ₁₀ H ₇)	1d	97
5	1	e (Ar = 4-MeO-C ₆ H ₄)	1e	91
6	2	a (Ar = Ph)	2a	98
7	2	b (Ar = 2-Me-C ₆ H ₄)	2b	95
8	2	c (Ar = 2,6-Me ₂ -C ₆ H ₃)	2c	99
9	2	d (Ar = 1-C ₁₀ H ₇)	2d	92
10	2	e (Ar = 4-MeO-C ₆ H ₄)	2e	>99
11 ^b	3	a (Ar = Ph)	3a	93
12 ^b	4	a (Ar = Ph)	4a	95

Interestingly, in a recent work of our research group previous to this PhD thesis, both palladium molecular complexes and palladium nanoparticles containing hybrid pyrazole-derived ligands with alkylether, alkylthioether or alkylamino moieties were prepared.[57] These two types of species (palladium complexes and palladium nanoparticles) display highly differentiated catalytic behavior in C-C coupling reactions since although both catalytic systems are able to catalyze the Suzuki-Miyaura reaction, only palladium nanoparticles performed a catalytic Ullmann-type reaction with bromoderivatives (scheme 3).



Scheme 3. Differentiated reactivity for palladium molecular complexes and palladium nanoparticles in the Suzuki-Miyaura reaction reported by our group.[57]

The activation of aryl chlorides as substrates, typically less reactive due to its relatively high C(Ph)-X bond energy (X=Cl, 97.1 kcal/mol; X=Br, 84 kcal/mol; X=I, 67 kcal/mol) has been a challenge for the scientific community during the last decades.[58,59] Therefore, several authors have designed ligands based on phosphines, pyrazoles, ionic liquids and N-heterocyclic carbenes (NHCs) to solve this problem, obtaining almost overall conversions in several cases.[56,60] For instance, Lin and co-workers prepared cube-like Pd NPs capped by 1,3-di(dodecyl)-imidazolium chloride, exhibiting high activities for the Suzuki-Miyaura coupling with different substituted aryl chlorides.[60k]

1.3.2 Leaching in metal nanoparticle catalysis for C-C coupling reactions

The fact of using metal nanoparticles as catalysts does not mean that they are the true catalytic systems. In fact, a controversy has also arisen concerning their exact nature in catalysis: heterogeneous or homogeneous.[9d,41,51,61,] In fact, several authors have proposed an homogeneous mechanism for C-C coupling reactions in which the nanoparticles act as *reservoirs* of Pd atoms or ions.[42b,62]

Dupont and co-workers described a study of the behavior of Pd NPs (1.7 nm) stabilized in imidazolium ionic liquids as catalyst in the Heck reaction between butyl acrylate and aryl iodides (Figure 21).[63]

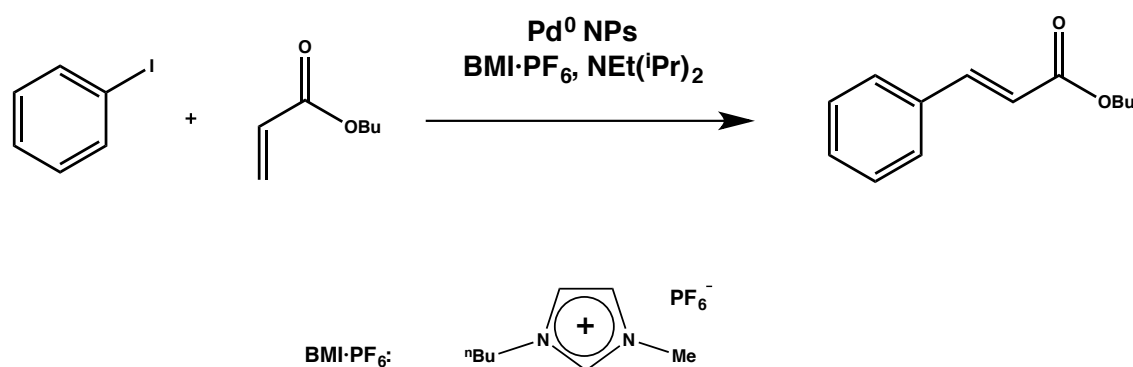


Figure 21. Heck reaction of butyl acrylate with iodobenzene. (Adapted from reference 63). BMI·PF₆ = 1-*n*-butyl-3-methylimidazolium hexafluorophosphate.

The reaction was performed in an ionic liquid/organic two-phase solvent. TEM analyses performed before and after the reaction indicated substantial increase in nanoparticle size (Figure 22).

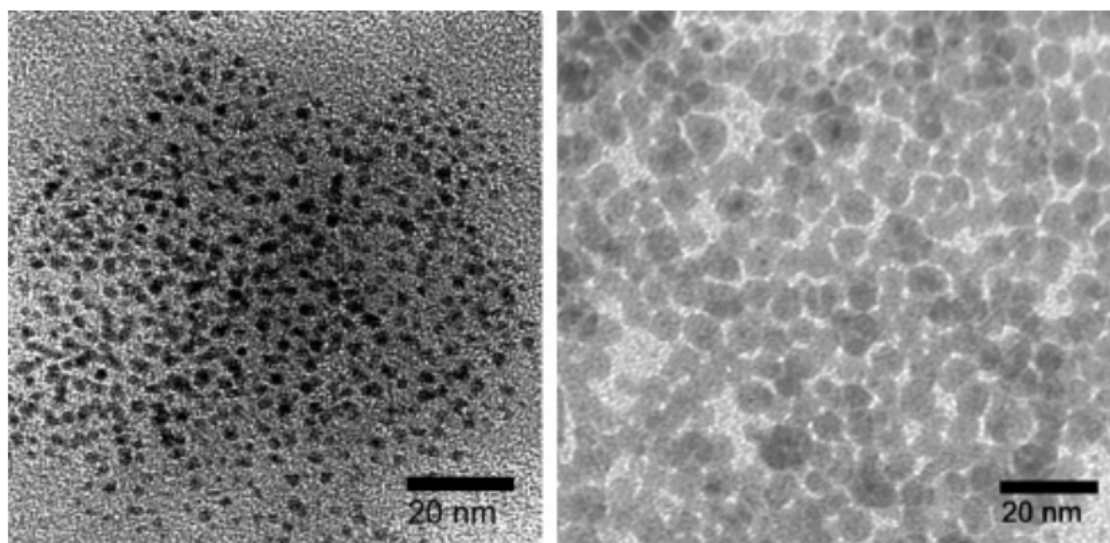


Figure 22. TEM micrographs showing the Pd NPs dispersed in BMI-PF₆ ionic liquid before (left) and after (right) catalysis, observed at 200 kV. (Adapted from reference 63).

In addition, ICP-AES analyses gave evidence of significant Pd leaching which varied during the course of the reaction. These results are coherent with the hypothesis that Pd NPs act as reservoirs of active species following the so-called dissolution-redeposition equilibrium or Ostwald ripening.

Thus, the presence of bases, solvation effects and other parameters as the temperature in the reaction conditions can promote the formation of catalytic active molecular species from the nanoparticles. In this way, the formation of molecular species can favor the Ostwald ripening in which the smaller nanoparticles are solved and deposited onto bigger nanoparticles through the time in order to achieve the most stable thermodynamic surface-to-volume state (Figure 23).[64]

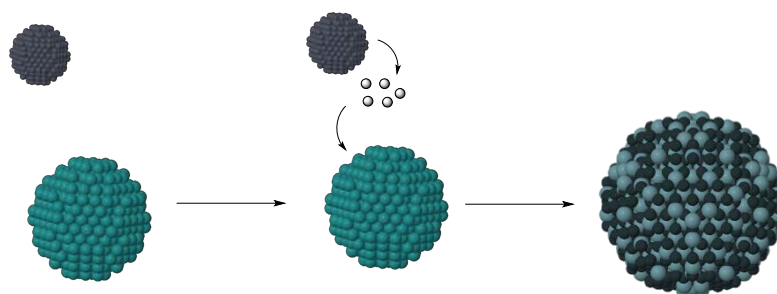


Figure 23. Ostwald ripening. (Adapted from reference 64).

One common leaching study to assess the nature of the active species under turnover conditions is the mercury poisoning. In this test, mercury is added to the catalytic mixture to poison the surface of the nanoparticles by forming an alloy, assuring no catalytic sites are available to interact with the substrates and therefore, no reaction is observed. However, mercury is not able to poison the molecular species so, if they are present and active, the catalytic activity is kept (Figure 24).[65]

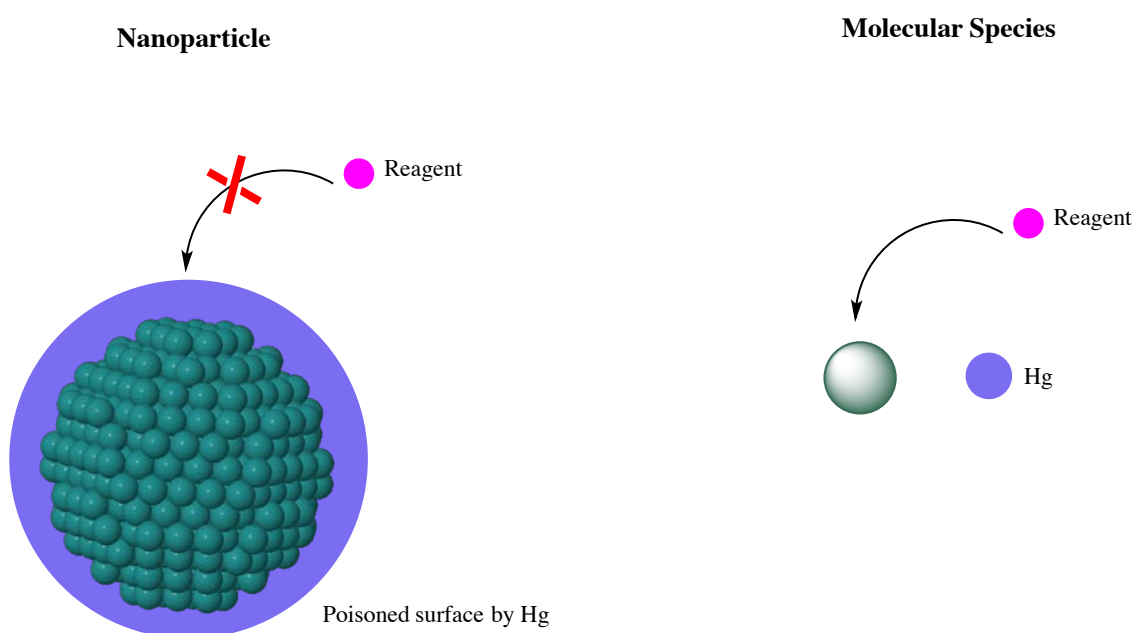


Figure 24. Mercury poisoning of a metal nanoparticle and poison-free molecular species.

It is mandatory to mention that a positive mercury test is not enough to assure that the catalytic performance arises from metal nanoparticles since, as stated above, they can act as reservoirs of molecular species. Thus, these molecular species can catalyze the target reaction followed by a disappearance by redeposition onto the NPs. Due to this fact, in 2006 Rothenberg and co-workers proved, using a special membrane reactor, how palladium atoms and ions leach from palladium nanoparticles in both, the Heck and Suzuki-Miyaura coupling reactions, resulting to be the true catalytic species.[66] The reactor is formed by two compartments, one containing the suspension of palladium nanoparticles of 15 nm average size and the other containing the reaction mixture, separated by a 5-nm porous membrane. Thus, the membrane is designed to allow the diffusion of leached palladium atoms or ions,

but not palladium nanoparticles. In this way, the monitoring of the reaction over time on both compartments gives direct information on the true catalyst (Figure 25). Thus, the authors observed the formation of soluble Pd species released from the surface of the nanoparticles in the nanoparticles-free compartment. Moreover, only in this second compartment, where the Pd species were formed, the catalytic reaction took place. Later, Rothenberg *et al.*[67] used the same device for analyzing the oxidation of silanes to silanols catalyzed by gold nanoparticles, confirming in this case that no gold escapes to the membrane permeate.

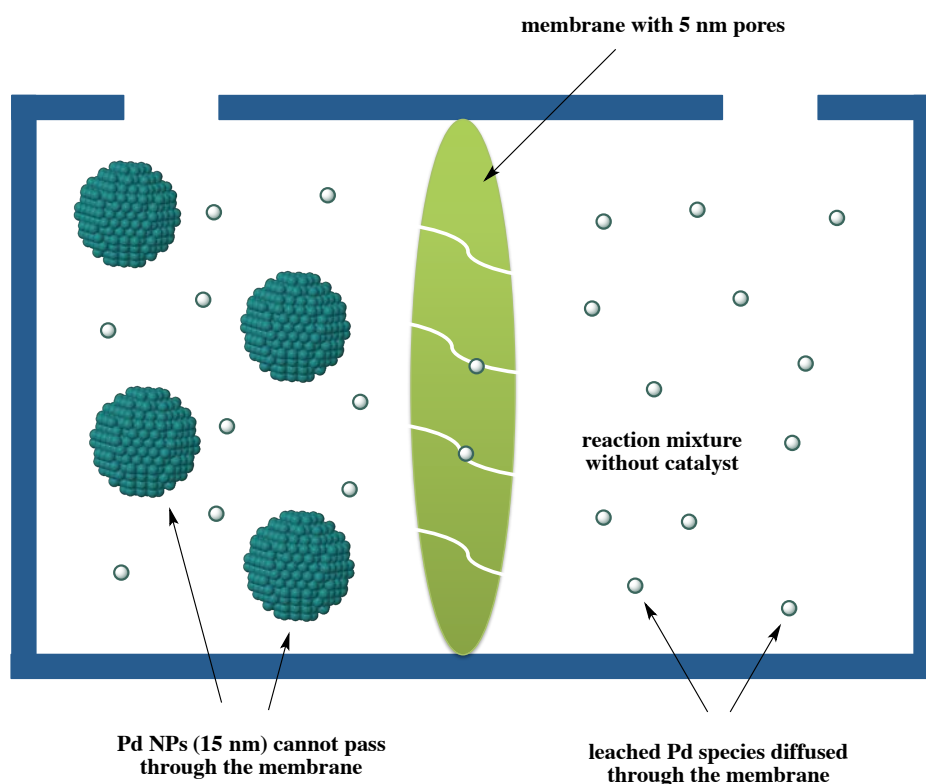


Figure 25. Scheme of the two-compartment membrane reactor designed by Rothenberg and co-workers to assess the nature of the active species in Pd-catalyzed C-C coupling reactions using Pd NPs. (Adapted from reference 67).

Additionally, there are several reports of palladium-based nanoparticles being deposited, encapsulated or embedded on a solid matrix[68] ranging from well-structured metal oxides,[69] clay[70] or zeolites[71] to softer matrices such as dendrimers[72] or polymers[73], in which researchers investigated the issue of leaching and leached material as the true catalyst.[74] For instance, Sreedhar and co-workers prepared a layered double hydroxide (LDH) $Mg_{1-x}Al_x(OH)_2Cl \cdot nH_2O$ -supported palladium nanoparticles for Heck olefination of chloroarene (Figure 26).[75] They determined by TEM studies that the size of the Pd clusters of 4-6 nm presented no changes over several catalytic cycles with no appreciable leaching, indicating that the nanoparticles do not seem to act as reservoirs in this reaction under these conditions.

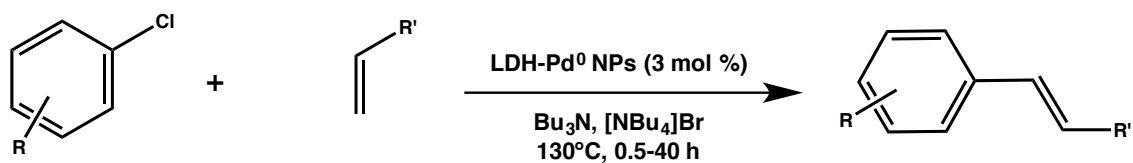


Figure 26. Heck olefination of chloroarenes with olefins using LDH-Pd⁰ NPs as catalyst. (Adapted from reference 75).

1.4 The energy problem

Human society has relied mostly on energy sources for its development. Nowadays, fossil fuels are the main energy source (Figure 27) but the CO₂ generated from their burning is one of the main reasons for the climate change, which will increase the frequencies of extreme weather events such as floods, droughts and heat waves producing forest changes and affecting the agriculture. Furthermore, the prediction for energy demands by the year 2050 is about 33 TW, which is more than a 100% increase with regard to what is consumed as of today (16 TW, 2015).[76] Thus, given the expected increase of global energy consumption and the drawbacks of using fossil fuels (ill-distributed, non renewable and highly CO₂ polluting), it is mandatory to find a new carbon-neutral renewable source of energy for the sustainable development of our society.

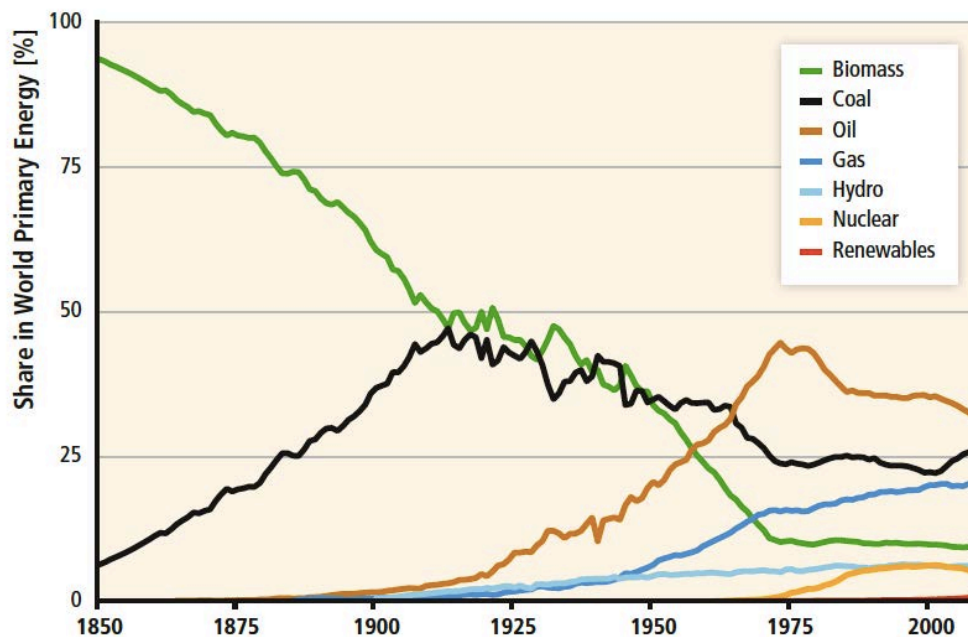
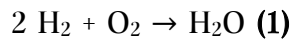


Figure 27. Structural change in world primary energy (in percent) over 1850 – 2008 illustrating the substitution of traditional biomass (mostly non-commercial) by coal and later by oil and gas. The emergence of hydro, nuclear and new renewable sources is also shown. (Adapted from reference 76e).

Different renewable sources exist nowadays including biomass, both wind and hydro powers, geothermal energy and solar energy, being the latter very promising since one hour of sunlight arriving to the Earth is almost as much as the yearly energy world consumption (ca. 13.7 TW).[77] Due to this fact, researchers have focused the investigation on this field, mainly in the conversion of solar energy into electricity by means of photovoltaic panels.[78] Although there is still room for improving their efficiency and decreasing their price, photovoltaic cells already represent a mature technology (at least talking about those based on silicon) that is well implemented in our market. However, photovoltaic panels generate electricity that has to be consumed immediately after being produced. If sunlight energy wants to be stored, transported and consumed on demand (that is the case in automotive devices) its conversion into a fuel (here called solar fuel) should be achieved.

1.4.1 Hydrogen production

An attractive and clean energy vector to solve this problem could be dihydrogen (H_2) since its combustion just releases gaseous water and energy (reaction 1).

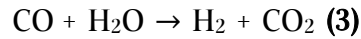
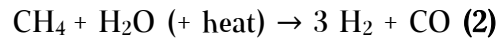


Hydrogen in molecular form can be produced from many different sources and ways that are presented in the following sections.

1.4.1.1 Steam methane reforming

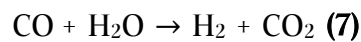
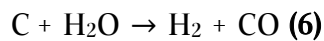
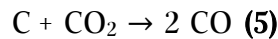
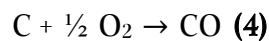
The steam methane reforming is a process that converts the natural gas or methane to hydrogen and carbon dioxide by reacting with steam in the presence of a catalyst (reactions 2 and 3). The produced hydrogen rich gas is typically of 70-75% hydrogen with smaller amounts of methane (2-6%), carbon monoxide (7-10%) and carbon dioxide (6-14%). Then, hydrogen can be separated from the other gases by flowing the produced feed through a hydrogen-permeable membrane or by condensing at different temperatures. However, the

steam reforming process implies the emission to the atmosphere of important amounts of greenhouse gases, such as carbon dioxide and carbon monoxide.



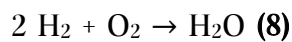
1.4.1.2 Gasification of coal

The gasification, also known as partial oxidation process, can produce hydrogen from a range of hydrocarbons including coal. In this process, the hydrocarbon reacts with low amounts of oxygen yielding a mixture of carbon monoxide and hydrogen at 1200°C to 1350°C (reactions 4 to 7). Then, hydrogen can be separated from the other gases as mentioned for the steam methane reforming (see above).



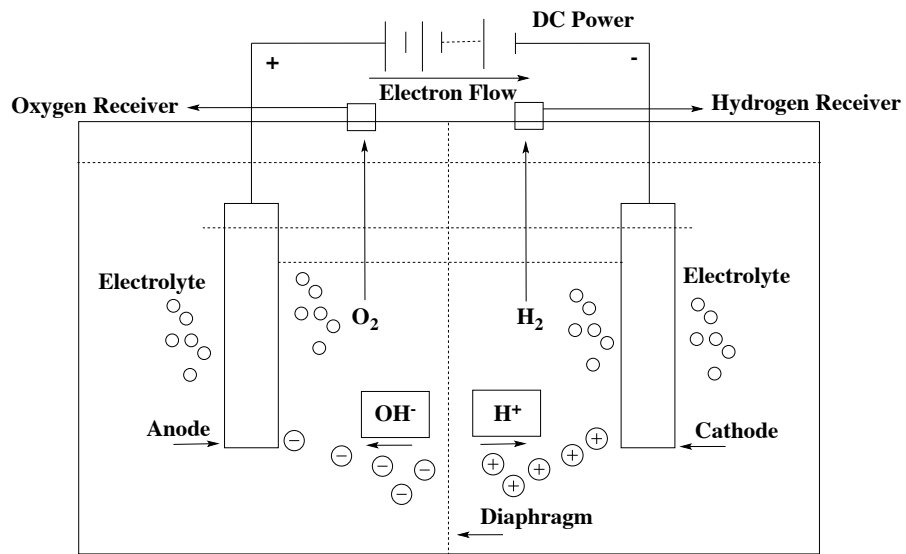
1.4.1.3 Electrolysis of water

The electrolytic process can split directly water into hydrogen and oxygen molecules using electricity and an electrolyzer device (reaction 8). Two types of electrolyzer devices can be differentiated: alkaline electrolyzers, which use potassium hydroxide electrolyte, and polymer exchange membranes (PEM) (Figures 36 and 37).



In alkaline electrolyzers systems, electrons are consumed by protons to form hydrogen on the cathode whereas hydroxyl anions are transferred through the electrolyte solution to the anode (Figure 36), where give away electrons and form O_2 . The electrolyte uses to be potassium hydroxide, which is not as corrosive as acids, the electrodes are made by nickel, which confers high activity at low cost, and finally, the diaphragm is made by asbestos or zirfon, which prevent intermixing of both, hydrogen and oxygen gases and is permeable to OH^- ions. Although at present alkaline electrolyzers are a well-developed technology, which operates with non-noble catalysts and exhibit a long-term stability, they present a reduced current density operation capacity (see Figure 28).

(a)



(b)

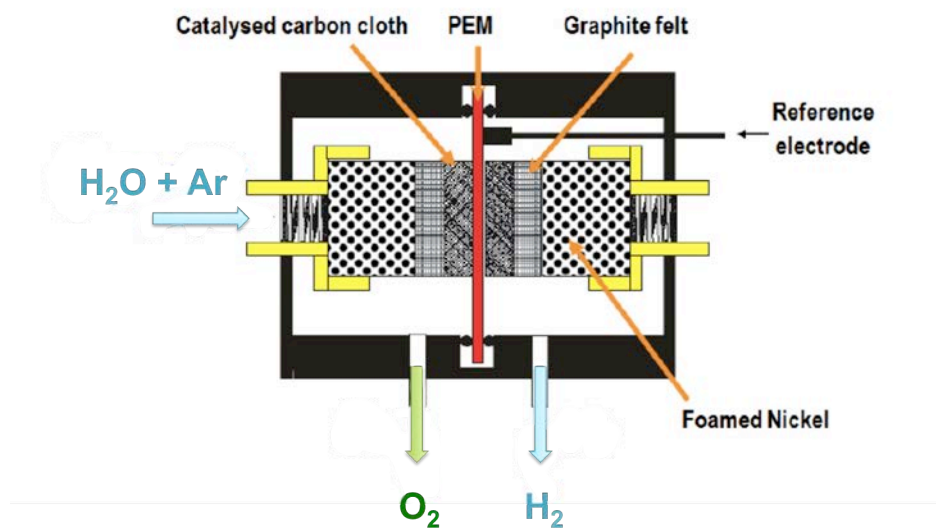


Figure 28. (a) Basic scheme of a water electrolysis system with alkaline electrolyte. (Adapted from reference 79).
 (b) Principle scheme of a PEM water electrolyzer. (Adapted from reference 80).

On the other hand, polymer exchange membranes (PEMs) employ heat-resistant polymer ion-exchange membranes, which are able to operate in a wide current density range (Figure 29). In these systems, the protons pass through the ion-exchange membrane to reach the opposing electrode. Thus, both, OH^- and H^+ ions are converted into oxygen and hydrogen gases in two different compartments (Figure 28).

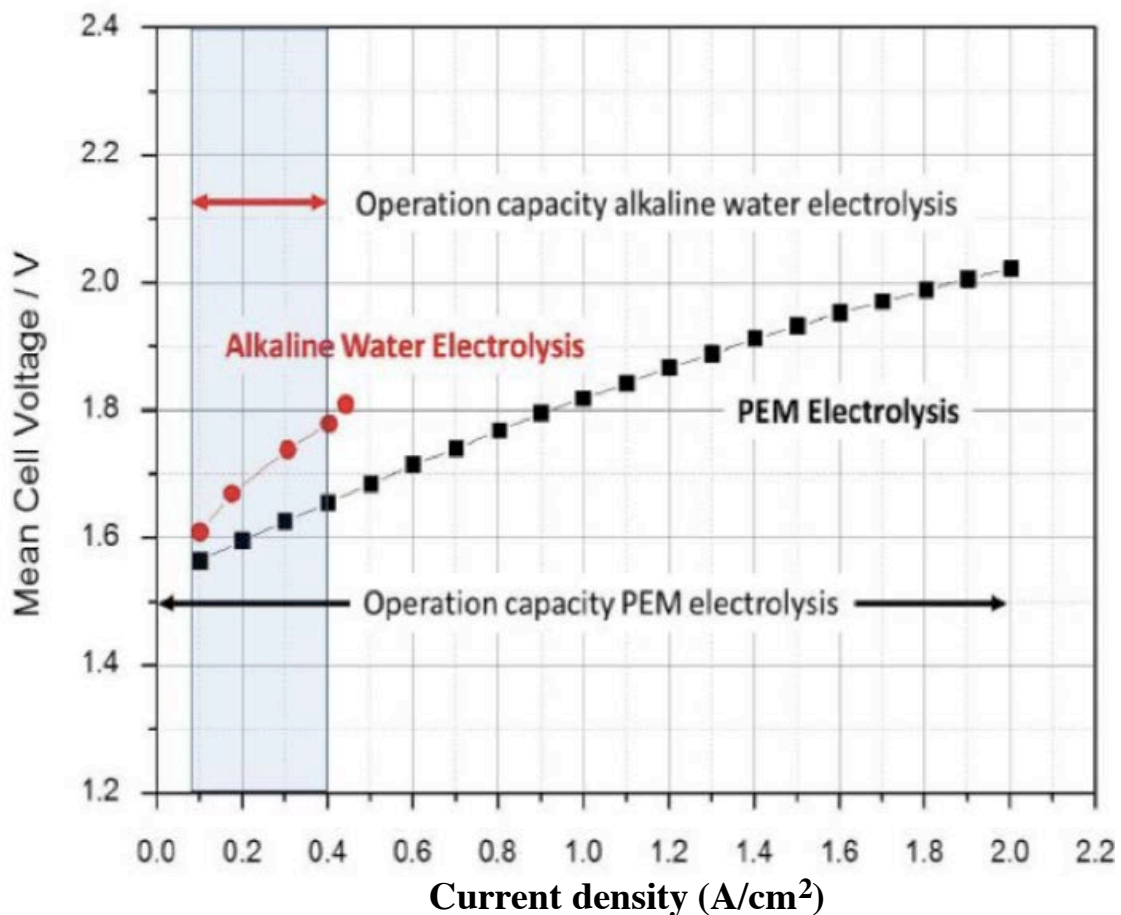


Figure 29. Voltage-current density performance of alkaline electrolyzers and polymer exchange membranes. (Adapted from reference 81).

It is important to mention that the electrolysis process is pretty expensive since it involves high energy expenditure, which can be harnessed from fossil fuels like oil, natural gas or coal, or from solar energy (when coupled to a photovoltaic device) to ensure no greenhouse gas emissions.

1.4.1.4 Biomass

The biomass-based plant is one of the best solutions to combine and integrate various processes for converting plant-based biomass to chemicals, energy and materials in order to maximize economic and environmental benefits, while minimizing waste and pollution. Thus, the conversion of biomass into hydrogen can be achieved by two technologies: the thermochemical and the biochemical processes. In the former, hydrogen-rich gas can be achieved by heating biomass at high temperature in the absence of oxygen producing an aqueous bio-oil phase after a water treatment. In the latter, a digestion of sugars by using enzymes is required to produce bio-ethanol (Figure 39). Once both the aqueous bio-oil and the bio-ethanol are produced a thermal treatment followed by steam reforming releases hydrogen gas and other hydrocarbons.

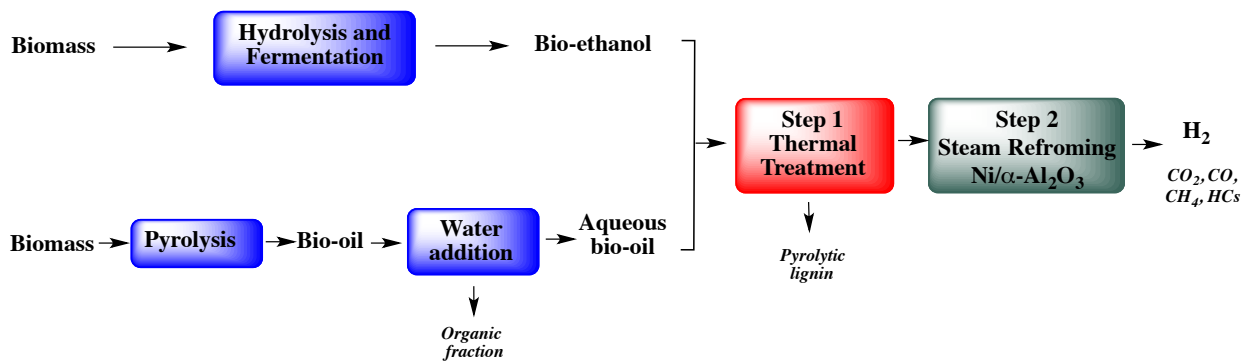


Figure 30. Schematic diagram for hydrogen production during biomass gasification and fermentation. (Adapted from reference 82).

Nevertheless, among the above mentioned methodologies, the most typically used nowadays to obtain H_2 is the steam reforming of natural gas, a non-renewable process which represents the 78% of the production (Figure 31).[83]

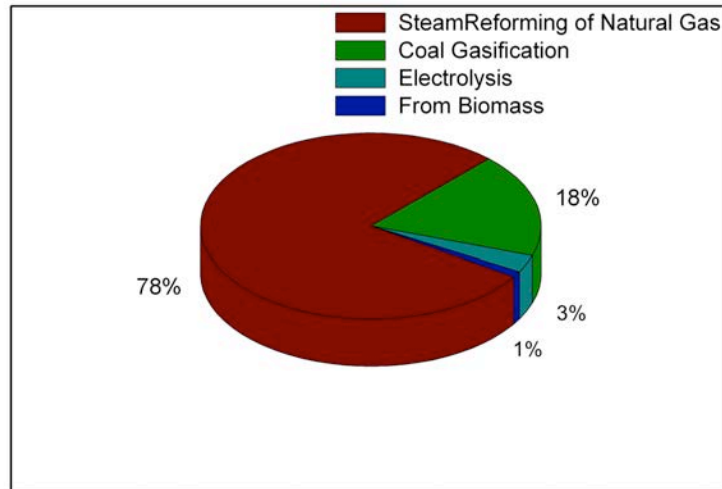


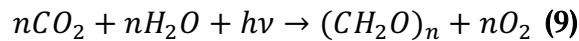
Figure 31. Percentage of hydrogen production methods in 2010. (Adapted from reference 83)

Together with the non-renewable nature of the most used production methods, the production of hydrogen from these technologies presents high production costs, which would be still higher if high purity H_2 is needed, as is the case for fuel cell applications. [84]

Hence, a different strategy should be considered to overcome these difficulties. For this purpose and as in many other cases, researchers have obtained inspiration from Nature, particularly from the photosynthetic processes where sunlight energy is stored in the chemical bonds of sugars and starches. The following sections will describe the grounds and state of the art of the field of artificial photosynthesis (see section 1.4.3), where researchers try to mimic Nature storing sunlight energy in the chemical bonds of a fuel such as dihydrogen.

1.4.2 Natural photosynthesis

Natural photosynthesis is the process used by green plants, algae chloroplasts and cyanobacteria to harvest sunlight energy in order to oxidize water and reduce CO_2 for a further production of energetically rich carbohydrates and molecular oxygen: the storing of sunlight energy into chemical bonds (reaction 9).



This process, involving a family of electronically-coupled proteins named photosystem II (PSII), cytochrome b_6f , photosystem I (PSI) and ATPsynthase embedded within the thylakoid membrane (Figure 32), presents thermodynamic and mechanistic challenges due to the high quantity of electrons involved and the number of bonds that have to be broken and formed.[85]

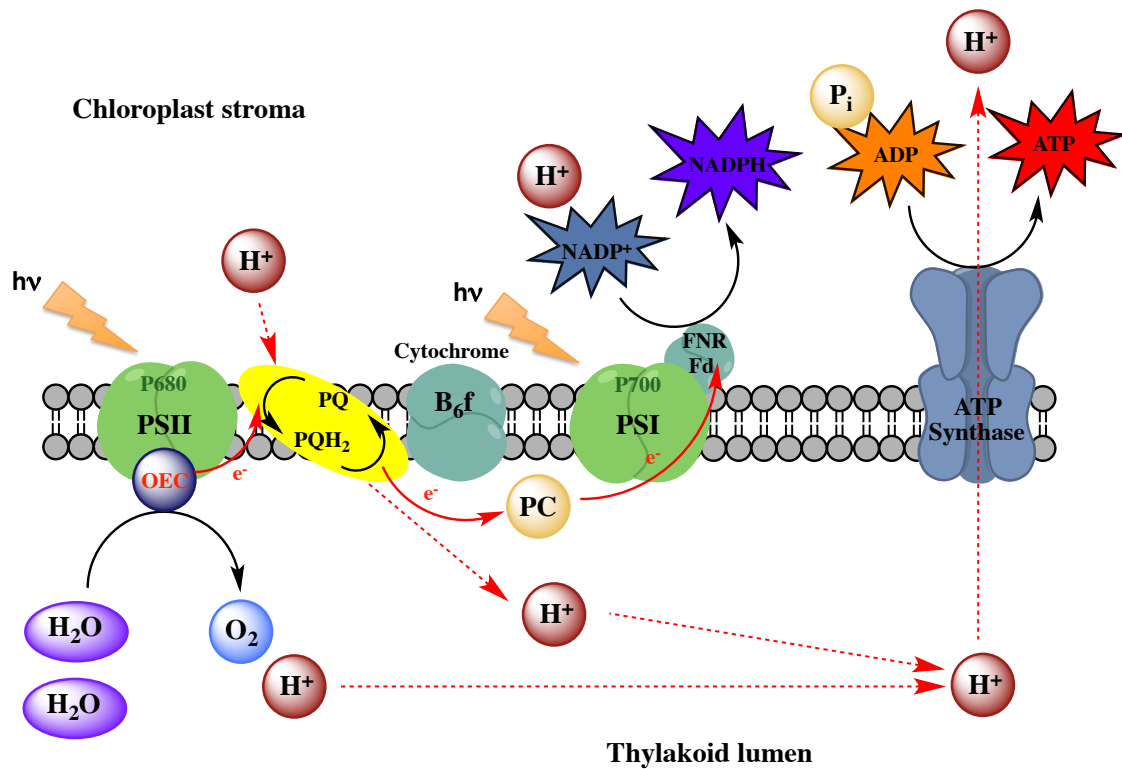


Figure 32. Schematic view of the thylakoid membrane and of the processes taking place in it.

During the photosynthesis process and after the absorption of four sunlight photons by chlorophyll P680, four protons and four electrons are detached from two water molecules together with the concomitant evolution of dioxygen. This gradient of electrons and protons is used by PSI to generate two NADPH and three ATP molecules. Once with both NADPH and ATP molecules generated, the formation of carbohydrates from CO₂ at later stages during the Calvin-Benson cycle is feasible.[86] On the oxidation side, a tyrosine residue in the PSII transfers an electron to the oxidized chlorophyll, which is then ready for the next photon absorption. The tyrosine residue then proceeds to oxidize the oxygen evolving complex (OEC). Thus, after the absorption of four sunlight photons by chlorophyll P680, the OEC is oxidized four times and is able to oxidize water to dioxygen.

For the scope of this work, the OEC and the reaction taking place in it (water oxidation reaction) are the most relevant topic and this is why they will be further developed. The OEC structure has been recently solved at 1.95 Å resolution by X-ray crystallographic studies by Shen *et al.* (Figure 33),[87] although it had been previously reported by other authors.[88,89] It presents a Mn₄O₅Ca molecular formula and consists of a cubane-like structure where three manganese and the calcium atoms are linked by oxo bridges. The fourth manganese atom is located outside the cubane-like structure and linked to two manganese atoms through a di- μ -bridge. Additionally, five amino acids and four water molecules are present in the OEC.

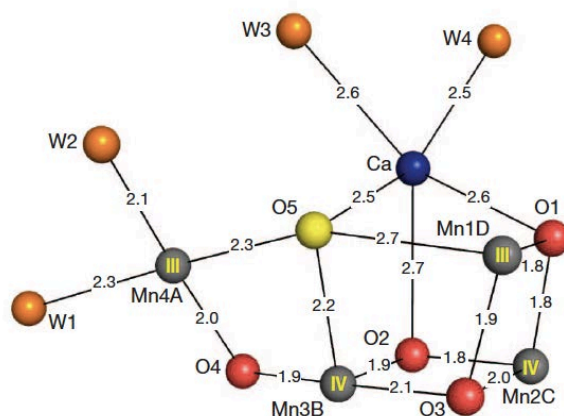


Figure 33. Structure of the OEC at 1.9 Å resolution. Manganese, purple; calcium, yellow; oxygen, red; water, orange. (Adapted from reference 87)

Although the exact mechanism for the water oxidation mediated by the OEC is still a matter of intense debate, it is accepted that during the so-called Kok-cycle (Figure 43) four electrons are released from the $\text{Mn}_4\text{O}_5\text{Ca}$ cluster, provoking its oxidation and further formation of an oxygen-oxygen double bond from two water molecules.[90]

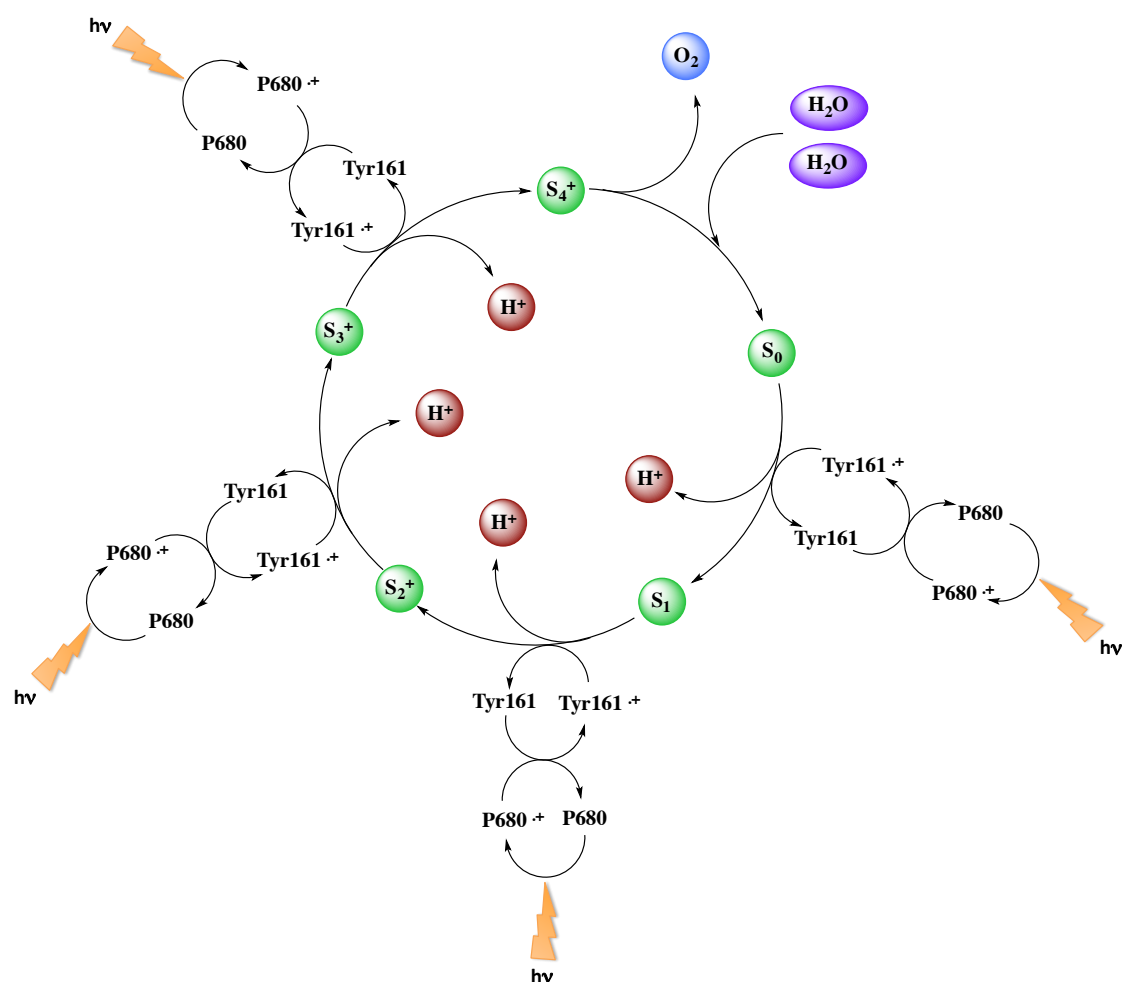


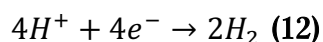
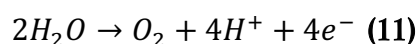
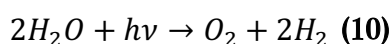
Figure 34. The Kok-cycle for the photooxidation of two water molecules. (Adapted from reference 90).

As shown in Figure 34, the OEC accumulates four oxidative equivalents to generate dioxygen, passing through five intermediate states S_i ($i = 0 - 4$) by transferring the electrons to the tyrosine residue (Tyr161) radical formed after the oxidative quenching of the excited P680 \cdot^+ .

It has been suggested that the Ca atom may play a significant role as a Lewis acid during water oxidation by modifying the nucleophilicity of its bounded water molecules.[91]

1.4.3 Artificial photosynthesis: the water splitting reaction

The water splitting reaction triggered by sunlight (equation 10) represents an attractive chemical method for storing sunlight energy into the chemical bonds of H_2 . [92] Thus, in order to split water into its fundamental constituents a first half reaction (water oxidation, equation 11) where two water molecules are oxidized to dioxygen releasing four protons and four electrons is followed by a second half reaction (proton reduction, equation 12) where these protons and electrons collapse to release two hydrogen molecules. These two redox half reactions should take place at physically separated locations so that the evolved gases O_2 and H_2 can be stored in different containers.



Given that single molecules/materials able to split water are elusive, a division-of-labor approach looks the most promising strategy. Therefore, the achievement of reliable water photosplitting technology necessitates the mastering of three main components: a light harvesting device (PS), a water oxidation catalyst (WOC) that speeds up the water oxidation reaction and a hydrogen evolving catalyst (HEC) that does the same job for the proton reduction reaction. Furthermore, these three components should be assembled into a single cell with a proton exchange membrane (PEM) and all these parts have to properly work in a

synchronized manner.[92,93] A schematic drawing of such a potential cell is shown in Figure 35. It can be thought of as a modification of the Grätzel cell, where instead of simply making electricity, this electricity is used to generate a chemical fuel, in this particular case H_2 .

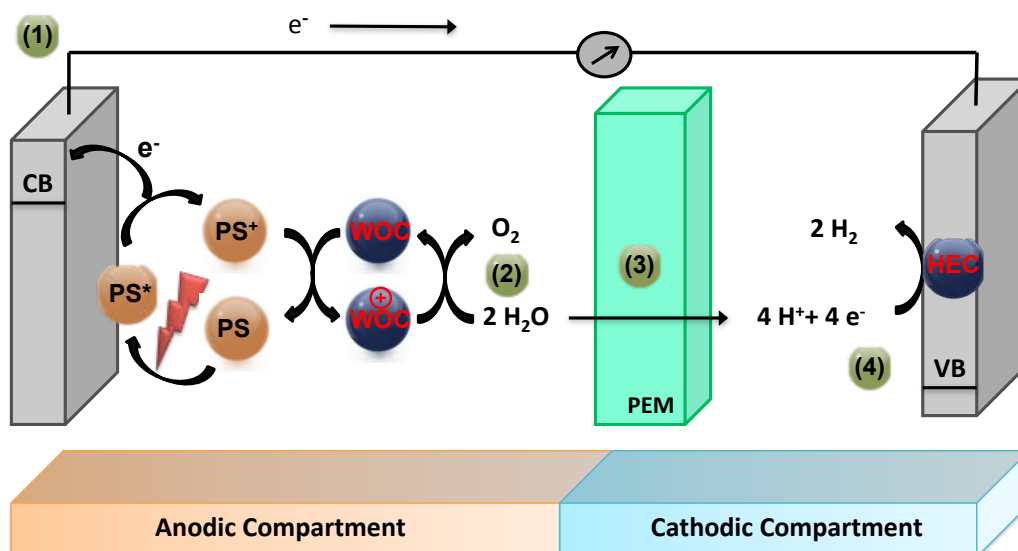


Figure 35. Schematic representation of a photoelectrochemical cell (PEC) performing the overall light-induced water splitting reaction. WOC = water oxidation catalyst, HEC = hydrogen evolving catalyst, PS = photosensitizer, PEM = proton exchange membrane, CB = conduction band of the anode semiconductor, VB = valence band of the cathode semiconductor.

As in natural photosynthesis, the water splitting process starts with the absorption of a photon by the photosensitizer which is excited (PS^*) and injects an electron in the conduction band of the anode semiconductor, generating the oxidized photosensitizer (1). The injected electrons proceed through the wires to the cathode, where the hydrogen evolving catalyst, reduces protons to hydrogen (4). The now oxidized photosensitizer (PS^+) is reduced by the water oxidation catalyst (WOC) to regenerate its initial form. Once the WOC has accumulated four oxidizing equivalents, an oxygen molecule is released (2), and the protons generated in the process migrate through the PEM (3) to the cathode semi cell where their reduction is carried out.

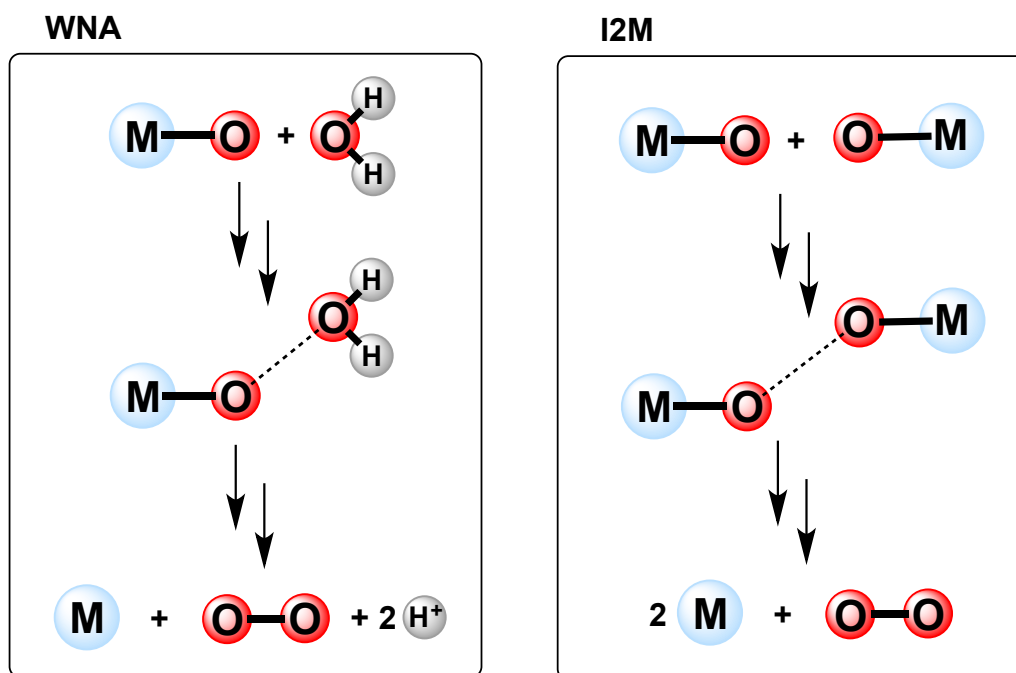
For an efficient PEC performance, many simultaneous reactions and processes have to take place harmoniously. However, the main bottleneck of the whole process is the water oxidation reaction, thermodynamically up-hill (1.23 V vs NHE at pH = 0) and intrinsically molecularly complex due to the need of a synchronized reorganization of multiple bonds.[94,95]

1.4.3.1 Water oxidation catalysis

With the aim of improving the kinetics of the water oxidation half reaction and inspired by nature's photosystem II -responsible of oxygen formation during photosynthesis-, during the last years chemists have been developing several electro- and photocatalysts[96] for this reaction at both molecular and heterogeneous level.

1.4.3.1.1 Mechanistic perspective

Heterogeneous catalysis (for instance with metal oxide nanoparticles) allows for an easy separation of catalysts and products and their recovery from the reaction media. Nevertheless, the intrinsic limitations of spectroscopic techniques for solid-state samples difficult their characterization at the molecular/atomic level and complicates obtaining mechanistic information. In contrast, molecular catalyst are excellent candidates to carry out these studies. Kinetic experiments, ^{18}O -labelling and DFT calculations have been combined to determine mechanistic details about the O-O bond formation step in water oxidation catalysis, unravelling two different mechanistic pathways (Scheme 4)[97]: (a) Water Nucleophilic Attack (WNA) to a Metal-Oxygen bond, or (b) Interaction between two Metal-Oxygen entities (I2M).



Scheme 4. Proposed O-O bond formation pathways (M = transition metal).

1.4.3.1.2 Evaluation of the catalytic activity of the catalysts

As in natural photosynthesis, artificial water oxidation catalysts (WOCs) have to accumulate four oxidative equivalents to release dioxygen. Ideally, this oxidation process would take place using photons. However, although the generation of light-driven systems is the final goal in this field, the use of chemical oxidants allows a simple and fast way of assessing the catalyst performance. Thus, a quick screening of the newly synthesized compounds before their integration inside a PEC can be carried out. Thus, both homogeneous and heterogeneous catalysts are usually tested using sacrificial oxidants: molecules that supply the oxidative equivalents required for the reaction, without the need for a full PEC device. By far, the most employed sacrificial chemical oxidants are $(NH_4)_2[Ce(NO_3)_6]$, $[Ru(bpy)_3]^{3+}$, sodium periodate and potassium peroxymonosulfate (or OXONE), although the latter is fallen into disuse.[98] However, the applicability of chemically-driven WOCs is impractical since the sacrificial chemical oxidant is irreversibly consumed, has a non-innocent character (it is an indiscriminate oxidant), is energetically inefficient (usually presenting high overpotentials) and

they are only stable at determined pH ranges (usually at acidic conditions), which compromises the stability of the catalyst.[99]

The electrochemical triggering of WOCs solve some of these mentioned issues concerning the sacrificial oxidants since it allows the control of the applied overpotential. However, the direct application of a potential to an homogeneous catalyst from a set of electrodes connected to a potentiostat usually ends up with a diffusion/electron-transfer controlled catalytic systems.[100] To solve this drawback, the catalysts can be anchored onto the electrode surface, thus providing the necessary catalyst-support electric connection for an efficient electron transfer.[101]

In the last two decades, well-defined molecular catalysts have attracted great attention as water oxidation[102] and hydrogen evolving[103] catalysts (WOCs and HECs, respectively) due to their straightforward synthesis, ease of characterization, tunable properties and easy investigation of their reaction mechanism in solution. However, an important debate about the real homogeneous nature of part of these systems has appeared since *in situ* formed metal nanoparticles have been identified several times as the real active species in catalysis.[96] This is commonly observed for first-row-based molecular complexes due to their intrinsic coordinative instability but also for any transition metal complex bearing oxidizable organic ligands. Thus, it is extremely important to check the nature of the catalytic species during and after the catalytic reaction.[104] Recently, our research group reported an example of such a transition, under turnover conditions, from a molecular complex to a highly active metal oxide WOC.[105] The system was originally intended as a molecular anode based on glassy carbon (GC) and the $[\text{Ru}(\text{bda})(\text{NO})(4\text{-pyridine-4-yl})]\text{benzenediazonium}$ complex (Figure 36) covalently attached by the electroreduction of a diazonium moiety present in the terpyridine-based ligand. Under catalytic conditions, the catalyst progressively decomposes to form RuO_2 (determined by EXAFS) at the surface of the electrode obtaining an outstanding electrocatalytic performance with this oxide-base catalyst (TOF of 300 s^{-1}). The highly efficient bimolecular (I2M) pathway taking place in solution is hampered in the solid state due to the restricted mobility of the catalyst and leads to high energy pathways that end up decomposing the system.

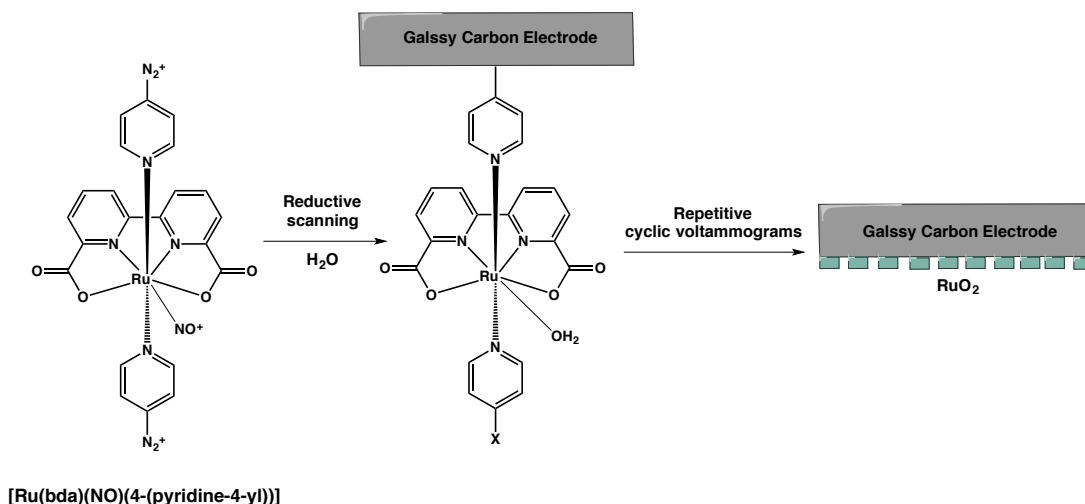


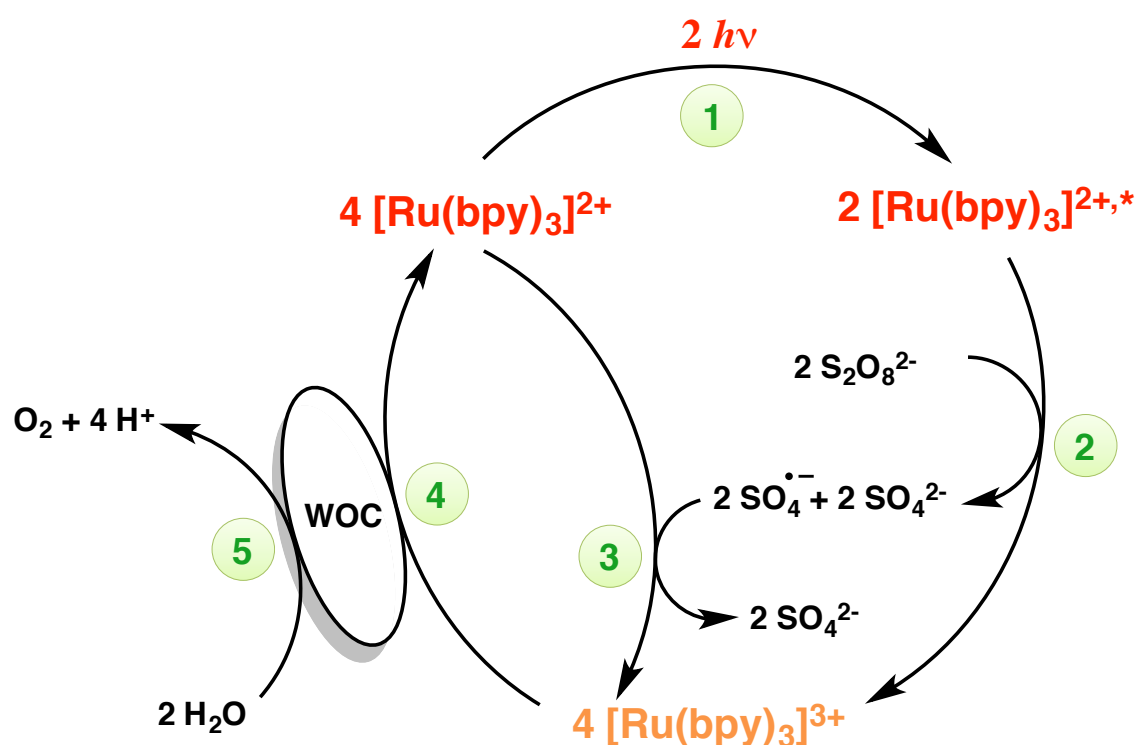
Figure 36. Anchoring of the $[\text{Ru}(\text{bda})(\text{NO})(4\text{-pyridine-4-yl})]$ benzenediazonium complex at the surface of the glassy carbon electrode and its evolution into RuO_2 under turnover conditions. (Adapted from reference 105).

1.4.3.1.3 Light-driven water oxidation catalysis

The use of metal oxide or hydroxide colloidal catalysts is of interest not only due to the practical incorporation on to the electrodes but also to their overall increased stability and robustness at extreme pH, potentials, etc.[93c], which are the requirements for a practical scalability and efficiency.

Typically, when a WOC demonstrates good performance (low overpotentials, fast kinetics and relatively high robustness) under chemical or electrochemical triggering, light-driven experiments are carried out. There is a standard protocol to study the catalytic reactivity of a given catalyst under this conditions, which is frequently based on $\text{Na}_2\text{S}_2\text{O}_8$ as sacrificial electron acceptor (SEA) and $[\text{Ru}(\text{bpy})_3]^{2+}$ (or its derivatives) as photosensitizer (PS), constituting this combination a prototypical dye-sensitized photoelectrochemical cell (DSPEC) system. $\text{Na}_2\text{S}_2\text{O}_8$ provides a good index for the catalytic reactivity since it prevents the oxidation of bipyridine from $[\text{Ru}(\text{bpy})_3]^{2+}$ and organic ligands from the catalysts, which competes with water oxidation. On the other hand, $[\text{Ru}(\text{bpy})_3]^{2+}$ has several characteristics that make it the photosensitizer of choice such as; (1) once $[\text{Ru}(\text{bpy})_3]^{3+}$ is formed by persulfate, its ability to react as a pure one-electron oxidant provides an easy standard protocol to study the catalytic reactivity of water oxidation catalysts, (2) the accessibility to a

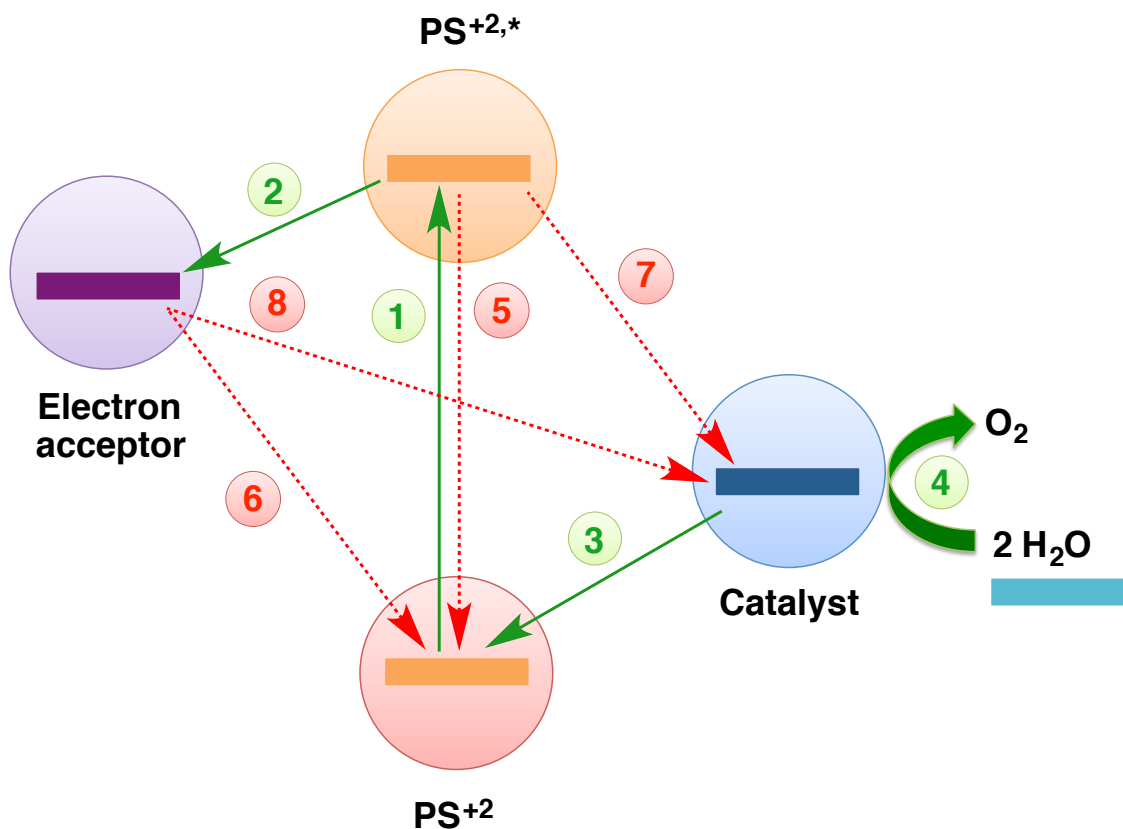
wide range of reduction potentials by tuning its aromatic bipyridine rings, and (3) the high photogeneration quantum yields of its excited states and, (4) the characteristic absorption spectra shown by both $[\text{Ru}(\text{bpy})_3]^{3+}$ and $[\text{Ru}(\text{bpy})_3]^{2+}$, which allow the water oxidation to be easily monitored by using a UV-Vis spectrophotometer.[106] As depicted in scheme 5, once $[\text{Ru}(\text{bpy})_3]^{2+}$ absorbs one photon generating the $[\text{Ru}(\text{bpy})_3]^{2+,*}$ excited state, $[\text{Ru}(\text{bpy})_3]^{3+}$ is produced in high quantum and chemical yields by the oxidative quenching of persulfate ($\text{S}_2\text{O}_8^{2-}$). In this oxidative quenching reaction, both $\text{S}_2\text{O}_4^{2-}$ anion and $\text{S}_2\text{O}_4^{\cdot-}$ radical anion are generated by dissociative electron transfer from $[\text{Ru}(\text{bpy})_3]^{2+,*}$ to $\text{S}_2\text{O}_8^{2-}$. Thus, the $\text{S}_2\text{O}_4^{\cdot-}$ radical anion can oxidize another equivalent of $[\text{Ru}(\text{bpy})_3]^{2+}$ to $[\text{Ru}(\text{bpy})_3]^{3+}$. At this point, the generated $[\text{Ru}(\text{bpy})_3]^{3+}$ species can oxidize the water oxidation catalyst driving the photocatalytic water oxidation reaction.



Scheme 5. Catalytic cycle of visible light-driven water oxidation with $\text{Na}_2\text{S}_2\text{O}_8$ and $[\text{Ru}(\text{bpy})_3]^{2+}$ using water oxidation catalyst (WOC). (1) Dye photoexcitation; (2) oxidative dye excited-state quenching by the sacrificial oxidant; (3) oxidative dye excited-state quenching by the catalyst; (4) hole injection/catalyst oxidation; (5) water oxidation.

In a prototypical dye-sensitized photoelectrochemical cell (DSPEC) system for water oxidation, the desired forward reactions (depicted by green arrows in scheme 6) are the

photoexcitation of the photosensitizers (reaction 1, scheme 6), its oxidative quenching by an electron acceptor (reaction 2, scheme 6) and the electron injection to the oxidized photosensitizer by the catalyst (reaction 3, scheme 6) that will promote water oxidation (reaction 4, Scheme 6). However, some parasitic processes contribute to decrease the DSPEC efficiency (represented by dotted red arrows in scheme 6), named back-electron transfer processes. These processes are the deactivation of phosphorescence (reaction 5, scheme 6), the excited-state oxidative quenching by the catalyst (reaction 7, scheme 6), the electron-hole recombination to the oxidized dye (reaction 6, scheme 6) and the electron-hole recombination to the oxidized catalyst (reaction 8, scheme 6).[107]



Scheme 6. Scheme of a prototypical dye-sensitized photoelectrochemical cell (DSPEC) system along with main energy levels and relevant electron transfer processes. (1) Dye photoexcitation; (2) electron injection/electron acceptor reduction; (3) hole injection/catalyst oxidation; (4) water oxidation; (5) dye radiative or nonradiative recombination; (6) electron-hole recombination to the oxidized dye; (7) oxidative dye excited-state quenching by the catalyst; (8) electron-hole recombination to the oxidized catalyst.

The first reaction involved in the water oxidation reaction is the photoexcitation of the photosensitizer (process 1, scheme 6). The electronic absorption spectra at room temperature of tris(bipyridyl)-based ruthenium(II) complexes consist of a broad band from 400-460 nm. This transition consists of a (spin allowed) metal-to-ligand charge transfer (MLCT) from a molecular orbital that has mostly Ru(II) d orbital character to a molecular orbital that has mostly ligand π orbital character. Therefore, these complexes are excited by MLCT transitions in which a singlet MLCT state is initially formed. However, this singlet state forms a triplet state by intersystem crossing (Figure 37).[108-110]

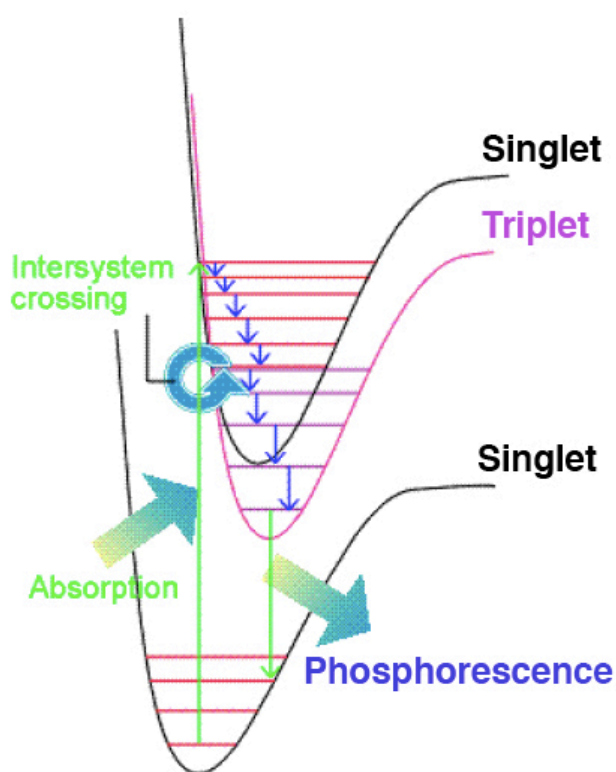
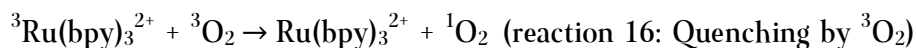
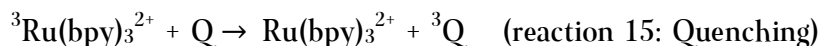
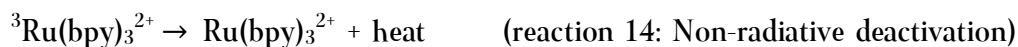


Figure 37. Jablonski diagram illustrating the phosphorescence reaction.

Since the triplet state is formed, the luminescence process is phosphorescence rather than fluorescence (reaction 13 below). At room temperature and in aqueous solution, these complexes show strong luminescence at about 600 nm with lifetimes around of *ca.* 600 ns. Two main processes that compete with the phosphorescence deactivation are the internal non-radiative process and the presence of quenchers (Q) as O₂ in its triplet state (reactions 14, 15 and 16; reaction 5 from Scheme 6).[111,112]



Thus, for the characterization of the excited states of the photosensitizers, the emission of their ${}^3\text{MLCT}$ bands (over 600 nm) have been analyzed through steady-state luminescence and emission lifetime techniques by means of quantum yields (ϕ , number of emitted photons relative to the number of absorbed photons) and lifetimes (τ , average time the molecule spends in the excited state prior to return to the ground state). Then, the one back-electron transfer process that could decrease the performance of the catalyst is the excited-state oxidative quenching by the catalyst (reaction 7, scheme 6).

Additionally, once the triplet state is formed, this ${}^3\text{MLCT}$ excited state can be quenched by an electron acceptor to form the oxidized photosensitizer (reaction 2, scheme 6). At this point, two back electron-transfer processes can occur: the electron-hole recombination to the oxidized dye (reaction 6, scheme 6) and the electron-hole recombination to the oxidized catalyst (reaction 8, scheme 6). These reactions can be modulated by the nature of the sacrificial electron acceptor. In order to compete with these non-desired phenomena, efficient catalysts (fast kinetics at low overpotentials) are required. Since some back electron-transfer processes can occur at this scenario, the excited-state oxidative quenching of the PS by the employed catalyst (reaction 7, scheme 6) becomes a pivotal reaction.

An alternative approach to study, tune and optimize the electron-transfer processes taking place between the different components in light-driven water oxidation is the photosensitizer-catalyst coupling. Despite several molecular examples of this approach have been reported in the last years,[113-116] examples of hybrid dyad systems combining a molecular PS with metal oxides are rare. In this context, Mallouk and co-workers studied the electron transfer phenomena involved in the photocatalytic water oxidation scenario for IrO_2 nanoparticles with bound and unbound ruthenium-based photosensitizers (Chart 1).[113]

They discovered that the nature of the sensitizer not only controls the size and aggregation of the nanoparticles but also the electronic communication towards IrO₂ (Chart 1). About the former aspect, for instance, [Ru(dpbpy)₃]¹²⁻ gives particles that are ca. 7 times larger than those observed with [Ru(dcb)₃]⁶⁻ or [Ru(dcb)₂(bpy(CONHSA)₂)]⁸⁻.

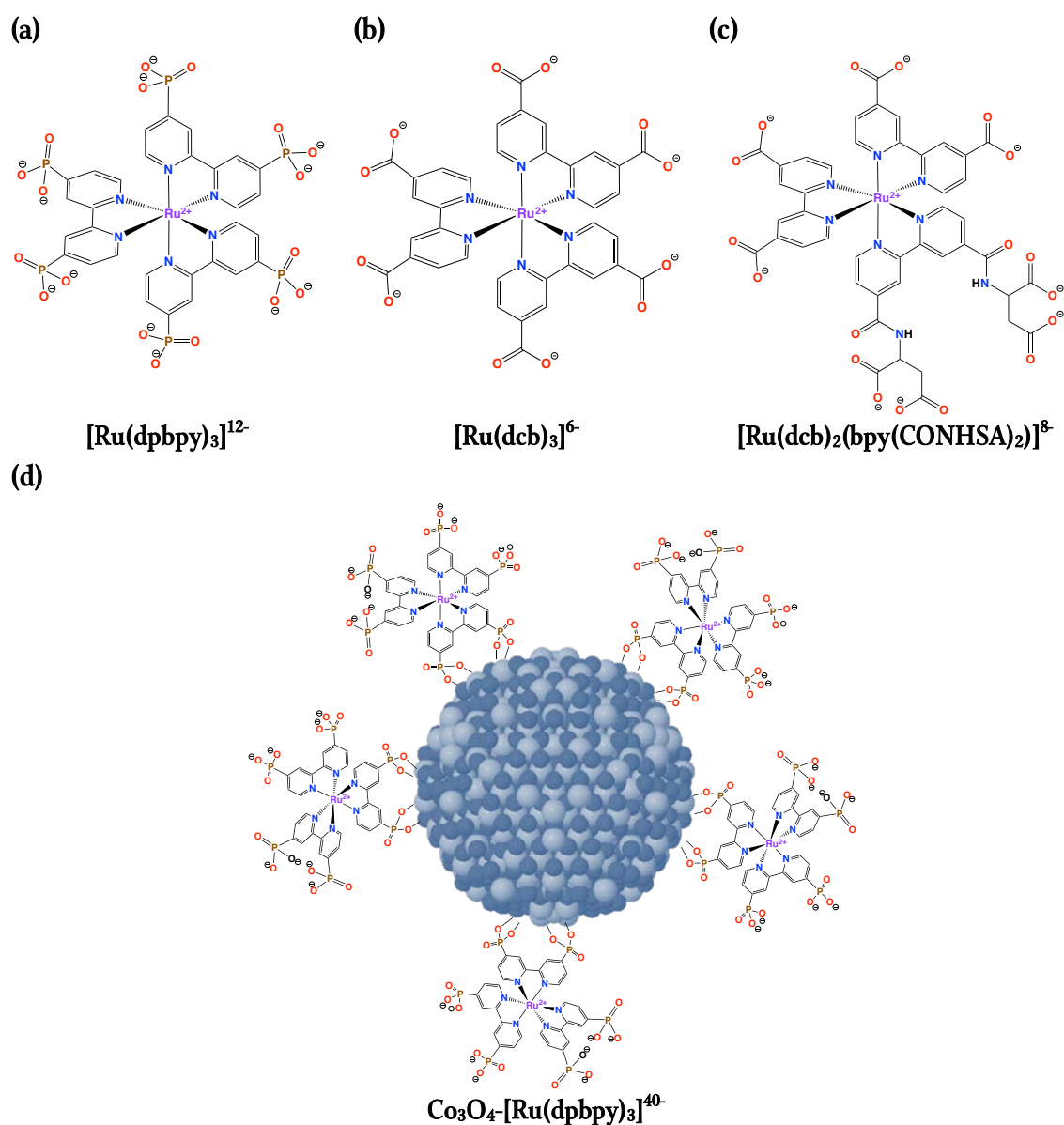


Chart 1. Ruthenium(II) polypyridyl compounds used for synthesizing sensitized IrO₂ NPs. (a) [Ru(dpbpy)₃]¹²⁻, (b) [Ru(dcb)₃]⁶⁻, (c) [Ru(dcb)₂(bpy(CONHSA)₂)]⁸⁻ and (d) the IrO₂-[Ru(dpbpy)₃]⁴⁰⁻.

Transient absorbance spectroscopy was used to study the kinetics of electron transfer between the oxidized sensitizer and IrO₂ NPs for both bound and unbound cases. The excited-state of the bound sensitizer molecules can be quenched by persulfate, which differs on the nature of the photosensitizer. For instance, electron injection from IrO₂ NP to the excited-state tethered photosensitizer (bleaching recovery process) is faster for [Ru(dcb)₂(bpy(CONHSA)₂)]⁸⁻ than for [Ru(dcb)₃]⁴⁻ (Figure 38a-b).

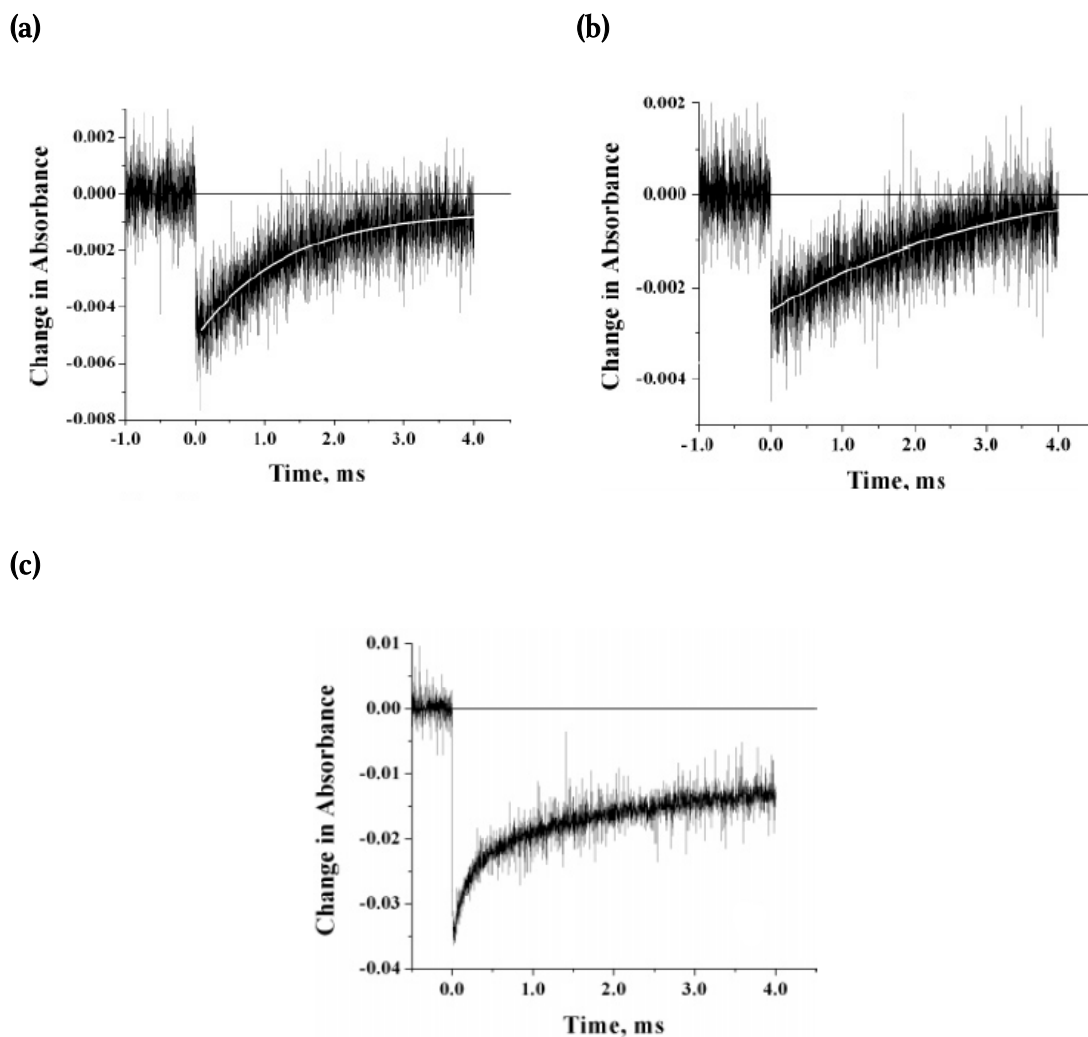


Figure 38. Single wavelength kinetic traces recorded at 450 nm following 532 nm, 10 ns laser excitation, showing the in situ formation and disappearance of Ru^{III} for IrO₂-bounded sensitizers. (a) [Ru(dcb)₂(bpy(CONHSA)₂)]⁸⁻. (b) [Ru(dcb)₃]⁴⁻. (c) succinate-IrO₂ NPs with [Ru(bpy)₃](PF₆)₂. (Adapted from reference 114).

However, as mentioned before, the excited-state of the sensitizer can be quenched by persulfate in a process that is kinetically competitive with the oxidative quenching of the tethered sensitizer by IrO₂ (reaction 7, scheme 5).

Comparing with photosensitizer-IrO₂ NPs dyads, for unbounded sensitizers, the disappearance of Ru^{III} and further formation of Ru^{II} is not completely achieved (Figure 38c) indicating a worst electronic coupling than for bounded systems.

Thus, this study is encouraging since it evidences not only the nature of the photosensitizer as a pivotal effect on electron-transfer processes but also its binding to the nanoparticles for the first time.

1.4.4 Water Oxidation mediated by Colloidal Cobalt-based nanocatalysts

Heterogeneous catalysts for water oxidation and proton reduction were known long before their homogeneous analogues.[117] For instance, in 1966, Bode *et al.* identified NiO_x as a water oxidation catalyst,[118] which was further investigated by Guibert and co-workers in 1980.[119] Also, in 1977, Morita and co-workers discovered that MnO₂ electrocatalytically evolved dioxygen under alkaline conditions.[120]. These systems are attractive due to their thermodynamic stability, high current densities, longevity, and more feasible introduction into potentially commercial photoelectrochemical cells from an engineering point of view.[121] Taking into account the recent progress in the synthesis of these materials at the nanoscale, with high surface areas, reproducibility and enhanced activities, they arise as interesting systems for catalyzing the reactions involved in artificial photosynthesis.[122]

1.4.4.1 Scope

Water electrolyzers require noble metal catalysts, such as Pt-based and Ir-based systems, in order to facilitate low overpotentials and fast kinetics in the water oxidation reaction.[123] However, given the scarcity of these metals, this approach is proving extremely difficult towards large-scale applications. Hence, the development of efficient and cost-effective catalysts from non-precious earth-abundant metals is of paramount importance.[124] Co-based nanosystems have attracted enormous interest as low-cost alternatives to noble-metal catalysts capable of catalyzing the OER taking also advantage of their large surface areas to volume ratios.[125] Although these systems have high electrical resistances, fortunately, it can be

mitigated by the use of conductive additives such as graphene, carbon nanotubes or N-doped carbon materials. These additives/supports also typically play a secondary role as stabilizers, expanding the relatively narrow range of alkaline pH where these type of catalysts are stable under catalytic conditions.[126-136]

The study of cobalt oxide nanoparticles as catalysts for the OER have attracted particular attention in recent years since their robustness, composition, activity and stability can be controlled through the nanostructuring methods. From here, Co-based NPs as catalysts for the OER have been synthesized by diverse synthetic methodologies such as (a) solvothermal methods,[126, 137-145] (b) decomposition of molecular precursors under electrocatalytic conditions,[146-148] (c) thermal decomposition of molecular precursors,[127, 149-155] (d) sol-gel chemistry,[155-157], (e) photochemical decomposition of molecular precursors,[158] (f) chemical oxidation[145, 159] and (g) pulsed-laser ablation[160]

Cobalt oxide-based catalysts have been studied electrochemically since the 50s, since different cobalt oxides such as CoO, Co₂O₃ and CoO₂ can be formed under basic conditions from molecular complexes under OER conditions.[161] In the 80s, Creutz and Sutin reported how Co^{II} salts precipitated as a heterogeneous CoO_x systems when combined with [Ru(bpy)₃]³⁺ as chemical oxidant at pH 7 but no studies for the determination of the true active catalysts were performed.[162] The most relevant breakthrough for Co-based oxides as catalysts for the OER took place in 2008, when Nocera and co-workers reported a heterogeneous phosphate-based cobalt catalyst (so-called CoP_i) showing outstanding performance at pH 7 ($\eta = 410$ mV) and a relatively simple synthesis. The catalyst is electrodeposited *in situ* on to the surface of an ITO electrode at water oxidation potentials from an aqueous solution containing Co(NO₃)₂ and K₃PO₄ or Na₃PO₄. [163] As determined by EXAFS spectra, the CoP_i catalyst is composed of Co-oxo/hydroxo clusters composed of edge-sharing CoO₆ octahedra. Casey *et al.*[164] performed ³¹P NMR analyses of the CoP_i system and suggested that phosphate anions are located in the interlayer region of a Co-based layered-double-hydroxide (LDH) structure, a model which was observed for similar systems by Stahl and co-workers (Figure 39).[165]

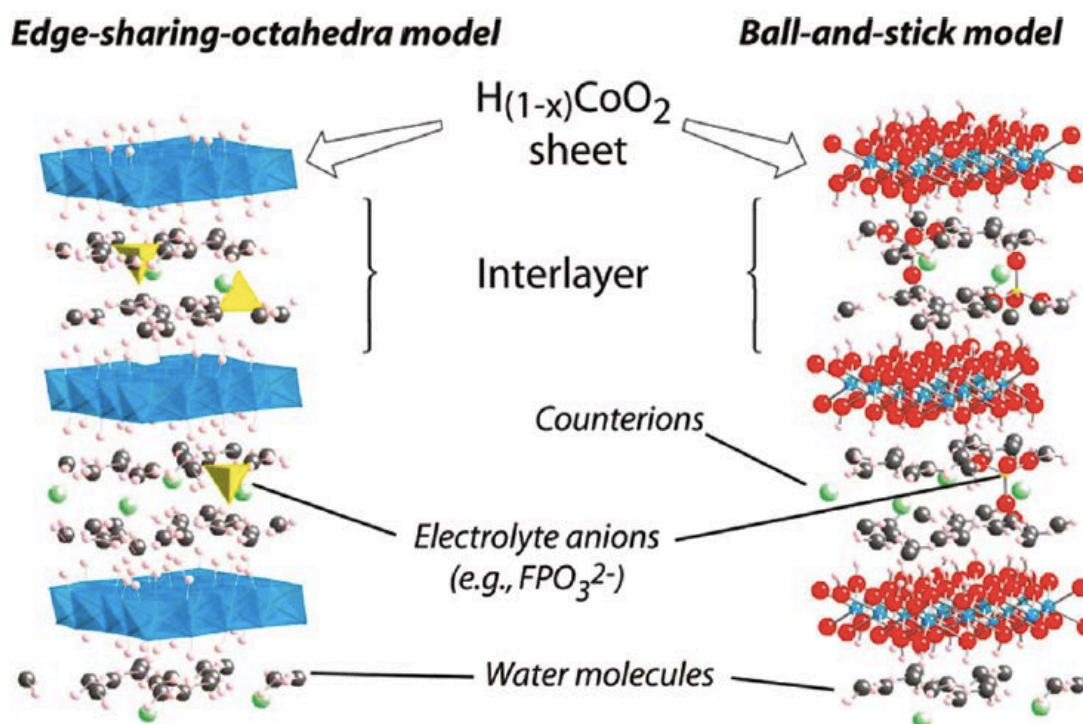


Figure 39. Depiction of cobalt-oxide layered structures that can undergo pH-dependent redox changes without lattice variations. During catalytic water oxidation, counterion movements and proton transfers rapidly compensate for changes in layer charge arising from changes in the cobalt oxidation states. (Adapted from reference 165).

The cobalt-phosphate (CoP_i) system has also been studied since it offers many attractive features for artificial photosynthesis such as simple synthesis procedure, low cost, mild operation conditions, self-repair mechanism and can characteristically undergo rapid redox reactions without large changes in structure.[163a] From here, and after several studies, Nocera and co-workers described the construction of an artificial leaf comprising earth-abundant elements: an hydrogen evolving catalyst made of NiMoZn and an oxygen evolving catalyst made of CoP_i . This device is able to harvest sunlight to split water in to H_2 and O_2 . [166]

Following the pioneering work of Nocera and co-workers, cobalt oxide NPs stabilized by phosphate-based ligands (CoP_i systems) have been recently intensely studied, showing that the presence of the P_i groups nearly doubled the photocurrent density observed in light-driven OER systems due to the increased photocatalytic stability of the P_i containing NPs.[146,159, 167,168]

1.4.4.2 Effect of NPs size, shape and composition on the catalytic activity

Several studies have dealt with the effect of size and shape of Co-related NPs on their OER activity. In general, it can be stated that smaller NPs show superior performances. For instance, Wang and co-workers evaluated the light-driven activity on the OER of Co₃O₄ NPs of 3, 10 and 40 nm average sizes finding that higher current densities were observed for the smaller ones, being the available surface essential for the activity, since a major degree of surface defects is present and thus, the binding ability of water molecules is improved.[172] Also, Weller *et al.* prepared chelated cobalt oxide NPs of 4.5 and 1.0 nm average size, finding that the latter showed higher TOFs but shorter lifetimes due to aggregation phenomena when triggered by light.[169]

On the other hand, cubane-like spinel-type cobalt oxide has received considerable attention in both electrochemical[125b,170-172] and photochemical[104,173,174] studies on the OER among a variety of Co-based catalysts due to the presence of Co³⁺ species and oxygen vacancies on the surface. In this context, Kurungot and Jiao studied Co₃O₄ NPs with different shapes, observing that blunt-edged nanocubes showed the smallest overpotentials and nanocubanes exhibit an order of magnitude higher TOF in photocatalytic OER compared to traditional Co₃O₄ spinel NPs.[126,175] In the same way, Dismukes and co-workers prepared Co-based spinel-like NPs with different shapes and found that the Co₄O₄ cubes motif present in one of these type of structures was the major determinant for their activity as OER catalysts. Although there is no direct evidence that identifies exactly what is responsible for the activity of cubic cores in the oxidation of water, it is thought that they may function analogously to the CaMn₄O₅ core of PSII (vide infra section 1.4.2).[157]

1.4.4.3 Catalytic activity dependence on the degree of crystallinity of the NPs and presence/absence of phosphate based ligands

Although it is true that the size, shape and composition are parameters of paramount importance to control the activity and the stability of the Co-based NPs as WOCs, the degree of crystallinity also plays a key role in these systems. There is an accepted consensus that amorphous materials not only exhibit higher WO activities but also larger stabilities.[138,141,157] Hence, a few authors have compared the WO activity of amorphous and crystalline Co nanocatalysts, observing that the former yield superior catalytic activities both under photochemical and electrochemical WO conditions because of their higher surface roughness.[138,140,141] For instance, Driess and co-workers prepared amorphous and crystalline cobalt oxide based NPs producing the formers superior catalytic activity under photochemical and electrochemical OER.[145] In addition to this, Frei and Jiao discovered how polycrystallinity of Co_3O_4 NPs is an important parameter for photochemically evolving oxygen (under $[\text{Ru}(\text{bpy})_3]^{2+}$ /persulfate presence) at modest overpotentials under mild pH and temperature conditions since very small crystalline domains enhance the WO activity.[173]

1.4.4.4 In situ-formed NPs vs. ex situ-formed NPs

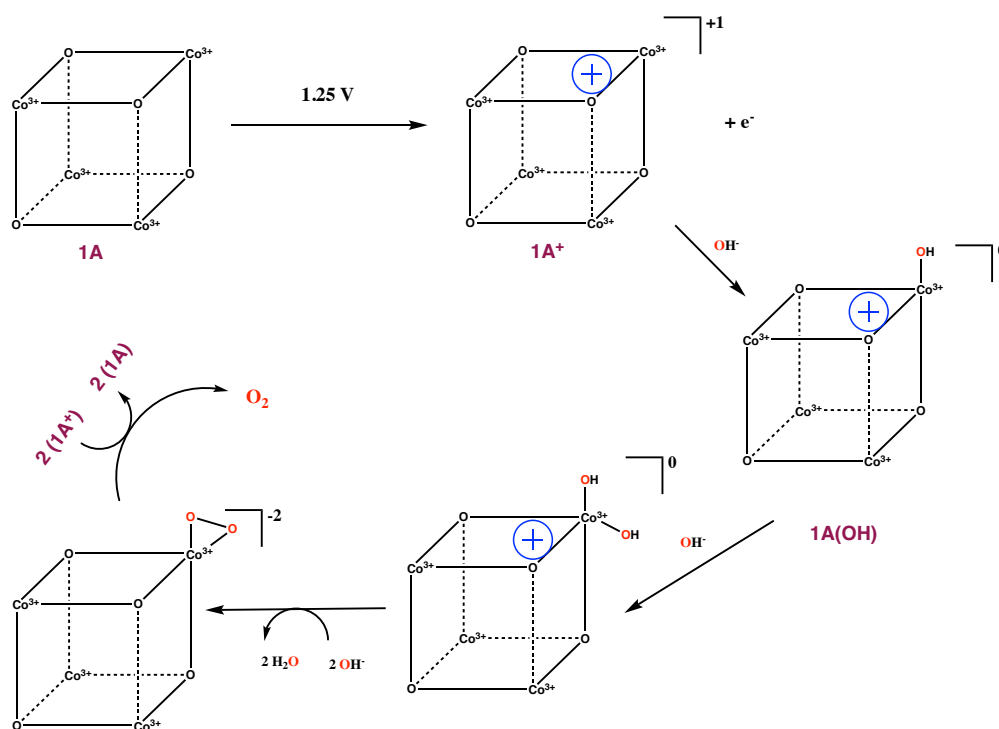
In general, cobalt-based nanocatalysts formed *in situ* exhibit higher performances than those prepared *ex situ*. This trend is observed with both photochemical and electrochemical triggering and has been attributed to the higher surface roughness and/or lower degree of crystallinity of the species formed under turnover conditions. [140,167,175,176] Several authors have investigated the activity of *in situ* formed cobalt-based NPs. For instance, Driess *et al.* have reported the *in situ* formation of amorphous $\text{CoO}(\text{OH})$ species during electrochemical WO from CoO_x ($1 < x < 2$) NPs.[145] Another relevant example is the work of Du and co-workers reporting the *in situ* electrochemical formation of CoO_x NPs onto the surface of FTO electrodes by decomposition of cobalt-based complexes. The authors show how the shape, the size and the catalytic activity of the NPs depend on the nature of the cobaloxime precursor employed during the NPs synthesis, fact attributed to the presence of

ligands in solution that controls both the nucleation process and the aggregation of the NPs while catalytically oxidizing water.[147,167]

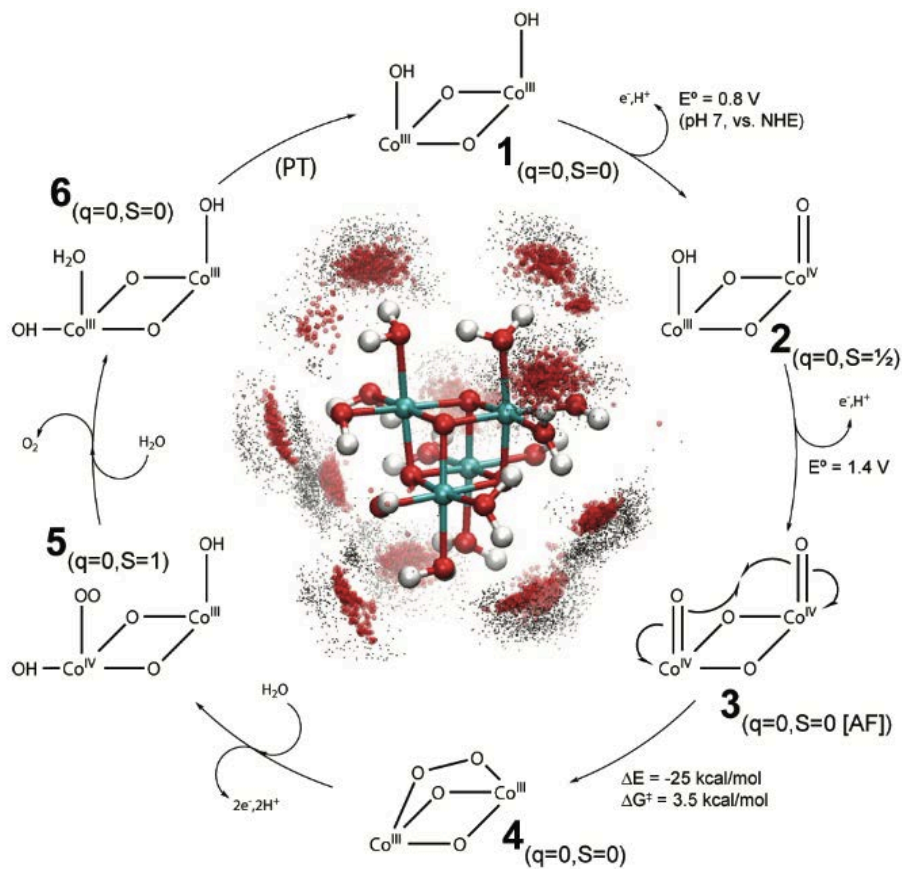
1.4.4.5 Mechanistic insights

As typically happens in catalysis, the comprehension of the mechanistic details of the water oxidation reaction is of paramount importance for the rational improvement of the employed catalysts. Even if the mechanistic scenario is relatively well-known from a molecular point of view, the mechanisms through which heterogeneous catalysts work are much less understood. Most heterogeneous catalysts are multimetal materials with different local structures, catalytic sites formed by one or more metal centers and short-lived transient species difficult to identify with the available spectroscopic techniques. Despite these difficulties, several studies, both computational and experimental, have been performed in order to elucidate the operating mechanism for cobalt-based NPs as water oxidation catalysts.

From the computational point of view, several DFT calculations have been performed to study the interaction of water with different Co-based nanocatalysts. Dismukes[177] and Van Voorhis[178] studied the energetic barriers for water oxidation in a Co_4O_4 environment. The former postulated that no water oxidation occurs by Co_4O_4 at neutral pH but, under basic conditions, coordinated hydroxide ions can form a cobalt-bound peroxide which evolves to O_2 (Scheme 7). The latter suggested a mechanism where a bis- μ -oxo-bridged Co^{III} hydroxide species is further oxidized until the bis- μ -oxo-bridged Co^{IV} oxide species and O-O bond formation takes place through the intramolecular interaction of two M-O units (I2M mechanism) (Scheme 8). In addition to this, Tilley *et al.*[179] spectroscopically evidenced a highly oxidized cobalt intermediate for the same Co_4O_4 structure, which is in accordance with Siegbahn *et al.*[180] who postulated that the Co-oxyl ($\text{Co-OO}\cdot$) radical is necessary for the catalytic activity of this fragment (species 5, Scheme 8).



Scheme 7. Proposed mechanism of hydroxide oxidation by Co_4O_4 . (Adapted from reference 177).



Scheme 8. Proposed mechanism of water oxidation catalysis by a Co_4O_4 structure. (Adapted from reference 178).

In another computational work, Chen and Selloni studied the interaction of water with the (110) NPs surface of the spinel cobalt oxide Co_3O_4 by DFT calculations. This surface shows two different terminations: one positively (A, Figure 40) and the other negatively charged (B, Figure 40). They found that the most difficult step of the oxygen evolution reaction is the second deprotonation to form an adsorbed O species (O^*). Moreover, the A-terminated surface is more active than the B-terminated surface since the former shows a larger density of cobalt states near the Fermi level, which stabilizes the O^* species and thus reduces the overpotential. [181]

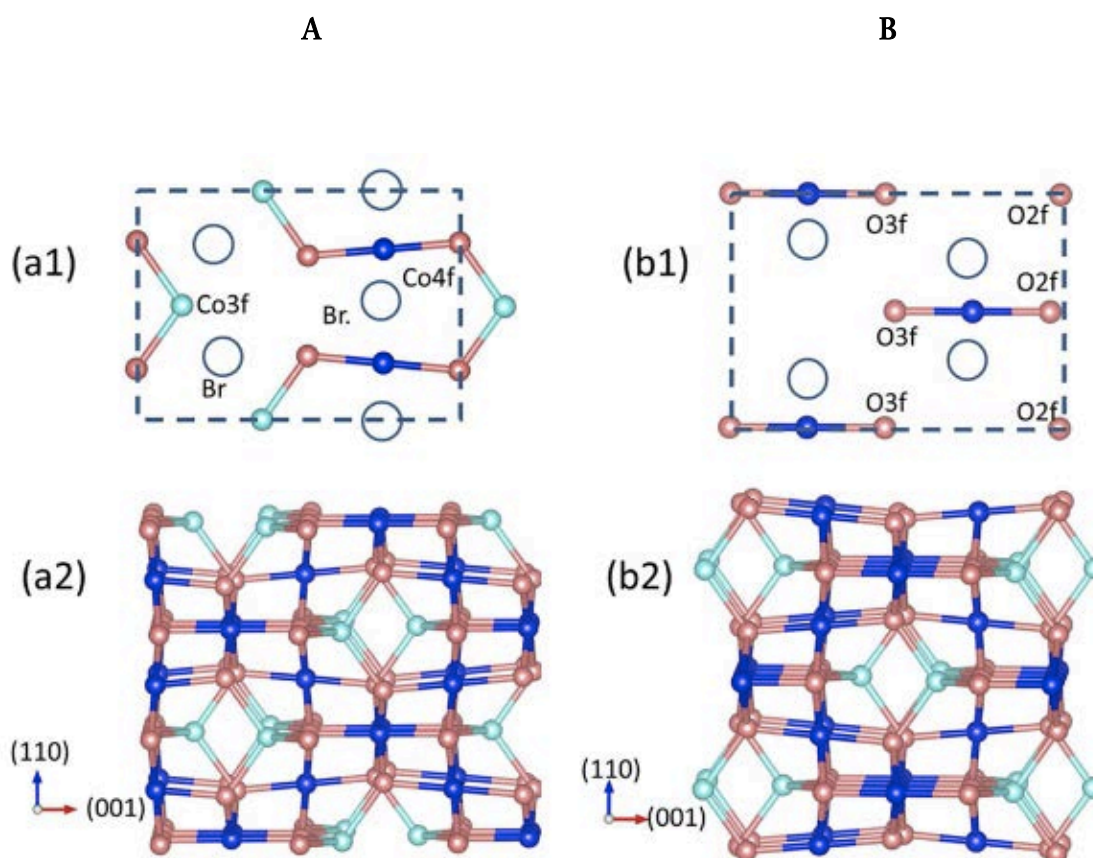


Figure 40. Stick-and-ball model of the Co_3O_4 (110) surface structure. Top (a1 and b1) and side (a2 and b2) views of A (left) and B (right) terminations. In the top views, empty blue circles indicate water and hydroxyl group adsorption sites. Dark and pale-blue spheres indicate Co atoms, which in bulk are octahedrally and tetrahedrally coordinated, respectively. Red spheres indicate oxygen atoms. (Reproduced from reference 181).

From the experimental point of view, some mechanistic proves have also been provided. On the one hand, Dau and co-workers[182] found electrochemically that O-O bond formation occurs at the edges of cobalt oxide nanoparticles by interaction of terminal oxygen-cobalt moieties (O_T) for cobalt oxide materials edge-sharing CoO_6 octahedra (Figure 41).

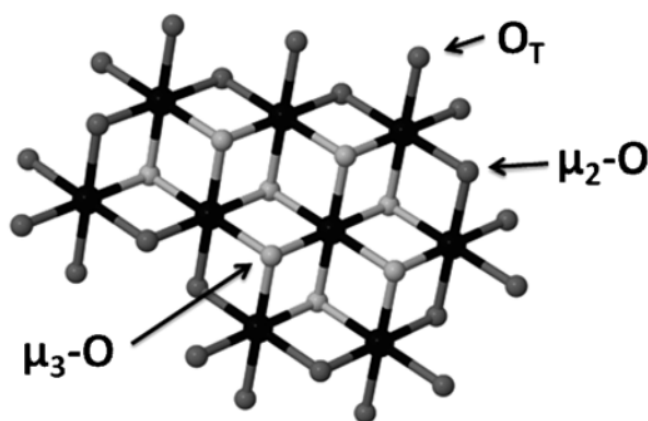


Figure 41. A Co-based catalyst consisting of edge-sharing CoO_6 octahedra. (Adapted from reference 182).

On the other hand, Tilley and co-workers synthesized ϵ -Co, CoO and Co_3O_4 NPs and checked the stability of the nanosystems in alkaline media by electrochemical methods, evidencing that after 20 CV scans all three catalysts showed nearly identical CV fingerprints, thus suggesting the existence of the same mechanism in all cases, during which a Co^{IV} state is reached.[139] However, it was not until 2014 that Frei and co-workers experimentally identified two intermediates during WO photocatalysis by Co_3O_4 NPs using time-resolved Fourier-transform IR spectroscopy.[183] In this context, they proposed a water nucleophilic attack (WNA) mechanism (Figure 43) in which two cofacial $Co(O)OH$ moieties undergo two oxidations and deprotonations (Proton-Coupled Electron-Transfer, PCET) in order to generate two terminal Co^{IV} oxo species. Then the attack of a water molecule generates a hydroperoxo species, which is converted into a superoxo intermediate. Finally, the addition of another water molecule leads the formation of O_2 . Furthermore, two types of sites with widely different photocatalytic efficiency were proposed depending on the presence/absence of adjacent $Co^{III}-OH$ groups (Figure 42 a and b).

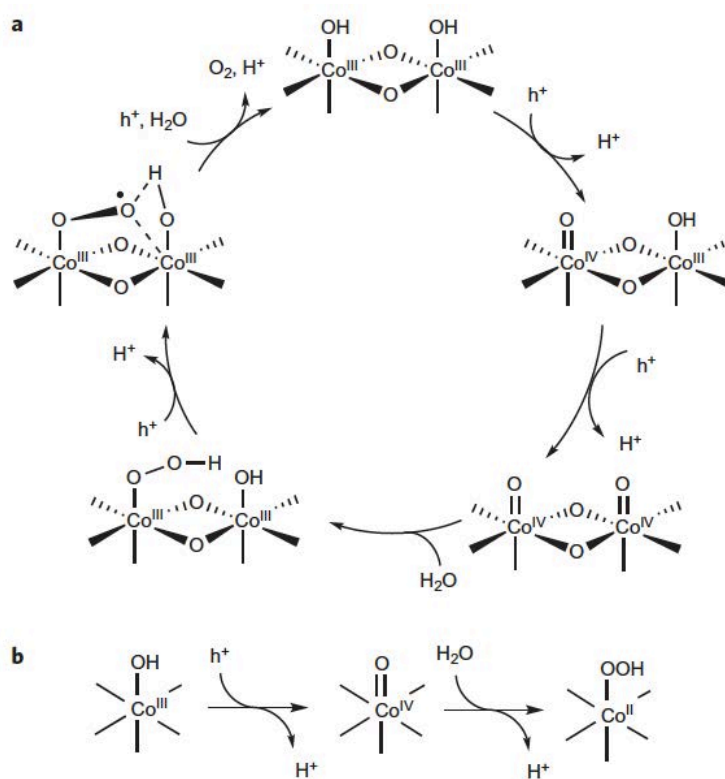


Figure 42. Proposed photocatalytic WO mechanism for Co_3O_4 NPs. **a.** WO mechanism for the fast Co_3O_4 surface site. **b.** Mechanism for the slow Co_3O_4 surface site. The O-O bond-forming step with H_2O in the fast cycle features the cooperative effect of adjacent electronically coupled $\text{Co}^{\text{IV}}=\text{O}$ sites, which is absent in the H_2O addition reaction at the slow site. (Reproduced from reference 183 with permission from *Nature*)

In addition to this, Yagi *et al.* have proposed that CO_3^{2-} anions from the buffer are also involved during the electrocatalytic WO (Figure 43) with $\text{CoO}(\text{OH})$ NPs.[184] In this model, the authors propose that at high CO_3^{2-} concentration, the hydroxo groups of the Co^{III} or Co^{IV} atoms can be partially exchanged by CO_3^{2-} anions, which promote the formation of the O-O bond through an oxidative proton-concerted oxygen atom transfer mechanism followed by the interaction of two Co-O units (I2M) thanks to the proton acceptor nature of CO_3^{2-} .

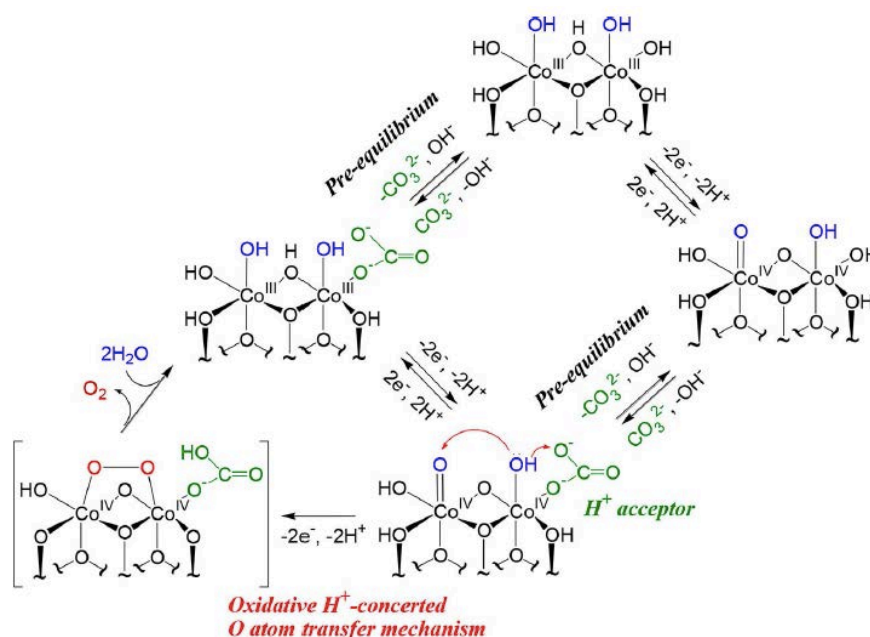


Figure 43. Proposed mechanism of electrocatalytic WO induced by CO_3^{2-} on CoO(OH) NPs. (Adapted from reference 184).

About the CoP_i system, Nocera *et al.*[163b,185] detected the formation of Co^{IV} species at water oxidation potentials by in situ EPR and X-ray techniques via electrodeposition from aqueous solutions containing phosphate and Co^{II} (CoP_i). In the CoP_i system the cobalt centers are responsible for evolving oxygen while phosphate anions promote the electrochemical self-healing of the catalyst. Thus, any Co²⁺ ion formed and released into solution during catalysis, will be redeposited upon oxidation to Co³⁺ in the presence of phosphates.[186] Additionally, in the CoP_i system, the thermodynamics of the catalyst is not altered by the presence of phosphate groups at the surface. Instead, although the role that phosphate groups play in CoP_i systems is not fully understood, it is thought that they are key for; (a) the dynamic processes taking place at the surface/water interface of CoP_i such as the accommodation of water molecules[149,187,188] and (b) extending the lifetime of photogenerated holes by suppressing recombination losses, a crucial point for explaining the higher performances showed by these CoP_i systems.[189-191]

Recently, Messinger and co-workers prepared cobalt/methylenediphosphonate oxide nanoparticles (Co/M2P-oxide NPs) and experimentally demonstrated using time-resolved ¹⁸O-labelling isotope-ratio membrane-inlet mass spectrometry (MIMS) that O₂ formation from

photocatalytic water oxidation occurs in Co/M2P-oxide NPs almost exclusively via intramolecular oxygen coupling (I2M) between two vicinal Co-O moieties.[159]

1.4.4.6 Supported Systems

As mentioned above, the formation/deposition of NPs onto different electrodes to evaluate their OER performances is a common practice. However, the objective evaluation of their efficiency as OER catalysts is not straightforward, both in the measurement and reporting of electrocatalytic data. This is mainly due to the wide range of pH values, temperatures and electrolyte compositions and concentrations used together with experimental aspects under turnover conditions such as for instance the formation of gas bubbles at the solid-liquid interface blocking part of the active surface of the nanocatalysts. In this context, different authors presented similar methodologies whose results are comparable. Jaramillo and co-workers[192] developed a benchmarking methodology for evaluating the activity, stability, and electrochemically active surface area (ECSA) for heterogeneous OER catalysts under certain standard conditions using a rotating ring-disk electrode (RRDE). The activity and stability of each nanocatalyst are measured using a combination of voltammetry, chronoamperometry and chronopotentiometry and the ECSA is estimated from double-layer capacitance measurements. Analogously, Tilley and co-workers[139] studied the activity and TOF values from double-layer capacitance measurements and current density-potential curves. Similarly, Müller *et al*.[126] determined overpotentials and turnover frequencies (TOFs) by measuring steady-state currents as function of voltage, preparing Tafel plots and applying a mass-loading correction.

For instance, Jaramillo tested the activity for Co₃O₄ NPs prepared by Müller by pulsed-laser ablation in liquids (PLAL) confirming their overpotential of 314 mV vs NHE at 0.5 mA.

On the other hand, for electrochemically-triggered systems, several authors focused on the use of channel-rich conducting carbon-based supports such as graphene,[126,132] nitrogen-doped carbon nanotubes (NCNTS)[133,193] and C₃N₄[127,130,131,134] in order to increase the stability of the Co-based nanocatalysts and their electron transfer and mass

transport during electrocatalysis since the porosity of these supports controls the generation of gas bubbles.

Interestingly, for Au supports,[194-196] Yeo and Bell[194] deposited Co_3O_4 NPs onto a Au support observing an excellent TOF value of 1.8 s^{-1} , which is interestingly 1.7 s^{-1} higher than those for other supported systems measured at similar conditions ($\eta = 350\text{-}400 \text{ mV}$ at 0.1 M KOH).[136] This enhancement in electrochemical activity deposited onto a Au support is attributed to the increase in surface Co^{IV} population as a result of enhanced oxidation of the cobalt oxide mediated by the Au support, facilitating the formation of Co-OOH species, which is postulated to be the rate-limiting step. As shown in Figure 44, the reaction begins with the adsorption and discharge of an OH^- anion at the anode surface to form adsorbed OH species (reaction 1, Figure 44). This step is followed by the reaction of OH^- with the adsorbed OH species to produce H_2O and adsorbed atomic O and the release of an electron (reaction 2, Figure 44). The third step in the sequence (reaction 3, Figure 44) involves the reaction of an OH^- anion with an adsorbed O atom to form adsorbed OOH species, which then undergo reaction with additional OH^- (reaction 4, Figure 44), resulting in the formation of adsorbed O_2 and H_2O and the release of an electron. Adsorbed O_2 then desorbs in the last step of the sequence (reaction 5, Figure 44).

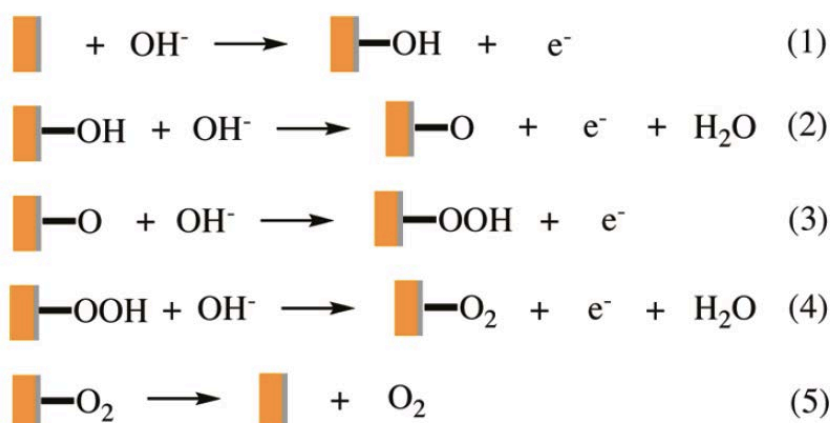


Figure 44. A schematic diagram depicting the mechanism for electrochemical oxygen evolution reaction on cobalt oxide/Au. The cobalt oxide (grey) overlayer is above the Au support (gold). (Adapted from reference 194).

On the basis of above mentioned mechanism, Rossmeisl *et al.*[195] postulated an explanation for this Au-based enhancement of activity by DFT calculations. In this study, the authors proposed that the Au support facilitates the formation of the intermediate species (e. g., metal-OH, -OOH) and it acts as proton acceptor from the Co-OOH intermediate to an adjacent Au=O acceptor site decreasing thus the overpotential for the OER by approximately 100 mV.

Supported photocatalytically-triggered systems can be divided in two categories; those combined with a $[\text{Ru}(\text{bpy})_3]^{2+}$ derivative as photosensitizer together with a sacrificial electron acceptor (i.e. $\text{S}_2\text{O}_8^{2-}$, photocatalytically-triggered systems) and those where the support employed acts at the same time as light-harvesting antenna, typically called photoanodes (photoelectrocatalytically-triggered systems).

1.4.4.7 Photocatalytically-triggered systems

Together with the $[\text{Ru}(\text{bpy})_3]^{2+}$ - $\text{S}_2\text{O}_8^{2-}$ pair in solution and light irradiation, diverse supports such as SBA-15,[172,173,197] SiO_2 ,[198,199] biopolymers[174] and Metal-Organic Frameworks (MOFs)[200] have been investigated in order to determine their influence over the OER performance of the Co-based catalysts employed. In general, it can be inferred that these supports act not only as size- stability- and aggregation-controllers of the NPs but also as medium permittivity-controllers. In general, higher performances are observed for porous supports since they offer a more accessible pathway to the NPs than those which are not porous. For instance, Vela *et al.* investigated the effect of the mesoporous silica thickness embedding Co_3O_4 NPs and their catalytic tests showed that thinner shells are preferable to assure a good permeability or diffusion of the photosensitizer and the electron acceptor species.[201] In addition to this, Jiao and Yusuf[202] studied Co_3O_4 NPs supported on KIT-6 and SBA-15 mesoporous silicas observing a higher WO activity for the former which is attributed to its 3D porous structure that offers more accessible pores than the 1D channels in SBA-15. Also, Jiao[202], Vela[201] Lyman[203] and Frei[204] prepared Co oxide-based NPs supported on different porous SiO_2 observing that the support not only controls the size of the NPs but also provides high stability, since no deactivation or aggregation was observed upon multiple water oxidation cycles.

1.4.4.8 Photoelectrocatalytically-triggered systems

Since the discovery of TiO₂ as stable photoanode for photoelectrochemical water cleavage by Honda and Fujishima in 1972,[205] considerable efforts have been made to seek an efficient and stable photoanode for water oxidation. Thus, studies have focused on semiconductor metal oxides such as TiO₂,[156, 206, 150,] ZnO,[156, 207, 208] WO₃,[131,153,209,210] BiVO₄,[146,211-213] Fe₂O₃,[140,214] Ag₃PO₄,[215] TaON[216-218] and Ta₃N₅,[219-222] For instance, ZnO has been considered as a model of UV-driven photoanode for water splitting, but its performance has been limited by fast charge-carrier recombination, extremely poor stability in aqueous solution, and slow kinetics of water oxidation. Thus, Tang *et al.*[223] prepared ZnO nanowire arrays (0.62 mA cm⁻² at 1.0 V vs RHE) and, once doped with CoP_i, an improved incident photon-to-current conversion efficiency (IPCE, 72%) and a higher photocurrent (0.75 mA cm⁻² at 1.0 V vs RHE) were obtained. Additionally, Park *et al.* Co-doped a ZnO photoanode and obtained not only a higher photocurrent density than the bare ZnO but also a lower overpotential (almost a reduction of 150 mV).[156] This same phenomenon has been observed for other supports. For instance, Zou and co-workers prepared Ta₃N₅ supporting Co₃O₄ NPs achieving a prominent photostability of the Ta₃N₅ since about 75% of initial stable photocurrent (3.1 mA cm⁻² at 1.2 V vs RHE, pH 7), which was maintained after 2 h irradiation.[222] Also, Abe and co-workers dispersed CoO_x NPs on to TaON photoanodes and observed both, a high IPCE (42%) and a high photocurrent (ca. 13 mA cm⁻² at 01.07 V vs RHE, pH 8) under visible light irradiation, also attributed to both, the efficient hole scavenging and the suppressing of the self-oxidative deactivation of the support by Co-based NPs.[216]

In conclusion, the use of different photoanodes as both, support and light-harvesters for Co-based nanoparticles has lead to an improved stability against photocorrosion (in comparison with those that only serve as light-harvesting antenna), showing no loss of photocurrent over prolonged testing. Although the electronic support-catalyst communication can be improved by tuning the structure of the support, the overall enhancement in current is due to efficient hole trapping by the surface Co-based NPs, their catalytic effect and the additional surface-protecting layer role.

1.4.4.9 Bimetallic systems

As shown above (see section 1.4.2) the OEC in PSII combines two metals, Mn and Ca.[224,225] Therefore, despite the role of the Ca^{2+} ion in the OEC is not well-understood, intense research in bimetallic systems for catalyzing the OER has been carried out. In general, the introduction of a second metal on cobalt-based NPs not only uses to increase their stability but also tend to decrease the observed overpotentials by facilitating the oxidation of the active metal sites and affecting their degree of crystallinity. Thus, several studies have been focused on combining Co with other metals, from which the most promising cases are ZnCo-based NPs,[142,156,226, 227] MnCo-based,[193,227-229] FeCo-based NPs,[132,138,230-232] and CoLi-based NPs.[227,233] For instance, Choi *et al.*[226] evaluated spinel-type ZnCo_2O_4 and Co_3O_4 nanocatalysts prepared from same synthesis conditions and with comparable morphologies, observing a relatively low overpotential for the former ($\eta = 0.39 \text{ V}$ at 10 mA cm^{-2} 1.62 V vs RHE pH 14). Also, Pfrommer *et al.*[142] demonstrated the excellent OER activity of Co(30%)-substituted ZnO NPs attributed to the self-oxidation of $\text{Co}^{\text{II/III}}$ atoms by ZnO NPs.

Dismukes and co-workers[233] prepared layered and cubic LiCoO_2 , and Co_3O_4 NPs observing that both LiCoO_2 systems presented a 50 mV lower overpotential ($\eta = 430 \text{ V}$ at 10 mA cm^{-2} pH 14) in comparison with Co_3O_4 NPs. For FeCo-based NPs, different authors found that the electrochemical OER activity of CoO_x can be largely enhanced by doping Fe into the metal oxide matrix due to a partial-charge-transfer-activation (PCTA) effect on metal ions. As mentioned before, Co^{IV} has been identified as the active centres for the OER. Therefore, the higher the oxidation potential of the $\text{Co}^{\text{IV}}/\text{Co}^{\text{III}}$ pair, the stronger the oxidizing ability of the catalyst. When Fe^{III} is doped into the materials a PCTA takes place, Fe^{III} being oxidized to Fe^{IV} . The transferred electrons during this process can then restrain the oxidation from Co^{II} to Co^{III} , resulting in less amount of Co^{III} and a higher $\text{Co}^{\text{IV}}/\text{Co}^{\text{III}}$ oxidation potential. This improves the electrochemical OER kinetics since a stronger oxidizing ability is achieved.[234] Thus, Geng *et al.*[132] prepared different $\text{Co}_x\text{Fe}_y\text{O}$ NPs and analyzed the dependence of the catalytic activity on their Co/Fe ratio observing a decrease of 50 mV on the overpotential for a Co/Fe ratio of 2:1.

Also, Driess and co-workers[138] synthesized amorphous cobalt-iron mixed metal oxide NPs observing a higher photochemical O₂ evolution as well as a lower electrochemical overpotential in comparison with commercial CoO. Finally, the same tendency to higher activities and stabilities have been observed for MnCo-based oxide NPs. Hu and Song[228] synthesized ultrathin nanoplates of cobalt-manganese layered double hydroxide (CoMn LDH), which presented an overpotential of 324 mV at 10 mA cm⁻², which is 44, 92 and 13 mV less than Co(OH)₂ + Mn₂O₃, spinel MnCo₂O₄ and IrO₂ NPs, respectively attributed to the formation of amorphous layers at the surface and possibly the accumulation of active Co^{IV} species in the amorphous layers due to a leaching of Mn ions. Interestingly, Dismukes *et al.*[227] prepared different LiMn_{2-x}Co_xO₄ NPs observing that substitution of Co^{III} for Mn^{III} causes an obvious increase in the current density followed by a decrease in the overpotential ($\eta = 370$ mV for LiMn_{0.25}Co_{1.75}O₄, 120 mV lower at 1 mA cm⁻²).

1.5 References

- [1] (a) Chorkendorff, I.; Niemantsverdriet, J. W. *Concepts of Modern Catalysis and Kinetics*, Wiley-VCH Verlag, Weinheim, 2007. (b) Kolasinski, K. W. *Surface Science: Foundations of Catalysis and Nanoscience*, John Wiley & Sons, Chichester, 2008. (c) Rothenberg, G. *Catalysis: Concepts and Green Applications*, Wiley-VCH, Weinheim, 2008. (d) Astruc, D. Ed., *Nanoparticles and Catalysis*, Wiley-VCH Verlag, Weinheim, 2008.
- [2] (a) Kurosawa, H.; Yamamoto, A. Ed., *Fundamentals of Molecular Catalysis*, Elsevier, Amsterdam, 2003. (b) Hermans, S.; Somorjai, G. A.; Zhou, B. *Nanotechnology in Catalysis*, Springer, New York, 2004.
- [3] Arends, I.; Sheldon R.; Hanefeld, U. *Green Chemistry and Catalysis*, Wiley-VCH, Weinheim, 2007.
- [4] (a) Van Leeuwen, P. W. N. M. *Homogeneous Catalysis: Understanding the Art*, Kluwer Academic Publishers, Dordrecht, 2004. (b) Herrmann, W. A.; Cornils, B. Ed., *Applied Homogeneous Catalysis with Organometallic Compounds: A comprehensive Handbook*, Wiley-VCH, Weinheim, 2002. (c) Bhaduri, S.; Mukesh, D. *Homogeneous Catalysis: Mechanisms and Industrial Applications*, Wiley-Interscience, New York, 2000.
- [5] (a) Neurock, M.; Van Santen, R. A. *Molecular Heterogeneous Catalysis: A Conceptual and Computational Approach*, Wiley-VCH, Weinheim, 2006. (b) Nascimento, M. A. Ed., *Theoretical Aspects of Heterogeneous Catalysis*, Kluwer Academic Publishers, Dordrecht, 2001. (c) Thomas, J. M.; Thomas, J. W. *Principles and Practice of Heterogeneous Catalysis*, VCH, Weinheim, 1997.
- [6] (a) Crabtree, R. H.; Peris, E. F. *Química Organometálica de los Metales de Transición*, Publicaciones de la Universitat Jaume I, Castellón, 1997. (b) Whyman, R. *Applied Organometallic Chemistry and Catalysis*, Oxford University Press, Oxford, 2001.
- [7] (a) Shiny, P. J.; Mukherjee, A.; Chandrasekaran, N. *Int. J. Pharm. Pharm. Sci.* **2013**, *5*, 239-241. (b) Ladj, R.; Bitar, A.; Eissa, M.; Mugnier, Y.; Le Dantec, R.; Fessi, H.; Elaissari, A. *J. Mater. Chem. B* **2013**, *1*, 1381-1396.
- [8] (a) Momose, K.; Takayama, S.; Hata, E.; Tomita, Y. *Opt. Lett.* **2012**, *37*, 2250-2252. (b) Stalmashonak, A.; Abdolvand, A.; Seifert, G. *Appl. Phys. Lett.* **2011**, *99*, 26765-26775.
- [9] (a) Tkachenko, A. G.; Xie, H.; Coleman, D.; Glomm, W.; Ryan, J.; Anderson, M. F.; Franzen, S.; Feldheim, D. L. *J. Am. Chem. Soc.* **2003**, *125*, 4700-4701. (b) Templeton, A. C.; Wuelfing, W. P.; Murray, R. W. *Acc. Chem. Res.* **2000**, *33*, 27-36. (c) Peyser, L. A.; Vinson, A. E.; Bartko, A. P.; Dickson, R. M. *Science* **2001**, *291*, 103-106. (d) Astruc, D.; Lu, F.; Aranzas, J. R. *Angew. Chem. Int. Ed.*, **2005**, *44*, 7852-72. (e) Moreno-Manas, M.; Pleixats, R. *Acc. Chem. Res.* **2003**, *36*, 638-643. (f) Aiken, J. D.; Finke, R. G. *J. Mol. Catal. A: Chem.* **1999**, *145*, 1-44. (g) Roucoux, A.; Schulz, J.; Patin, H. *Chem. Rev.* **2002**, *102*, 3757-3778. (h) Duran Pachon, L.; Rothenberg, G. *App. Organomet. Chem.* **2008**, *22*, 288-99. (i) Durand, J.; Teuma, E.; Gomez, M. *Eur. J. Inorg. Chem.* **2003**, *191*, 187-207.
- [10] (a) Edwards, P. P.; Johnston, R. L.; Rao, C. N. R. *On the Size-Induced Metal-Insulator Transition in Clusters and Small Particles, in Metal Clusters in Chemistry*, Braunstein, P.; Oro, L. A.; Raithby, P. R., Ed., Wiley, Weinheim, 1999. (b) Roduner, E. *Chem. Soc. Rev.* **2006**, *35*, 583-592.
- [11] (a) Teo, B. K.; Sloane, N. J. A. *Inorg. Chem.* **1985**, *24*, 4545-4558. (b) Aiken III, J. D.; Finke, R. G. *J. Mol. Catal. A: Chem.* **1999**, *145*, 1-44. (c) Poole, Ch. P.; Owens, F. J. *Introducción a la Nanotecnología*, Reverté, Barcelona, 2007.
- [12] Finke, R. G. *Metal Nanoparticles: Synthesis, Characterization and Applications*, Feldheim, D. L.; Foss, C. A., Jr., Ed., Marcel Dekker, New York, 2002.
- [13] Toshima, N.; Yonezawa, T. *New J. Chem.* **1998**, *22*, 1179-1201.
- [14] Willner, I.; Mandler, D. *J. Am. Chem. Soc.* **1989**, *111*, 1330-1336.
- [15] Philippot, K.; Chaudret, B. *C. R. Chim.* **2003**, *6*, 1019-1034.
- [16] Bönemann, H.; Richards, R. M. *Eur. J. Inorg. Chem.* **2001**, 2455-2480.
- [17] Schmid, G.; Chi, L. F. *Adv. Mater.* **1998**, *10*, 515-526.
- [18] Wilcoxon, J. P.; Abrams, B. L. *Chem. Soc. Rev.* **2006**, *35*, 1162-1194.
- [19] Cushing, B. L.; Kolesnichenko, V. L.; O'Connor, C. J. *Chem. Rev.* **2004**, *104*, 3893-3946.

- [20] (a) Tan, C. K.; Newberry, V.; Webb, T. R.; McAuliffe, C. A. *J. Chem. Soc., Dalton Trans.* **1987**, *6*, 1299-1303. (b) Kopple, K.; Meyerstein, D.; Meisel, D. *J. Phys. Chem.* **1980**, *84*, 870-875. (c) Mayer, A. B. R.; Hausner, S. H.; Mark, J. E. *Polym. J.* **2000**, *32*, 15-22. (d) Esumi, K.; Nakamura, R.; Suzuki, A.; Torigoe, K. *Langmuir* **2000**, *16*, 7842-7846. (e) Borsla, A.; Wilhelm, A. M.; Delmas, H. *Catal. Today* **2001**, *66*, 389-395.
- [21] (a) Faraday, M. *Philos. Trans. R. Soc. London* **1857**, *151*, 183-224. (b) Enüstün, B. V.; Turkevich, J. *J. Am. Chem. Soc.* **1963**, *85*, 3317-3328. (c) Turkevich, J.; Kim, G. *Science* **1970**, *169*, 873-879. (d) Turkevich, J.; Stevenson, P. C.; Hillier, J. *Faraday Discuss. Chem. Soc.* **1951**, *11*, 55-75.
- [22] (a) Reetz, M. T.; Helbig, W. *J. Am. Chem. Soc.* **1994**, *116*, 7401-7402. (b) Reetz, M. T.; Helbig, W.; Quaiser, S. A. in *Active Metals: Preparation, Characterization, Applications*, Fürstner, A. Ed., VCH, New York, 1996.
- [23] Yin, B.; Ma, H.; Wang, S.; Chen, S. *J. Phys. Chem. B* **2003**, *107*, 8898-8904.
- [24] Chaudret, B.; Philippot, K. *Oil Gas Sci. Tech.* **2007**, *62*, 799-817.
- [25] Ould Ely, T.; Amiens, C.; Chaudret, B.; Snoeck, E.; Verelst, M.; Respaud, M.; Broto, J.-M. *Chem. Mater.* **1999**, *11*, 526-529.
- [26] Pan, C.; Pelzer, K.; Philippot, K.; Chaudret, B.; Dassenoy, F.; Lecante, P.; Casanove, M.-J. *J. Am. Chem. Soc.* **2001**, *123*, 7584-7593.
- [27] Rodríguez, A.; Amiens, C.; Chaudret, B.; Casanove, M.-J.; Lecante, P.; Bradley, J. S. *Chem. Mater.* **1996**, *8*, 1978-1986.
- [28] Ciuculescu, D.; Amiens, C.; Respaud, M.; Lecante, P.; Falqui, A.; Chaudret, B. *Mod. Phys. Lett. B* **2007**, *21*, 1153-1159.
- [29] Dassenoy, F.; Casanove, M.-J.; Lecante, P.; Verelst, M.; Snoeck, E.; Mosset, A. Ould Ely, T.; Amiens, C.; Chaudret, B. *J. Chem. Phys.* **2000**, *112*, 8137-8145.
- [30] González-Gálvez, D.; Nolis, P.; Philippot, K.; Chaudret, B.; van Leeuwen, P. W. N. M. *ACS Catal.* **2012**, *2*, 317-321.
- [31] (a) Klabundem K. J.; Sato, A.; Kodama, K.-Y.; Hirano, M.; Komiya, S. *Inorg. Chim. Acta* **1999**, *294*, 266-269. (b) Benfield, F. W. S.; Green, M. L. H.; Ogden, J. S.; Young, D. *J. Chem. Soc., Chem. Commun.* **1973**, *22*, 866-867.
- [32] (a) Esumi, K.; Suzuki, M.; Tano, T.; Torigoe, K.; Meguro, K. *Colloids Surf.* **1991**, *55*, 9-14. (b) Esumi, K.; Tano, T.; Meguro, K. *Langmuir* **1989**, *5*, 268-270. (c) Esumi, K.; Sadakane, O.; Torigoe, K.; Meguro, K. *Colloids Surf.* **1992**, *62*, 255-257.
- [33] (a) Aiken III, J. D.; Lin, Y.; Finke, R. G. *J. Mol. Catal. A: Chem.* **1996**, *114*, 29-51. (b) Belapurkar, A. D.; Kapoor, S.; Kulshreshtha, S. K.; Mittal, J. P. *Mater. Res. Bull.* **2001**, *36*, 145-151. (c) Wolak, S.; Vidal, L.; Becht, J.-M.; Michelin, L.; Balan, L. *Nanotechnology* **2016**, *27*, 345601.
- [34] (a) Suslick, K. S.; Choe, S. B.; Cichowlas, A. A.; Grinstaff, M. W. *Nature* **1991**, *353*, 414-416. (b) Dhas, N. A.; Cohen, H.; Gedanken, A. *J. Phys. Chem. B* **1997**, *101*, 6834-6838.
- [35] Zaarour, M.; El Roz, M.; Dong, B.; Retoux, R.; Aad, R.; Cardin, J.; Dufour, C.; Gourbilleau, F.; Gilson, J.-P.; Mintova, S. *Langmuir* **2014**, *30*, 6250-6256.
- [36] Nikolaev, S. A.; Smirnov, V. V. *Cat. Today* **2009**, *147S*, S336-S339.
- [37] Nakamura, I.; Yamanoi, Y.; Imaoka, T.; Yamamoto, K.; Nishihara, H. *Angew. Chem. Int. Ed.* **2011**, *50*, 5830-5833.
- [38] Pellagatta, J. L.; Blandy, C.; Collière, V.; Choukroun, R.; Chaudret, B.; Cheng, P.; Philippot, K. *J. Mol. Catal. A: Chem.* **2002**, *178*, 55-61.
- [39] Liu, M.; Yu, W.; Liu, H.; Zheng, J. *J. Colloid Interface Sci.* **1999**, *214*, 231-237.
- [40] (a) Yeung, L. K.; Crooks, R. M. *Nano Lett.* **2001**, *1*, 14-17. (b) Yeung, L. K.; Lee Jr, C. T.; Johnston, K. P.; Crooks, R. M. *Chem. Commun.* **2001**, 2290-2291.
- [41] Pérez-Lorenzo, M. *J. Phys. Chem. Lett.* **2012**, *3*, 167-174.
- [42] (a) Reetz, M. T.; Westermann, E.; Lohmer, R.; Lohmer, G. *Tetrahedron Lett.* **1998**, *39*, 8449-8452. (b) Reetz, M. T.; Westermann, E. *Angew. Chem. Int. Ed.* **2000**, *39*, 165-168.
- [43] Ye, E.; Tan, H.; Li, S.; Fan, W. Y. *Angew. Chem. Int. Ed.* **2006**, *45*, 1120-1123.

- [44] (a) Inés, B.; SanMartin, R.; Moure, M. J.; Domínguez, E. *Adv. Synth. Catal.* **2009**, *351*, 2124-2132. (b) Karimi, B. B.; Enders, D. *Org. Lett.* **2006**, *8*, 1237-1240.
- [45] Weissermel, K.; Arpe, H.-J. *Industrial Organic Chemistry*, VCH, New York, 1993.
- [46] (a) Jansat, S.; Picurelli, D.; Pelzer, K.; Philippot, K.; Gomez, M.; Muller, G.; Lecante, P.; Chaudret, B. *New J. Chem.* **2006**, *30*, 115-122. (b) Widegren, J. A.; Finke, R. G. *J. Mol. Catal. A: Chem.* **2003**, *191*, 187-207.
- [47] Dyson, P. J. *Dalton Trans.* **2003**, 2964-2974.
- [48] Barichelli, P.; Morfes, G. Páez, D. E. *J. Mol. Catal. A: Chem.* **2001**, *176*, 1-10.
- [49] (a) Torborg, C.; Beller, M. *Adv. Synth. Catal.* **2009**, *351*, 3027-3043. (b) Magano, J.; Dunetz, J. R. *Chem. Rev.* **2011**, *111*, 2177-2250.
- [50] (a) Cornelio, B.; Rance, G. A.; Laronze-Cochard, M.; Fontana, A.; Sapi, J.; Khlobystov, A. N. *J. Mater. Chem. A* **2013**, *1*, 8737-8744. (b) Sanhes, D.; Raluy, E.; Rétory, S.; Saffon, N.; Teuma, E.; Gómez, M. *Dalton Trans.* **2010**, *39*, 9719-9726.
- [51] Fihri, A.; Bouhrara, M.; Nekoueishahraki, B.; Basset, J.-M.; Polshettiwar, V. *Chem. Soc. Rev.* **2011**, *40*, 5181-5203.
- [52] Miyaura, N.; Suzuki, A. *Chem. Rev.* **1995**, *95*, 2457-2483.
- [53] Barder, T. E.; Walker, S. D.; Martinelli, J. R.; Buchwald, S. L. *J. Am. Chem. Soc.* **2005**, *127*, 4685-4696.
- [54] Reetz, M. T.; Breibauer, R.; Wanninger, K. *Tetrahedron Lett.* **1996**, *37*, 4499-4502.
- [55] (a) Narayanan, R.; El-Sayed, M. A. *Top. Catal.* **2008**, *47*, 15-21. (b) Li, Y.; Hong, X. M.; Collard, D. M.; El-Sayed, M. A. *Org. Lett.* **2000**, *2*, 2385-2388. (c) Favier, I.; Massou, S.; Teuma, E.; Philippot, K.; Chaudret, B.; Gómez, M. *Chem. Commun.* **2008**, *28*, 3296-3298. (d) Narayanan, R.; El-Sayed, M. A. *J. Am. Chem. Soc.* **2003**, *125*, 8340-8347. (e) Durand, J.; Teuma, E.; Gómez, M. *Eur. J. Inorg. Chem.* **2008**, *23*, 3577-3586.
- [56] Chahdoura, F.; Pradel, C.; Gómez, M. *Adv. Synth. Catal.* **2013**, *355*, 3648-3660
- [57] Peral, D.; Gómez-Villarraga, F.; Sala, X.; Pons, J.; Bayon, J. C.; Ros, J.; Guerrero, M.; Vendier, L.; Lecante, P.; Garcia-Anton, J.; Philippot, K. *Catal. Sci. Technol.* **2013**, *3*, 475-489.
- [58] (a) Miyaura, N.; Suxuki, A. *J. Chem. Soc., Chem. Commun.* **1979**, *19*, 866-867. (b) Miyaura, N.; Yanagi, T.; Suzuki, A. *Synth. Commun.* **1981**, *11*, 513-519.
- [59] Blanksby, S. J.; Ellison, G. B. *Acc. Chem. Res.*, **2003**, *36*, 255-263.
- [60] (a) Shen, W. *Tetrahedron Lett.* **1997**, *38*, 5575-5578. (b) Littke, A. F.; Fu, G. C. *Angew. Chem. Int. Ed.* **1998**, *37*, 3387-3388. (c) Andreu, M. G.; Zapf, A.; Beller, M. *Chem. Commun.* **2000**, *24*, 2475-2476. (d) Baillie, C.; Zhang, L.; Xiao, J. *J. Org. Chem.* **2004**, *69*, 7779-7782. (e) Colacot, T. J.; Shea, H. A.; *Org. Lett.* **2004**, *6*, 3731-3734. (f) Netherton, M. R.; Fu, G. C. *Angew. Chem. Int. Ed.* **2002**, *41*, 3910-3912. (g) Zapf, A.; Beller, M. *Chem. Commun.* **2005**, *4*, 432-440. (h) Zapf, A.; Ehrentraut, A.; Beller, M. *Angew. Chem. Int. Ed.* **2000**, *39*, 4153-4155. (i) John, A.; Shaikh, M. M.; Ghosh, P. *Inorg. Chim. Acta* **2010**, *363*, 3113-3121. (j) Xu, Q.; Duan, W.-L.; Lei, Z.Y.; Zhu, Z.-B.; Shi, M. *Tetrahedron* **2005**, *61*, 11225-11229. (k) Lu, J.-T.; Lin, J. C. Y.; Lin, M.-C.; Khupse, N. D.; Lin, I. J. B. *Langmuir* **2014**, *30*, 10440-10448.
- [61] Balanta, A.; Godard, C.; Claver, C. *Chem. Soc. Rev.* **2011**, *40*, 4973-4985.
- [62] (a) de Vries, J. G. *Dalton Trans.* **2006**, 3421-429. (b) Shmidt, A. F.; Mametova, L. V. *Kinet. Catal.* **1996**, *37*, 406-408. (c) Bhanage, B. M.; Shirai, M.; Arai, M. *J. Mol. Catal. A: Chem.* **1999**, *145*, 69-74. (d) de Vries, A. H. M.; Parlevliet, F. J.; Schmieder-van de Vondervoort, L.; Mommers, J. H. M.; Henderickx, H. J. W.; Walet, M. A. M.; de Vries, J. G. *Adv. Synth. Catal.* **2002**, *344*, 996-1002. (e) de Vries, A. H. M.; Mulders, J. M. C. A.; Mommers, J. H. M.; Henderickx, H. J. W.; de Vries, J. G. *Org. Lett.* **2003**, *5*, 3285-3288.
- [63] Cassol, C. C.; Umpierre, A. P.; Machado, G.; Wolke, S. I.; Dupont, J. *J. Am. Chem. Soc.* **2005**, *127*, 3298-3299.
- [64] Ratke, L.; Voorhees, P. W. *Growth and Coarsening: Ostwald Ripening in Material Processing*, Springer, Berlin, 2002.
- [65] Guerrero, M.; Costa, N. J. S.; Vono, L. L. R.; Rossi, L. M.; Gusevskayad, E. V.; Philippot, K. *J. Mater. Chem. A* **2013**, *1*, 1441-1449.

- [66] (a) Thathagar, M. B.; ten Elshof, J. E.; Rothenberg, G. *Angew. Chem. Int. Ed.* **2006**, *45*, 2886-2890. (b) Gaikwad, A. V.; Holuigue, A.; Thathagar, M. B.; ten Elshof, J. E.; Rothenberg, G. *Chem. Eur. J.* **2007**, *13*, 6908-6913.
- [67] Gitis, V.; Beerthuis, R.; Shiju, N. R.; Rothenberg, G. *Catal. Sci. Technol.* **2014**, *4*, 2156-2160.
- [68] Campelo, J. M.; Luna, D.; Luque, R.; Marinas, J. M.; Romero, A. A. *ChemSusChem* **2009**, *2*, 18-45.
- [69] (a) Kantam, M. L.; Roy, S.; Roy, M.; Sreedhar, B.; Choudary, B. M. *Adv. Synth. Catal.* **2005**, *347*, 2002-2008. (b) Kantam, M. L.; Roy, S.; Roy, M.; Subhas, M. S.; Likhar, P. R.; Sreedhar, B.; Choudary, B. M. *Synlett.* **2006**, 2747. (c) Gniewek, A.; Ziółkowski, J. J.; Trzeciak, A. M.; Zawadzki, M.; Grabowska, H.; Wrzyszc, J. *J. Catal.* **2008**, *254*, 121-130. (d) Monopoli, A.; Nacci, A.; Calò, V.; Ciminale, F.; Cotugno, P.; Mangone, A.; Giannossa, L. C.; Azzone, P.; Cioffi, N. *Molecules* **2010**, *15*, 4511-4525. (e) Budroni, G.; Corma, A.; García, H.; Primo, A. *J. Catal.* **2007**, *251*, 345-353.
- [70] (a) Martínez, A. V.; Mayoral, J. A.; García, J. I. *Appl. Catal. A* **2014**, *472*, 21-28. (b) Varadwaj, G. B. B.; Rana, S.; Parida, K. *J. Phys. Chem. C* **2014**, *118*, 1640-1651. (c) Borah, B. J.; Borah, S. J.; Saikia, K.; Dutta, D. K. *Appl. Catal. A* **2014**, *479*, 350.
- [71] (a) Ren, N.; Yanga, Y.-H.; Zhang, Y.-H.; Wang, Q.-R.; Tang, Y. *J. Catal.* **2007**, *246*, 215-222. (b) Choi, M.; Lee, D.-H.; Na, K.; Yu, B.-W.; Ryoo, R. *Angew. Chem. Int. Ed.* **2009**, *48*, 3673-3676. (c) Okumura, K.; Matsui, H.; Tomiyama, T.; Sanada, T.; Honma, T.; Hirayama, S.; Niwa, M. *ChemPhysChem* **2009**, *10*, 3265-3272. (d) Durapa, F.; Rakap, M.; Aydemir, M.; Ozkar, S. *Appl. Catal. A* **2010**, *382*, 339. (e) Okumura, K.; Romiyama, T.; Okuda, S.; Yoshida, H.; Niwa, M. *J. Catal.* **2010**, *273*, 156-166.
- [72] (a) García-Martínez, J. C.; Lezutekong, R.; Crooks, R. M. *J. Am. Chem. Soc.* **2005**, *127*, 5097-5103. (b) Ornelas, C.; Ruiz, J.; Salmon, L.; Astruc, D. *Adv. Synth. Catal.* **2008**, *350*, 837-845. (c) Murugan, E.; Jebaranjitham, J. N.; Usha, A. *Appl. Nanosci.* **2012**, *2*, 211-222. (d) Deraedt, C.; Salmon, L.; Astruc, D. *Adv. Synth. Catal.* **2014**, *356*, 2525-2538. (e) Noh, J.-H.; Meijboom, R. *J. Colloid. Interface Sci.* **2014**, *415*, 57-69. (f) Pittelkow, M.; Poulsen, K. M.; Boas, U.; Christensen, J. B. *Langmuir* **2003**, *19*, 7682-7684.
- [73] (a) Ogasawaram, S.; Kato, S. *J. Am. Chem. Soc.* **2010**, *132*, 4608-4613. (b) Gallon, B. J.; Kojima, R. W.; Kaner, R. B.; Diaconescu, P. L. *Angew. Chem. Int. Ed.* **2007**, *46*, 7251-7254. (c) Ohtaka, A.; Teratani, T.; Fujii, R.; Ikeshita, K.; Shimomura, O.; Nomura, R. *Chem. Commun.* **2009**, 7188-7190. (d) Evangelisti, C.; Panziera, N.; Perticib, P.; Vitulli, G.; Salvadori, P.; Battocchio, C.; Polzonetti, G. *J. Catal.* **2009**, *262*, 287-293. (e) Lin, C.-A.; Luo, F.-T. *Tetrahedron Lett.* **2003**, *44*, 7565-7568. (f) Jiang, X.; Wei, G.; Zhang, X.; Zhang, W.; Zheng, P.; Wen, F.; Shi, L. *J. Mol. Catal. A: Chem.* **2007**, *277*, 102. (g) Schweizer, S.; Becht, J.-M.; Drian, C. L. *Tetrahedron* **2010**, *66*, 765-772. (h) Kim, J.-H.; Kim, J.-W.; Shokouhimehr, M.; Lee, Y.-S. *J. Org. Chem.* **2005**, *70*, 6714-6720.
- [74] (a) Davies, I. W.; Matty, L.; Hughes, D. L.; Reider, P. J. *J. Am. Chem. Soc.* **2001**, *123*, 10139-10140. (b) Richardson, J. M.; Jones, C. W. *J. Catal.* **2007**, *251*, 80-93. (c) Biffis, A.; Zecca, M.; Basato, M. *Eur. J. Inorg. Chem.* **2001**, 1131-1133. (d) Pröckl, S. S.; Kleist, W.; Köhler, K. *Tetrahedron* **2005**, *61*, 9855-9859. (e) Pröckl, S. S.; Kleist, W.; Gruber, M. A.; Köhler, K. *Angew. Chem. Int. Ed.* **2004**, *43*, 1881-1882. (f) Köhler, K.; Kleist, W.; Pröckl, S. S. *Inorg. Chem.* **2007**, *46*, 1876-1883. (g) Lysén, M.; Köhler, K. *Synthesis* **2006**, *4*, 692-698. (h) Kleist, W.; Pröckl, S. S.; Köhler, K. *Catal. Lett.* **2008**, *125*, 197-200.
- [75] Choudary, B. M.; Madhi, S.; Chowdari, N. S.; Kantam, M. L. Sreedhar, C. *J. Am. Chem. Soc.* **2002**, *124*, 14127-14136.
- [76] (a) *Exhausting profiles of oil products*, Exxon-Mobile, 2004; (b) *Solar Energy Utilization Workshop* U.S. Department of Energy, Washington DC, 2005; (c) *New Science for a Secure and Sustainable Energy Future* U.S. Department of Energy, 2008; (d) *Research Needs and Impacts in Predictive Simulation for Internal Combustion Engines (PreSICE)* U.S. Department of Energy, 2011. (e) Edenhofer, O.; Pichs-Madruga, R.; Sokona, Y.; Farahani, E.; Kadner, S.; Seyboth, K.; Adler, A.; Baum, I.; Brunner, S.; Eickemeier, P.; Kriemann, B.; Savolainen, J.; Schlömer, S.; von Stechow, C.; Zwickel, T.; Minx, J. C. (eds.) *IPCC: Climate Change 2014: Mitigation of Climate Change. Contribution of Working Group III to the Fifth Assessment Report of the Intergovernmental Panel on Climate Change.*; Cambridge University Press: Cambridge, UK, 2014.

- [77] (a) *BP Statistical Review of World Energy*, **2015**. (b) Schiermeier, Q.; Tollefson, J.; Scully, T.; Witze, A.; Morton, O. *Nature* **2008**, *454*, 816-823.
- [78] (a) Styring, S. *Faraday Discuss.* **2012**, *155*, 357-376. (b) Branker, K.; Pathak, M. J. M.; Pearce, J. M. *Renew. Sust. Energ. Rev.* **2011**, *15*, 4470-4482.
- [79] Santos, D. M. F.; Sequeira, C. A. C. *Quim. Nova* **2013**, *36*, 1176-1193.
- [80] Borisov, G.; Stoyanova, A.; Lefterova, E.; Slavcheva, E. *Izvestiya po Khimiya Bulgarska Akademiya na Naukite* **2015**, *45*.
- [81] Mergel, J.; Carmo, M.; Fritz, D. *Transition to Renewable Energy Systems*, Weinheim: Wiley-VCH, 2013.
- [82] Remiro, A.; Valle, B.; Oar-Arteta, L.; Aguayo, A. T.; Bilbao, J.; Gayubo, A. G. *Int. J. Hydrogen Energy* **2014**, *39*, 6889-6898.
- [83] Dincer, I.; Acar, C. *Int. J. Hydrogen Energy* **2015**, *40*, 11094-11111.
- [84] Lewis, N. S.; Nochera, D. G. *Proc. Natl. Acad. Sci. U.S.A.* **2006**, *103*, 15729-15735.
- [85] Romain, S.; Vigara, L.; Llobet, A. *Acc. Chem. Res.* **2009**, *42*, 1944-1953.
- [86] (a) Raven, P. H.; Evert, R. F.; Eichorn, S. E.; *Biology of Plant*, seven ed., Freeman, W. H. and Company Publishers, New York, 2005. (b) Allakhverdiev, S. I. *J. Photochem. Photobiol. B: Biol.* **2011**, *104*, 1-8.
- [87] Suga, M.; Akita, F.; Hirata, K.; Ueno, G.; Murakami, H.; Nakajima, Y.; Shimizu, T.; Yamashita, K.; Yamamoto, M.; Ago, H.; Shen, J.-R. *Nature* **2015**, *517*, 99-103.
- [88] Umena, Y.; Kawakami, K.; Shen, J.-R.; Kamiya, N. *Nature* **2011**, *473*, 55-60.
- [89] (a) Ferreira, K. N.; Iverson, T. M.; Maghlaoui, K.; Barber, J.; Iwata, S. *Science* **2004**, *303*, 1831-1838. (b) Loll, B.; Kern, J.; Saenger, W.; Zouni, A.; Biesiadka, J. *Nature* **2005**, *438*, 1040-1044. (c) Guskov, A.; Kern, J.; Gabdulkhakov, A.; Broser, M.; Zouni, A.; Saenger, W. *Nat. Struct. Mol. Biol.* **2009**, *16*, 334-342.
- [90] (a) Dau, H.; Haumann, M. *Biochim. Biophys. Acta, Bioenerg.* **2007**, *1767*, 472-483. (b) Renger, G. *J. Photochem. Photobiol. B: Biol.* **2011**, *104*, 35-43. (c) Siegbahn, P. E. M. *J. Photochem. Photobiol. B: Biol.* **2011**, *104*, 94-99. (d) Kusunoki, M. *J. Photochem. Photobiol. B: Biol.* **2011**, *104*, 100-110. (e) Najafpour, M. M.; Isaloo, M. A.; Eaton-Rye, J. J.; Tomo, T.; Nishihara, H.; Satoh, K.; Carpentier, R.; Shen, J.-R.; Allakhverdiev, S. J. *Biochim. Biophys. Acta, Bioenerg.* **2014**, *1837*, 1395-1410.
- [91] Yachandra, V. K.; Yano, J. *J. Photochem. Photobiol. B: Biol.* **2011**, *104*, 51-59.
- [92] Bofill, R.; García-Antón, J.; Escriche, L.; Sala, X.; Llobet, A. In: *Comprehensive Inorganic Chemistry*, II, eds. Reedijk, J & Poepelmeier, K.; Elsevier **2013**, *Vol 8*, 505-523.
- [93] (a) Francas, F.; Sala, X.; Benet-Buchholz, J.; Escriche, L.; Llobet, A. *ChemSusChem* **2009**, *2*, 321-329. (b) Berardi, S.; Drouet, S.; Francàs, L.; Gimbert-Suriñach, C.; Guttentag, M.; Richmond, C.; Stoll, T.; Llobet, A. *Chem. Soc. Rev.* **2014**, *43*, 7501-7509. (c) Walter, M. G.; Warren, E. L.; McKone, J. R.; Boettcher, S. W.; Mi, Q.; Santori, E. A.; Lewis, N. S. *Chem. Rev.* **2010**, *110*, 6446-6473. (d) Gao, Y.; Ding, X.; Liu, J.; Wang, L.; Lu, Z.; Li, I.; Sun, L. *J. Am. Chem. Soc.* **2013**, *135*, 4219-4222. (e) Sasaki, Y.; Kato, H.; Kudo, A. *J. Am. Chem. Soc.* **2013**, *135*, 5441-5449. (f) Brimblecombe, R.; Koo, A.; Dismukes, G. C.; Swiegers, G. F.; Spiccia, L. *J. Am. Chem. Soc.* **2010**, *132*, 2892-2894. (h) Li, L.; Duan, L.; Xu, Y.; Gorlov, M.; Hagsfeldt, A.; Sun, L. *Chem. Commun.* **2010**, *46*, 7307-7309.
- [94] Bofill, R.; García-Antón, J.; Escriche, L.; Sala, X. *J. Photochem. Photobiol. B* **2015**, *152*, 71-81
- [95] (a) Sanderson, K. *Nature* **2008**, *452*, 400. (b) Nocera, D. G. *Acc. Chem. Res.* **2012**, *45*, 767-776.
- [96] (a) Stracke, J. J.; Finke, R. G. *J. Am. Chem. Soc.* **2011**, *133*, 14872-14875. (b) Junge, H. *Chem. Eur. J.* **2012**, *18*, 12749-12758.
- [97] Sala, X.; Maji, S.; Bofill, R.; García-Antón, J.; Escriche, L.; Llobet, A. *Acc. Chem. Res.* **2014**, *47*, 504-516.
- [98] Parent, A. R.; Crabtree, R. H.; Brudvig, G. W. *Chem. Soc. Rev.* **2013**, *42*, 2247-2252.
- [99] Llobet, A. *Molecular Water Oxidation Catalysis*, Wiley, Chichester, 2014.
- [100] Howells, A. R.; Sankarraj, A.; Shannon, C. *J. Am. Chem. Soc.* **2004**, *126*, 12258-12259.
- [101] (a) Belanger, D.; Pinson, J. *Chem. Soc. Rev.* **2011**, *40*, 3995-4048. (b) Pinson, J.; Espreafico, E. M.; Tfouni, E. *Mol. Pharmaceutics* **2013**, *10*, 3544-3554.

- [102] (a) Sala, X.; Romero, I.; Rodríguez, M.; Escriche, L.; Llobet, A. *Angew. Chem. Int. Ed.* **2009**, *48*, 2842-2852. (b) Duan, L.; Tong, L.; Xu, Y.; Sun, L. *Energy Environ. Sci.* **2011**, *4*, 3296-3313. (c) Hettterscheid, D. G. H.; Reek, J. N. H. *Angew. Chem. Int. Ed.* **2012**, *51*, 9740-9747.
- [103] (a) Kurandasa, I.; Chang, C. J.; Long, J. R. *Nature* **2010**, *464*, 1329-1333. (b) Sun, Y.; Bigi, J. P.; Piro, N. A.; Tang, M. L.; Chang, C. J. *J. Am. Chem. Soc.* **2011**, *133*, 9212-9215. (c) Sudstrom, E. J.; Yang, X.; Thoi, V. S.; Karunadasa, H. I.; Chang, C. J.; Long, J. R.; Head-Gordon, M. *J. Am. Chem. Soc.* **2012**, *134*, 5233-5242. (d) Sun, Y.; Sun, J.; Long, J. R.; Yang, P.; Chang, C. J. *Chem. Sci.* **2013**, *4*, 118-124.
- [104] Harriman, A.; Pickering, I. J.; Thomas, J. M.; Christensen, P. A. *J. Chem. Soc., Faraday Trans. 1* **1988**, *84*, 2795-2806.
- [105] Matheu, R.; Francàs, L.; Chernev, P.; Ertem, M. Z.; Batista, V.; Haumann, M.; Sala, X.; Llobet, A. *ACS Catal.* **2015**, *5*, 3422-3429.
- [106](a) Sartorel, A.; Bonchio, M.; Campagna, S.; Scandola, F. *Chem. Soc. Rev.* **2013**, *42*, 2262-2280. (b) Lewandowska-Andralojc, A.; Polyansky, D. E. *J. Phys. Chem. A* **2013**, *117*, 10311-10319.
- [107] De Angelis, F.; Pastore, M. *J. Am. Chem. Soc.* **2015**, *137*, 5798-5809.
- [108] Lakowicz, J. R. *Principles of fluorescence spectroscopy*, 2006, Springer Science, New York.
- [109] Turro, N. J.; Scaiano, J. C.; Ramamurthy, V. *Principles of molecular photochemistry: an introduction*, 2009, University Science Books, Sausalito.
- [110] Wilke, B. M.; Castellano, F. N. *J. Chem. Ed.* **2013**, *90*, 786-789.
- [111] Timpson, C. J.; Carter, C. C.; Olmsted III, J. *J. Phys. Chem.* **1989**, *93*, 4116-4120.
- [112] Wilkinson, F.; Helman, W. R.; Ross, A. B. *J. Phys. Chem. Ref. Data* **1993**, *22*, 113-150.
- [113] Hoertz, P. G.; Kim, Y.-I.; Youngblood, W. J.; Mallouk, T. E. *J. Phys. Chem. B* **2007**, *111*, 6845-6856.
- [114] Youngblood, W.J.; Lee, S.-H. A.; Kobayashi, Y.; Hernandez-Pagan, E.A.; Hoertz, P. G.; Moore, T.A.; Moore, A.L.; Gust, D.; Mallouk, T.E. *J. Am. Chem. Soc.* **2009**, *131*, 926-927.
- [115] Zhao, Y.; Swierk, J. R.; Jr, D. M.; Sherman, B.; Youngblood, W. J.; Qin, D.; Lentz, D. M.; Moore, A.L.; Moore, T.A.; Gust, D.; Mallouk, T.E. *Proc. Natl. Acad. Sci. USA* **2012**, *109*, 15612-15616.
- [116] Youngblood, W. J.; Lee, S.-H. A.; Maeda, K.; Mallouk, T. E. *Acc. Chem. Res.* **2009**, *42*, 1966-1973.
- [117] (a) Harriman, A.; Thomas, J. M.; Millward, G. R. *New J. Chem.* **1987**, *11*, 757-762. (b) Mills, A. *Chem. Soc. Rev.* **1989**, *18*, 285-316.
- [118] Bode, H.; Dehmelt, K.; Witte, J. *Electrochim. Acta* **1966**, *11*, 1079-IN1071.
- [119] Oliva, P.; Leonardi, J.; Laurent, J. F.; Delmas, C.; Braconnier, J. J.; Figlarz, M.; Fievet, F.; Guibert, A. *J. Power Sources* **1982**, *8*, 229-255.
- [120] Morita, M.; Iwakura, C.; Tamura, H. *Electrochim. Acta* **1977**, *22*, 325-328.
- [121] (a) Hambourger, M.; Gervaldo, M.; Svedruzic, D.; King, P. W.; Gust, D.; Ghirardi, M.; Moore, A. L.; Moore, T. A. *J. Am. Chem. Soc.* **2008**, *130*, 2015-2022. (b) Youngblood, W. J. *J. Am. Chem. Soc.* **2009**, *131*, 926-927. (c) Youngblood, W. J.; Lee, S.-H. A.; Maeda, K.; Mallouk, T. E. *Acc. Chem. Res.* **2009**, *42*, 1966-1973.
- [122] (a) Gorlin, Y.; Jaramillo, T. F. *J. Am. Chem. Soc.* **2010**, *132*, 13612-13614. (b) Fukuzumi, S.; Yamada, Y. *J. Mater. Chem.* **2012**, *22*, 24284-24296.
- [123] Greeley, J.; Jaramillo, T. F.; Bonde, J.; Chorkendorff, I. B.; Norskov, J. K. *Nat. Mater.* **2006**, *5*, 909-913.
- [124] Zhao, Y.; Nakamura, R.; Kamiya, K.; Nakanishi, S.; Hashimoto, K. *Nat. Commun.* **2013**, *4*, 2390.
- [125] (a) Gorlin, Y.; Jaramillo, T. F. *J. Am. Chem. Soc.* **2010**, *132*, 13612-13614. (b) Liang, Y.; Li, Y.; Wang, H.; Zhou, J.; Wang, J.; Regier, T.; Dai, H. *Nat. Mater.* **2011**, *10*, 780-786.
- [126] Blakemore, J.D.; Gray, H.B.; Winkler J.R.; Müller, A.M. *ACS Catal.* **2013**, *3*, 2497-2500.
- [127] Wang, J.; Gao, D.; Wang, G.; Miao, S.; Wu, H.; Li, J.; Bao, X. *J. Mater. Chem. A* **2014**, *2*, 20067-20074.
- [128] Chang, Y.; Shi, N.-E.; Zhao, S.; Xu, D.; Liu, C.; Tang, Y.-J.; Dai, Z.; Lan, Y.-Q.; Han, M.; Bao, J. *ACS Appl. Mater. Interfaces* **2016**, *8*, 22534-22544.
- [129] Li, S.; Peng, S.; Huang, L.; Cui, X.; Al-Enizi, A. M.; Zheng, G. *ACS Appl. Mater. Interfaces*, **2016**, *8*, 20534-20539.

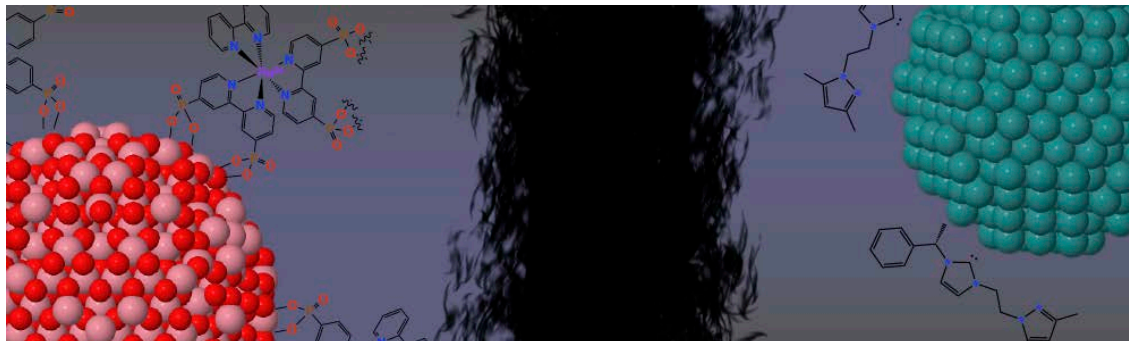
- [130] Jin, H.; Wang, J.; Su, D.; Wei, Z.; Pang, Z.; Wang, Y. *J. Am. Chem. Soc.* **2015**, *137*, 2688-2694.
- [131] Hou, Y.; Zuo, F.; Dagg, A.P.; Liu, J.; Feng, P. *Adv. Mater.* **2014**, *26*, 5043-5049.
- [132] Geng, J.; Kuai, L.; Kan, E.J.; Wang, Q.; Geng, B.Y. *ChemSusChem* **2015**, *8*, 659-664.
- [133] Lu, X.; Zhao, C. *J. Mater. Chem. A* **2013**, *1*, 12053-12059.
- [134] Zhang, J.; Grzelczak, M.; Hou, Y.; Maeda, K.; Domen, K.; Fu, X.; Antonietti, M.; Wang, X. *Chem. Sci.* **2012**, *3*, 443-446.
- [135] Zhang, X.; Liu, R.; Zang, Y.; Liu, G.; Wang, G.; Zhang, Y.; Zhang, H.; Zhao, H. *Chem. Commun.* **2016**, *52*, 5946-5949.
- [136] Zhao, Y.; Chen, S.; Sun, B.; Huang, X.; Liu, H.; Yan, Y.; Sun, K.; Wang, G. *Sci. Rep.* **2015**, *5*, 7629.
- [137] Wu, X.; Scott, K. *J. Mater. Chem.* **2011**, *21*, 12344-12351.
- [138] Indra, A.; Menezes, P.W.; Sahraie, N.R.; Bergmann, A.; Das, C.; Tallarida, M.; Schmeißer, D.; Strasser, P.; Driess, M. *J. Am. Chem. Soc.* **2014**, *136*, 17530-17536.
- [139] Chou, N.H.; Ross, P.N.; Bell, A.T.; Tilley, T.D. *ChemSusChem* **2011**, *4*, 1566-1569.
- [140] Xi, L.; Tran, P.D.; Chiam, S.Y.; Bassi, P.S.; Mak, W.F.; Mulmudi, H.K.; Batabyal, S.K.; Barber, J.; Loo, J.S.C.; Wong, L.H. *J. Phys. Chem. C* **2012**, *116*, 13884-13889.
- [141] Liu, H.; Patzke, G.R. *Chem. Asian J.* **2014**, *9*, 2249-2259.
- [142] Pfrommer, J.; Lublow, M.; Azapira, A.; Göbel, C.; Lücke, M.; Steigert, A.; Pogrzeba, M.; Menezes, P. W.; Fischer, A.; Schedel-Niedrig, T.; Driess, M. *Angew. Chem. Int. Ed.* **2014**, *53*, 5183-5187.
- [143] Cao, G.-L.; Yan, Y.-M.; Liu, T.; Rooney, D.; Guo, Y.-F.; Sun, K.-N. *Carbon* **2015**, *94*, 680-686.
- [144] Chang, J.; Xiao, Y.; Xiao, M.; Ge, J.; Liu, C.; Xing, W. *ACS Catal.* **2015**, *5*, 6874-6878.
- [145] Indra, A.; Menezes, P.W.; Das, C.; Göbel, C.; Tallarida, M.; Schmeißer, D.; Driess, M. *J. Mater. Chem. A* **2017**, *5*, 5171-5177.
- [146] Pilli, S.K.; Furtak, T.E.; Brown, L.D.; Deutsch, T.G.; Turner, J.A.; Herring, A.M. *Energy Environ. Sci.* **2011**, *4*, 5028-5034.
- [147] Han, A.; Wu, H.; Sun, Z.; Jia, H.; Du, P. *Phys. Chem. Chem. Phys.* **2013**, *15*, 12534-12538.
- [148] Liu, Y.; Guo, S.-X.; Ding, L.; Ohlin, C.A.; Bond, A.M.; Zhang, J. *ACS Appl. Mater. Interfaces* **2015**, *7*, 16632-16644.
- [149] Ahn, H.S.; Tilley, T.D. *Adv. Funct. Mater.* **2013**, *23*, 227-233.
- [150] Maeda, K.; Ishimaki, K.; Okazaki, M.; Kanazawa, T.; Lu, D.; Nozawa, S.; Kato, H.; Kakihana, M. *ACS Appl. Mater. Interfaces* **2017**, *9*, 6114-6122.
- [151] Liu, G.; Karuturi, S.K.; Simonov, A.N.; Fekete, M.; Chen, H.; Nasiri, N.; Le, N.H.; Narangari, P.R.; Lysevych, M.; Gengenbach, T.R.; Lowe, A.; Tan, H.H.; Jagadish, C.; Spiccia, L.; Tricoli, A. *Adv. Energy Mater.* **2016**, *6*, 1600697-1600705.
- [152] Meghdadi, S.; Amirnasr, M.; Zhiani, M.; Jallili, F.; Jari, M.; Kiani, M. *Electrocatalysis* **2017**, *8*, 122-131.
- [153] Zhan, F.; Liu, W.; Li, W.; Li, J.; Yang, Y.; Li, Y.; Chen, Q. *Int. J. Hydrogen Energ.* **2016**, *41*, 11925-11932.
- [154] Fang, S.; Li, S.; Ge, L.; Han, C.; Qiu, P.; Gao, Y. *Dalton Trans.* **2017**, doi: 10.1039/c6dt04682g.
- [155] Chang, Y.; Shi, N.-E.; Zhao, S.; Xu, D.; Liu, C.; Tang, Y.-J.; Dai, Z.; Lan, Y.-Q.; Han, M.; Bao, J. *ACS Appl. Mater. Interfaces* **2016**, *8*, 22534-22544.
- [156] Jang, D.M.; Kwak, I.H.; Kwon, E.L.; Jung, C.S.; Im, H.S.; Park, K.; Park, J. *J. Phys. Chem. C* **2015**, *119*, 1921-1927.
- [157] Gardner, G.P.; Go, Y.B.; Robinson, D.M.; Smith, P.F.; Hadermann, J.; Abakumov, A.; Greenblatt, M.; Dismukes, G.C. *Angew. Chem. Int. Ed.* **2012**, *51*, 1616-1619.
- [158] Wee, T.-L.; Sherman, B.D.; Gust, D.; Moore, A.L.; Moore, T.A.; Liu, Y.; Scaiano, J.C. *J. Am. Chem. Soc.* **2011**, *133*, 16742-16745.
- [159] Koroidov, S.; Anderlund, M.F.; Styring, S.; Thapperb, A.; Messinger, J. *Energy Environ. Sci.* **2015**, *8*, 2492-2503.
- [160] Singh, S.K.; Dhavale, V.M.; Kurungot, S. *ACS Appl. Mater. Interfaces* **2015**, *7*, 442-451.

- [161] El Wakkad, S. E. S.; Hickling, A. *Trans. Faraday Soc.* **1950**, *46*, 820-824.
- [162] (a) Brunschwig, B. S.; Chou, M. H.; Creutz, C.; Ghosh, P.; Sutin, N. *J. Am. Chem. Soc.* **1983**, *105*, 4832-4833. (b) Ghosh, P. K.; Brunschwig, B. S.; Chou, M.; Creutz, C.; Sutin, N. *J. Am. Chem. Soc.* **1984**, *106*, 4772-4783.
- [163] (a) Kanan, M. W.; Nocera, D. G. *Science* **2008**, *321*, 1072-1075. (b) McAlpin, J. G.; Surendranath, Y.; Dincă, M.; Stich, T. A.; Stoian, S. A.; Casey, W. H.; Nocera, D. G.; Britt, R. D. *J. Am. Chem. Soc.* **2010**, *132*, 6882-6883.
- [164] Harley, S. J.; Mason, H. E.; McAlpin, J. G.; Britt, R. D.; Casey, W. H. A. *Chem. Eur. J.* **2012**, *18*, 10476-10479.
- [165] Gerken, J. B.; McAlpin, J. G.; Chen, J. Y. C.; Rigsby, M. L.; Casey, W. H.; Britt, R. D.; Stahl, S. S. *J. Am. Chem. Soc.* **2011**, *133*, 14431-14442.
- [166] Nocera, D. G. *Acc. Chem. Res.* **2012**, *45*, 767-776.
- [167] Risch, M.; Shevchenko, D.; Anderlund, M.F.; Styting, S.; Heidkamp, J.; Lange, K.M.; Thapper, A.; Zaharieva, I. *Int. J. Hydrogen Energy* **2012**, *37*, 8878-8888.
- [168] Hu, X.L.; Piccinin, S.; Laio, A.; Fabris, S. *ACS Nano* **2012**, *6*, 10497-10504.
- [169] Walsh, D.; Sanchez-Ballester, N.M.; Ariga, K.; Tanaka, A.; Weller, M. *Green Chem.* **2015**, *17*, 982-990.
- [170] (a) Rasiyah, P.; Tseung, A. C. C. *J. Electrochem. Soc.* **1983**, *130*, 365-368. (b) Brossard, L. *J. Appl. Electrochem.* **1991**, *21*, 612-618. (c) Singh, R. N.; Mishra, D.; Anindita; Sinha, A. S. K.; Singh, A. *Electrochem. Commun.* **2007**, *9*, 1369-1373. (d) Hamdani, M.; Singh, R. N.; Chartier, P. *Int. J. Electrochem. Sci.* **2010**, *5*, 556-577.
- [171] Iwakura, C.; Honji, A.; Tamura, H. *Electrochim. Acta* **1981**, *26*, 1319.
- [172] Grzelczak, M.; Zhang, J.; Pfrommer, J.; Hartmann, J.; Driess, M.; Antonietti, M.; Wang, X. *ACS Catal.* **2013**, *3*, 383-388.
- [173] Jiao, F.; Frei, H. *Angew. Chem. Int. Ed.* **2009**, *48*, 1841-1844.
- [174] Kim, Y.-Y.; Meldrum, F.C.; Walsh, D. *Polymer Chem.* **2011**, *2*, 1375-1379.
- [175] Hutchings, G.S.; Zhang, Y.; Li, J.; Yonemoto, B.T.; Zhou, X.; Zhu, K.; Jiao, F. *J. Am. Chem. Soc.* **2015**, *137*, 4223-4229.
- [176] Hong, D.; Jung, J.; Park, J.; Yamada, Y.; Suenobu, T.; Lee, Y.-M.; Nam, W.; Fukuzumi, S. *Energy Environ. Sci.* **2012**, *5*, 7606-7616.
- [177] Smith, P. F.; Hunt, L.; Laursen, A. B.; Sagar, V.; Kaushik, S.; Calvino, K. U. D.; Marotta, G.; Mosconi, E.; De Angelis, F.; Dismukes, G. C. *J. Am. Chem. Soc.* **2015**, *137*, 15460-15468.
- [178] Wang, L.-P.; Van Voorhis, T. *J. Phys. Chem. Lett.* **2011**, *2*, 2200-2204.
- [179] Nguyen, A. I.; Ziegler, M. S.; Oña-Burgos, P.; Sturzbecher-Hohne, M.; Kim, W.; Bellone, D. E.; Tilley, T. D. *J. Am. Chem. Soc.* **2015**, *137*, 12865-12872.
- [180] Li, X.; Siegbahn, P. E. *J. Am. Chem. Soc.* **2013**, *135*, 13804-13813.
- [181] Chen, J.; Selloni, A. *J. Phys. Chem. Lett.* **2012**, *3*, 2808-2814.
- [182] Risch, M.; Klingan, K.; Ringleb, F.; Chernev, P.; Zaharieva, I.; Fischer, A.; Dau, H. *ChemSusChem* **2012**, *5*, 542-549.
- [183] Zhang, M.; de Respini, M.; Frei, H. *Nat. Chem.* **2014**, *6*, 362-367.
- [184] Aiso, K.; Takeuchi, R.; Masaki, T.; Chandra, D.; Saito, K.; Yui, T.; Yagi, M. *ChemSusChem* **2017**, *10*, 687-692.
- [185] Kanan, M. W.; Yano, J.; Surendranath, Y.; Dincă, M.; Yachandra, V. K.; Nocera, D. G. *J. Am. Chem. Soc.* **2010**, *132*, 13692-13701.
- [186] (a) Reece, S. Y.; Hamel, J. A.; Jarvi, T. D.; Esswein, A. J.; Pijpers, J. J.; Nocera, D. G. *Science* **2011**, *224*, 645-648. (b) Steinmiller, E. M. P.; Choi, K. S. *P. Natl. Acad. Sci. USA* **2009**, *49*, 20633-20636.
- [187] González-Flores, D.; Sánchez, I.; Zaharieva, I.; Klingan, K.; Heidkamp, J.; Chernev, P.; Menezes, P.W.; Driess, M.; Dau, H.; Montero, M. L. *Angew. Chem. Int. Ed.* **2015**, *54*, 2472-2476.
- [188] Ryu, J.; Jung, N.; Jang, J. H.; Kim, H.-J.; Yoo, S.-J. *ACS Catal.* **2015**, *5*, 4066-4074

- [189] Klhar, B.; Gimenez, S.; Fabregat-Santiago, F.; Bisquert, J.; Hamann, T. W. *J. Am. Chem. Soc.* **2012**, *134*, 16693-16700.
- [190] Wang, T.; Hung, H.-T.; Cheng, Y.-R.; Huang, M.-C.; Ksieh, Y.-K.; Wang, C.-F. *RSC Adv.* **2016**, *6*, 28236-28247.
- [191] Kwapien, K.; Piccinin, S.; Fabris, S. *J. Phys. Chem. Lett.* **2013**, *4*, 4223-4230.
- [192] (a) McCrory, C. C. L.; Jung, S.; Peters, J. C.; Jaramillo, T. F. *J. Am. Chem. Soc.* **2013**, *135*, 16977-16987. (b) McCrory, C. C. L.; Jung, S.; Ferrer, I. M.; Chatman, S. M.; Peters, J. C.; Jaramillo, T. F. *J. Am. Chem. Soc.* **2015**, *137*, 4347-4357.
- [193] Zhao, A.; Masa, J.; Xia, W.; Maljusch, A.; Willinger, M.-G.; Clavel, G.; Xie, K.; Schlögl, R.; Schuhman, W.; Muhler, M. *J. Am. Chem. Soc.* **2014**, *136*, 7551-7554.
- [194] Yeo, B.S.; Bell, A.T. *J. Am. Chem. Soc.* **2011**, *133*, 5587-5593.
- [195] Frydendal, R.; Busch, M.; Halck, N.B.; Paoli, E.A.; Krtil, P.; Chorkendorff, I. Rossmeisl, J. *ChemCatChem.* **2015**, *7*, 149-154.
- [196] Fester, J.; García-Melchor, M.; Walton, A.S.; Bajdich, M.; Li, Z.; Lammich, L.; Vojvodic, A.; Lauritsen, J.V. *Nat. Commun.* **2017**, *8*, 14169-14176.
- [197] Yusuf, S.; Jiao, F. *ACS Catal.* **2012**, *2*, 2753-2760.
- [198] Zidki, T.; Zhang, L.; Shafirovich, V.; Lyamar, S.V. *J. Am. Chem. Soc.* **2012**, *134*, 14275-14278.
- [199] Lin, C.-C.; Guo, Y.; Vela, J. *ACS Catal.* **2015**, *5*, 1037-1044.
- [200] Han, J.; Wang, D.; Du, Y.; Xi, S.; Hong, J.; Yin, S.; Chen, Z.; Zhou, T.; Xu, R. *J. Mater. Chem. A* **2015**, *3*, 20607-20613.
- [201] Lin, C.-C.; Guo, Y.; Vela, J. *ACS Catal.* **2015**, *5*, 1037-1044.
- [202] Yusuf, S.; Jiao, F. *ACS Catal.* **2012**, *2*, 2753-2760.
- [203] Zidki, T.; Zhang, L.; Shafirovich, V.; Lyamar, S.V. *J. Am. Chem. Soc.* **2012**, *134*, 14275-14278.
- [204] Jiao, F.; Frei, H. *Angew. Chem. Int. Ed.* **2009**, *48*, 1841-1844.
- [205] Fujishima, A.; Honda, K. *Nature* **1972**, *238*, 37-38.
- [206] Wolcott, A.; Smith, W. A.; Kuykendall, T. R.; Zhao, Y.; Zhang, J. Z. *Small* **2009**, *5*, 104-111.
- [207] Yang, X. Y.; Wolcott, A.; Wang, G. M.; Sobo, A.; Fitzmorris, R. C.; Qian, F.; Zhang, J. Z.; Li, Y. *Nano Lett.* **2009**, *9*, 2331-2336.
- [208] Li, M.; Chang, K.; Wang, T.; Liu, L.; Zhang, H.; Li, P.; Ye, J. *J. Mater. Chem. A* **2015**, *3*, 13731-13737.
- [209] Chakrapani, V.; Thangala, J.; Sunkara, M. K. *Int. J. Hydrogen Energy* **2009**, *34*, 9050-9059.
- [210] Huang, J.; Zhang, Y.; Ding, Y. *ACS Catal.* **2017**, *7*, 1841-1845.
- [211] Park, Y.; McDonald, K. J.; Choi, K. S. *Chem. Soc. Rev.* **2013**, *42*, 2321-2337.
- [212] Wang, J.; Osterloh, F.E. *J. Mater. Chem. A* **2014**, *2*, 9405-9411.
- [213] Zhong, M.; Hisatomi, T.; Kuang, Y.; Zhao, J.; Liu, M.; Iwase, A.; Jia, Q.; Nishiyama, H.; Minegishi, T.; Nakabayashi, M.; Shibata, N.; Katayama, C.; Shibano, H.; Kudo, A.; Yamada, T.; Domen, K. *J. Am. Chem. Soc.* **2015**, *137*, 5053-5060.
- [214] Sivula, K.; Zboril, R.; Le Formal, F.; Robert, R.; Weidenkaff, A.; Tucek, J.; Frydrych, J.; Grätzel, M. *J. Am. Chem. Soc.* **2010**, *132*, 7436-7444.
- [215] Martin, D. J.; Umezawa, N.; Chen, X.; Ye, J.; Tang, J. *Energy Environ. Sci.* **2013**, *6*, 3380-3386.
- [216] Higashi, M.; Domen, K.; Abe, R. *J. Am. Chem. Soc.* **2012**, *134*, 6968-6971.
- [217] Gujral, S. S.; Simonov, A. N.; Higashi, M.; Fang, X.-Y.; Abe, R.; Spiccia, L. *ACS Catal.* **2016**, *6*, 3404-3417.
- [218] Higashi, M.; Tomita, O.; Abe, R. *Top. Catal.* **2016**, *59*, 740-749.
- [219] Cong, Y.; Park, H.S.; Wang, S.; Dang, H.X.; Fan, F.-R.F.; Mullins, C.B.; Bard, A. J. *J. Phys. Chem. C* **2012**, *116*, 14541-14550.
- [220] Hou, J.; Wang, Z.; Yang, C.; Cheng, H.; Jiao, S.; Zhu, H. *Energy Environ. Sci.* **2013**, *6*, 3322-3330.
- [221] Chen, S.; Shen, S.; Liu, G.; Qi, Y.; Zhang, F.; Li, C. *Angew. Chem. Int. Ed.* **2015**, *54*, 3047-3051.

-
- [222] Liao, M.; Feng, J.; Luo, W.; Wang, Z.; Zhang, J.; Li, Z.; Yu, T.; Zou, Z. *Adv. Funct. Mater.* **2012**, *22*, 3066-3074.
- [223] Jiang, C.; Moniz, S. J. A.; Khraisheh, M.; Tang, J. *Chem. Eur. J.* **2014**, *20*, 12954-12961.
- [224] Robinson, D. M.; Go, Y. B.; Mui, M.; Gardner, G.; Zhang, Z.; Mastrogiovanni, D.; Garfunkel, E.; Li, J.; Greenblatt, M.; Dismukes, G. C. *J. Am. Chem. Soc.* **2013**, *135*, 3494-3501.
- [225] Hocking, R.K.; Brimblecombe, R.; Chang, L.Y.; Singh, A.; Cheah, M.H.; Glover, C.; Casey, W.H.; Spiccia, L. *Nat. Chem.* **2011**, *3*, 461-466.
- [226] Kim, T. W.; Woo, M. A.; Regis, M.; Choi, K.-S. *J. Phys. Chem. Lett.* **2014**, *5*, 2370-2374.
- [227] Cady, C.W.; Gardner, G.; Maron, Z.O.; Retuerto, M.; Go, Y. B.; Segan, S.; Greenblatt, M.; Dismukes, G.C. *ACS Catal.* **2015**, *5*, 3403-3410.
- [228] Song, F.; Hu, X. *J. Am. Chem. Soc.* **2014**, *136*, 16481-16484.
- [229] Li, D.; Baydoun, H.; Verani, C. N.; Brock, S. L. *J. Am. Chem. Soc.* **2016**, *138*, 4006-4009.
- [230] Khan, S.A.; Khan, S.B.; Asiri, A.M. *J. Mater. Sci.: Mater. Electron.* **2016**, *27*, 5294-5302.
- [231] Xu, Y.-F.; Wang, X.-D.; Chen, H.-Y.; Kuang, D.-B.; Su, C.-Y. *Adv. Funct. Mater.* **2016**, *26*, 4414-4421.
- [232] Cui, X.; Ren, P.; Deng, D.; Deng, J.; Bao, X. *Energy Environ.Sci.* **2016**, *9*, 123-129.
- [233] Gardner, G.; Al-Sharab, J.; Danilovic, N.; Go, Y.B.; Ayers, K.; Greenblatta, M.; Dismukes, G.C. *Energy Environ. Sci.* **2016**, *9*, 184-192.
- [234] (a) Smith, R. D. L.; Prévot, M. S.; Fagan, R. D.; Zhang, Z. P.; Sedach, P. A.; Siu, M. K. J.; Trudel, S.; Berlinguette, C. P. *Science* **2013**, *340*, 60-63. (b) Smith, R. D. L.; Prévot, M. S.; Fagan, R. D.; Trudel, S.; Berlinguette, C. P. *J. Am. Chem. Soc.* **2013**, *135*, 11580-11586. (c) Corrigan, D. A. *J. Electrochem. Soc.* **1987**, *134*, 377-384. (d) Trotochaud, L.; Young, S. L.; Ranney, J. K.; Boettcher, S. W. *J. Am. Chem. Soc.* **2014**, *136*, 6744-6753.

Chapter II. Objectives

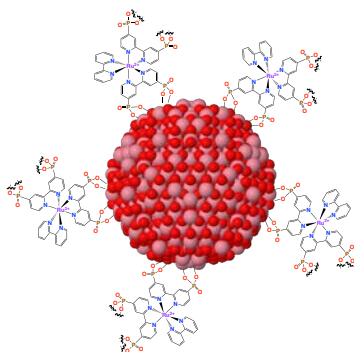
II

Within the state-of-the-art of metal or metal oxide NPs as nanocatalysts presented in Chapter 1, and more specifically Co_3O_4 NPs for water oxidation catalysis or Pd(0) NPs for Suzuki Miyaura reactions, the present Chapter exposes the main objectives of this thesis.

Co-based Dyads for Light-Driven Water Oxidation

The water splitting (WS) reaction, when triggered by sunlight, is a pivotal alternative to other non-renewable energy sources widely used nowadays such as fossil fuels. In WS, reductive equivalents are initially obtained from the oxidation of water, a thermodynamically up-hill process with sluggish kinetics that is generally identified as the bottleneck of the whole process. Therefore, and taking into account the previous background exposed in Chapter 1 concerning the advantages of using systems at the nanoscale for catalytic applications, the general aim of this thesis is the achievement of reliable water oxidation catalysts (WOCs) for light-driven water oxidation based on earth-abundant transition-metal nanostructures.

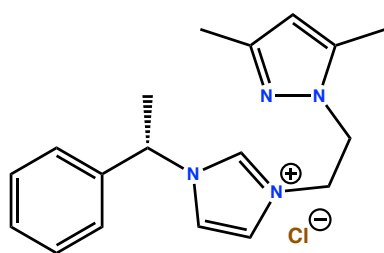
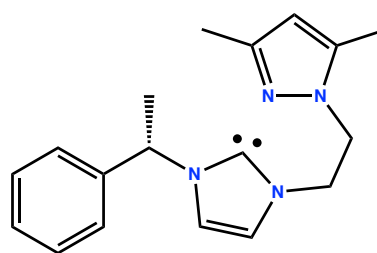
In order to achieve the light-driven photo-production of O_2 , it is mandatory the mastering of two main components and, particularly, their harmonic interaction: a light harvesting device or photosensitizer (PS) and a water oxidation catalyst. About the latter, cobalt oxide-based nanoparticles are promising candidates as WOCs since they are made of a relatively cheap first-row metal and have shown both relatively high catalytic activities and good stabilities at neutral and basic pH. On the other hand, tris(bipyridyl)Ru(II) complexes have been extensively studied as photosensitizers in the water oxidation reaction due to their excellent properties as light-harvesting units. Therefore, cobalt oxide-based WOCs and tris(bipyridyl)Ru(II) complexes will be chosen and combined in this thesis with the goal of attaining dyad systems at the nanoscale for light-driven water oxidation catalysis and better understanding the key parameters controlling their efficient catalytic performance. In order to attain this general goal, the following specific objectives have been designed:



- 1) Synthesize Co(0) NPs through the mild decomposition of organometallic precursors under reductive conditions and attain from them homogeneous in size CoO_x species by controlled oxidation methods.
- 2) Evaluate and benchmark the electrocatalytic and photocatalytic capacity of the prepared CoO_x nanomaterials towards the water oxidation reaction.
- 3) Synthesize PS-CoO_x dyad systems through the covalent anchoring of phosphonate-containing PS moieties at the surface of the CoO_x nanomaterials prepared in 2) and evaluate their photocatalytic capacity of oxidizing water compared to that of unbound PS/CoO_x mixtures.
- 4) Study the rate of the electron-transfer events taking place in the photocatalytic systems described in 2) and 3) through flash photolysis/transient absorbance methods and use the data obtained to rationally design improved second-generation PS-CoO_x dyad systems.

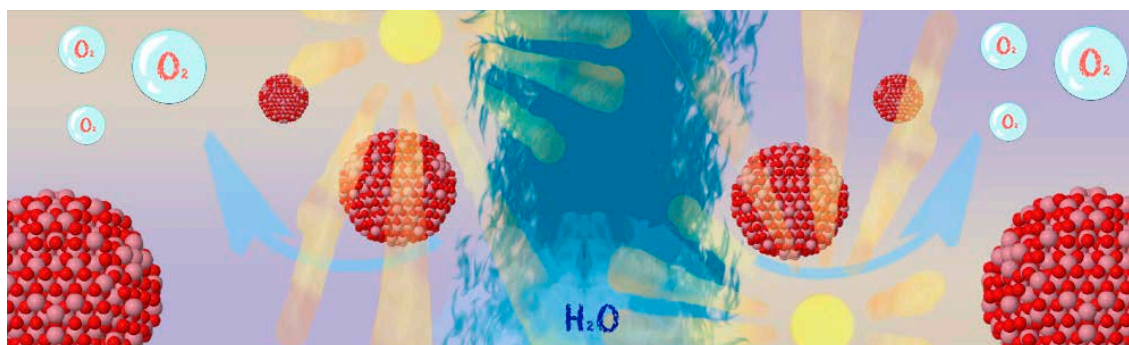
Colloidal vs. Molecular Pd-based Catalysts in C-C Coupling Reactions

Palladium is the most versatile transition metal in chemical catalysis reactions and many of these processes cannot be catalyzed by other transition metals. Furthermore, Pd(0) NPs have shown large catalytic efficiency in C-C coupling reactions specially when non-aggregated homogeneous NPs of 1-4 nm size are used as catalysts. Following these precedents, our group has recently prepared Pd(0) NPs stabilized by the two following ligands; 1-[2-(3,5-dimethylpyrazol-1-yl)ethyl]-3-((S)-1-phenylethyl)-3*H*-imidazol-1-ium chloride (**HL·Cl**) and 1-[2-(3,5-dimethylpyrazol-1-yl)ethyl]-3-((S)-1-phenylethyl)-3*H*-imidazol-2-ylidene (**L**) N-heterocyclic carbene ligands (see their structure below).

**HL·Cl****L**

In this work, the reactivity of these systems as Suzuki-Miyaura catalysts will be tested. Since different reactivity has been evidenced for molecular and colloidal Pd catalysts, the comparison with the analogous palladium(II) complexes will be also carried out.

Chapter III. Coordination of photosensitive Ru-polypyridylic complexes at the surface of Co_3O_4 nanoparticles: hybrid dyads for light-driven water oxidation



III

A novel method for the preparation of Co_3O_4 nanocatalysts and their corresponding derivatives covalently functionalized by light-harvesting photosensitizers is presented hereafter. The set of nanomaterials has been thoroughly characterized by ICP, HREM, XPS, IR and Wide Angle X-ray Scattering, while electrochemical and photophysical studies have been carried out with the bare NPs and the hybrid PS-NP systems, respectively, to extract conclusions with regards to their respective ability to electro- and photo-oxidize water.

Table of Contents

3.1 Abstract	97
3.2 Introduction.....	99
3.3 Experimental Section	101
3.3.1 General	101
3.3.2 Characterization techniques.....	101
3.3.3 Synthesis protocols	105
3.3.4 Preparation of electrodes	106
3.4 Results and Discussion	107
3.4.1 Synthesis and characterization of the nanomaterials.....	107
3.4.2 Electrocatalytic behavior in water oxidation catalysis	113
3.4.3 Photochemical water oxidation catalysis.....	116
3.4.4 Photophysical studies	121
3.5 Conclusions.....	129
3.6 Supporting information	131
3.6.1 Estimation of Co content in Co ₃ O ₄ NPs.....	131
3.6.2 Estimation of the number of 1-heptanol molecules per Co NP	131
3.6.3 Estimation of the number of Co atoms per Co ₃ O ₄ , PS1-Co ₃ O ₄ and PS2-Co ₃ O ₄ NPs	132
3.6.4 Estimation of the number of 1-heptanol molecules per Co ₃ O ₄ NP	133
3.6.5 Estimation of the number of 1-heptanol and PS molecules per PS1-Co ₃ O ₄ NP and PS2-Co ₃ O ₄ NP.....	134
3.6.6 Calculation of TON (O ₂ molecules/NP).....	135
3.6.7 Calculation of TON (O ₂ molecules/PS).....	135
3.6.8 Calculation of TOF (O ₂ molecules/NP).....	136
3.6.9 Calculation of TOF (O ₂ molecules/PS).....	136
3.6.10 PMMA Coating	136
3.6.11 Quenching of [Photosensitizer] ^{+2,*} by S ₂ O ₈ ²⁻	136

3.6.12 PS used and Characterization of Co and Co₃O₄ NPs and PS1-Co₃O₄ and PS2-Co₃O₄ hybrid systems	137
3.6.13 Electroinduced water oxidation experiments	141
3.6.14 Photoinduced water oxidation experiments and related data	144
3.6.15 Photophysical studies	150
3.7 References	155

3.1 Abstract

Cobalt nanoparticles (NPs) have been easily prepared by hydrogenation of the organometallic complex [Co(η^3 -C₈H₁₃)(η^4 -C₈H₁₂)] in heptanol in the absence of any other stabilizer and then oxidized to Co₃O₄ NPs in mild oxidative reaction conditions. After deposition onto a glassy carbon rotating disk electrode, the electrocatalytic performance of the latter have been tested in 1M NaOH solution and their activity benchmarked with that of state-of-the-art Co₃O₄ NPs through ECSA and specific current density measurements. Furthermore, the covalent grafting of photosensitive polypyridylic-based Ru^{II} complexes onto the surface of Co₃O₄ NPs afforded hybrid nanostructured materials able to photooxidize water into O₂. These hybrid nanocatalysts display better catalytic performance than simple mixtures of non-grafted photosensitizers (PS) and Co₃O₄ NPs, thus evidencing the advantage of the direct coupling between the two entities for the photo-induced water oxidation reaction. This study represents the first work in which 1st row transition metal oxide NPs covalently attached to polypyridylic-based Ru^{II} PS are shown to be active in photocatalytic water oxidation.

3.2 Introduction

Non-renewable fossil fuels are still nowadays the main energy source used by mankind. However, their fast depletion due to the constant increase of the global energy consumption and their relationship with the worrying levels of greenhouse gases and climate change make the development of less polluting and renewable energy sources a central topic for the scientific community. In this context, sunlight-driven water-splitting is a very attractive solution [1]. The water splitting reaction, in which both oxygen and hydrogen gas are generated in the anode and cathode, respectively, represents an attractive alternative method for obtaining energy in the form of the highly energetic H-H chemical bond [2], as long as the energy used to produce the hydrogen gas is renewable. Nevertheless, the anodic oxidation of water into O₂ is a thermodynamically uphill, mechanistically complex and kinetically slow (high overpotentials) process, in which four electrons have to be removed from two water molecules and an O=O double bond has to be formed [3]. With the aim of improving the kinetics of this half reaction and inspired by Nature's photosystem II -responsible of oxygen formation during photosynthesis-, chemists have been developing several photocatalytic systems during the past years [4,5]. Thus, several homogeneous and heterogeneous water oxidation catalysts (WOCs) have been tested in the presence of a photosensitizer (PS), a chromophore able to harvest photons and convert their energy into free electrons [6]. However, the catalytic performance of these systems is often limited by the insufficient rate of electron transfer from the WOC to the PS and the undesired back-electron transfer phenomena between the PS and the WOC [6,7]. Within this context, covalently bound *molecular* PS-WOC dyad systems have proven to be more efficient in photocatalytic WO since the rate of electron transfer from the WOC to the PS is significantly faster [8,9]. Thus, *molecular* PS-WOC dyad systems based on 2nd and 3rd row transition elements [9,10,11] and abundant 1st row elements [12,13] have been successfully employed in photocatalytic WO.

Transition from homogeneous to colloidal/heterogeneous species recurrently takes place during WO catalysis [14,15,16], particularly when 1st row transition-metals and/or easily oxidizable ligands are employed [17]. Despite the high activity often shown by these *in-situ* formed species, their size, composition and reactivity are poorly controlled. Therefore, the *ex-situ* synthesis of metal nanoparticle (NP) catalysts with well-controlled size and surface

properties might allow a better tuning of their catalytic performance. In this sense, the photocatalytic performance in WO of colloidal dye (PS)-decorated IrO_x suspensions has been reported by Mallouk and co-workers [7,8,18]. In these hybrid dyads, the PS serves both as NP stabilizer and light-harvester, thus helping to overcome the thermodynamically unfavorable barrier associated with water oxidation. However, to our knowledge no examples of WOC are known so far in which the PS is covalently bound to abundant 1st row transition metal oxide NPs, which would reduce the global cost of the water splitting process.

Recent literature data thus underline the interest of a rational design of hybrid PS-NP catalysts for the WO reaction. Within this context, the organometallic approach, which is recognized to be highly efficient to prepare NPs with high control over the size, composition and surface properties [19], may offer new opportunities towards the synthesis of hybrid PS-NP materials with a covalent bonding between the PS and the NP surface. By this way, one can expect to have at disposal well-controlled hybrid catalytic materials in order to study the influence of the direct link between the PS and the NP surface on their reactivity, being able to adjust the dyads to reach better catalytic performances. With this idea in mind, we decided to investigate the grafting of polypyridyl-Ru^{II} complexes acting as PSs at the surface of Co₃O₄ NPs prepared by organometallic chemistry as a route to obtain advanced WO photocatalysts. Therefore, herein we here report the synthesis and full characterization of novel hybrid PS-NP materials formed by covalently attaching light-harvesting [Ru(bpy)₃]²⁺ derived-complexes to preformed abundant first row cobalt oxide NPs (Co₃O₄ NPs), and their use as catalysts in the photoinduced oxidation of water in comparison with colloidal mixtures of non-bonded PS and Co₃O₄ NPs, and Co₃O₄ NPs alone. Finally, flash photolysis/transient absorbance methods have been used to analyze the electronic coupling between the different components of the photocatalytic mixtures.

3.3 Experimental Section

3.3.1 General

All operations concerning the synthesis and preparation of samples for characterization of Co nanoparticles were carried out using standard Schlenck tube, Fisher-Porter glassware and vacuum line techniques or in a glove-box (Braun) under argon atmosphere. Reagents and solvents were degassed before use according to a freeze-pump-thaw process. The (cyclooctadienyl)(1,5-cyclooctadiene)cobalt(I), [Co(η^3 -C₈H₁₃)(η^4 -C₈H₁₂)], complex was purchased from Nanomeps-Toulouse. 1-Heptanol, sodium persulfate, sodium hydroxide, sodium hexafluorosilicate, and sodium bicarbonate were acquired from Sigma-Aldrich. Dihydrogen and argon were purchased from Alphagaz. 1-Heptanol was dried over activated molecular sieves (4 Å) prior to use and other reagents were employed as received unless otherwise specified. Solvents (THF, pentane, dichloromethane, diethyl ether) were purified before use by filtration on adequate alumina columns in a purification apparatus (MBraun) and handled under argon atmosphere.

3.3.2 Characterization techniques

Transmission electron microscopy observations at low (TEM) and high resolution (HREM) were performed at the “Centre de Microcaractérisation Raymond Castaing” in Toulouse (UMS-CNRS 3623) and at the “Servei de Microscòpia” of the UAB. TEM grids were prepared by drop-casting of the crude colloidal solution in 1-heptanol for the cobalt material or a dispersion in 1-heptanol for the cobalt oxide material onto a holey carbon-coated copper grid, and under argon atmosphere in a glove-box for Co samples. Pumping with a Gatan turbo pumping station model 655 was carried out before analysis. TEM analyses were performed on JEOL JEM 1011 or JEM-2011 electron microscopes operating at 100 kV with point resolution of 4.5 Å. HREM observations were carried out with a JEOL JEM 2100 F electron microscope working at 200 kV with a point resolution of 2.5 Å and equipped with X-ray analysis PGT (light elements detection, resolution 135 eV). Cs-corrected STEM HAADF EDX observations were performed using a JEOL JEM-ARM200F Cold FEG instrument equipped with a EDS/EELS detector with

a resolution point $<1.9 \text{ \AA}$. Statistical size distributions were built *via* manual analysis of enlarged micrographs by measuring *ca.* 200 non-touching nanoparticles. The analyses were done by assuming that the nanoparticles are spherical. Nanoparticle sizes are quoted as the mean diameter \pm the standard deviation. FFT analysis was carried out using Digital micrograph software.

Wide-angle X-ray scattering (WAXS) measurements were performed at CEMES-CNRS in Toulouse. Samples were measured in 1.0 mm diameter Lindemann glass capillaries. The samples were irradiated with graphite monochromatized molybdenum $K\alpha$ (0.071069 nm) radiation and the X-ray scattering intensity measurements were performed using a dedicated two-axis diffractometer. Radial distribution functions (RDF) were obtained after Fourier transformation of the corrected and reduced data.

Infrared (IR) spectra were recorded inside the glove-box with a Bruker Alpha FT-IR spectrometer in the range $4000\text{--}600 \text{ cm}^{-1}$ in attenuated total reflectance (ATR) mode. IR spectra of Co_3O_4 NPs were also recorded in the range $4000\text{--}400 \text{ cm}^{-1}$ on a thermonicolet IR200 spectrometer in transmission mode with samples prepared as KBr pellets.

ICP-OES measurements were performed on an Optima 4300DV Perkin-Elmer system. Samples were prepared by taking 5 mg of the NP powders and digesting them with *aqua regia* under microwave conditions followed by a dilution of the mixture with HCl 1% (v/v).

X-ray photoelectron spectroscopy (XPS) studies were performed at the Catalan Institute of Nanoscience and Nanotechnology (ICN2) on a SPECS EA10P hemispherical analyzer using a non-monochromated X-ray source (Al $K\alpha$ line of 1486.6eV and 300W) placed perpendicularly to the analyzer axis and calibrated using the 1s line of C. The measurements were made in ultra-high vacuum at residual pressure around 10^{-8} Pa.

Steady-state luminescence and lifetime measurements

Fluorescence quantum yield studies of degassed solutions were performed using a Fluorolog-3 (Jobin Yvon) spectrofluorometer with iHR-320 and photomultipliers from Hamamatsu Photonics: R2658 (range 185 – 1100 nm) with reference $[\text{Ru}(\text{bpy})_3]^{2+}$ in water ($\Phi_s = 0.028$). The excitation wavelength was chosen to correspond to the maximum of the molecule absorption band (450 nm). The correction of the emission spectrum was performed with respect

to the spectral sensitivity of detector and excitation source stabilities. Quantum yields of molecular systems (for optical diluted solutions) were determined versus the standard [Ru(bpy)₃]²⁺ in Milli-Q water of known quantum yield according to eq (1)

$$\Phi_x = \Phi_s \cdot \left(\frac{I_x}{I_s}\right) \cdot \left(\frac{F_x}{F_s}\right) \cdot \left(\frac{\eta_x}{\eta_s}\right)^2 \quad (1)$$

where I is the integrated emission intensity of the standard (S) and sample (x) solutions; F_S and F_X are the fraction of light absorbed by the respective solutions; Φ_s is the quantum yield of the standard and η_S and η_x denote the refractive index of the respective media. All solutions were thoroughly purged by saturating them with ultra pure argon gas.

Electrochemical characterization and electrocatalytic water oxidation experiments

Electrochemical characterization of the nanomaterials was performed at pH 14 on an IJ-Cambria HI-660 potentiostat using a three-electrode cell. Typical cyclic voltammetry (CV) experiments were carried out at a scan rate of 1 mV/s or 100 mV/s. For the stability tests, a fluorine tin oxide (FTO) electrode (1 cm² area) supporting the Co₃O₄ NPs was used as the working electrode, a platinum mesh as the auxiliary electrode and a saturated Hg/HgSO₄ (sat. K₂SO₄) calomel electrode as the reference electrode. For the benchmarking experiments with Co₃O₄ NPs, electrochemical experiments were performed on a Biologic SP-150 potentiostat using the EC Lab software for data handling. The potentiostat was equipped with a R11V016 Radiometer CTV101 speed control unit fixed at 3000 rpm. For all other experiments, a glassy carbon rotatory disk electrode (RDE, 0.07 cm² area) supporting the Co₃O₄ NPs was used as the working electrode, a platinum mesh as the auxiliary electrode and an Ag/AgCl electrode as the reference electrode. The RDE was polished with 0.05 μm alumina paste, and washed with distilled water and acetone before each measurement. Bulk electrolysis experiments were performed on a IJ-Cambria HI-660 potentiostat connected to an external high current booster (5 A) using a FTO/Co₃O₄ NPs-PMMA (PMMA = poly(methylmethacrylate)) as the working electrode, a platinum wire as the counter electrode and Ag/AgCl (3.5 M KCl) as the reference electrode in a homemade two chambers electrochemical reactor separated by a Vycor frit. Additional inlets were closed by Subaseal® septa to ensure a hermetic sealing. Oxygen evolution was analyzed with a gas-phase Clark-type oxygen electrode (Unisense O_x-N needle microsensor).

The electrode was calibrated using argon saturated and air saturated water before each experiment. The overpotential η was calculated by the equation $\eta = V_{\text{applied}} - E_{\text{pH}} - iR$, where V_{applied} is the applied potential vs. NHE ($V_{\text{applied}} = E_{\text{applied}} + 0.245$), $E_{\text{pH}} = 1.23 - 0.059 \text{ pH}$ vs. NHE, i is the stable current under the corresponding potential and R is the solution resistance measured by the iR compensation function. In bulk electrolysis experiments, the theoretical yield of oxygen produced was calculated by assuming that all charges were used for the $4e^-$ oxidation of water following the Faraday law $n = Q / 4F$, where n is the number of moles of oxygen, Q is the total charge deduced from the bulk electrolysis, and F is the Faraday constant.

Photoinduced water oxidation studies

The photoinduced water oxidation experiments were performed in a specific dark thermostated chamber (Hansatech Instruments) with an integrated Clark-type electrode that measured the produced oxygen in the liquid phase, with no headspace left. In a typical experiment, the chosen amount of photosensitizer (**PS0**, **PS1** or **PS2**, see Figure S1 in the Supplementary Material) in the optimized conditions for **PS1** ($1.54 \cdot 10^{-3}$ mmol; 6.0 eq with respect to moles of $\text{Co}_3\text{O}_4(\text{heptanol})_{2.8}$ units), a high molar excess of $\text{Na}_2\text{S}_2\text{O}_8$ (10.71 mg, 0.045 mmol, 175 eq) and the Co_3O_4 NPs (0.15 mg, $2.56 \cdot 10^{-4}$ mmol of $\text{Co}_3\text{O}_4(\text{heptanol})_{2.8}$ units, 1 eq) were introduced into the dark chamber thermostated at 25.0 °C followed by 1.5 mL of $\text{Na}_2\text{SiF}_6 - \text{NaHCO}_3$ ($0.02 - 0.04 \text{ mol} \cdot \text{L}^{-1}$, pH=5.6) buffer solution (1.5 mL total volume). In non-optimized conditions but for comparison purposes, similar PS: Co_3O_4 NP ratios than those of the respective **PS1**- Co_3O_4 and **PS2**- Co_3O_4 hybrid systems (0.09:1.0 and 0.15:1.0, respectively, see Supplementary Material) were also assayed. Thus, **PS1** ($1.84 \cdot 10^{-4}$ mmol, 0.13 eq) or **PS2** ($1.58 \cdot 10^{-4}$ mmol, 0.11 eq), a high molar excess of $\text{Na}_2\text{S}_2\text{O}_8$ (28.8 mg, 0.121 mmol, 82 eq) and the Co_3O_4 NPs (0.83 mg, $1.45 \cdot 10^{-3}$ mmol of $\text{Co}_3\text{O}_4(\text{heptanol})_{2.8}$ units, 1 eq) were introduced into the dark chamber thermostated at 25.0 °C followed by 1.5 mL of $\text{Na}_2\text{SiF}_6 - \text{NaHCO}_3$ ($0.02 - 0.04 \text{ mol} \cdot \text{L}^{-1}$, pH=5.6) buffer solution (1.5 mL total volume). Finally, for the hybrid systems, **PS1**- Co_3O_4 (0.62 mg, $1.5 \cdot 10^{-3}$ mmol, 1 eq) and **PS2**- Co_3O_4 (0.82 mg, $1.6 \cdot 10^{-3}$ mmol, 1 eq) and a high molar excess (72 eq) of $\text{Na}_2\text{S}_2\text{O}_8$ (26.12 mg, 0.11 mmol, and 27.86 mg, 0.12 mmol, respectively) were added. For all experiments, the solution was stirred and degassed before closure of the chamber with a screw cap equipped with a septum. After calibration and baseline collection, the opening of

the windows of the chamber provoked the irradiation of the solution. The illumination was provided by a 150 W Xenon Arc Lamp (LS-150, ABET technology), equipped with a 400 nm cut-off filter and calibrated to 1 sun (100 mW cm⁻², 1.37 mA) by using a calibrated silicon photodiode. Control experiments were carried out following the same protocol.

3.3.3 Synthesis protocols

Photosensitizers

The photosensitizers used in this work (see Figure S1 in the Supplementary Material) were prepared according to literature data [20,21] and obtained with Cl⁻ as counterion.

Co nanoparticles

[Co(η^3 -C₈H₁₃)(η^4 -C₈H₁₂)] (120 mg, 0.43 mmol) as cobalt source and anhydrous 1-heptanol (20 mL) as both solvent and stabilizer were mixed into a Fisher-Porter reactor under an argon atmosphere inside a glove-box, leading to a brownish solution. Then, the Fisher-Porter reactor was pressurized with 3 bar of H₂ and the reaction mixture was kept under vigorous stirring overnight, after which a dark colloidal dispersion was obtained. Excess H₂ was eliminated under vacuum. A TEM grid was prepared under argon for TEM analysis of the crude colloidal solution. The application of a magnet on the reactor walls allowed to attract the Co NPs as a solid and then to isolate them from 1-heptanol, which was then removed *via* cannula. The Co NPs were then washed with degassed anhydrous pentane (4 x 20 mL) and dried under vacuum. ICP-OES (w/w%): Co (35.35%). Recovered: 46 mg.

Co₃O₄ nanoparticles

Co₃O₄ NPs were prepared by treatment of isolated Co NPs under ambient air at room temperature during 6 days. Recovered: 35 mg of a black powder. Estimated Co content: 31.33% (see experimental details in Supplementary Material).

PS-Co₃O₄ NP hybrids

A solution of **PS1** (11 mg, 0.014 mmol, 0.24 eq) or **PS2** (13 mg, 0.014 mmol, 0.24 eq) in methanol (0.4 mL) was added to a colloidal dispersion of Co₃O₄ NPs (33 mg, 0.058 mmol) in 1-heptanol (0.6 mL). The reaction mixture was kept under vigorous stirring for 4 days in the dark. Then, precipitation of the crude product was achieved by adding isopropanol (1.5 mL) and diethyl ether (10 mL) and centrifuging at 1000 rpm for 10 min. The obtained crude product and water (1 mL) were introduced in a cellulose membrane bag for dialysis against deionized water (2 L). Dialysis was pursued until the external dialysis solution remained colourless. Then, centrifugation allowed to recover a solid, which was washed 3 times with a mixture of diethylether/isopropanol (8:2) to remove water and 3 times again with diethylether before drying under vacuum. The Ru/Co ratio of the obtained PS-Co₃O₄ NPs hybrids was calculated from ICP-OES measurements. PS-Co₃O₄ NPs hybrids were stored in the dark. ICP-OES (w/w%): **PS1-Co₃O₄**, Ru (2.23%), Co (43.60%); **PS2-Co₃O₄**, Ru (3.12%), Co (35.22%). Recovered: 19 mg for **PS1-Co₃O₄**; 18 mg for **PS2-Co₃O₄**.

3.3.4 Preparation of electrodes

RDE/Co₃O₄ and GC/Co₃O₄ NPs: 15 μ L of a dispersion of Co₃O₄ NPs (1 mg) in THF (250 μ L) were deposited onto the 0.07 cm² glassy carbon (GC) disk from the rotatory disk electrode (RDE) or onto a GC electrode and let dry under air.

FTO/Co₃O₄ NPs-PMMA: A dispersion of Co₃O₄ NPs (2 mg) in 1-heptanol (500 μ L) was prepared. Then, the NPs were deposited by spin-coating 15 μ L of this dispersion onto an FTO electrode followed by evaporation of the solvent in a furnace at 100°C for 10 min. After that, the FTO/Co₃O₄ NPs electrode was dipped into a 0.5% wt PMMA dichloromethane solution for a few seconds (<10 sec) and air-dried.

3.4 Results and Discussion

3.4.1 Synthesis and characterization of the nanomaterials

Since the direct synthesis of ultrafine Co₃O₄ NPs is challenging [22], the strategy followed here to get the target PS-Co₃O₄ NPs hybrids is a three step process: 1) Co NPs with an average size of a few nanometers and narrow size distribution were synthesized; 2) these NPs were oxidized into the target Co₃O₄ nanomaterial while keeping their morphological features unchanged, and 3) Ru^{II}-polypyridyl complexes with pendant functions were grafted at the surface of the Co₃O₄ NPs. Literature survey points out that to reach Co NPs with an average size of a few nanometers, narrow size distribution and controlled surface chemistry, the reducing agent and metal precursor should be carefully chosen. One of the best precursors in this regard is the organometallic complex [Co(η^3 -C₈H₁₃)(η^4 -C₈H₁₂)], which upon hydrogenation releases only cobalt atoms and cyclooctane, a non-coordinating molecule [23]. This avoids any competition between the stabilizing agent introduced and reaction by-products observed in other cases. The NPs produced by this way display high reactivity towards air [24,25], even at low temperature, which is a prerequisite to keep the morphological parameters unchanged during the oxidation process and reach Co₃O₄ NPs of controlled average size and size distribution. In order to exclude the use of strongly coordinating stabilizers at the surface of the NPs and thus favor the grafting of the polypyridyl Ru complexes, Co NPs were prepared in 1-heptanol taking inspiration from a previous work on Ru NPs [26]. Briefly, the synthesis of Co NPs was performed by decomposition of the organometallic precursor [Co(η^3 -C₈H₁₃)(η^4 -C₈H₁₂)] in a 1-heptanol solution under 3 bar of H₂ and at room temperature in the absence of any other stabilizer. TEM analysis carried out from the so-obtained crude dark-brown colloidal solution revealed the formation of a monodisperse population of spherical NPs of mean size 3.0 ± 0.1 nm (Figure 1). These particles are well-dispersed on the TEM grid and display a narrow size distribution with a standard deviation below 5% of the mean size.

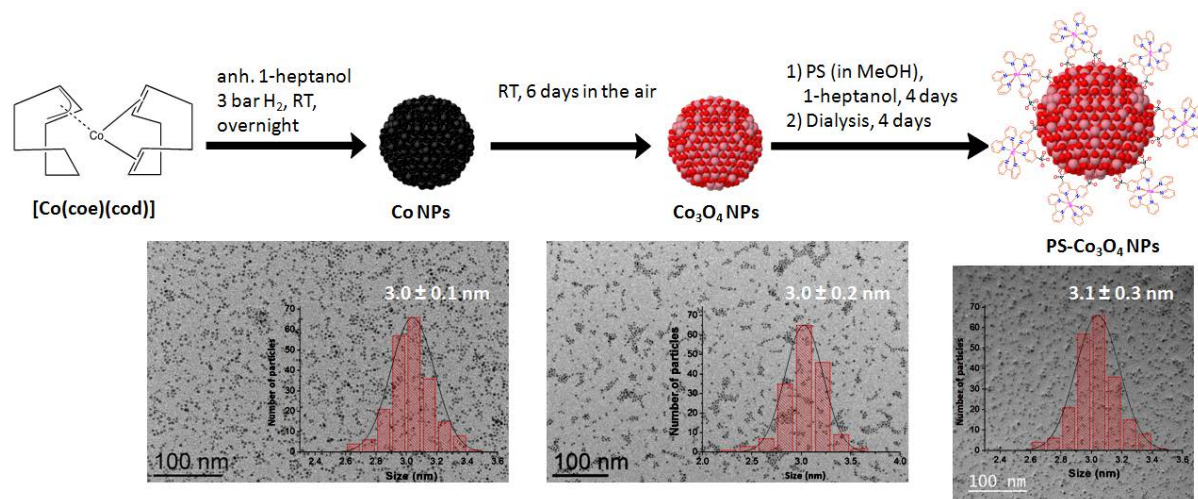


Figure 1. From left to right, synthesis and TEM images of Co, Co_3O_4 and PS- Co_3O_4 NPs (PS in the example shown is PS1).

Recovery of the NPs from the 1-heptanol colloidal solution was performed by application of a magnet on the reactor walls (magnetic filtration). Then, successive washings with anhydrous pentane followed by drying of the obtained solid under vacuum afforded Co NPs under the form of a black fine powder for further characterization. A WAXS analysis of the sample confirmed the presence of Co NPs in the α (hcp) and ϵ (metastable cubic) crystalline structures as evidenced by the good match observed between experimental data and the combination of reference patterns (PDF 01-080-6668 and PDF 04-017-5578, respectively) (Figure 2) and with a coherence length of *ca.* 2.5 nm (Figure S2). The Co content in the sample determined by ICP-OES (35.35%) suggests an empirical formula $(1\text{-heptanol})_{0.9}\text{Co}_1$ (see Supporting Information). This points to more than one 1-heptanol molecule per surface Co atom, suggesting the formation of strongly interacting multilayers around the NPs.

Complete conversion of the Co NPs previously described into Co_3O_4 NPs was achieved in soft reaction conditions by simple exposure of the particles in the solid state under ambient air for 6 days. The average size of the final NPs was estimated to 3.0 ± 0.2 nm from TEM images (Figure 1) recorded after redispersion of the powder in 1-heptanol. So the size of the initial Co NPs is kept after air treatment as the result of the mild reaction conditions applied for the transformation of cobalt into cobalt oxide. Importantly, the NPs are well dispersed on the TEM images, indicating the absence of extended aggregation during the oxidation process.

Oxidation of the Co NPs into Co_3O_4 could be attested by WAXS, XPS analyses and by IR spectroscopy.

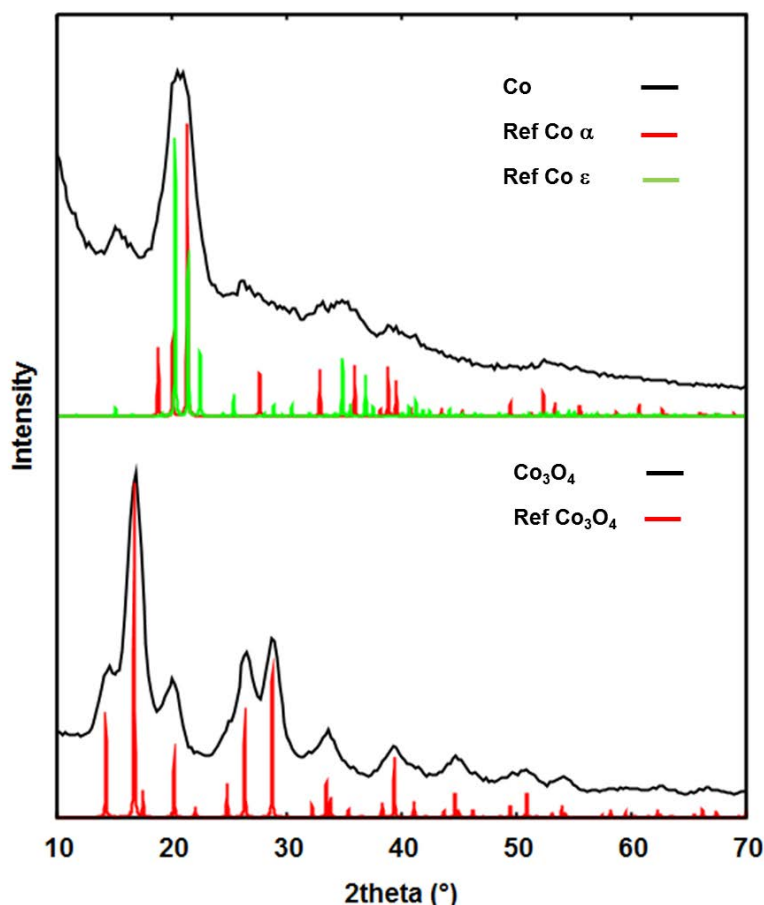


Figure 2. WAXS analysis of Co NPs (top) and Co_3O_4 NPs (bottom) in comparison with Co α / Co ϵ and Co_3O_4 phase diagrams for Co NPs and Co_3O_4 NPs, respectively.

WAXS measurements evidenced the presence of nanoparticles displaying a coherence length of ca. 3.0 nm (Figure S2) and a crystalline structure corresponding to the Co_3O_4 phase as shown by the good match observed between experimental data and the reference pattern (PDF 04-005-4386) (Figure 2). The perfect agreement between the coherence length and the mean size determined by TEM points towards well crystallized nanoparticles. In XPS (Figure 3), the Co_3O_4 NPs show two main peaks at ca. 780.0 and 795.5 eV, corresponding to the Co $2p_{3/2}$ and Co $2p_{1/2}$ components, respectively, accompanied by two broad satellite peaks with

very low intensity at higher energies (*ca.* 788 and 805 eV). According to the literature data, the presence of satellite peaks are an indication of the presence of unpaired electrons in the sample, *i.e.*, the presence of Co^{II} (d^7) atoms [27], while both the positions and the intensities of all 4 types of bands observed in the XPS spectrum clearly match the data already reported for the mixed Co^{II} - Co^{III} oxide Co_3O_4 [27,28]. IR spectroscopy revealed the presence of typical Co-O stretching bands centered at 666 and 575 cm^{-1} [29] within the Co_3O_4 structure (green line, Figure 4) confirming the crystallinity and structure of the nanomaterial. Ill-defined absorptions in the 1600-1400 cm^{-1} region could correspond to adsorbed water and carbonate molecules. All together these results show the transformation of pre-formed Co NPs into crystalline Co_3O_4 NPs while keeping the initial particle size thanks to the use of soft reaction conditions.

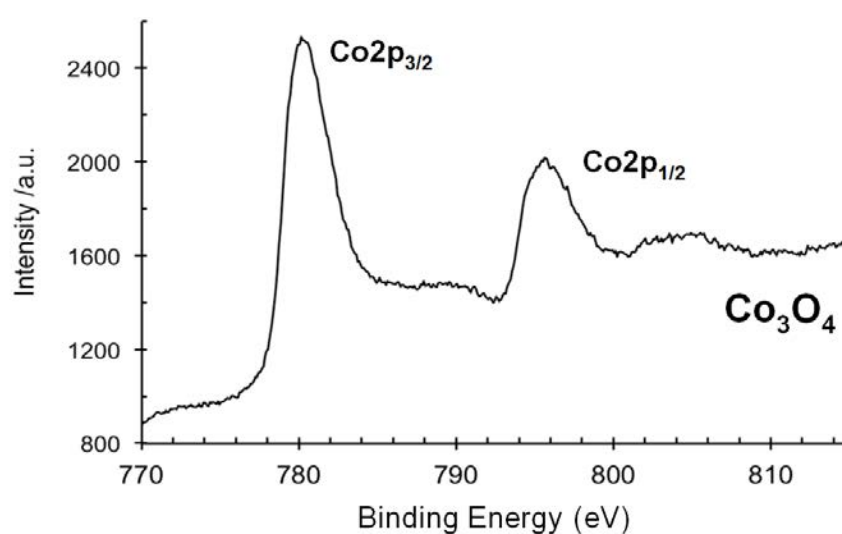


Figure 3. Co 2p XPS spectrum of Co_3O_4 NPs obtained after 6 days of exposure to air.

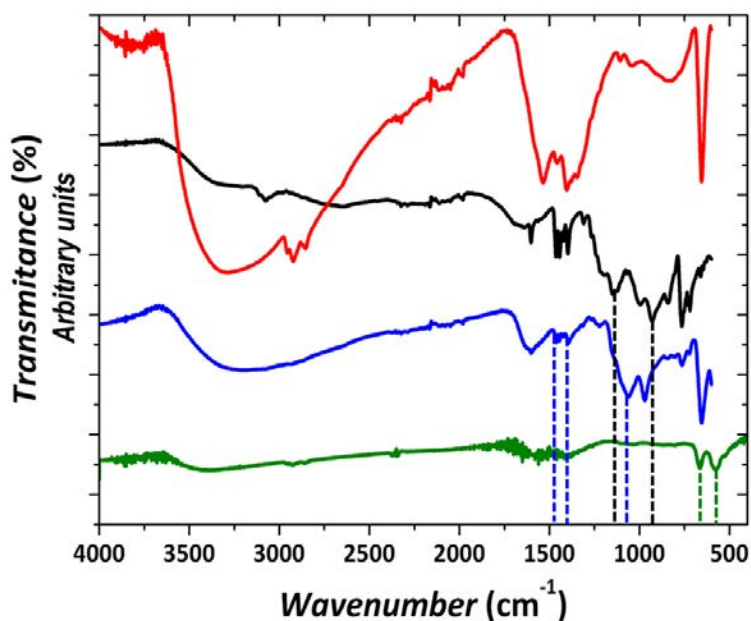


Figure 4. Overlay of ATR-IR spectra of Co_3O_4 NPs (red), free **PS1** (black) and **PS1- Co_3O_4** NPs hybrid material (blue) and of IR spectrum of a KBr pellet of Co_3O_4 NPs (green). The transmittance of each sample has been shifted along the y-axis for comparison purposes. The positions of the bands described along the text have been added as dotted lines.

The next step was the building of the hybrid nanomaterials (**PS- Co_3O_4** NPs) by grafting polypyridylic-based Ru^{II} complexes at the surface of the Co_3O_4 NPs. For this purpose Ru^{II} complexes displaying phosphonic acid pending groups (**PS1** with two and **PS2** with four) as well as a Ru^{II} trisbipyridine complex ($[\text{Ru}(\text{bpy})_3]^{2+}$) without anchoring groups as a reference (**PS0**) were prepared following literature data [20,21] (Figure S1) for their use as PS.

The phosphonic acid anchoring group is well known to efficiently interact with metal oxide surfaces [30]. The PS grafting was performed by mixing a 1-heptanol colloidal dispersion of Co_3O_4 NPs with a methanol solution of the chosen complex ($[\text{Ru}^{\text{II}} \text{ complex}]/[\text{Co}_3\text{O}_4 \text{ NPs}]=0.1$) and leaving the obtained reaction mixture under vigorous stirring in the dark for 4 days. The nanohybrid materials were recovered by centrifugation and further purified from unreacted Ru complexes by dialysis against deionized water. This procedure was applied for **PS1** and **PS2** complexes giving rise to the **PS1- Co_3O_4** and **PS2- Co_3O_4** hybrids, which could be recovered as black powders after evaporation of water under vacuum. From ICP-OES analysis, it can be inferred that these nanomaterials show $(1\text{-heptanol})_{0.80}(\text{PS1})_{0.09}\text{-Co}_3\text{O}_4$ and $(1\text{-$

heptanol)_{0.97}(PS2)_{0.15}-Co₃O₄ empirical formulas, which corresponds to the incorporation of around 19 PS1 and 32 PS2 complexes per Co₃O₄ NP (see Supplementary Material for further details). The attachment of PS1 and PS2 complexes at the surface of the Co₃O₄ NPs was attested by ATR-IR spectroscopy (Figures 4 and S5, respectively).

As it can be seen on Figure 4 (black spectrum) the PS1 complex shows two absorption bands at 1149 and 928 cm⁻¹ corresponding to the free P=O and P-OH units, respectively [31,32]. The PS1-Co₃O₄ hybrid nanomaterial (blue spectrum) shows bands in the 1465-1394 cm⁻¹ region, indicative of the presence of the bipyridine backbone of the PS. No free P=O nor P-OH bands are visible, but there is a band at 1061 cm⁻¹ that can be attributed to -P(O-Co)₃ units [32] (by comparison with the 1016 cm⁻¹ value found for -P(O-Zn)₃), thus supporting the grafting of PS1 to the surface of Co₃O₄ NPs by a tridentate binding and the use of all possible anchoring points. Additionally, neither CH₃ nor CH₂ stretching bands are clearly observed at *ca.* 2900 cm⁻¹, indicating that a partial replacement of the 1-heptanol molecules by the PS1 molecules at the NP surface may have taken place and/or that part of the 1-heptanol initially present could have been released from the NPs surface during dialysis. Therefore, we cannot exclude the possible presence of residual 1-heptanol molecules on the surface of the hybrid NPs. TEM analysis from the aqueous colloidal dispersion of the hybrid material revealed the presence of nano-objects with homogeneous shape (spherical) that display a mean size of 3.1 ± 0.3 nm (Figure 1). The results show that the initial size and morphology of the Co₃O₄ NPs are maintained after anchoring the PS1 at their surface. Also, WAXS investigation of their structure indicated a preserved Co₃O₄ structure with an estimated coherence length of *ca.* 3.0 nm. The presence of Ru was evidenced through STEM-EDX analysis only in the vicinity of the NPs, indicating a successful purification process (Figure S4). The PS2-Co₃O₄ NP hybrid material was characterized accordingly, with very similar results to the PS1-Co₃O₄ hybrid material (Figures S5, S6 and S7). Based on ICP-OES analysis, incorporation of 19 PS1 and 32 PS2 complexes per Co₃O₄ NP is estimated (see Supplementary Material for further detail). The higher grafting density obtained in the case of the PS2-Co₃O₄ hybrid could be related to the statistically more favored interaction between the surface and the chelating biphosphonate bipyridine ligands.

To sum-up this first part, easily obtained Co NPs could be transformed into Co₃O₄ NPs in mild reaction conditions while preserving their morphology. These results highlight: 1) the efficiency of our synthetic approach where 1-heptanol acts both as solvent and stabilizer for

the preparation of small and well-controlled in size Co NPs; 2) the possibility to access to small Co_3O_4 NPs easily by a soft oxidative treatment with a preserved morphology, and 3) the possibility to graft polypyridylic-based Ru^{II} complexes at the Co_3O_4 NPs surface despite the coverage of the surface by 1-heptanol molecules to get hybrid nanostructured materials with multiple functionalities, namely PS and catalyst. The catalytic properties of the obtained Co_3O_4 NPs and hybrid PS- Co_3O_4 NPs materials are described hereafter.

3.4.2 Electrocatalytic behavior in water oxidation catalysis

The electrocatalytic performance of the prepared ultrafine Co_3O_4 NPs were studied in 1 M NaOH solution after their deposition onto a glassy carbon rotating disk electrode (GC-RDE). The electrode was prepared by depositing three drops of 5 μL from a THF dispersion (1 mg of Co_3O_4 NPs in 250 μL of THF) of the NPs onto the glassy carbon disk of the RDE (See Supplementary Material for further details). Figure 5a shows the rotating disk voltammetry (RDV) of the as-deposited Co_3O_4 NPs where a steep increase in intensity above 0.7 V vs. NHE is visible. This increase in intensity is attributed to the oxidation of water into molecular oxygen [33,34,35], which in our case happens at an onset overpotential (η) of *ca.* 0.29 V.

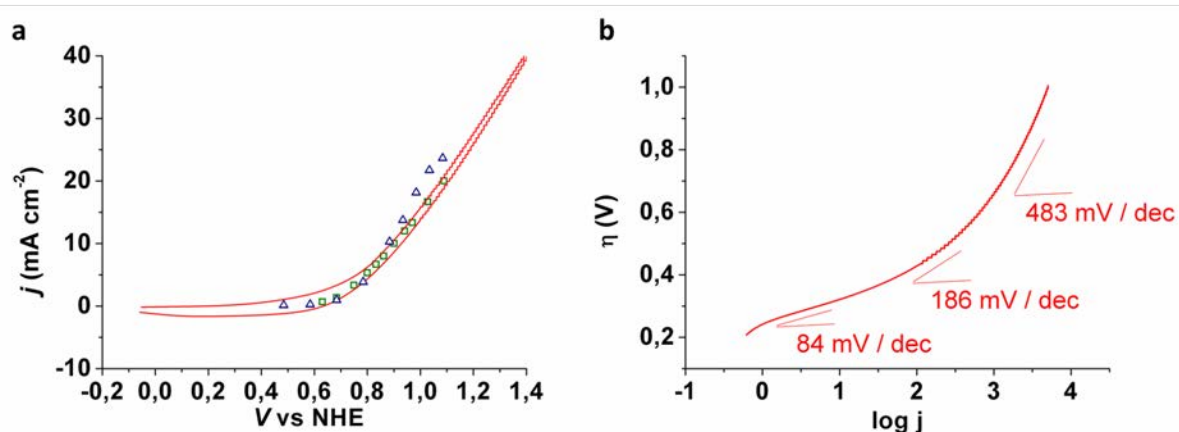


Figure 5. Representative RDV for the deposited Co_3O_4 NPs onto a GC-RDE electrode at 0.01 V/s scan rate and 1600 rpm in O_2 -saturated 1 M NaOH (a) and Tafel plot derived from the voltammogram (b). The results of 30 s chronopotentiometric steps (open green squares) and chronoamperometric steps (open blue triangles) (Fig. S8) are also shown for comparison in (a). The close overlay of both data sets with the RDV measurement suggests good approximation of steady-state conditions [36,37].

The electrocatalytic performance of our Co_3O_4 NPs deposited onto GC-RDE was further compared with other electrocatalysts following the benchmarking methodology reported by Jaramillo *et al.* [33,34,35]. Thus, the electrochemically active surface area (ECSA) of the Co_3O_4 modified GC-RDE was estimated to be 0.175 cm^2 from the electrochemical double-layer capacitance (C_{dl}) by measuring the non-Faradaic capacitive current associated with double-layer charging from the scan-rate dependence of CVs [38,39] over a 0.145-0.245 V vs. NHE potential range (Fig. S10). The roughness factor (RF) was calculated by dividing the estimated ECSA by the geometric area of the electrode, and these factors as well as those corresponding to the electrocatalytic activity of our nanocatalyst are compared with those of the state-of-the-art Co_3O_4 NPs in the same electrolyte in Table 1. However, it is important to note that the ECSA serves only as an approximate guide for the determination of the RF, since the accuracy of the data lies normally within an order of magnitude [34]. Therefore, comparison with literature data can only be analyzed in terms of general tendencies. As depicted in Table 1, the Co_3O_4 modified GC-RDE catalyst reported herein (entry 1) shows an onset overpotential (η_{onset}) of *ca.* 0.29 V vs. NHE, which lies close to the reported values for Co_3O_4 NPs in graphene [40,41] (entries 3 and 6) and SWCNTs [42] (entry 7). To achieve a current density of $10 \text{ mA}\cdot\text{cm}^{-2}$, approximately the current density expected for a 10% efficient solar-to-fuel conversion device [34,43,44,45], a $\eta_{10\text{mA}/\text{cm}^2}$ of 0.486 V is required (entry 1, this work). This value is close to the $\eta_{10\text{mA}/\text{cm}^2}$ reported for Co_3O_4 NPs of similar RF by Jaramillo *et al.* [35] (entry 4) but higher than the $\eta_{10\text{mA}/\text{cm}^2}$ values published for catalytic systems with nearly two orders of magnitude higher RF [46,47] (entries 2 and 5). Even so, it falls within the reported area of interest for catalyst benchmarking [33,34,35]. Most interestingly, when the current at an η of 0.35 V (j_g) is normalized by the ECSA [48,49], a normalized current density (j_s) of 1.04 mA cm^{-2} is obtained. This value is significantly higher than that reported by Jaramillo *et al.* for their Co_3O_4 -based nanocatalyst of similar RF and $\eta_{10\text{mA}/\text{cm}^2}$ (entry 4) and also for all other nanostructured metal oxide electrocatalysts deposited onto GC-RDE [35]. Thus, the Co_3O_4 modified GC-RDE nanocatalyst reported herein is very active at low η (0.35 V). However, at a higher η (0.5 V), it shows the same current density than the analogous system reported by Jaramillo *et al.* [35] (entry 4). This is due to the higher slope of the Tafel plot above $\eta = 0.35 \text{ V}$ (approx. $100 \text{ mV}\cdot\text{dec}^{-1}$, Figure 5b) compared to the analogous system described by Jaramillo (approx. $60 \text{ mV}\cdot\text{dec}^{-1}$).

Table 1. Benchmarking parameters vs. NHE for Co₃O₄ NPs in 1 M NaOH using a GC-RDE^a and comparison with state-of-the-art data also reported at pH 14. ^bDeposited on Ni foam. ^cIn graphene nanocomposite. ^dDeposited onto GC-RDE. ^eIn N-doped graphene nanocomposite. ^fIn N-doped graphene deposited onto Ni foam. ^gIn SWCNTs. ^hdeposited onto an FTO electrode.

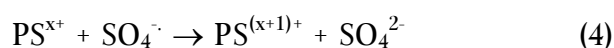
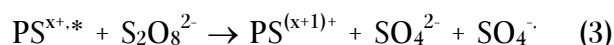
Entry	Catalyst	ECSA/ cm ²	RF	η_{onset}/V	$\eta_{10mA/cm^2, t=0h}/V$	$\eta_{10mA/cm^2, t=1h}/V$	$j_{g,\eta=0.35V}/mA \cdot cm^{-2}$	$j_{s,\eta=0.35V}/mA \cdot cm^{-2}$	ϵ (%)	Ref.
1	3.5 nm Co ₃ O ₄ NPs ^a	0.175	2.5	0.29	0.486 ^g	0.480 ^g	2.6	1.04	95 ^g	this work
2	10 nm Co ₃ O ₄ NPs ^b	429	429	---	0.290	---	ca. 25	ca. 0.06	95	46
3	ca. 10 nm Co ₃ O ₄ NPs ^c	---	---	0.24	0.313	0.313	ca. 30	---	---	40
4	ca. 70 nm Co ₃ O ₄ NPs ^d	1.52	7.8	---	0.50	0.51	0.06	0.039	---	35
5	50 nm Co ₃ O ₄ nanocubes ^e	6.44	91.2	---	0.28	---	ca. 70	ca. 0.77	---	47
6	4-8 nm Co ₃ O ₄ NPs ^f	---	---	ca. 0.27	0.31	---	ca. 35	---	---	41
7	6 nm Co ₃ O ₄ NPs ^g	---	---	ca. 0.28	0.593	---	ca. 1.8	---	---	42

Both stability and Faradaic efficiency (ϵ) are key parameters for a catalyst to be suitable for practical applications in WO catalysis. To analyze them, an FTO electrode was loaded with 15 μ L of a dispersion of our Co₃O₄ NPs (2 mg in 500 μ L of 1-heptanol) by spin-coating, and afterwards a poly(methyl methacrylate) (PMMA) layer was added as “gluing” material [50]. The generated FTO/Co₃O₄NPs-PMMA electrode showed onset η of ca. 0.29 V (see Figure S11b), identical to that of the Co₃O₄ NPs on GC-RDE (see Table 1), highlighting the negligible effect of the support used. The FTO/Co₃O₄NPs-PMMA electrode was then hold at a constant current density of 10 mA·cm⁻² in a current-controlled experiment for 1h in 1M NaOH. As shown in Figure S11a, the system showed a stable operating η_{10mA/cm^2} , changing negligibly from $\eta_{10mA/cm^2, t=0h} = 0.486$ V to $\eta_{10mA/cm^2, t=1h} = 0.480$ V during 1 h (entry 1, Table 1). Comparison of the CV polarization curves measured before and after this current-controlled experiment shows a slight increase in the observed current density after catalytic turnover (Figure S11b). This global increase in current density is indicative of a certain activation of the Co ions in Co₃O₄ NPs such as an increase in the Co^{+3/+4}/Co⁺² population ratio, as suggested by Frei and co-workers [51], and/or an elimination of 1-heptanol molecules present at the surface of the NPs increasing the number of exposed active sites. XPS analysis of the resulting electrode after electrolysis shows that the composition of the NPs remains intact as Co₃O₄ (Figure S12), thus pointing to the removal of 1-heptanol molecules from the surface of the NPs under catalytic conditions as the origin of the observed activation process. Furthermore, the activation of the NPs does not

affect significantly the Tafel slopes (Figure S11c), which are very similar before and after catalytic turnover. In addition, a Faradaic efficiency of 95% was determined by quantifying the amount of O₂ generated during a bulk electrolysis (0.886 V vs. NHE corresponding to an initial current density of 10 mA·cm⁻²) using an O₂-probe and dividing the total amount of produced O₂ by the theoretical O₂ amount calculated from the total charge that has passed through the system (Figure S9), thus confirming the production of O₂ as the only reaction taking place.

3.4.3 Photochemical water oxidation catalysis

The efficiency of the Co₃O₄ NPs as a photocatalyst for WO was first evaluated in Na₂SiF₆-NaHCO₃ (0.02-0.04 M, pH 5.60) in the presence of **PS0**, **PS1** or **PS2** as photosensitizer (Figure S1), using sodium peroxodisulfate as the sacrificial electron-acceptor (SEA) and gas phase Hansatech-type microsensors for measuring the evolved oxygen (Figures S13-15). The set of reactions involved in this photocatalytic process is depicted in Scheme S1. It is noteworthy that the semi-conducting Co₃O₄ NPs alone do not behave as photocatalysts for this reaction. The photoactive species responsible for the activation of the Co₃O₄ NPs in WO is PS^{(x+1)+}, which is generated after a three-step process as follows:



The influence of PS concentration on the turnover number (TON) has been studied with **PS1** in order to determine the best [PS]/[Co₃O₄(heptanol)_{2.8} units] ratio to be used (Figure S16). The curve (TON vs. **PS1** equiv) obtained reaches a plateau at *ca.* 6.0 equiv of PS. Consequently, a PS: Co₃O₄(heptanol)_{2.8} units ratio of 6.0:1.0 was then chosen for the following photochemical WO studies. As it can be seen in Table 2 (entries 1-3), all the tested PS (Figure S1) could oxidize the Co₃O₄ NPs. These results are consistent with the electrochemical analysis of the Co₃O₄ NPs shown above, since their onset potential under these conditions at pH 5.6 (*ca.* 1.1 V vs. NHE, Fig. S3) is lower than that of the Ru^{III}/Ru^{II} redox couple for all PS tested (1.2-1.3 V vs. NHE, Fig. S17). TON and TOF (turnover frequency, min⁻¹) values were determined from the estimated total number of NPs and of PS molecules present on each sample (see Supplementary Material for detailed calculations). Thus, the TON per NP obtained for the

catalytic mixtures made of Co₃O₄ NPs plus **PS0**, **PS1** or **PS2** are all similar and within the range 453–604 (entries 1, 2, 3 in Table 2). Concerning the TOF per NP, it is reduced to approximately its half when doubling the number of phosphonate groups present (67.9 vs. 36.2 min⁻¹ for **PS1** and **PS2**, respectively; entry 2 vs. entry 3). The TOF per PS is also reduced in a similar amount (0.053 vs. 0.028 min⁻¹ for **PS1** and **PS2**, respectively). One potential reason for the reduced TOF values for the **PS2** case could be that the presence of 4 phosphonate binding groups could allow the simultaneous binding of a single **PS2** unit onto two Co₃O₄ NPs, thus favoring their aggregation, in contrast to the **PS1** system. This hypothesis is confirmed when comparing the TEM images of the as-synthesized hybrid **PS1**-Co₃O₄ and **PS2**-Co₃O₄ systems (Figure 1 and Figure S6, respectively), where higher aggregation and lower dispersion of the NPs is obtained for **PS2**-Co₃O₄. At this point, it is also worth mentioning that the limiting factors that may stop the O₂ evolution in such photocatalytic systems are usually the degradation of the PS (Scheme S2) and the pH decrease due to the release of protons during the reaction [52,53,54]. However, it is interesting to note that O₂ evolution was not resumed under our conditions after the addition of an extra aliquot of PS; thus, some kind of inhibition of the whole photocatalytic system and not only PS degradation takes place. This inhibition could be caused by the progressive increase in the ionic strength of the medium (sulfate ions are produced during catalysis), as this can negatively affect the performance of the NPs due to a reduction of the quenching efficiency of the photoexcited PS (PS^{x+*}) by peroxodisulfate (eq. 3) [55]. In addition, another phenomenon that typically explains the reduced performance of nanocatalysts with time in the presence of the NaSiF₆-NaHCO₃ buffer is the hydrolysis of the buffer to generate SiO₂ particles, which can provoke the adsorption of the cationic PS molecules onto their surface, thus competing with the catalytic NPs and reducing the global catalytic performance. [18] This last hypothesis has been confirmed by HREM and STEM analyses of the recovered nanocatalyst after photocatalytic turnover in the presence of **PS1**, in which Co₃O₄ NP aggregates of *ca.* 50 nm attached to a higher Si-containing aggregate are observed (Figure S18).

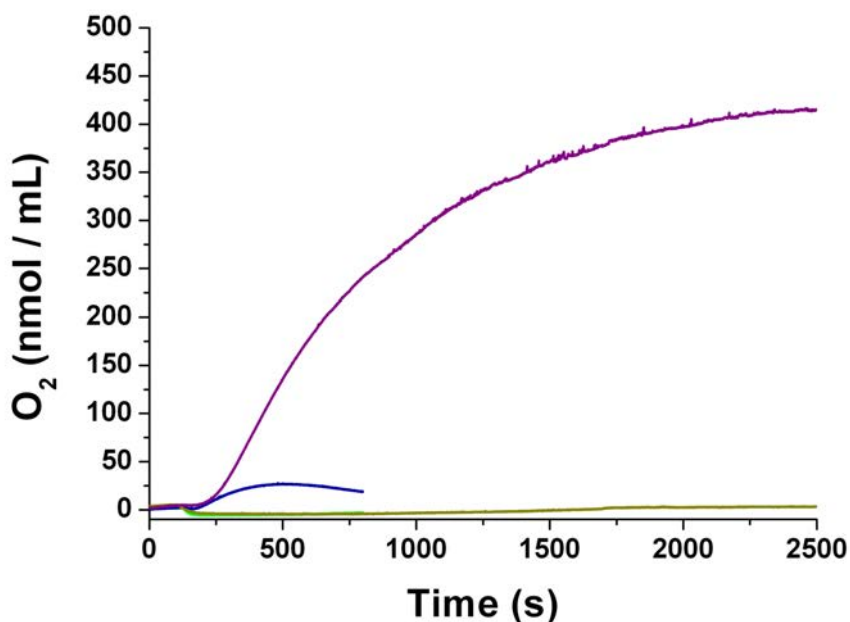


Figure 6. Hansatech-detected photocatalytic oxygen production by different Co_3O_4 -PS systems. Green line: Co_3O_4 NPs ($9.66 \cdot 10^{-4}$ M) in the presence of **PS1** ($1.23 \cdot 10^{-4}$ M) and $\text{Na}_2\text{S}_2\text{O}_8$ ($7.85 \cdot 10^{-2}$ M). Khaki line: Co_3O_4 NPs ($9.95 \cdot 10^{-4}$ M) in the presence of **PS2** ($1.05 \cdot 10^{-4}$ M) and $\text{Na}_2\text{S}_2\text{O}_8$ ($8.08 \cdot 10^{-2}$ M). Blue line: **PS1**- Co_3O_4 NPs ($1.02 \cdot 10^{-3}$ M) in the presence of $\text{Na}_2\text{S}_2\text{O}_8$ ($7.32 \cdot 10^{-2}$ M). Purple line: **PS2**- Co_3O_4 NPs ($1.09 \cdot 10^{-3}$ M) in the presence of $\text{Na}_2\text{S}_2\text{O}_8$ ($7.87 \cdot 10^{-2}$ M). All measurements were performed in Na_2SiF_6 - NaHCO_3 (0.02-0.04 M, pH 5.60) buffer solution. Irradiation provided by a Xe lamp equipped with a 400 nm cut-off filter and calibrated to 1 sun (100 mW cm^{-2}). $T = 25^\circ\text{C}$. Note that for experiments in which few oxygen is evolved, we observe a decrease of the signal inside the chamber when exposed to light due to the reaction of the singlet state of PS with the residual oxygen traces [56].

Concerning the **PS1**- Co_3O_4 and **PS2**- Co_3O_4 hybrid materials, the number of PS per Co_3O_4 NP unit were estimated to be 0.09 and 0.15, respectively (see Supplementary Material). Thus, in order to compare the photocatalytic performance of these hybrid dyads with that of the corresponding unbound systems, similar PS/ Co_3O_4 ratios were applied under catalytic conditions for the two control experiments (Figure 6). As shown in Table 2, the oxygen evolved by both unbound systems is almost negligible (entries 4 and 5 and Fig. 6). This can be attributed to the kinetic prevalence of the deactivation processes described above (PS degradation, NP aggregation) competing with oxygen evolution when very low concentrations of unbound PS are used. Conversely, the same PS/ Co_3O_4 ratio is fairly more active when bound PS- Co_3O_4 hybrid systems are employed (entries 6 and 7). Comparison of entries 6 and 7 in Table 2 shows the rather superior activity of **PS2**- Co_3O_4 (TON and TOF per NP of 82 and 2.05 min^{-1} , respectively) versus **PS1**- Co_3O_4 (TON and TOF per NP of 5.4 and 0.90 min^{-1} , respectively). Thus, the superior PS surface functionalization in **PS2**- Co_3O_4 (32 PS molecules per NP vs. the

19 molecules present in **PS1-Co₃O₄**) enhances the kinetics of oxygen evolution and better stabilizes the catalytic system, increasing its durability under photocatalytic conditions (purple line, Figure 6). When the kinetics of oxygen evolution is normalized by the PS concentration, TOF values of both hybrid systems get closer (rightmost column in Table 2, entries 6 and 7), thus confirming the relationship between the rate of photocatalytic turnover and the degree of functionalization of the NPs surface. In terms of stability, the weakness of P-O-M bonds has been extensively identified as a main deactivation pathway of grafted molecular complexes and dye-sensitized systems when employed as catalysts for the oxidation of water [31,32,57]. Thus, the superior number of anchoring groups present in **PS2** (4 phosphonate groups vs. the 2 present in **PS1**) can also contribute to the superior longevity of the **PS2-Co₃O₄** hybrid system.

Table 2. TON and TOF (min⁻¹) per NP and per PS obtained as a function of PS nature in photochemical WO measurements with single Co₃O₄ NPs and hybrid PS-Co₃O₄ NPs at pH 5.6.

Entry	System	PS:Co ₃ O ₄ ratio	TON (O ₂ /NP)	TOF min ⁻¹ (O ₂ /NP)	TON (O ₂ /PS)	TOF min ⁻¹ (O ₂ /PS)
1	Co ₃ O ₄ + PS0	6.0:1.0	453	49.4	0.35	0.038
2	Co ₃ O ₄ + PS1	6.0:1.0	566	67.9	0.44	0.053
3	Co ₃ O ₄ + PS2	6.0:1.0	604	36.2	0.47	0.028
4	Co ₃ O ₄ + PS1	0.09:1.0	< 1	-	< 1	-
5	Co ₃ O ₄ + PS2	0.15:1.0	< 1	-	< 1	-
6	PS1-Co ₃ O ₄	0.09:1.0	5.4	0.90	0.28	0.046
7	PS2-Co ₃ O ₄	0.15:1.0	82.0	2.05	2.53	0.063

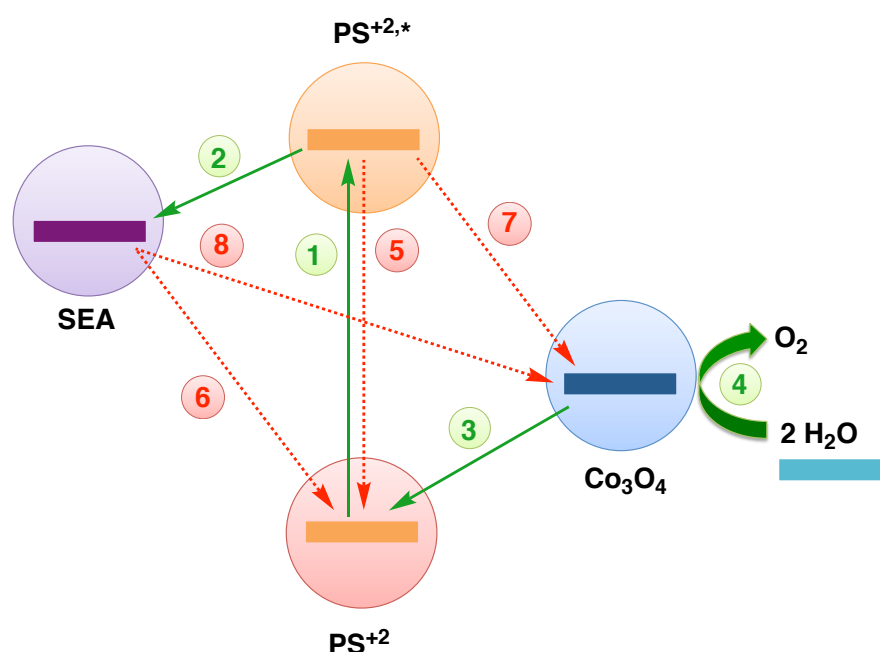
To further study the fate of our hybrid dyad nanocatalysts under photocatalytic WO conditions, the crude of reaction after a 1h photocatalytic test with **PS1-Co₃O₄** was dialyzed against 2 L of deionized water for 4 days followed by centrifugation and air-drying. Some partial aggregation was observed by TEM analysis, although less intense than for the non-anchored system (Figure S19), thus confirming the above proposed protective role of the attached **PS1** molecules against aggregation. On the other hand, IR spectroscopy showed the loss of **PS1** (Figure S20), since the intensity of the bpy bands at 1400-1500 cm⁻¹ and the -P(O-Co)₃ bands at *ca.* 1060 cm⁻¹ decreases after photocatalysis. Also, ICP-OES analyses evidence the decrease

in the [Ru]/[Co] ratio from 0.03 to 0.003 after catalysis. This loss in PS can be not only due to its decomposition, which is kinetically competitive with the oxidation of water [54], but also to its decoordination from the surface of the Co_3O_4 NPs, as commonly observed in related systems [31,32,57].

In summary, the results shown in this section highlight the benefits of the dyad approach where the direct connection between the Co_3O_4 nanocatalyst and the PS facilitates electron-transfer and stabilizes the system against aggregation under turnover conditions due to the protective effect of the PS layer at the surface of the Co_3O_4 NPs. However, the data shown also emphasize the relative instability of the $-\text{P}(\text{O}-\text{Co})_3$ bonds under turnover conditions and the need of further research for developing more stable systems with higher durability.

3.4.4 Photophysical studies

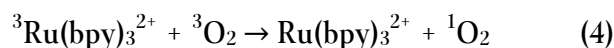
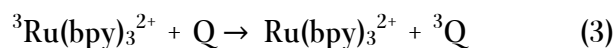
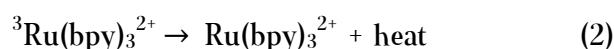
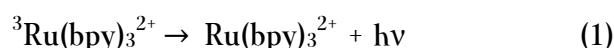
In a prototypical dye-sensitized photoelectrochemical cell (DSPEC) system for water oxidation, the desired forward reactions (depicted by green arrows in Scheme 5) are the photoexcitation of the photosensitizers (reaction 1), its oxidative quenching by an electron acceptor (2) and the electron injection to the oxidized photosensitizer by the catalyst (3) that will promote water oxidation (4). However, some parasitic processes contribute to decrease the DSPEC efficiency (represented by dotted red arrows in Scheme 5), named back-electron transfer processes.[58]



Scheme 1. Scheme of a prototypical dye-sensitized photoelectrochemical cell (DSPEC) system along with main energy levels and relevant desired (in green) and undesired (in red) electron transfer processes. (1) Dye photoexcitation; (2) electron injection/electron acceptor reduction; (3) hole injection/catalyst oxidation; (4) water oxidation; (5) dye radiative or nonradiative recombination; (6) electron-hole recombination to the oxidized dye; (7) oxidative dye excited-state quenching by the catalyst; (8) electron-hole recombination to the oxidized catalyst.

In order to rationalize the kinetics of oxygen evolution as well as the different electron transfer phenomena described above, different photophysical techniques have been employed. These experiments were carried out in a 3-months stay in the laboratory of Professor Nathan McClenaghan at the Institute des Sciences Moléculaires in Bordeaux.

The first reaction involved in the water oxidation reaction is the photoexcitation of the photosensitizer (process 1, Scheme 1). The electronic absorption spectra at room temperature of tris(bipyridyl)-based ruthenium(II) complexes consists of a broad band centered within the 400-460 nm range. This transition consists of a (spin allowed) metal-to-ligand charge transfer (MLCT) from a molecular orbital that has mostly Ru(II) *d* orbital character to a molecular orbital that has mostly ligand π orbital character. Therefore, these complexes are excited by MLCT transitions in which a singlet MLCT state is initially formed. However, this singlet state forms a triplet state by intersystem crossing.[59,60,61] Since the triplet state is formed, the luminescence process is phosphorescence rather than fluorescence (eq. 1). At room temperature and in aqueous solution, these complexes show strong luminescence at about 600 nm with lifetimes of *ca.* 600 ns. Two main processes that compete with the phosphorescence deactivation are the internal non-radiative process and the presence of quenchers such as O₂ in its triplet state (equations 2, 3 and 4).[62,63]



Thus, in order to characterize the excited states of the photosensitizers, the emission of their ³MLCT bands (over 600 nm) have been analyzed through steady-state luminescence and emission lifetime techniques by means of quantum yield (Φ , number of emitted photons relative to the number of absorbed photons) and lifetime (τ , average time the molecule spends in the excited state prior to return to the ground state) measurements. Data gathered in Table 3 shows that the quantum yield Φ in the presence of oxygen (Φ_{O_2}) is lower than in the presence of Ar (Φ_{Ar}) because of the fluorescence quenching effect of the O triplet state formed for the former case. Accordingly, lifetimes in the presence of O₂ ($\tau_{\text{O}_2}^0$) are smaller than in the presence of Ar (τ_{Ar}^0). Thus, the undesirable deactivation of the photosensitizer' excited-states (reaction 5, Scheme 1) can be diminished by bubbling argon in the reaction media. Moreover, the similarity of Φ_{Ar} in the free and hybrid systems (entries 3,4 vs. 5,6, Table 3) indicates that no back-electron transfer process exists between the excited PS and the Co₃O₄ NPs in the hybrid

systems. Furthermore, since a back-electron transfer process that could decrease the global performance is the PS excited-state oxidative quenching by Co₃O₄ NPs (process 7 in Scheme 1), Co₃O₄ NPs were added to the buffered solutions containing the different PS and their lifetimes have been recorded in the presence of Ar (τ_{NPs}^0). As shown in Table 3, no significant differences are observed between τ_{Ar}^0 and τ_{NPs}^0 . Thus, we can assume that no interactions occur between the PS* and free Co₃O₄ NPs, and that no back-electron transfer takes place.

Once the triplet state is formed, this ³MLCT excited state can be quenched by an electron acceptor to form the oxidized photosensitizer (reaction 2, Scheme 1). This aspect of the experiment is fairly routine since phosphorescence quenching obeys standard quenching kinetics, so-called Stern-Volmer kinetics.[64] The Stern-Volmer equation (equation 5) is used to describe the changes in quantum efficiency of the reaction (ϕ), as well as the change in luminous intensity (I), and also lifetime (τ).

$$\frac{I^0}{I} = \frac{\Phi_{\text{Ar}}}{\Phi} = \frac{\tau^0}{\tau} = 1 + k_q \tau^0 [Q] \quad (5)$$

Thus, the photooxidation of the different photosensitizers (**PS0**, **PS1**, **PS2**) as well as that of the **PS1-Co₃O₄** and **PS2-Co₃O₄** hybrid systems while adding S₂O₈²⁻ as a quencher was investigated by steady-state luminescence quenching and emission lifetime techniques in Na₂SiF₆ – NaHCO₃ (0.02 – 0.04 M, pH 5.60) (Figure S21, see Supp. Mat. For experimental details). The Stern-Volmer (SV) plots, I⁰/I vs. [S₂O₈²⁻] (where I⁰ and I are the emission intensity of the excited PS (PS*) in the absence and presence of the quencher, respectively) for all PS (alone and attached to Co₃O₄ NPs) are shown in Fig. 6. The SV plots for the **PS1-Co₃O₄** and **PS2-Co₃O₄** hybrid systems show a linear trend, intercepting the y axis at (0,1). For the free PS, the SV plots significantly deviate from linearity. These results are similar to those previously reported by Musaev [65] and Bard [66] for [Ru(bpy)₃]²⁺ (**PS0** in our work) and the same quencher in a different electrolyte. They showed that the SV plot is described by a model that takes into account the formation of ground-state ion pairs between the emitter and the quencher. In this case, two different quenching processes can occur: a collisional or dynamic quenching (bimolecular pathway, Scheme S3b) or a static or complex formation quenching (unimolecular pathway, Scheme S3a) [67,68]. The dynamic quenching occurs when the excited photosensitizer collides with the quencher, following the conventional Stern-Volmer behavior.

However, in some cases the photosensitizer can initially form a stable ion-pair complex with the quencher, followed by a photoexcitation of the whole system (Scheme S3). The model that considers both quenching processes at the same time gives rise to the following equation for quenching emission [66]:

$$\frac{I^0}{I} = \frac{(1+K_{eq}[S_2O_8^{2-}])(1+k_q\tau^0[S_2O_8^{2-}])}{1+\frac{\tau'}{\tau^0} \frac{(K_{eq}[S_2O_8^{2-}])(1+k_q\tau^0[S_2O_8^{2-}])}{(1+k'_q\tau'[S_2O_8^{2-}])}} \quad (6)$$

where K_{eq} is the equilibrium constant of ion pair formation, and the unimolecular decay time and the bimolecular quenching constant of the excited emitter in the free form are, respectively, τ^0 and k_q , while in ion pair state are τ' and k'_q . Under conditions of negligible ion-pair formation, $K_{eq}[S_2O_8^{2-}] \ll 1$, that is, under dynamic (or bimolecular) quenching, eq 6 is simplified to the Stern-Volmer equation:

$$\frac{I^0}{I} = \frac{\Phi_{Ar}}{\Phi} = \frac{\tau^0}{\tau} = 1 + k_q\tau^0[S_2O_8^{2-}] \quad (7)$$

while for $K_{eq}[S_2O_8^{2-}] \gg 1$, that is, under static (or unimolecular) quenching

$$\frac{I^0}{I} = \frac{1+k_q\tau^0[S_2O_8^{2-}]}{\left(\frac{\tau'}{\tau^0}\right)(1+k_q\tau^0[S_2O_8^{2-}])(1+k'_q\tau'[S_2O_8^{2-}])^{-1}} \quad (8)$$

and when $k'_q\tau'[S_2O_8^{2-}]$ in the denominator is large compared to 1, then

$$\frac{I^0}{I} = \frac{\tau^0}{\tau'} + k'_q\tau'[S_2O_8^{2-}] \quad (9)$$

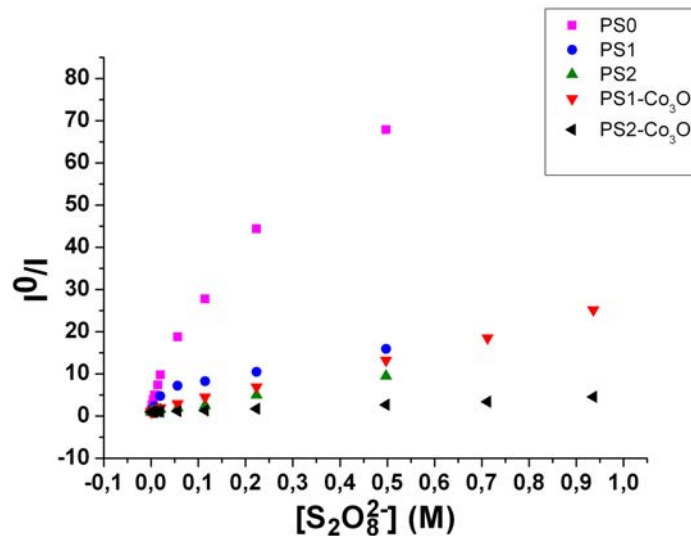


Figure 7. SV plots for all the PS and PS-Co₃O₄ systems at pH 5.60. All solutions were purged with argon.

As shown in Figure 7, curves for **PS1-Co₃O₄** and **PS2-Co₃O₄** fit well into eq 7, suggesting that the equilibrium constant corresponding to the formation of an S₂O₈²⁻/PS-Co₃O₄ ion pair is negligible and most quenchers are not in the ion-pair ground-state. Thus, the quenching proceeds through a bimolecular pathway. On the contrary, for all free PS there is a deviation from linearity of the SV plots at [S₂O₈²⁻] <15 mM, which indicates the formation of a ground-state ion pair between PS and S₂O₈²⁻. Assuming that k_q and k_q' are similar [66], these SV plots can be fitted by eq 6, and the results of all fittings are listed in Table 3. Also, the SV plots of **PS0**, at [S₂O₈²⁻] > 50 mM show a change in the curvature, with an extrapolated intercept at the x axis origin away from (0,1) (Figure 7), which suggests that adsorption of the cationic PS to negatively charged silica particles (originated from Na₂SiF₆ hydrolysis) [18] or dynamic quenching processes are taking place as a result of the increased ionic strength [66,69,70].

Table 3. Results of kinetic analysis of the $\{PS^*, S_2O_8^{2-}\}$ and $\{Co_3O_4-PS^*, S_2O_8^{2-}\}$ systems at pH 5.6 ^a Quantum yield in air-saturated buffer solutions in the absence of quencher. ^b Quantum yield in argon-saturated buffer solutions in the absence of quencher. ^c From lifetime measurements in the absence of $S_2O_8^{2-}$ in an argon-saturated buffer solution. ^d From lifetime measurements in the absence of $S_2O_8^{2-}$ in an air-saturated buffer solution. ^e From lifetime measurements in the absence of $S_2O_8^{2-}$ in an argon-saturated buffer solution in the presence of Co_3O_4 NPs. ^f Calculated from intercept of SV plots (τ^0/τ') and τ^0 . ^g Intercept of SV plots at variable $[S_2O_8^{2-}]$. ^h From slope of SV plots at variable $[S_2O_8^{2-}]$. ⁱ Computational best fit to equation 5 (see text). ^j Calculated from equation 9 (see text). ^k Calculated for 0.3 M $S_2O_8^{2-}$. ^l Calculated for 0.019 M $S_2O_8^{2-}$.

Entry	System	Φ_{O_2} , ^a	Φ_{Ar} , ^b	τ_{Ar}^0 , ^c ns	$\tau_{O_2}^0$, ^d ns	τ_{NPs}^0 , ^e ns	τ' , ^f ns	τ^0/τ' , ^g	k_q (k_q'), ^h $M^{-1} s^{-1}$	K_{eq} , ⁱ M^{-1}	k_{ET} , ^j s^{-1}	$k_q[S_2O_8^{2-}]^k$, s^{-1}	$k_q[S_2O_8^{2-}]^l$, s^{-1}
1	PS0 no buffer	0.028	0.042	550	366	N/A	108	5.09	$3.9 \cdot 10^8$	$6.93 \cdot 10^2$	$7.4 \cdot 10^6$	$1.17 \cdot 10^8$	$7.41 \cdot 10^6$
2	PS0	0.021	0.032	558	364	550	55	10.22	$4.39 \cdot 10^8$	$2.46 \cdot 10^2$	$1.65 \cdot 10^7$	$1.32 \cdot 10^8$	$8.34 \cdot 10^6$
3	PS1	0.026	0.031	501	420	512	109	4.59	$3.17 \cdot 10^7$	$1.29 \cdot 10^2$	$7.17 \cdot 10^6$	$9.52 \cdot 10^6$	$6.02 \cdot 10^5$
4	PS2	0.023	0.029	429	340	425	312	1.37	$7.50 \cdot 10^7$	$2.81 \cdot 10^1$	$8.72 \cdot 10^5$	$2.25 \cdot 10^7$	$1.43 \cdot 10^6$
5	PS1- Co_3O_4	0.025	0.030	497	414	497	-	-	$5.05 \cdot 10^7$	-	-	$1.52 \cdot 10^7$	$9.60 \cdot 10^5$
6	PS2- Co_3O_4	0.022	0.030	412	327	412	-	-	$1.94 \cdot 10^7$	-	-	$5.82 \cdot 10^6$	$3.69 \cdot 10^5$

On the other hand, the intrinsic radiative and nonradiative rate constants of {PS^{••}S₂O₈²⁻}^{*} ion pairs should be similar to those of the PS^{*} due to the weak (a few kilocalories per mole) electrostatic interaction between PS and S₂O₈²⁻ [65]. Then, the photoinduced unimolecular electron transfer (ET) rate (k_{ET}) can be estimated as

$$k_{ET} = \frac{1}{\tau'} - \frac{1}{\tau^0} \quad (9)$$

At 0.3 M concentration of S₂O₈²⁻, the bimolecular ET rates $k_q[S_2O_8^{2-}]$ are faster than the unimolecular ET rates (k_{ET}) for all systems at pH 5.6 (Table 3), suggesting that at this concentration S₂O₈²⁻ deactivates the unimolecular quenching process since it inhibits the formation of the ground-state {PS^{••}S₂O₈²⁻} ion pairs [65]. However, under catalytic conditions (0.019 M S₂O₈²⁻) the bimolecular quenching is basically favored for **PS2** ($k_q[S_2O_8^{2-}] \geq k_{ET}$), whereas the unimolecular quenching is preferential for **PS0** and **PS1** ($k_{ET} > k_q[S_2O_8^{2-}]$).

For all systems, their photooxidation by S₂O₈²⁻ has also been studied at pH 8.4, in which all PS are deprotonated (Table S1, Figures S22 and S23). Under these conditions we can see no deviations from linearity for the Stern-Volmer plots, since the unimolecular ET mechanism is clearly disfavored now due to the repulsion that appears between the negatively charged PS and S₂O₈²⁻ at basic pH.

Transient absorption spectroscopy was also used to study the difference between the free **PS1** and the **PS1-Co₃O₄** hybrid systems. No significant differences were observed between the free PS and that attached to Co₃O₄ NPs (Figure S24), and in both cases the ground-state bleaching of **PS1** at 452 nm and the formation of the **PS1**^{*} excited state near 360 nm could be observed (Figure S25). Thus, undesired back electron transfer from the Co₃O₄ NPs to **PS1**^{*} is not observed in any of both systems, as otherwise deduced from the comparison between τ_{Ar}^0 and τ_{NPs}^0 (Table 3), meaning that **PS1**^{*} probably remains excited until its reaction with S₂O₈²⁻.

Unfortunately, the oxidation of Co₃O₄ nanoparticles by PS⁺³ (reaction 3, Scheme 1 above) has not been possible to study by transient spectroscopy due to scattering effects.

3.5 Conclusions

In conclusion, we have demonstrated that the use of 1-heptanol resulted to be both a proper solvent and stabilizing agent for the synthesis of 3 nm Co⁰ NPs, preventing their aggregation. The Co⁰ NPs have been oxidized into Co₃O₄ NPs by air-exposure in very mild conditions preserving their morphology and dispersion. When deposited at the surface of a GC-RDE electrode and in 1M NaOH, these ultrafine Co₃O₄ NPs electrocatalytically oxidize water with an onset η of *ca.* 0.29 V and $\eta_{10\text{mA}/\text{cm}^2}$ of 0.486 V, showing ECSA normalized current densities (j_s) of 1.04 mA cm⁻² at $\eta = 0.35$ V, a value that fairly outperforms that of all benchmarked nanostructured metal oxide electrocatalysts deposited onto GC-RDE. Despite stable and showing 95% Faradaic efficiency, the system is less competitive at higher current densities due to its Tafel slope of *ca.* 100 mV·dec⁻¹.

Ru^{II} photosensitizers displaying phosphonic acid pending groups (**PS1** with two and **PS2** with four) were attached to the surface of Co₃O₄ NPs, yielding PS-Co₃O₄ hybrid systems with different degree of surface functionalization: (1-heptanol)_{0.80}(PS1)_{0.09}-Co₃O₄ and (1-heptanol)_{0.97}(PS2)_{0.15}-Co₃O₄, which corresponds to the incorporation of around 19 **PS1** and 32 **PS2** complexes per Co₃O₄ NP. The capacity of these dyad systems to photooxidize water into dioxygen using visible light and S₂O₈²⁻ as sacrificial electron acceptor at pH 5.6 was evaluated and the results compared with those of unbound systems of the same components and concentrations. The benefits of the dyad approach arise when observing the inactivity of the unbound Co₃O₄/PS systems with regards to the significant TON and TOF values per NP (5.4 / 0.90 min⁻¹ and 82 / 2.05 min⁻¹) obtained for **PS1**-Co₃O₄ and **PS2**-Co₃O₄, respectively. The better performance of the latter over the former was attributed to the higher surface functionalization of **PS2**-Co₃O₄, that enhance the kinetics of WO and protect better the catalytic entity under catalytic conditions against aggregation. These data stress the important role of the direct connection between the PS and the nanocatalyst by; 1) favoring their efficient electronic communication that allows being kinetically competitive with the typical side deactivation processes of light-driven WO and 2) minimizing catalyst aggregation under turnover conditions by means of the protective/stabilizing PS layer at the surface of the Co₃O₄ NPs.

Additionally, both bound PS-NP and unbound PS/Co₃O₄ systems have been photophysically studied observing that no back electron transfer from the excited dye to the Co₃O₄ NPs takes place in any case, evidencing a good electronic communication in the PS-NP dyad.

Summarizing, this work opens the way towards precisely defined 1st row RuPS-NP hybrid dyads by means of the so-called organometallic approach as synthetic methodology, which provides well-controlled and fully characterized cobalt, cobalt oxide and RuPS-Co₃O₄ nanomaterials. The latter species have proven capable to photooxidize water into dioxygen at pH 5.6, being fairly superior to their unbound Co₃O₄/PS counterparts under identical conditions. Therefore, the fine tuning of this system through the length and nature of the PS-Co₃O₄ connection is expected to lead to a better understanding of the key parameters governing the catalytic process and is already under way in our laboratories.

Contribution

Jonathan De Tovar synthesized and characterized the Ru(II)-polypyridylic complexes, Co₃O₄ NPs, PS-Co₃O₄ dyads, and carried out the electrochemical and photochemical catalytic experiments and the photophysical analysis.

3.6 Supporting information

3.6.1 Estimation of Co content in Co₃O₄ NPs

As the oxidation is carried out in solid state, and the boiling point of the ligand is too high to allow for significant spontaneous evaporation, we hypothesize that the mass change in the sample is only due to the gain in oxygen.

100 g of the Co NPs sample contain 35.35 g of Co, which corresponds after oxidation to a mass of 48.17 g of Co₃O₄ determined as follows:

$$35.35 \text{ g Co} \cdot \frac{1 \text{ mole Co}}{58.9 \text{ g Co}} \cdot \frac{1 \text{ mole Co}_3\text{O}_4}{3 \text{ moles Co}} \cdot \frac{240.8 \text{ g Co}_3\text{O}_4}{1 \text{ mole Co}_3\text{O}_4} = 48.17 \text{ g Co}_3\text{O}_4$$

The mass gain is thus (48.17 – 35.35) = 12.82 g and the final mass of the material is (100 + 12.82) = 112.82 g.

Hence one can estimate the %Co in the oxidized material:

$$\frac{35.35 \text{ g Co}}{112.82 \text{ g}} \cdot 100 = 31.33 \%$$

3.6.2 Estimation of the number of 1-heptanol molecules per Co NP

The 1-heptanol content can be estimated as follows, under the hypothesis that it is the only by-product present in the material, and given the %Co weight determined by ICP-OES.

In 100 g of the Co NPs there are 35.35 g Co $\cdot \frac{1 \text{ mole Co}}{58.9 \text{ g Co}} = 0.6 \text{ moles Co}$. Then, 100 g – 35.35 g Co = 64.65 g hept, which corresponds to $64.65 \text{ g hept} \cdot \frac{1 \text{ mol hept}}{116.2 \text{ g hept}} = 0.56 \text{ moles hept}$. Thus, the heptanol/Co ratio is $\frac{0.56 \text{ moles hept}}{0.6 \text{ moles Co}} = 0.9$

Therefore, the empirical formula for Co NPs is (1-heptanol)_{0.9}-Co, pointing to more than one 1-heptanol molecule per Co surface atom.

The density reported for bulk Co is 8.9 g/cm³ and its molar mass 58.9 g/mole. Taking into account the Avogadro number value of 6.02·10²³ atoms/mole, the number of Co atoms / nm³ can be calculated as follows:

$$\frac{8.9 \cdot 10^{-21} \text{ g/nm}^3}{58.9 \text{ g/mole}} \cdot 6.02 \cdot \frac{10^{23} \text{ atoms}}{\text{mole}} = 91 \text{ Co atoms/nm}^3$$

In a first approximation the Co NPs are spherical, with an average diameter of 3 nm, so the particle volume is 14.1 nm³ and the number of Co atoms per particle is 1283 atoms. Therefore, each Co NP is surrounded by an average of 1155 molecules of 1-heptanol given the heptanol/Co ratio of 0.9.

3.6.3 Estimation of the number of Co atoms per Co₃O₄, PS1-Co₃O₄ and PS2-Co₃O₄ NPs

For this calculation we consider that Co₃O₄ NPs as well as PS1-Co₃O₄ and PS2-Co₃O₄ NPs have the same average size (3 nm) given the error bar of their respective size distributions (3.0 ± 0.2 for Co₃O₄, 3.1 ± 0.2 for PS1-Co₃O₄ and 3.0 ± 0.3 for PS2-Co₃O₄) and that they are spherical. So the particle volume is 14.1 nm³.

Given the density and the molar mass of the Co₃O₄ unit (in the bulk), one can calculate:

$$\begin{aligned} \text{number of molecular units} &= \frac{6.11 \text{ g Co}_3\text{O}_4}{1 \text{ nm}^3} \cdot \frac{1 \text{ mole Co}_3\text{O}_4}{240.8 \text{ g Co}_3\text{O}_4} \cdot \frac{6.02 \cdot 10^{23} \text{ molecules}}{\text{mole}} \\ &= 15.3 \text{ Co}_3\text{O}_4 \text{ molecular units /nm}^3 \end{aligned}$$

So the number of Co₃O₄ molecular units per NP is 14.1·15.3 = 216 Co₃O₄ molec/NP (or 3·216 = 648 Co atoms/Co₃O₄ NP).

3.6.4 Estimation of the number of 1-heptanol molecules per Co₃O₄ NP

The Co content of Co₃O₄(heptanol)_x NPs is 31.33% (see above). Thus, we can calculate for 100 g of Co₃O₄(heptanol)_x NPs an “average molecular weight” of the material:

$$31.33 \text{ g Co} \cdot \frac{1 \text{ mole Co}}{58.93 \text{ g Co}} \cdot \frac{1 \text{ mol Co}_3\text{O}_4(\text{hept})_x}{3 \text{ moles Co}} = 0.177 \text{ moles Co}_3\text{O}_4(\text{hept})_x$$

$$\frac{100 \text{ g Co}_3\text{O}_4(\text{hept})_x}{0.177 \text{ moles Co}_3\text{O}_4(\text{hept})_x} = 564.3 \text{ g/mole Co}_3\text{O}_4(\text{hept})_x$$

From this average MW we can estimate the number of heptanol molecules per molecular Co₃O₄ unit supposing that there are no other impurities on the material. We first calculate mass of oxide anions:

$$31.33 \text{ g Co} \cdot \frac{1 \text{ mole Co}}{58.9 \text{ g Co}} \cdot \frac{4 \text{ moles } O^{2-}}{3 \text{ moles Co}} \cdot \frac{16 \text{ g } O^{2-}}{1 \text{ mole } O^{2-}} = 11.34 \text{ g } O^{2-}$$

For 100 g of material, we have 11.34 g of O²⁻. Thus, 100-31.33-11.34 = 57.32 g of heptanol. In moles:

$$57.32 \text{ g heptanol} \cdot \frac{1 \text{ mole heptanol}}{116.2 \text{ g heptanol}} = 0.493 \text{ moles heptanol}$$

Therefore, the heptanol:Co₃O₄ ratio will be

$$\frac{0.493 \text{ moles heptanol}}{0.177 \text{ moles Co}_3\text{O}_4(\text{hept})_x} = 2.78 \text{ molecules of heptanol/Co}_3\text{O}_4$$

So the ratio will be Co₃O₄(heptanol)_{2.8}

3.6.5 Estimation of the number of 1-heptanol and PS molecules per PS1-Co₃O₄ NP and PS2-Co₃O₄ NP

The Co content of PS1-Co₃O₄NPs is 43.60%. Thus, we can calculate for 100 g of PS1-Co₃O₄ NPs an “average molecular weight” of the material:

$$43.60 \text{ g Co} \cdot \frac{1 \text{ mole Co}}{58.93 \text{ g Co}} \cdot \frac{1 \text{ mole Co}_3\text{O}_4}{3 \text{ moles Co}} = 0.2466 \text{ moles } (\text{PS1})_y\text{Co}_3\text{O}_4(\text{hept})_x$$

$$\frac{100 \text{ g } (\text{PS1})_y\text{Co}_3\text{O}_4(\text{hept})_x}{0.2466 \text{ moles } (\text{PS1})_y\text{Co}_3\text{O}_4(\text{hept})_x} = 405.5 \text{ g/mole } (\text{PS1})_y\text{Co}_3\text{O}_4(\text{hept})_x$$

If we now calculate the mass of oxide anions:

$$43.60 \text{ g Co} \cdot \frac{1 \text{ mole Co}}{58.93 \text{ g Co}} \cdot \frac{4 \text{ moles } O^{2-}}{3 \text{ moles Co}} \cdot \frac{16 \text{ g } O^{2-}}{1 \text{ mole } O^{2-}} = 15.78 \text{ g } O^{2-}$$

and the mass of PS1 according to the ICP-OES value of 2.23% Ru:

$$2.23 \text{ g Ru} \cdot \frac{1 \text{ mole Ru}}{101.7 \text{ g Ru}} \cdot \frac{1 \text{ mole PS1}}{1 \text{ mole Ru}} \cdot \frac{800.49 \text{ g PS1}}{1 \text{ mole PS1}} = 17.66 \text{ g PS1 (or 0.022 moles)}$$

Therefore, we have 100-43.60-15.78-17.66 = 22.95 g of heptanol in 100 g of sample. In moles:

$$22.95 \text{ g heptanol} \cdot \frac{1 \text{ mole heptanol}}{116.2 \text{ g heptanol}} = 0.1975 \text{ moles heptanol}$$

which means a ratio of:

$$\frac{0.1975 \text{ moles heptanol}}{0.2466 \text{ moles } (\text{PS1})_y\text{Co}_3\text{O}_4(\text{hept})_x} = 0.80 \text{ molecules of heptanol/Co}_3\text{O}_4$$

$$\frac{0.0221 \text{ moles PS1}}{0.2466 \text{ moles } (\text{PS1})_y\text{Co}_3\text{O}_4(\text{hept})_x} = 0.09 \text{ molecules of PS1/Co}_3\text{O}_4$$

So the ratio will be (PS1)_{0.09}Co₃O₄(heptanol)_{0.80}

Then, given that in a single Co₃O₄ NP there are 216 Co₃O₄ molecules (see above), in a (PS1)_{0.09}Co₃O₄(heptanol)_{0.80} NP there are 19 PS1 molecules.

Analogously, for the PS2-Co₃O₄ system we have found ICP-OES values of 35.22% Co and 3.12% Ru, which account for an average MW of 501.96 g/mole and a (PS2)_{0.15}Co₃O₄(heptanol)_{0.97} formula. Also, if supposing the presence of 216 Co₃O₄ molecules per NP, there are 32 PS2 molecules per hybrid NP.

3.6.6 Calculation of TON (O₂ molecules/NP)

The turnover number per NP was obtained by dividing the number of moles of O₂ obtained during the photocatalytic experiments by the total number of moles of Co₃O₄, PS1-Co₃O₄ or PS2-Co₃O₄ NPs present in the weighted sample assuming that each NP contains 648 Co atoms (independently of whether it is a pure Co₃O₄ or a hybrid PS-Co₃O₄ material, see above) and using the %Co obtained in each respective ICP-OES measurement.

For example, we obtained 6.45·10⁻⁷ moles O₂ in 16.7 min using 0.13 mg of Co₃O₄ NPs and 6 equivalents of PS2. So TON per NP (entry 3) was calculated as follows:

$$\frac{6.45 \cdot 10^{-7} \text{ moles } O_2}{0.13 \cdot 10^{-3} \text{ g Co}_3\text{O}_4\text{NPs}} \cdot \frac{100 \text{ g Co}_3\text{O}_4 \text{ NPs}}{31.33 \text{ g Co}} \cdot \frac{58.93 \text{ g Co}}{1 \text{ mole Co}} \cdot \frac{648 \text{ moles Co}}{1 \text{ mole NP}} = 604 \frac{\text{moles } O_2}{\text{mole NP}}$$

3.6.7 Calculation of TON (O₂ molecules/PS)

To obtain the TON per PS the number of moles of O₂ obtained during the photocatalytic experiments are divided by the total number of moles of PS (anchored or not).

For example, we obtained 6.45·10⁻⁷ moles O₂ in 16.7 min using 0.13 mg of material PS2-Co₃O₄. So TON per NP was calculated as follows:

$$\frac{6.45 \cdot 10^{-7} \text{ moles } O_2}{0.13 \cdot 10^{-3} \text{ g Co}_3\text{O}_4\text{NPs}} \cdot \frac{100 \text{ g Co}_3\text{O}_4 \text{ NPs}}{31.33 \text{ g Co}} \cdot \frac{58.93 \text{ g Co}}{1 \text{ mole Co}} \cdot \frac{3 \text{ moles Co}}{6 \text{ moles PS2}} = 0.466 \frac{\text{moles } O_2}{\text{mole PS2}}$$

3.6.8 Calculation of TOF (O_2 molecules/NP)

The turnover frequency per NP is calculated by dividing TON per NP by the number of minutes the catalysis has taken place until reaching a plateau.

3.6.9 Calculation of TOF (O_2 molecules/PS)

The turnover frequency per PS is obtained by dividing the TON per PS by the number of minutes the catalysis has taken place until reaching a plateau.

3.6.10 PMMA Coating

A poly(methyl methacrylate) (PMMA) coating was formed onto the FTO electrode supporting Co_3O_4 NPs by simply dipping this electrode in dichloromethane (DCM) with 0.5 % wt concentration of PMMA. After soaking the electrode in the PMMA solution for a few seconds (< 10 sec), the electrode was air-dried.

3.6.11 Quenching of [Photosensitizer]^{+2,*} by $S_2O_8^{2-}$

Solutions of $S_2O_8^{2-}$ of different concentrations were prepared with a constant amount of photosensitizer or hybrid material. Thus, after bubbling the mixture with argon for 20 min, quantum yields and lifetimes were recorded for each concentration of $S_2O_8^{2-}$. The excited-state lifetime of [photosensitizer]^{+2,*}, τ^0 , was determined from luminescence decay data following excitation at 450 nm. The counterion present in all solutions was Cl⁻.

3.6.12 PS used and Characterization of Co and Co₃O₄ NPs and PS1-Co₃O₄ and PS2-Co₃O₄ hybrid systems

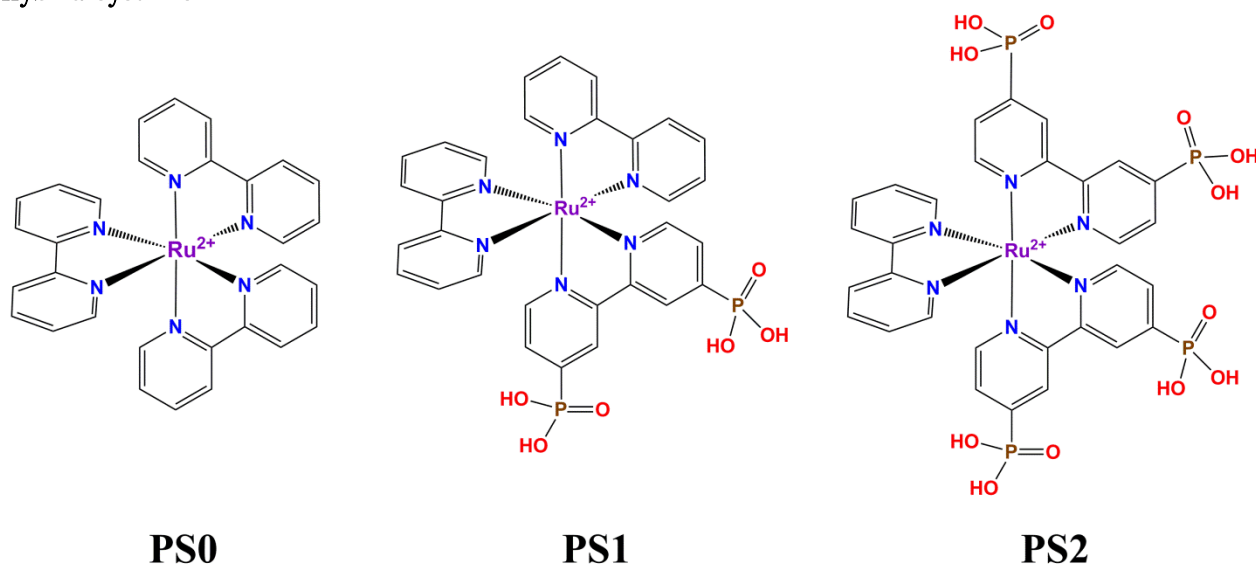
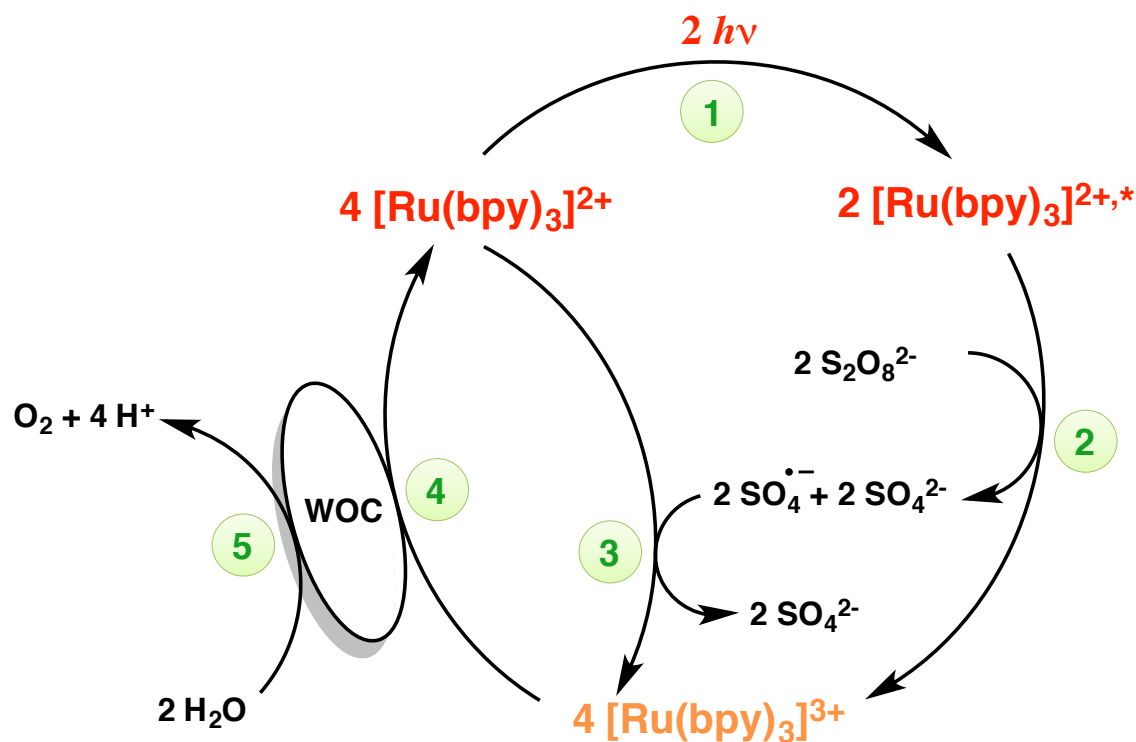


Figure S1. [Ru(bpy)₃]²⁺ (PS0) and modified [Ru(bpy)₃]²⁺ complexes with 2 and 4 phosphonic acid coordinating pending groups (PS1 and PS2, respectively) used as photosensitizers.



Scheme S1. Catalytic cycle of visible light-driven water oxidation with Na₂S₂O₈ and [Ru(bpy)₃]²⁺ using Co₃O₄ NPs as water oxidation catalyst (WOC). (1) Dye photoexcitation; (2) oxidative dye excited-state quenching by the sacrificial oxidant; (3) oxidative dye excited-state quenching by the catalyst; (4) hole injection/catalyst oxidation; (5) water oxidation.

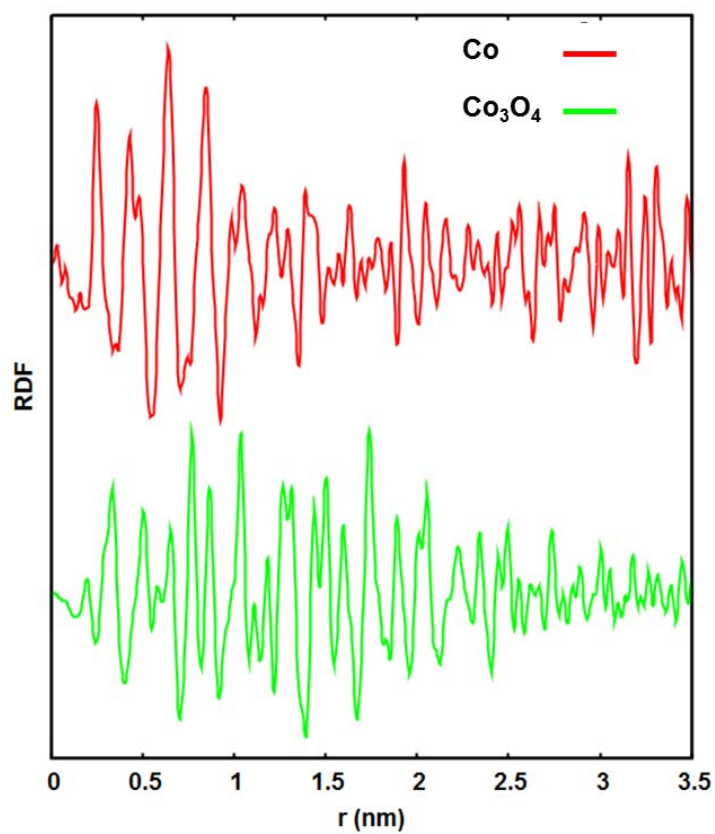


Figure S2. RDF of Co NPs (red) and of Co_3O_4 NPs (green).

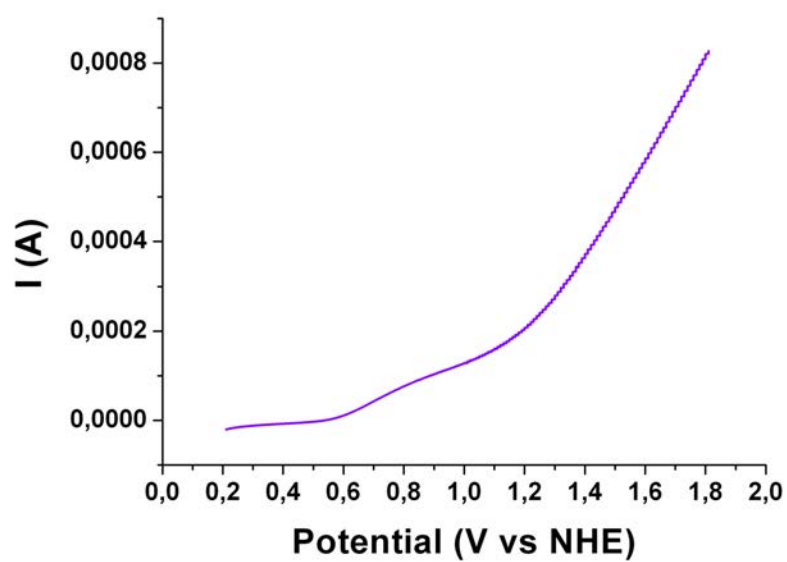


Figure S3. LSV of Co_3O_4 NPs measured at 1 mV/s scan rate.

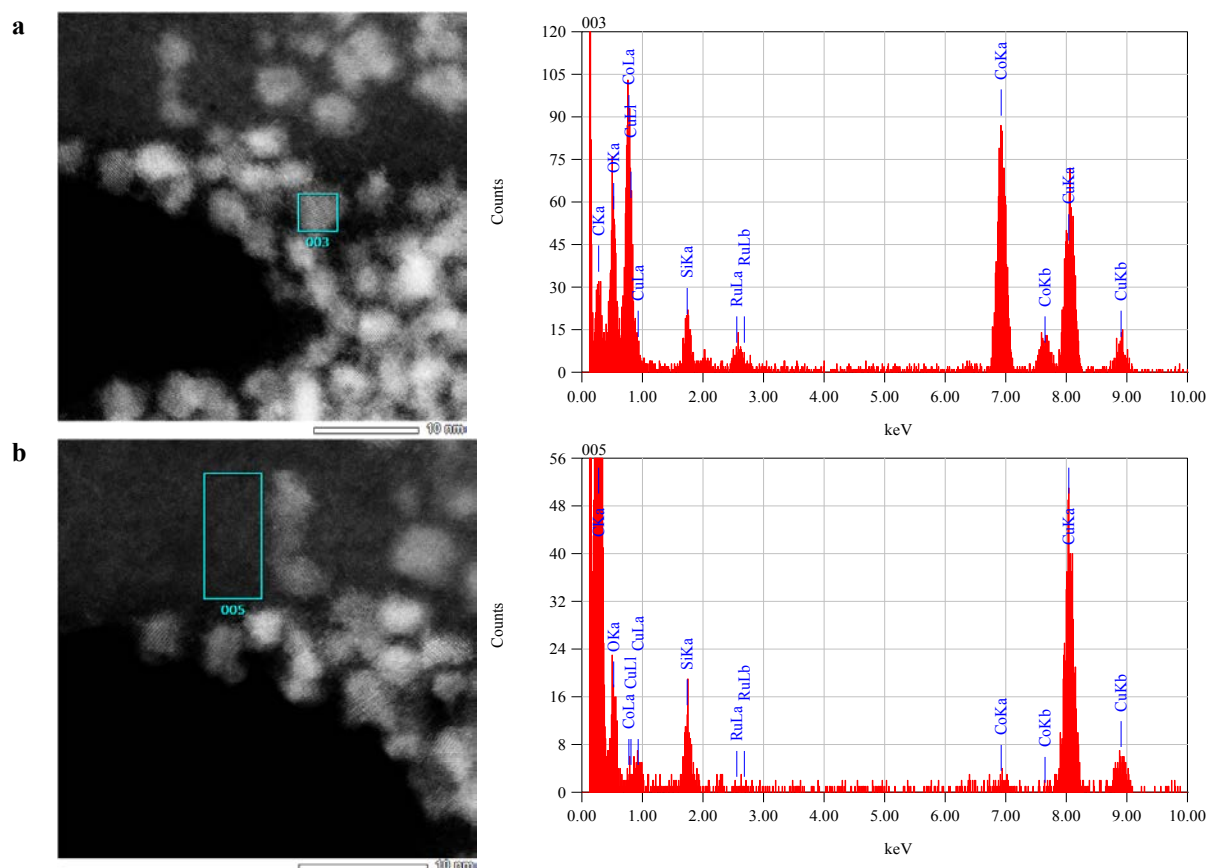


Figure S4. STEM (left) and EDX (right) analyses of the PS1- Co_3O_4 hybrid material in a selected (003) nanoparticle (a) and a free-nanoparticle (005) region (b).

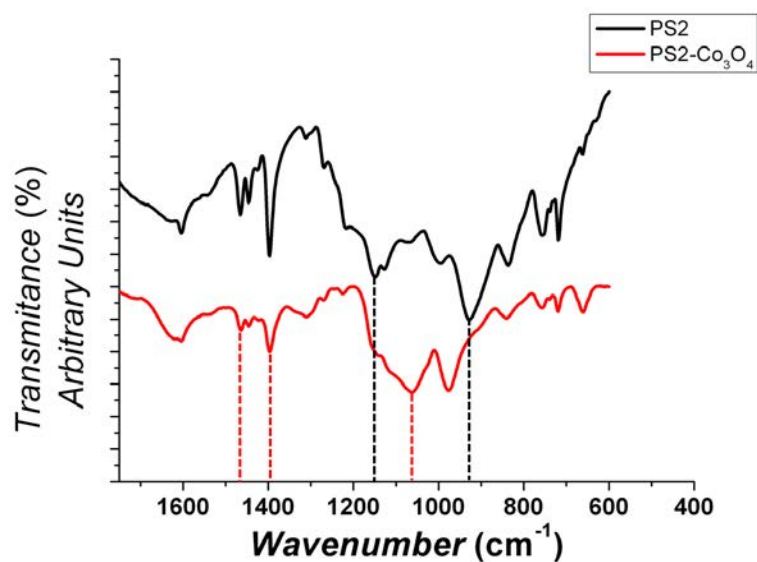


Figure S5. ATR-IR spectra of PS2 (black) and PS2- Co_3O_4 NPs hybrid material (red). The transmittance of each sample has been shifted along the y axis for comparison purposes. The positions of the bands described along the text have been added as dotted lines.

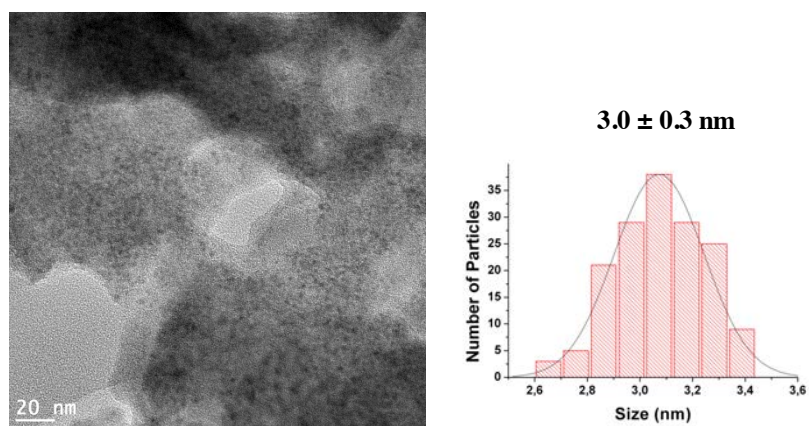


Figure S6. HREM micrograph and size histogram of the PS2-Co₃O₄ hybrid.

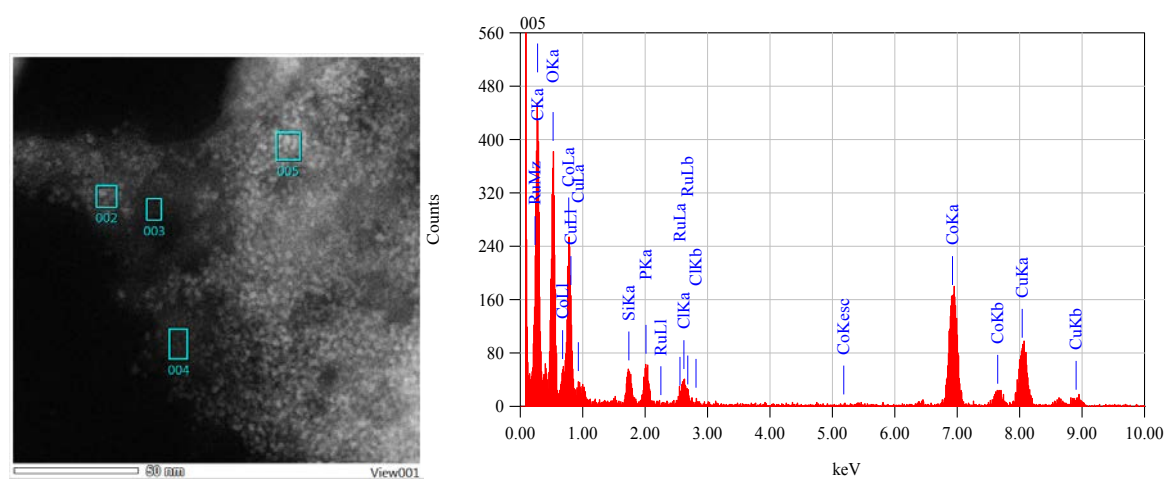


Figure S7. STEM and EDX analyses of the PS2-Co₃O₄ NPs hybrid system in a selected (005) nanoparticle region.

3.6.13 Electroinduced water oxidation experiments

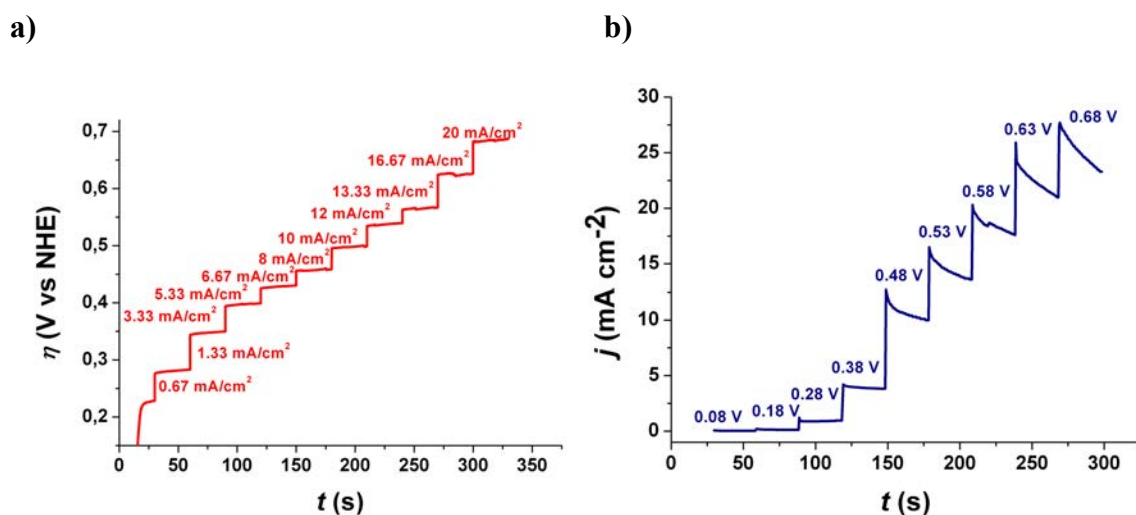


Figure S8. Representative 30 s current steps from 0.67 mA/cm^2 to 20 mA/cm^2 (a) and representative 30 s potential steps from 0 V to 0.68 V η vs. NHE at 3200 rpm and $0.01 \text{ V}\cdot\text{s}^{-1}$ scan rate in 1M NaOH (b) for the deposited Co_3O_4 NPs onto a GC-RDE electrode in 1M NaOH. In (a) the measured η at each applied current density have been converted into the applied potential vs. NHE according to $V_{\text{app}} = \eta + E_{\text{pH}} + iR$ and shown as open green squares in Fig. 5a, whereas in (b) the measured current densities at each applied η are shown as open blue triangles in Figure 5a.

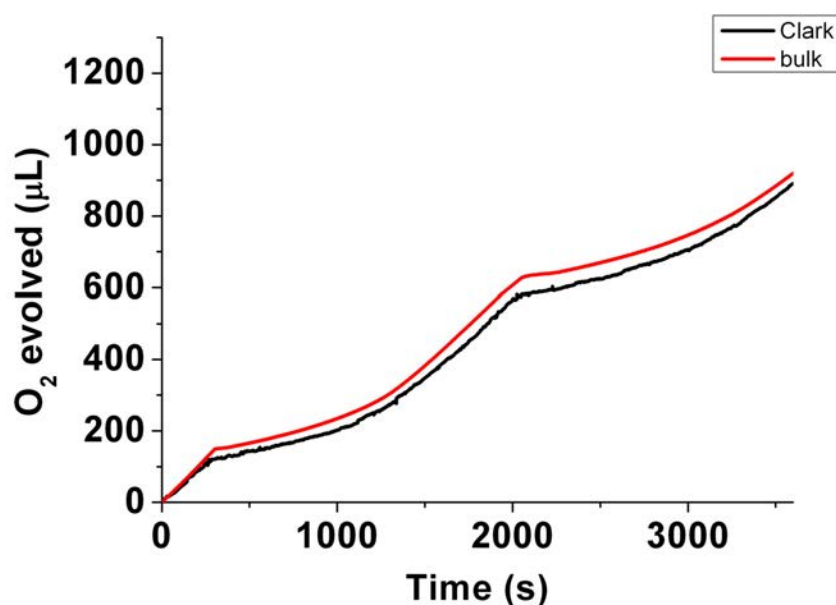


Figure S9. Theoretical (red) and experimental (black) oxygen evolution by bulk electrolysis at 0.886 V vs. NHE for a FTO/ Co_3O_4 NPs-PMMA electrode in a 1M NaOH solution.

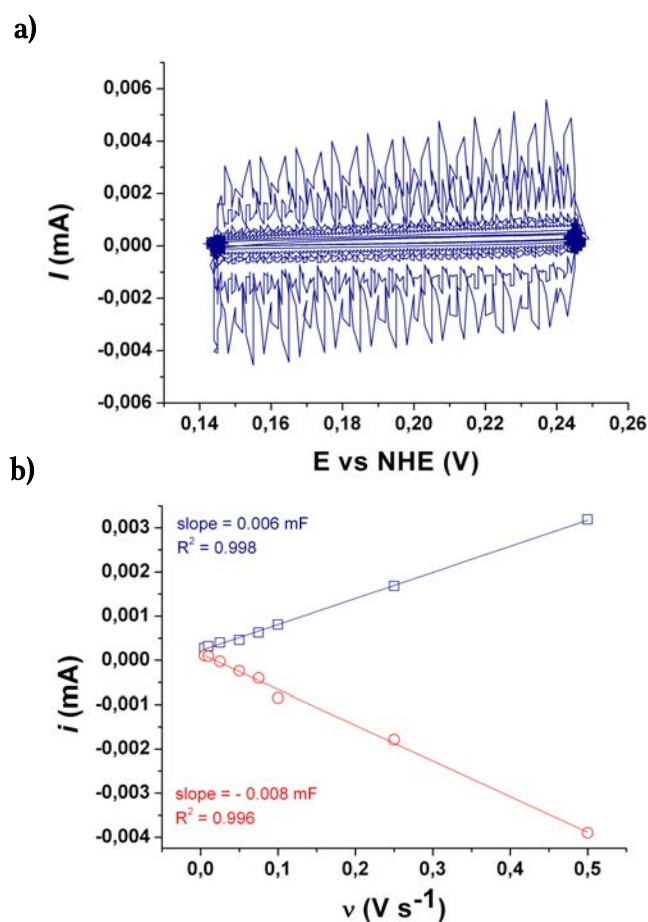


Figure S10. Double-layer capacitance measurements for determining the ECSA for the deposited Co_3O_4 NPs at pH 14 onto a RDE. (a) Cyclic voltammograms were measured in a non-Faradaic region of the voltammogram at the following scan rates: 0.005, 0.010, 0.025, 0.050, 0.075, 0.1, 0.25 and 0.5 V/s. The working electrode was held at each potential vertex for 10 s before beginning the next sweep. All currents are assumed to be due to capacitive charging. (b) The cathodic (open red circles) and anodic (open blue squares) charging currents measured at 0.195 V vs. NHE plotted as a function of scan rate. The double-layer capacitance has been measured as the average of the absolute value of the slopes of the linear fits to the data.

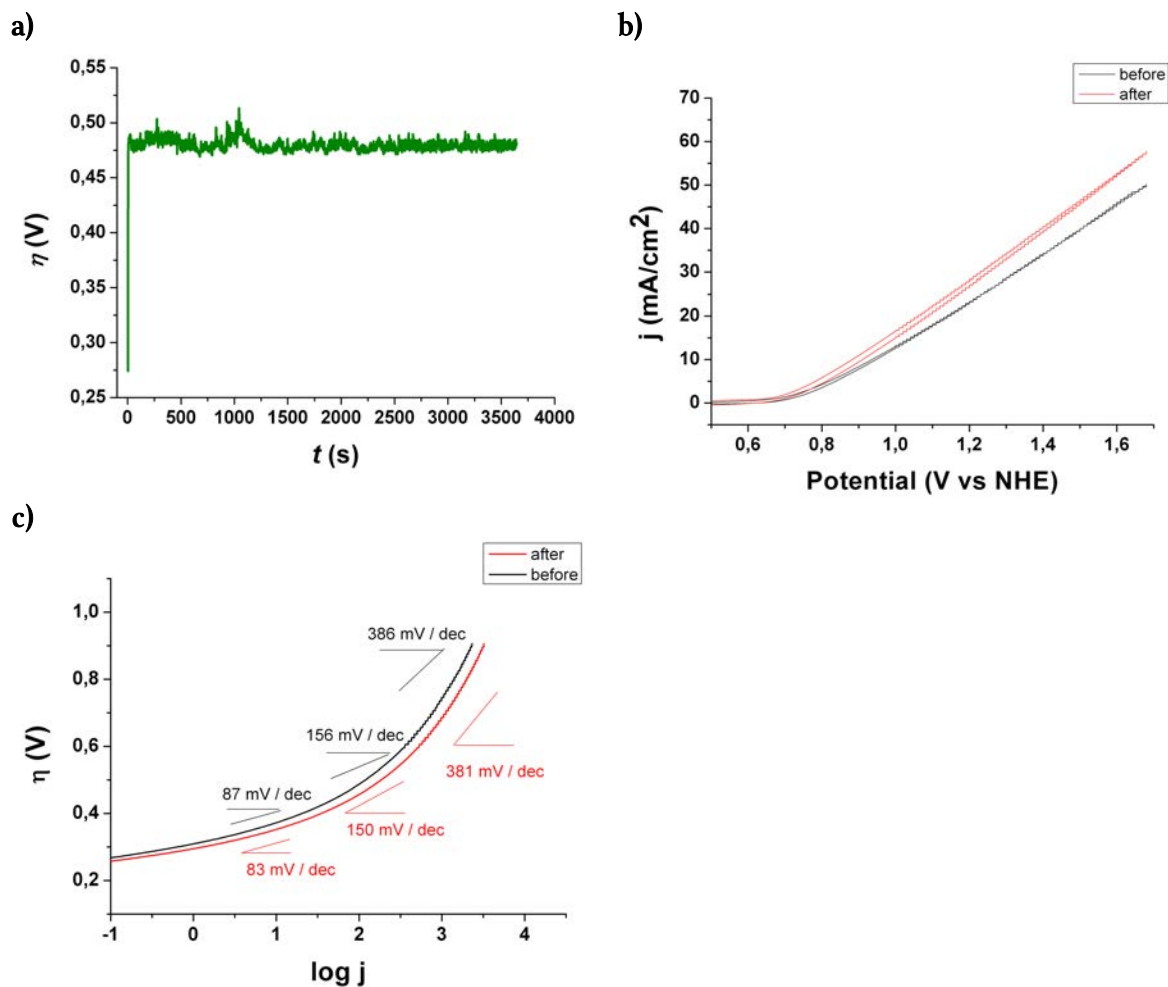


Figure S11. (a) Representative 1 h controlled current electrolysis at $10 \text{ mA}\cdot\text{cm}^{-2}$ per geometric area and 1M NaOH for FTO/ Co_3O_4 NPs-PMMA (a), CV before (black) and after (red) the electrolysis (b) and Tafel plots derived from CV experiments registered before (black) and after (red) the electrolysis (c).

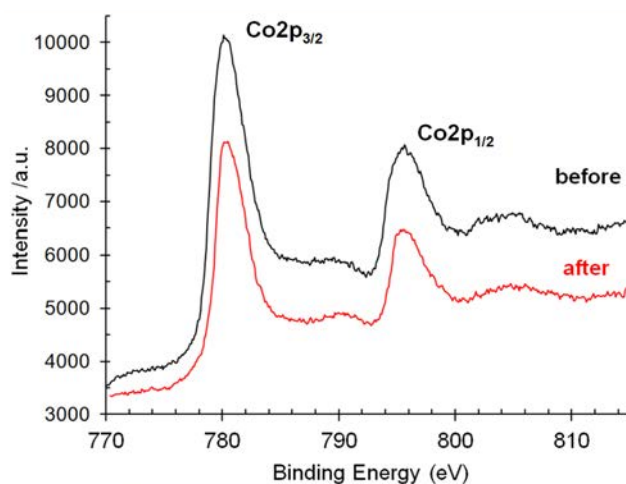


Figure S12. Co 2p XPS spectra of Co_3O_4 NPs before (black) and after (red) performing a 1 h bulk electrolysis with a FTO/ Co_3O_4 NPs-PMMA electrode at 0.886 V vs. NHE in 1M NaOH.

3.6.14 Photoinduced water oxidation experiments and related data

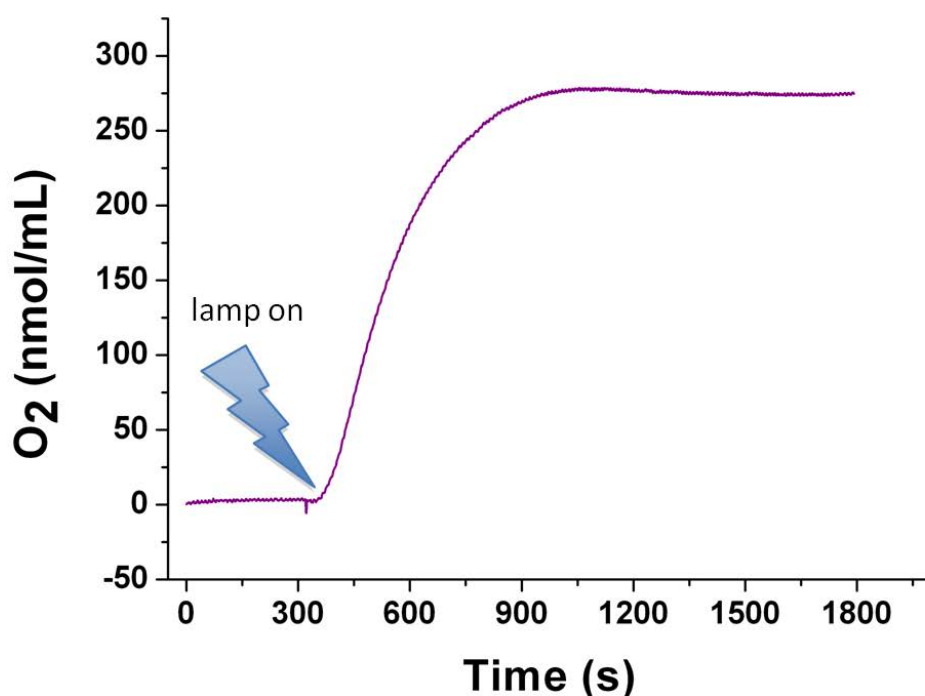


Figure S13. Hansatech-detected photocatalytic oxygen production by Co_3O_4 NPs in the presence of **PS0** as PS. Reaction conditions: $1.2 \cdot 10^{-4}$ M Co_3O_4 NPs; $2.1 \cdot 10^{-2}$ M $\text{Na}_2\text{S}_2\text{O}_8$; $7.3 \cdot 10^{-4}$ M **PS0** in Na_2SiF_6 - NaHCO_3 (0.02-0.04 M, pH 5.6) buffer solution. Irradiation provided by a Xe lamp equipped with a 400 nm cut-off filter and calibrated to 1 sun ($100 \text{ mW} \cdot \text{cm}^{-2}$). $T = 25^\circ\text{C}$.

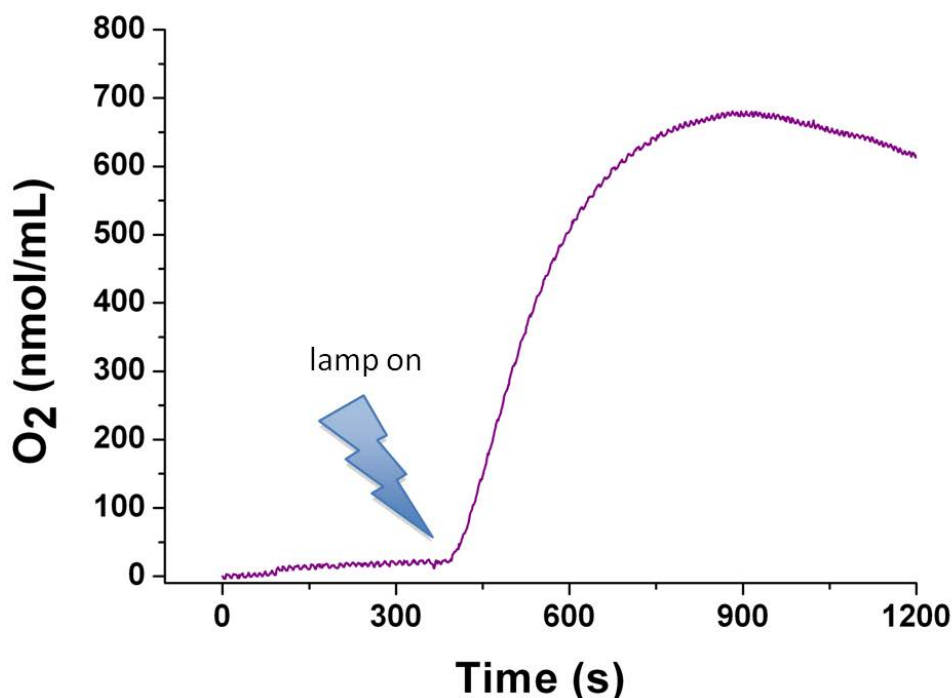


Figure S14. Hansatech-detected photocatalytic oxygen production by Co_3O_4 NPs in the presence of **PS1** as PS. Reaction conditions: $2.5 \cdot 10^{-4}$ M Co_3O_4 NPs; $4.3 \cdot 10^{-2}$ M $\text{Na}_2\text{S}_2\text{O}_8$; $1.5 \cdot 10^{-3}$ M **PS1** in Na_2SiF_6 - NaHCO_3 (0.02-0.04 M, pH 5.6) buffer solution. Irradiation provided by a Xe lamp equipped with a 400 nm cut-off filter and calibrated to 1 sun ($100 \text{ mW} \cdot \text{cm}^{-2}$). $T = 25^\circ\text{C}$.

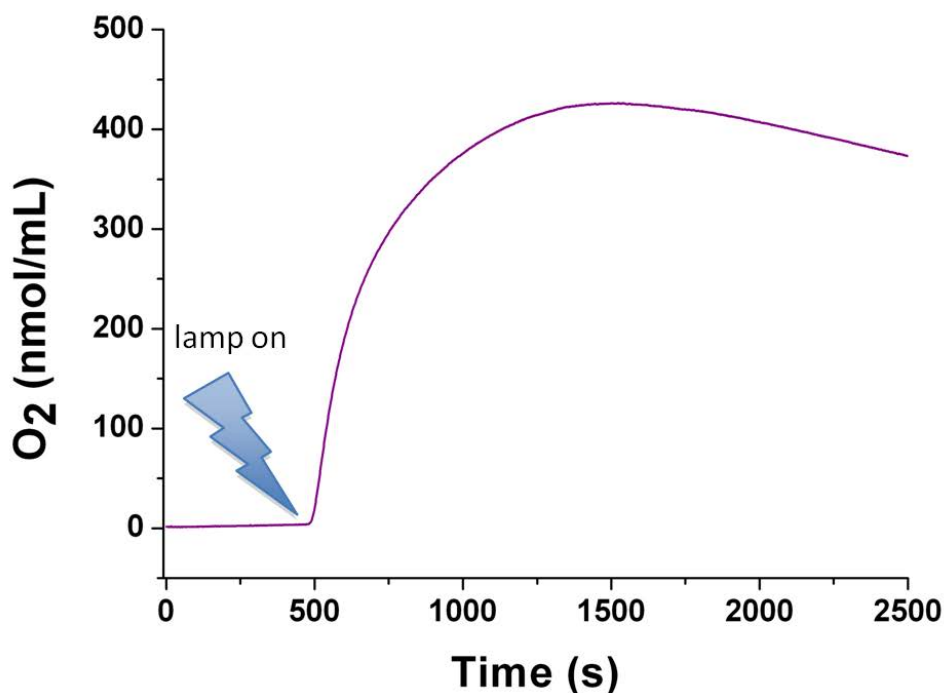


Figure S15. Hansatech-detected photocatalytic oxygen production by Co_3O_4 NPs in the presence of PS2 as PS. Reaction conditions: $1.54 \cdot 10^{-4}$ M Co_3O_4 NPs; $2.67 \cdot 10^{-2}$ M $\text{Na}_2\text{S}_2\text{O}_8$; $9.16 \cdot 10^{-4}$ M PS2 in Na_2SiF_6 - NaHCO_3 (0.02-0.04 M, pH 5.6) buffer solution. Irradiation provided by a Xe lamp equipped with a 400 nm cut-off filter and calibrated to 1 sun ($100 \text{ mW} \cdot \text{cm}^{-2}$). T = 25°C.

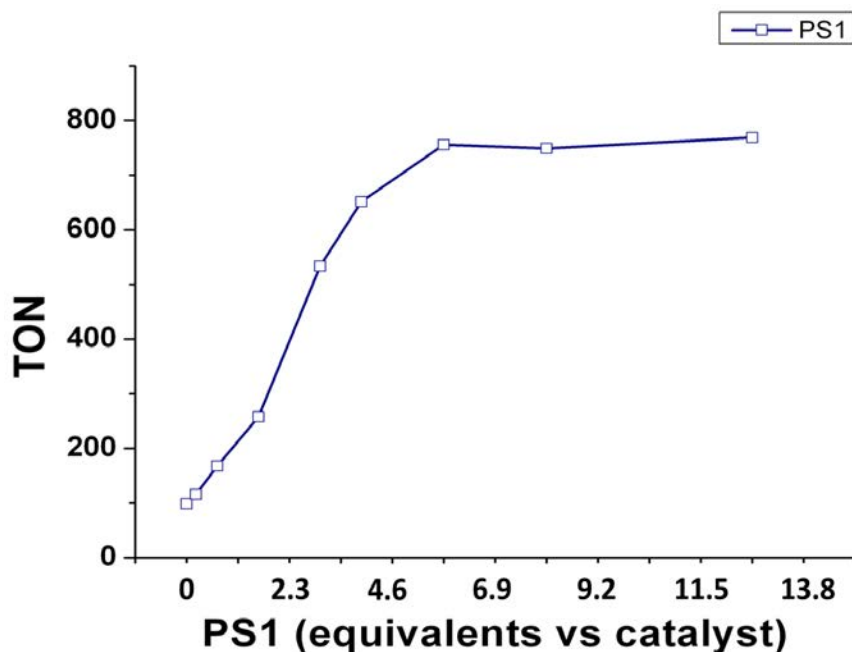


Figure S16. TON vs. PS1 equiv. in photochemical WO measurements in the presence of 1 equiv. of $\text{Co}_3\text{O}_4(\text{heptanol})_{2.8}$ units and 72 equiv. of $\text{Na}_2\text{S}_2\text{O}_8$ at pH 5.6.

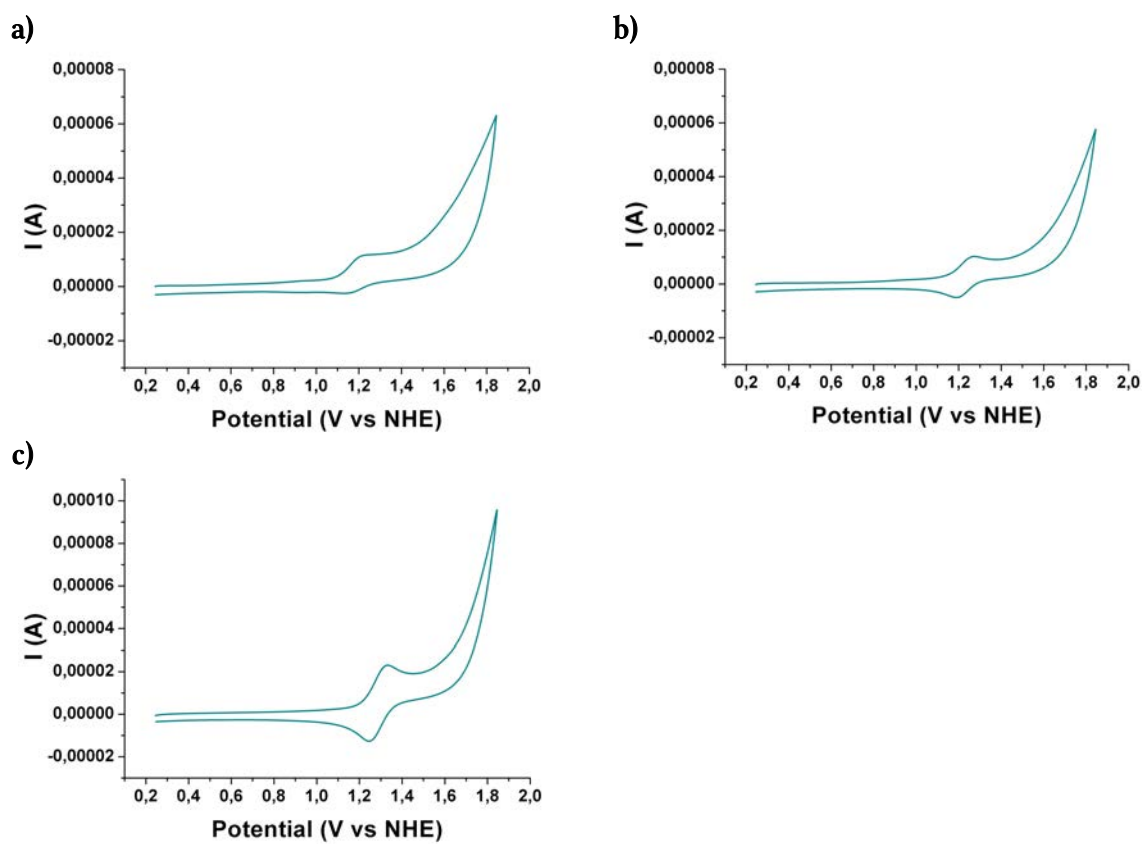


Figure S17. CVs of free **PS0** (a), **PS1** (b) and **PS2** (c) photosensitizers in a Na_2SiF_6 - NaHCO_3 (0.02-0.04 M, pH 5.60) buffer solution.

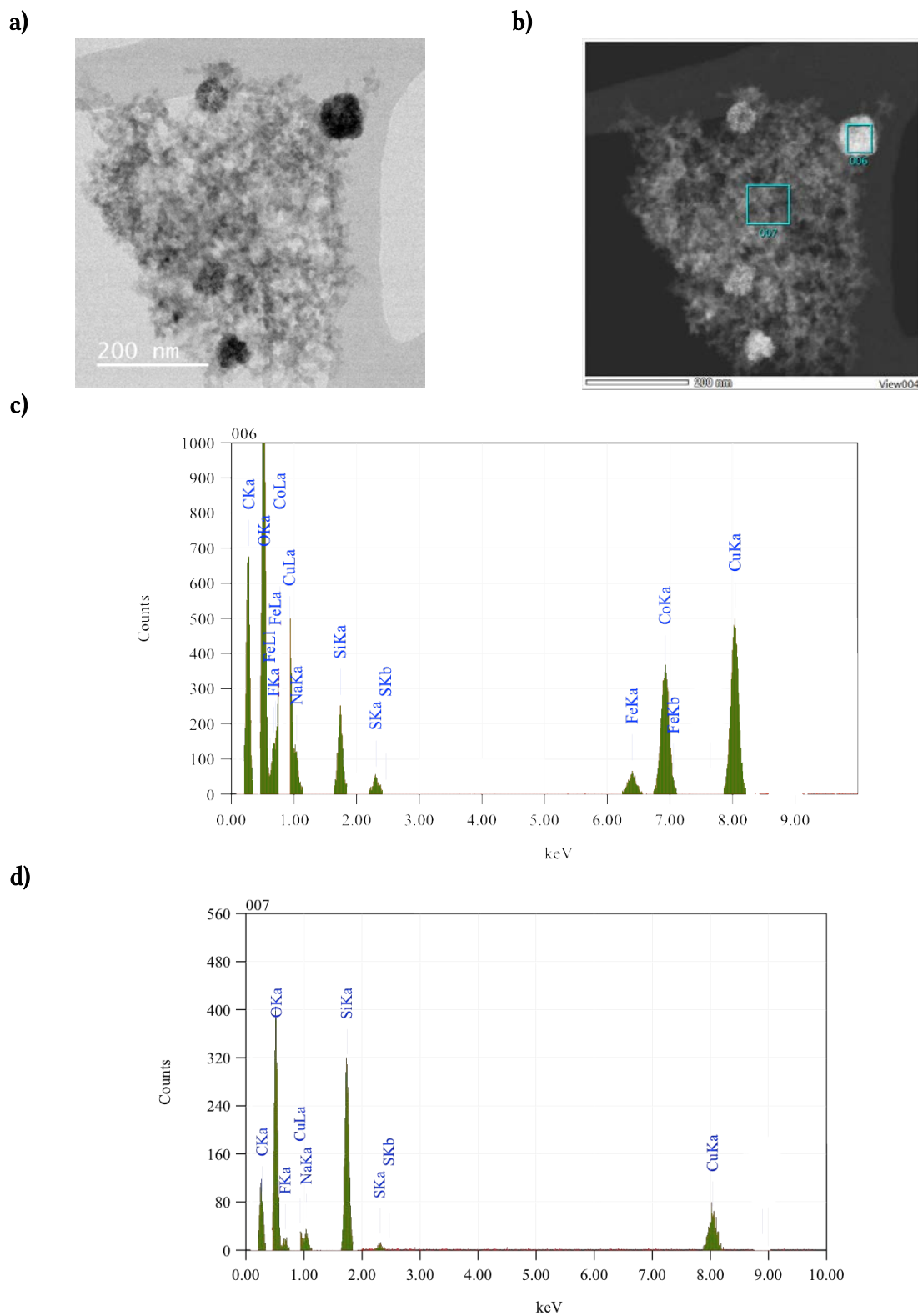


Figure S18. HREM (a) and STEM (b) images of the aggregated crude of reaction at pH 5.6 after the photocatalysis of Co_3O_4 NPs in the presence of **PSI**, and EDX analyses of the 006 selected region containing Co (c) and of the 007 region containing Si (d).

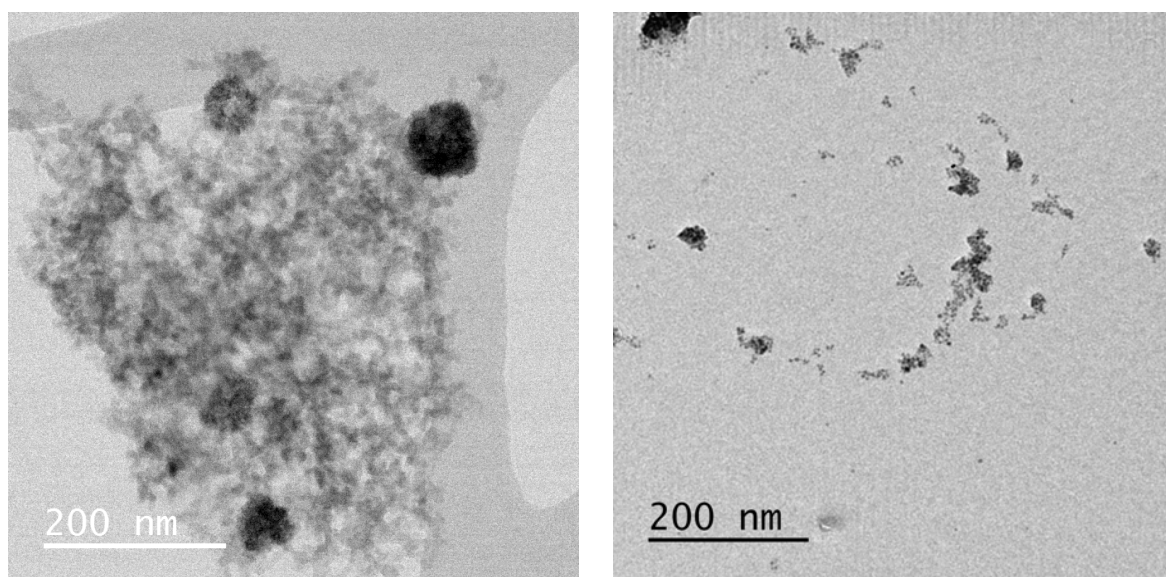


Figure S19. HREM image of the aggregated crude of reaction at pH 5.6 after the photocatalysis of Co_3O_4 NPs in the presence of PS1 (a) and TEM micrograph of dialyzed PS1- Co_3O_4 NPs after performing a 1 h photocatalytic WO catalysis at pH 5.6 (b).

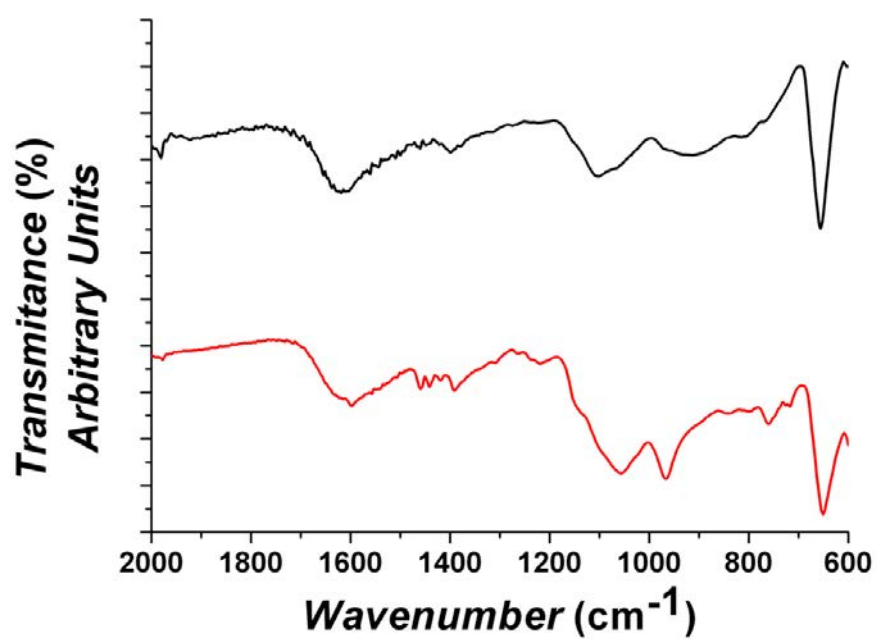
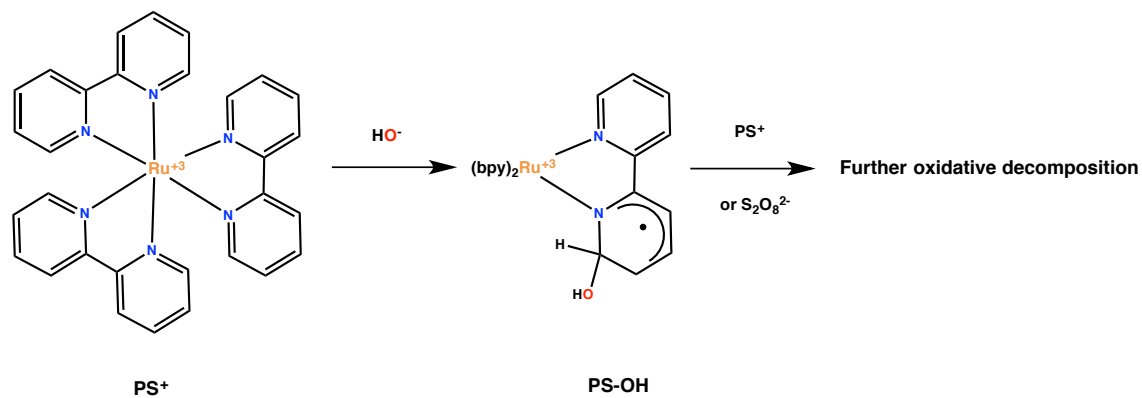
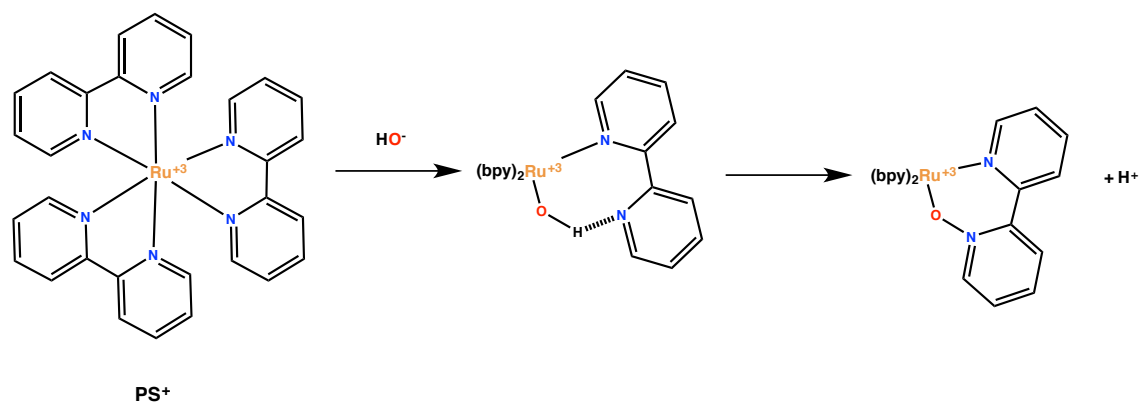


Figure S20. IR spectra of PS1- Co_3O_4 NPs before (red) and after (black) WO photocatalysis at pH 5.6. The transmittance of each sample has been shifted along the Y axis for comparison purposes.

a)



b)



Scheme S2. Reactions leading to the decomposition of the photosensitizer.

3.6.15 Photophysical studies

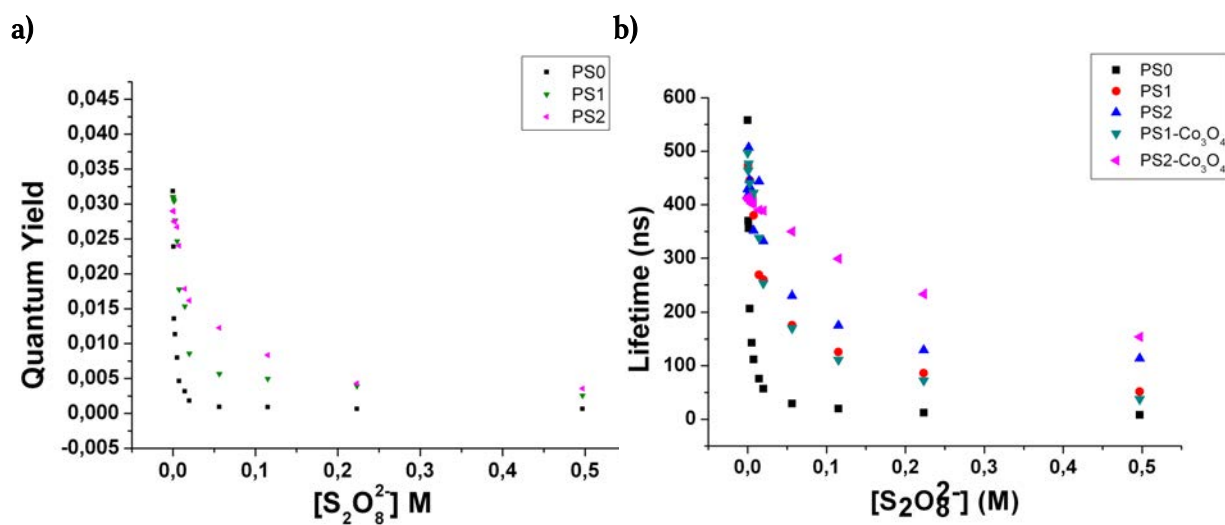
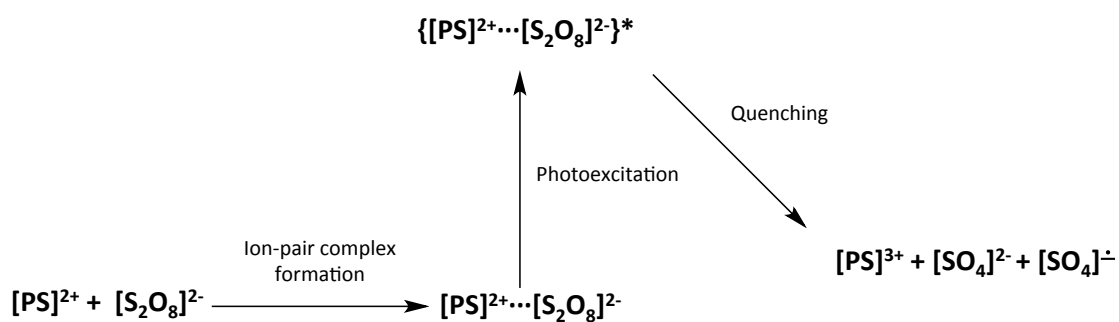
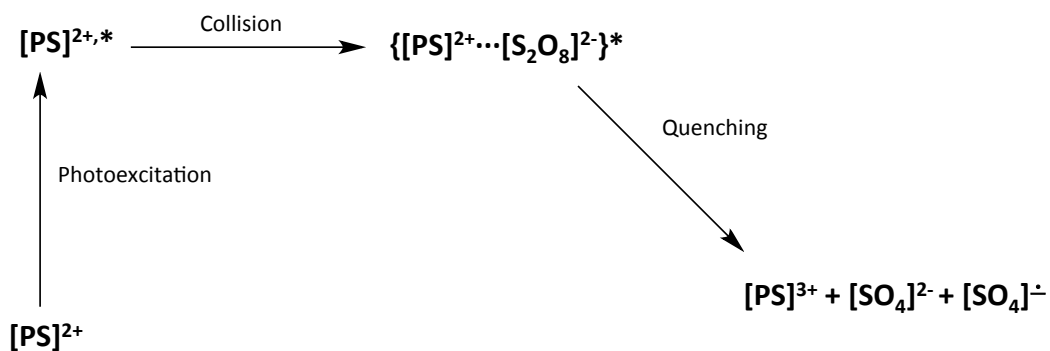


Figure S21. Quantum yield (a) and lifetime (b) of different PS or hybrid PS-Co₃O₄ NP systems as a function of [S₂O₈²⁻] at pH 5.60.

a) Unimolecular Pathway (Static Quenching)



b) Bimolecular Pathway (Dynamic Quenching)



Scheme S3. Schematic representation of static (a) and dynamic (b) quenching.

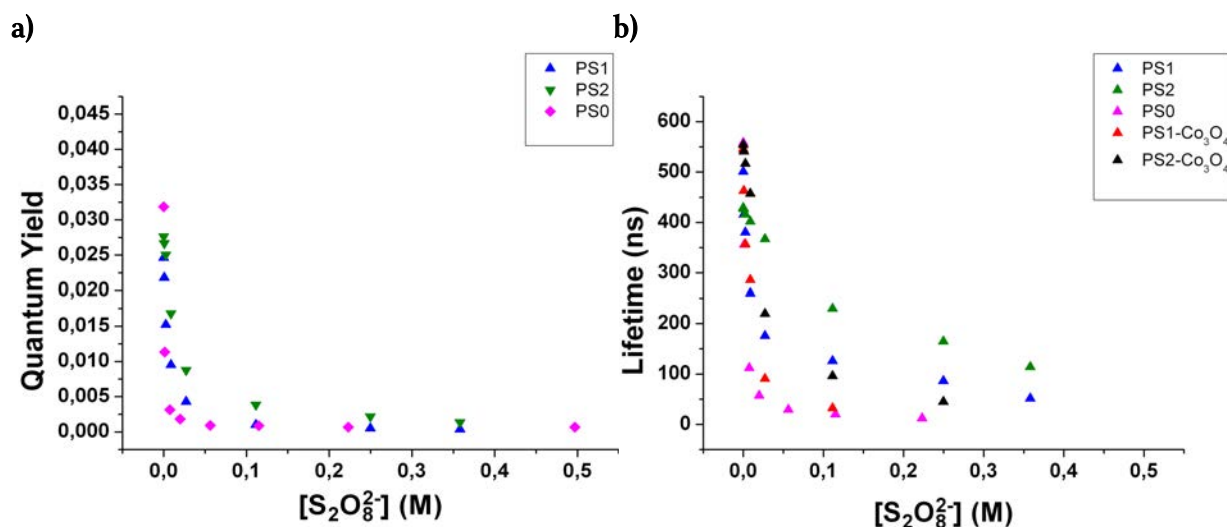


Figure S22. Quantum yield (a) and lifetime (b) of different PS or hybrid PS- Co_3O_4 NP systems as a function of $[\text{S}_2\text{O}_8^{2-}]$ at pH 8.4.

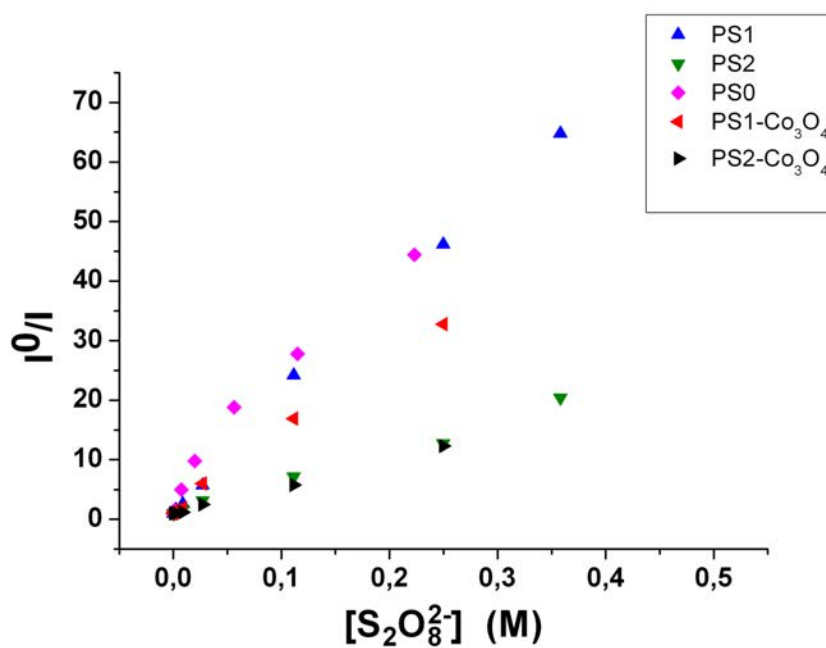


Figure S23. SV plots for all the PS and PS- Co_3O_4 NPs systems at pH 8.4. All solutions were purged with argon.

Table S1. Results of kinetic analysis of the {[PS]^{*}, S₂O₈²⁻} and {Co₃O₄-[PS]^{*}, S₂O₈²⁻} systems at pH 8.4. ^a Quantum yield in air-saturated buffer solution in the absence of quencher. ^b Quantum yield in argon-saturated buffer solution in the absence of quencher. ^c From lifetime measurements in the absence of S₂O₈²⁻ in an argon-saturated buffer solution. ^d Calculated from intercept of SV plots (τ^0/τ') and τ^0 . ^e Intercept of SV plots at variable [S₂O₈²⁻]. ^f From slope of SV plots at variable [S₂O₈²⁻]. ^g Computational best fit to equation 5 (see text) ^h Calculated from equation 9 (see text). ⁱ Calculated for 0.3 M S₂O₈²⁻. ^j Calculated for 0.019 M S₂O₈²⁻.

System	Φ_{O_2} , ^a	Φ_{Ar} , ^b	τ^0 , ^c ns	τ' , ^d ns	τ^0/τ' , ^e	k_q (k_q'), ^f M ⁻¹ s ⁻¹	K_{eq} , ^g mM ⁻¹	k_{ET} , ^h s ⁻¹	k_q [S ₂ O ₈ ²⁻] ⁱ , s ⁻¹	k_q [S ₂ O ₈ ²⁻] ^j , s ⁻¹
PS0 no buffer	0.028	0.042	550	108	5.09	$3.9 \cdot 10^8$	$6.93 \cdot 10^2$	$7.4 \cdot 10^6$	$1.17 \cdot 10^8$	$7.41 \cdot 10^6$
PS0	0.021	0.032	558	55	10.22	$4.39 \cdot 10^8$	$2.46 \cdot 10^2$	$1.65 \cdot 10^7$	$1.32 \cdot 10^8$	$8.34 \cdot 10^6$
PS1	0.019	0.025	540	-	-	$3.32 \cdot 10^8$	-	-	$9.96 \cdot 10^7$	$6.64 \cdot 10^6$
PS2	0.024	0.028	548	-	-	$9.43 \cdot 10^7$	-	-	$2.83 \cdot 10^7$	$1.89 \cdot 10^6$
PS1 -Co ₃ O ₄	0.020	0.026	546	-	-	$2.61 \cdot 10^8$	-	-	-	$5.23 \cdot 10^6$
PS2 -Co ₃ O ₄	0.025	0.029	554	-	-	$8.13 \cdot 10^7$	-	-	-	$1.63 \cdot 10^6$

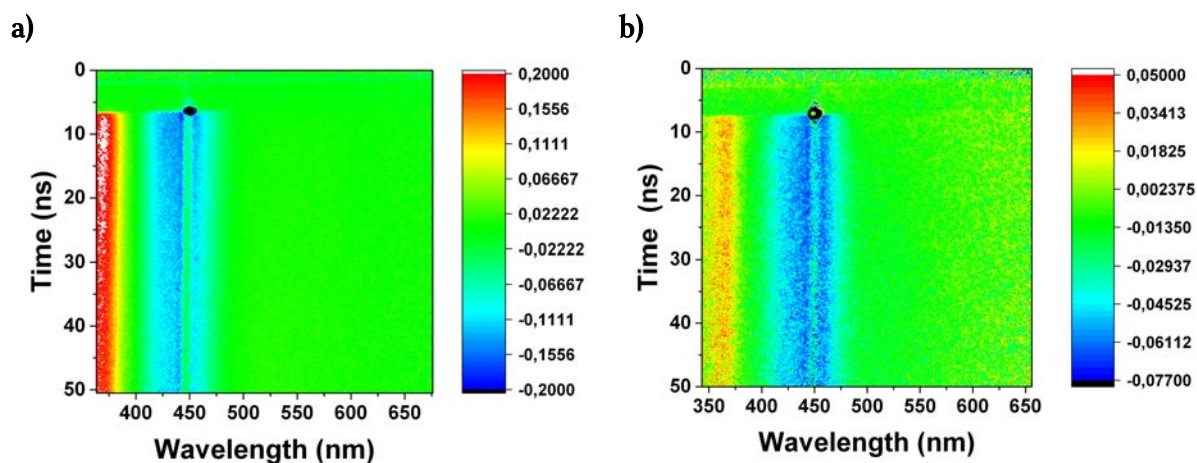


Figure S24. 2D transient spectra of free PS1 (a) and PS1- Co_3O_4 NP hybrid system (b).

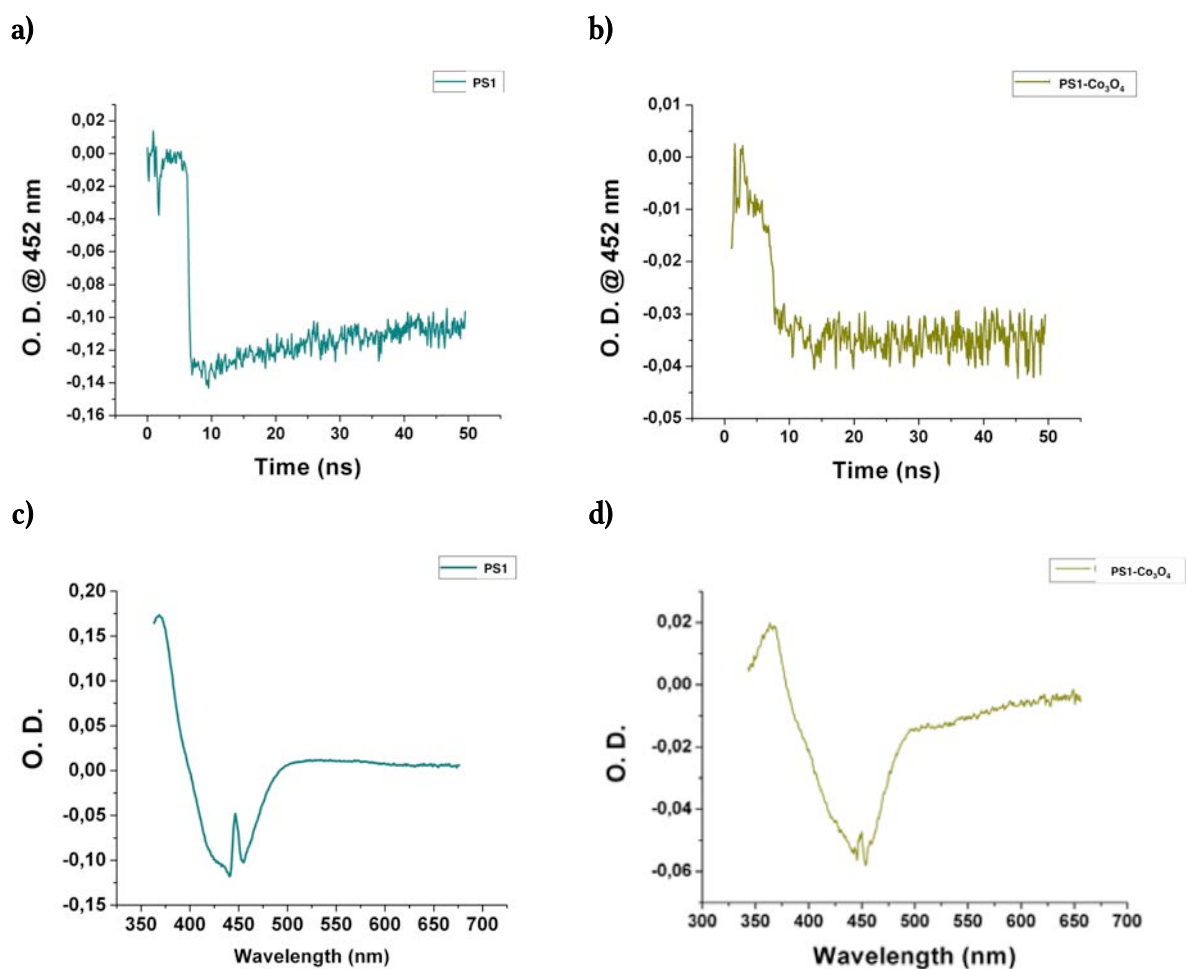


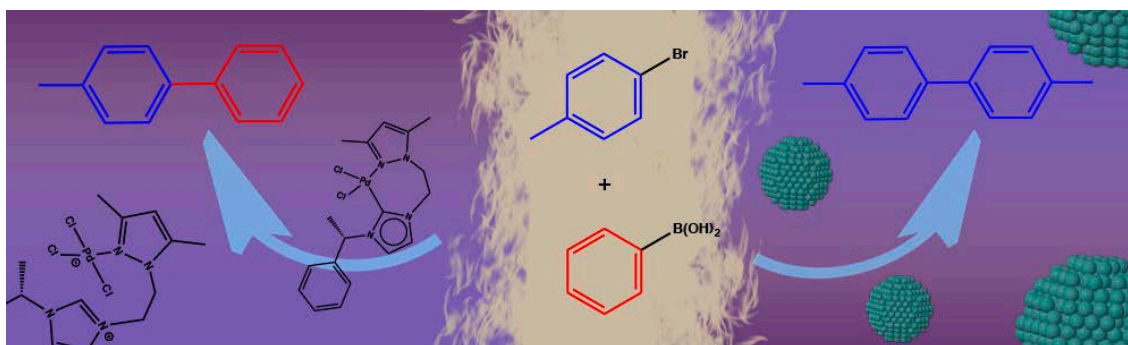
Figure S25. Disappearance of PS1 as a function of time according to the 452 nm signal for free PS1 (a) and PS1- Co_3O_4 NPs (b), and 1D transient spectra for free PS1 (c) and PS1- Co_3O_4 NPs (d) showing the disappearance of PS1 at 452 nm and the formation of a PS1* excited state at 360 nm.

3.7 References

- [1] Berardi, S.; Drouet, S.; Francàs, L.; Gimbert-Suriñach, C.; Guttentag, M.; Richmond, C.; Stoll, T.; Llobet, A. *Chem. Soc. Rev.* **2014**, *43*, 7501-7519.
- [2] Bofill, R.; García-Antón, J.; Escriche, L.; Sala, X.; Llobet, A. Water Oxidation, in: Reedijk, J.; Poeppelmeier, K. (Eds.), *Comprehensive Inorganic Chemistry, II*, Elsevier, **2013**, Vol 8, pp. 505-523.
- [3] Bofill, R.; García-Antón, J.; Escriche, L.; Sala, X. *J. Photochem. Photobiol. B: Biol.* **2015**, *152*, 71-81.
- [4] Lewis, N. S. *Science* **2016**, *351*, aad19201-aad19209.
- [5] Kärkäs, M. D.; Verho, O.; Johnston, E. V.; Akermark, B. *Chem. Rev.* **2014**, *114*, 11863-12001.
- [6] Limburg, B.; Bouwman, E.; Bonnet, S. *ACS Catal.* **2016**, *6*, 5273-5284.
- [7] Youngblood, W. J.; Lee, S.-H. A.; Kobayashi, Y.; Hernandez-Pagan, E. A.; Hoertz, P. G.; Moore, T. A.; Moore, A. L.; Gust, D.; Mallouk, T. E. *J. Am. Chem. Soc.* **2009**, *131*, 926-927.
- [8] Youngblood, J.; Lee, S. H.; Maeda, K.; Mallouk, T. E. *Acc. Chem. Res.* **2009**, *46*, 1966-1973.
- [9] Ashford, D. L.; Gish, M. K.; Vannucci, A. K.; Brennaman, M. K.; Templeton, J. L.; Papanikolas, J. M.; Meyer, T. J. *Chem. Rev.* **2015**, *115*, 13006-13049.
- [10] Kaveevivitchai, N.; Chitta, R.; Zong, R.; El Ojaimi, M.; Thummel, R. P. *J. Am. Chem. Soc.* **2012**, *134*, 10721-10724.
- [11] Li, H.; Li, F.; Zhang, B.; Zhou, X.; Yu, F.; Sun, L. *J. Am. Chem. Soc.* **2015**, *137*, 4332-4335.
- [12] Lopez, A. M.; Natali, M.; Pizzolato, E.; Chiorboli, C.; Bonchio, M.; Sartorel, A.; Scandola, F. *Phys. Chem. Chem. Phys.* **2014**, *16*, 12000-12007.
- [13] Karlsson, E. A.; Lee, B.-L.; Liao, R.-Z.; Akermark, T.; Kärkäs, M. D.; Becerril, V. S.; Siegbahn, P. E. M.; Zou, X.; Abrahamsson, M.; Akermark, B. *ChemPlusChem* **2014**, *79*, 936-950.
- [14] Hocking, R. K.; Brimblecombe, R.; Chang, L.-Y.; Singh, A.; Cheah, M. H.; Glover, C.; Casey, W. H.; Spiccia, L. *Nat. Chem.* **2011**, *3*, 461-466.
- [15] Kanan, M. W.; Nocera, D. G. *Science* **2008**, *321*, 1072-1075.
- [16] Wang, H.-Y.; Liu, J.; Zhu, J.; Styring, S.; Ott, S.; Thapper, A. *Phys. Chem. Chem. Phys.* **2014**, *16*, 3661-3669.
- [17] Garrido-Barrios, P.; Gimbert-Suriñach, C.; Matheu, R.; Sala, X.; Llobet, A. *Chem. Soc. Rev.* **2017**, *46*, 6088-6098.
- [18] Hoertz, P. G.; Kim, Y.-I.; Youngblood, W. J.; Mallouk, T. E. *J. Phys. Chem. B* **2007**, *111*, 6845-6856.
- [19] Amiens, C.; Chaudret, B.; Ciuculescu-Pradines, D.; Collière, V.; Fajerwerg, K.; Fau, P.; Kahn, M.; Maisonnat, A.; Philippot, K. *New J. Chem.* **2013**, *37*, 3374-3401.
- [20] Norris, M. R.; Concepcion, J. J.; Glasson, C. R. K.; Fang, Z.; Lapidés, A. M.; Ashford, D. L.; Templeton, J. L.; Meyer, T. J. *Inorg. Chem.* **2013**, *52*, 12492-12501.
- [21] Jansa, P.; Baszczyński, O.; Procházková, E.; Dračínský, M.; Janeba, Z. *Green Chem.* **2012**, *14*, 2282-2288.
- [22] Salavati-Niasari, M.; Khansari, A. *CR. Chimie* **2014**, *17*, 352-358.
- [23] Osuna, J.; de Caro, D.; Amiens, C.; Chaudret, B.; Snoeck, E.; Respaud, M.; Broto, J.-M.; Fert, A. *J. Phys. Chem.* **1996**, *100*, 14571-14574.
- [24] Verelst, M.; Ely, T. O.; Amiens, C.; Snoeck, E.; Lecante, P.; Mosset, A.; Respaud, M.; Broto, J.-M.; Chaudret, B. *Chem. Mat.* **1999**, *11*, 2702-2708.
- [25] Amiens, C. *Faraday Discuss.* **2004**, *125*, 293-309.
- [26] Pelzer, K.; Philippot, K.; Chaudret, B. *Z. Phys. Chem.* **2003**, *217*, 1539-1547.
- [27] Biesinger, M. C.; Payne, B. P.; Grosvenor, A. P.; Lau, L. W. M.; Gerson, A. R.; Smart, R. St. C. *Appl. Surf. Sci.* **2011**, *257*, 2717-2730.
- [28] Yang, J.; Lu, H.; Martens, W. N.; Frost, R. L. *J. Phys. Chem. C* **2010**, *114*, 111-119.
- [29] Jiang, J.; Li, L. *Materials Letters* **2007**, *61*, 4894-4896.
- [30] Paniagua, S. A.; Giordano, A. J.; O'Neil; Smith, L.; Barlow, S.; Li, H.; Armstrong, N. R.; Pemberton, J. E.; Brédas, J.-L.; Mardern, S. R. *Chem. Rev.* **2016**, *16*, 7117-7158.
- [31] Guerrero, G.; Mutin, P. H.; Vioux, A. *Chem. Mater.* **2001**, *13*, 4367-4373.
- [32] Guerrero, G.; Alauzun, J. G.; Granier, M.; Laurencin, D.; Mutin, P. H. *Dalton Trans.* **2013**, *42*, 12569-12585.
- [33] McCrory, C. C. L.; Jung, S.; Ferrer, I. M.; Chatman, S. M.; Peters, J. C.; Jaramillo, T. F. *J. Am. Chem. Soc.* **2015**, *137*, 4347-4357.

- [34] McCrory, C. C. L.; Jung, S.; Peters, J. C.; Jaramillo, T. F. *J. Am. Chem. Soc.* **2013**, *135*, 16977-16987.
- [35] Jung, S.; McCrory, C. C. L.; Ferrer, I. M.; Peters, J. C.; Jaramillo, T. F.; *J. Mater. Chem. A* **2016**, *4*, 3068-3076.
- [36] Prater, K. B.; Bard, A. J. *J. Electrochem. Soc.* **1970**, *117*, 207-213.
- [37] Bard, A. J.; Faulkner, L. R. (Eds.), *Electrochemical Methods: Fundamentals and Applications, 2nd ed.*, John Wiley & Sons, Inc.: Hoboken, NJ, **2001**, pp. 353-354.
- [38] Trasatti, S.; Petrii, O. A. *Pure Appl. Chem.* **1991**, *63*, 711-734.
- [39] Benck, J. D.; Chen, Z.; Kuritzky, L. Y.; Forman, A. J.; Jaramillo, T. F. *ACS Catal.* **2012**, *2*, 1916-1923.
- [40] Zhao, Y.; Chen, S.; Sun, B.; Su, D.; Huang, X.; Liu, H.; Yan, Y.; Sun, K.; Wang, G. *Sci. Rep.* **2015**, *5*, 7629.
- [41] Liang, Y.; Li, Y.; Wang, H.; Zhou, J.; Wang, J.; Regier, T.; Dai, H. *Nat. Mater.* **2011**, *10*, 780-786.
- [42] Wu, J.; Xue, Y.; Yan, X.; Yan, W.; Cheng, Q.; Xie, Y. *Nano Res.* **2012**, *5*, 521-530.
- [43] Walter, M. G.; Warren, E. L.; McKone, J. R.; Boettcher, S. W.; Mi, Q.; Santori, E. A.; Lewis, N. S. *Chem. Rev.* **2010**, *110*, 6446-6473.
- [44] Weber, M. F.; Dignam, M. J. *J. Electrochem. Soc.* **1984**, *131*, 1258-1265.
- [45] Gorlin, Y.; Jaramillo, T. F. *J. Am. Chem. Soc.* **2010**, *132*, 13612-13614.
- [46] Chou, N. H.; Ross, P. N.; Bell, A. T.; Tilley, T. D. *ChemSusChem* **2011**, *4*, 1566-1569.
- [47] Singh, S. K.; Dhavale, V. M.; Kurungot, S. *ACS Appl. Mater. Interfaces* **2015**, *7*, 442-451.
- [48] Gasteiger, H. A.; Kocha, S. S.; Sompalli, B.; Wagner, F. T. *Appl. Catal. B* **2005**, *56*, 9-35.
- [49] Suntivich, J.; May, K. J.; Gasteiger, H. A.; Goodenough, J. B.; Shao-Horn, Y. *Science* **2011**, *334*, 1383-1385.
- [50] Wee, K.-R.; Brennaman, M. K.; Alibabaei, L.; Farnum, B. H.; Sherman, B.; Lapidus, A. M.; Meyer, T. J. *J. Am. Chem. Soc.* **2014**, *136*, 13514-13517.
- [51] Zhang, M.; de Respinis, M.; Frei, H. *Nat. Chem.* **2014**, *6*, 362-367.
- [52] Chen, H.-C.; Hettler, D. G. H.; Williams, R. M.; van der Vlugt, J. I.; Reek, J. N. H.; Brouwer, A. M. *Energy Environ. Sci.* **2015**, *8*, 975-982.
- [53] Comte, P.; Nazeeruddin, M. K.; Rotzinger, F. P.; Frank, A. J.; Grätzel, M. *J. Mol. Catal.* **1989**, *52*, 63-84.
- [54] Ghosh, P. K.; Brunschwig, B. S.; Chou, M.; Creutz, C.; Sutin, N. *J. Am. Chem. Soc.* **1984**, *106*, 4772-4783.
- [55] Lewandowska-Andralojc, A.; Polyansky, D. E.; Zong, R.; Thummel, R. P.; Fujita, E. *Phys. Chem. Chem. Phys.* **2013**, *15*, 14058-14068.
- [56] Baptista, M. S.; Cadet, J.; Mascio, P. D.; Ghogare, A. A.; Greer, A.; Hamblin, M. R.; Lorente, C.; Nunez, S. C.; Ribeiro, M. S.; Thomas, A. H.; Vignoni, M.; Yoshimura, T. M. *Photochem. Photobiol.* **2017**, *93*, 912-919.
- [57] Francàs, L.; Richmond, C.; Garrido-Barros, P.; Planas, N.; Roeser, S.; Benet-Buchholz, J.; Escriche, L.; Sala, X.; Llobet, A. *Chem. Eur. J.* **2016**, *22*, 5261-5268.
- [58] De Angelis, F.; Pastore, M. *J. Am. Chem. Soc.* **2015**, *137*, 5798-5809.
- [59] Lakowicz, J. R. *Principles of fluorescence spectroscopy*, **2006**, Springer Science, New York.
- [60] Turro, N. J.; Scaiano, J. C.; Ramamurthy, V. *Principles of molecular photochemistry: an introduction*, **2009**, University Science Books, Sausalito.
- [61] Wilke, B. M.; Castellano, F. N. *J. Chem. Ed.* **2013**, *90*, 786-789.
- [62] Timpson, C. J.; Carter, C. C.; Olmsted III, J. *J. Phys. Chem.* **1989**, *93*, 4116-4120.
- [63] Wilkinson, F.; Helman, W. R.; Ross, A. B. *J. Phys. Chem. Ref. Data* **1993**, *22*, 113-150.
- [64] Stern, O.; Volmer, M. *Phys. Zetischr.* **1919**, *20*, 183-188.
- [65] Kaledin, A. L.; Huang, Z.; Geletii, Y. V.; Lian, T.; Hill, C. L.; Musaev, D. G. *J. Phys. Chem. A* **2010**, *114*, 73-80.
- [66] White, H. S.; Becker, W. G.; Bard, A. J. *J. Phys. Chem.* **1984**, *88*, 1840-1846.
- [67] Rehm, D.; Weller, A. *Bunsenges Ber. Phys. Chem.* **1969**, *73*, 834-839.
- [68] Rehm, D.; Weller, A. *Isr. J. Chem.* **1970**, *8*, 259-271.
- [69] Bolletta, F.; Maestri, M.; Moggi, L. *J. Phys. Chem.* **1973**, *77*, 861-862.
- [70] Bard, A. J.; Fox, M. A. *Acc. Chem. Res.* **1995**, *28*, 141-145.

Chapter IV. Dissimilar Catalytic Behavior of Molecular or Colloidal Palladium Systems with a New NHC Ligand



IV

Both molecular and colloidal Pd systems based both on an ionic liquid or its N-heterocyclic carbene (NHC) are tested in C-C coupling processes. The conversion, yield and the different reactivity are discussed for the set of four systems.

This chapter consists in the following paper:

Gómez-Villarraga, F.; **De Tovar, J.**; Guerrero, M.; Nolis, P.; Parella, T.; Lecante, P.; Romero, N.; Escriche, L.; Bofill, R.; Ros, J.; Sala, X.; Philippot, K.; García-Antón, J. *Dalton Trans.* **2017**, *46*, 11768-11778.

Table of Contents

4.1 Abstract	161
4.2 Introduction	162
4.3 Experimental Section	164
4.3.1 Syntheses of ligands and both catalytic molecular and nanoparticles systems	164
4.3.2 Catalytic Experiments	164
4.3.2 Suzuki-Miyaura Reactions	164
4.4 Results and Discussion	165
4.4.1 Presentation of the catalytic systems	165
4.4.2 Catalytic Experiments with Pd molecular or colloidal systems	169
4.5 Conclusions	181
4.6 References	183

4.1 Abstract

New palladium complexes and nanoparticles stabilized by 1-[2-(3,5-dimethylpyrazol-1-yl)ethyl]-3-((S)-1-phenylethyl)-3*H*-imidazol-2-ylidene (**L**) N-heterocyclic carbene (NHC) (**C1** and **N1**, respectively) or 1-[2-(3,5-dimethylpyrazol-1-yl)ethyl]-3-((S)-1-phenylethyl)-3*H*-imidazol-1-ium chloride (**HL·Cl**) ligands (**C2** and **N2**, respectively) have been tested in the Suzuki-Miyaura coupling. Three different reactions have been observed depending on the catalytic system: i) the Suzuki-Miyaura reaction takes place with Pd molecular complexes; ii) a secondary reaction, the dehalogenation of the substrate, is always detected and iii) the C-C homocoupling between two molecules of bromoarenes is observed with colloidal catalysts.

4.2 Introduction

During the last few years the rapid development in cross-coupling reactions of unactivated substrates mediated by metal complexes has prompted the design of a huge family of achiral and chiral phosphine ligands.[1] As alternative ligands to phosphines for transition metals, N-heterocyclic carbenes (NHCs) have become paramount ligands in catalysis and beyond.[2] This can be explained not only by their remarkably strong σ -binding and steric tunability,[3] but also because they are able to stabilize highly unusual and hitherto elusive reactive species such as metal nanoparticles (MNPs) thanks to their stability under oxidative conditions once coordinated.[4] Thus, NHCs have become ligands of paramount importance in nanochemistry given their advantageous behavior for the stabilization and functionalization of MNPs.[5] Although different families of NHCs have been largely explored in various important organic transformations when combined with metal pre-catalysts, those bearing imidazolium salts as core structures are the most frequently employed given their straightforward syntheses and feasible tuning properties.[6]

Different methodologies can be followed to obtain and stabilize NPs in different media while controlling their size, shape and composition, which, in turn, can tune their unique properties.[7] The use of coordinating ligands is of particular interest to prepare MNPs because it gives the possibility to modulate their surface properties as known for the synthesis of molecular complexes.[8] As a consequence, ligand-stabilized MNPs became very attractive for applications in catalysis.[9] MNPs not only are able to catalyze reactions also catalyzed by molecular complexes (i.e. C-C coupling or hydrogenation of olefins) but also reactions that cannot be catalyzed by these species (such as the hydrogenation of arenes).

Furthermore, palladium is the most versatile transition metal in chemical catalysis reactions since many of these processes cannot be catalyzed by other transition metals.[10] Thus, Pd(0) NPs have shown large catalytic efficiency in C-C coupling reactions specially when non-aggregated homogeneous NPs of 1-4 nm size are used as catalysts.[11]

The Suzuki-Miyaura reaction is one of the most important cross-coupling processes from an industrial point of view.[12] It allows to easily obtain biaryl products, important intermediates in the organic syntheses of various target products ranging from performance

materials to pharmaceuticals.[13] Although noble metal complexes are usually employed as catalysts for this reaction, MNPs merit also to be studied since playing with stabilizing ligands may tune their catalytic performance.[14] Therefore, comparing the catalytic behavior of both Pd complexes and Pd NPs bearing the same ligands can provide useful information to discriminate the potential in catalysis of both species and find the most appropriate catalytic system depending on the target application.

A recent work of García-Antón, Philippot and co-workers has focused on discerning the catalytic behavior of colloidal and molecular palladium systems in C-C coupling reactions. For example, it has been found that Pd molecular/colloidal systems containing new hybrid pyrazole-derived ligands with alkylether, alkylthioether or alkylamino moieties lead to different catalytic output depending on the system.[15]

In this chapter, Pd systems based on a new NHC-pyrazole hybrid ligand are presented. Interestingly, as it will be described hereafter, different behaviors were observed in C-C coupling catalysis that illustrates the possibility to optimize the catalytic system according to the final aim.

4.3 Experimental Section

4.3.1 Syntheses of ligands and both catalytic molecular and nanoparticles systems

The ligands, catalytic palladium complexes and palladium nanoparticles were prepared following the procedures described in reference 16 as well as in the research thesis of Dr. Fernando Gómez Villarraga.[17]

4.3.2 Catalytic Experiments

The quantification of the catalytic reactions was carried out in a HP5890 Hewlett Packard gas chromatograph equipped with a FID detector and a HP-5 column (5% diphenylpolysiloxane and 95% dimethylpolysiloxane). The products obtained in the catalytic reactions were identified using a G1800A Hewlett Packard gas chromatograph with an electron impact ionization detector and a HP-5 column (5% diphenylpolysiloxane and 95% dimethylpolysiloxane). The mass spectra of the catalytic products are in agreement with those published in the literature.[18,19]

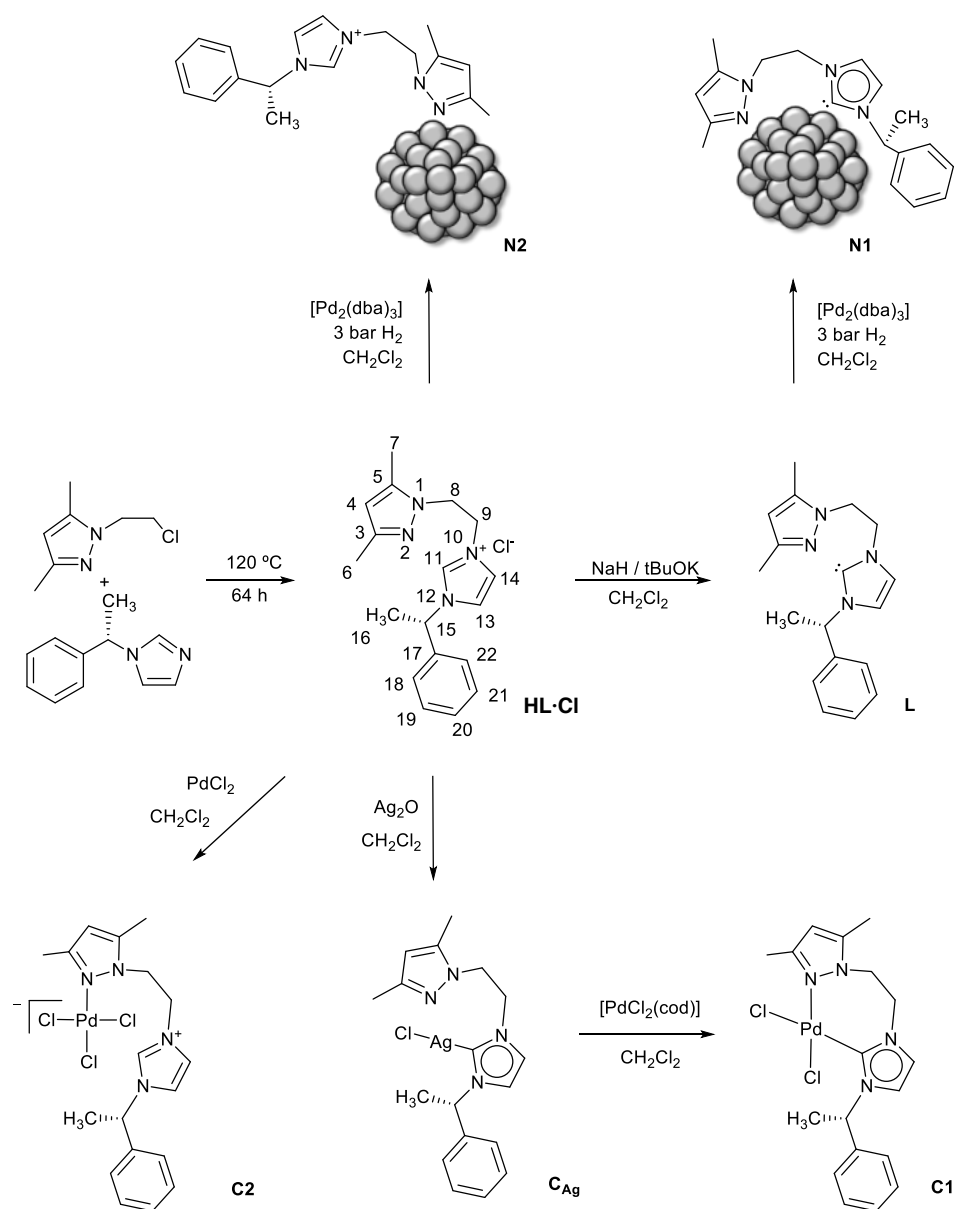
4.3.2 Suzuki-Miyaura Reactions

In a two-neck round-bottom flask fitted with a reflux condenser and a septum, 4-halogenotoluene (2.5 mmol), phenylboronic acid (3.125 mmol), ^tBuOK (5.0 mmol), and naphthalene (0.5 mmol) as internal standard were dissolved in DMF/H₂O (10 mL, 4/1). Next, the palladium organometallic complex (1.10⁻³ mmol) or palladium nanoparticles (1.10⁻³ mmol Pd atoms) were added. The solution was vigorously stirred and heated at 100° C for 6 h under nitrogen. Then, the reaction crude was cooled to room temperature and the products were extracted with a mixture of diethyl ether/brine (20 mL, 1/1). The organic phase was analyzed by GC and GC-MS.

4.4 Results and Discussion

4.4.1 Presentation of the catalytic systems

Following with the research of Dr. Fernando Gómez Villarraga,[17] two type of palladium complexes (**C1** and **C2**) and two type of palladium nanoparticles (**N1** and **N2**) have been prepared as shown in Scheme 1.

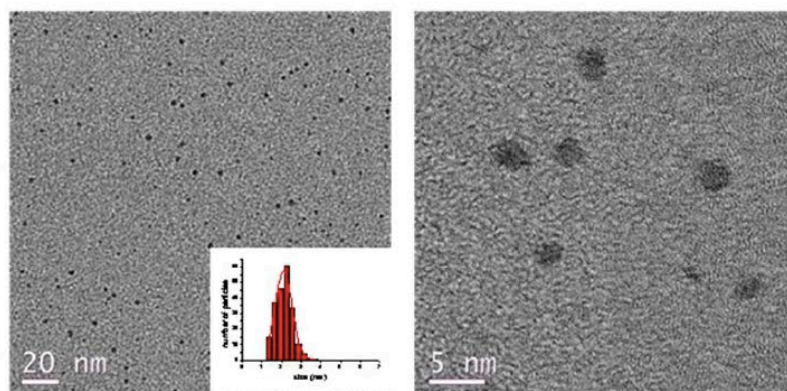


Scheme 1. Synthetic procedure for the preparation of the different catalytic systems used in this work.

For the synthesis of **HL·Cl**, 1-(2-chloroethyl)-3,5-dimethyl-1*H*-pyrazole and 1-(*S*)-(phenylethyl)imidazole were heated solventless at 120 °C for 64 h. The deprotonation of **HL·Cl** to yield 1-[2-(3,5-dimethylpyrazol-1-yl)ethyl]-3-((*S*)-1-phenylethyl)-3*H*-imidazol-2-ylidene (**L**) was achieved by reacting **HL·Cl** with NaH and a catalytic amount of ^tBuOK in anhydrous dichloromethane.

On the one hand, the imidazolium salt **HL·Cl** and its deprotonated NHC **L** ligands have been used to prepare nanoparticles **N2** and **N1**, respectively, according to the organometallic approach, in mild reaction conditions. From here, **N1** resulted in spherical particles presenting a mean size of 2.1(0.9) nm (Figure 1a). With the same methodology, **N2** nanoparticles resulted in an aggregated NPs mixture of isolated NPs of 3.2(0.9) nm mean size and superstructures (Figure 1b). From these results and given the main difference of two ligands (where **L** is a carbene while **HL·Cl** is not deprotonated), it is believed that the stabilization of the Pd NPs takes place by the coordination of **L** through the carbene (M-C) and pyrazolic (M-N) groups to the surface of the Pd NPs whereas **HL·Cl** would only coordinate through the pyrazolic group (scheme 1). Additionally, the presence of the ligands **L** or **HL·Cl** in **N1** or **N2**, respectively, has been demonstrated by IR spectroscopy, ICP-OES and elemental analyses.

a)



b)

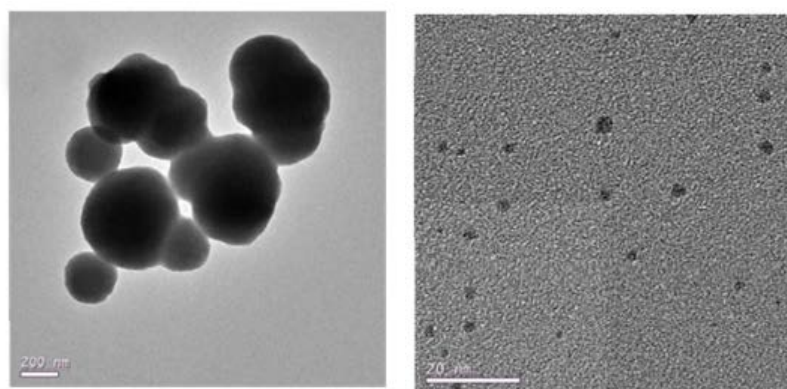


Figure 1. HRTEM micrographs and corresponding size-histograms of Pd nanoparticles stabilized with (a) L and (b) HL·Cl, both in a [L]/[Pd] = 0.5 ratio.[16]

On the other hand, complex **C1** has been prepared through a silver carbene transmetallation. Thus, a silver complex C_{Ag} is synthesized by reacting silver dioxide and HL·Cl in anhydrous dichloromethane where the proton of the imidazolium salt is no longer present, thus confirming the deprotonation of the imidazolium group and formation of the Ag-NHC bond. Further, C_{Ag} is reacted with $[PdCl_2(cod)]$ in anhydrous dichloromethane to obtain the carbenic **C1** Pd complex (Figure 2). Also, the direct reaction of HL·Cl with $PdCl_2$ in acetonitrile yielded the complex **C2** where the existence of the protonated ligand HL^+ is confirmed by 1H NMR spectroscopy.

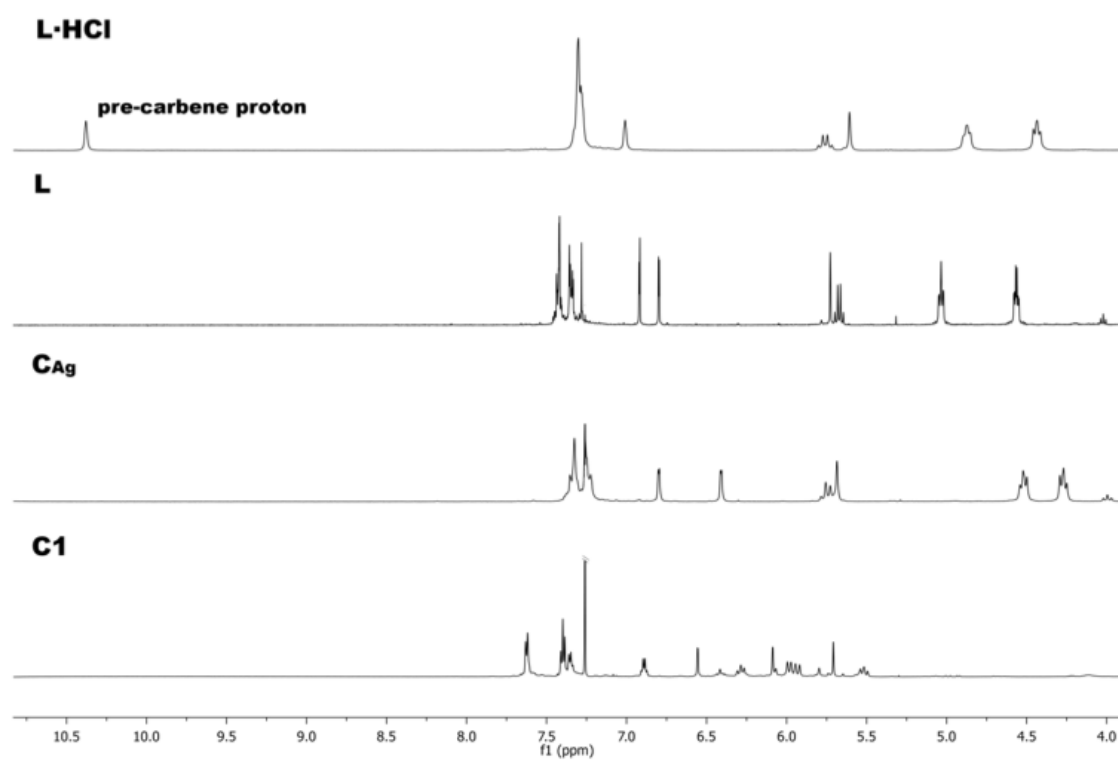
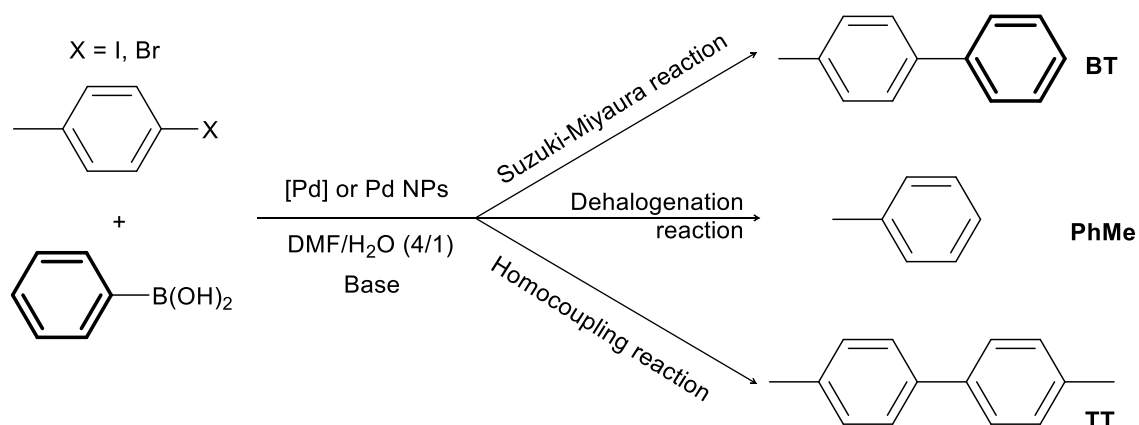


Figure 2. ¹H NMR of **HL·Cl** and **C_{Ag}** registered at 360 MHz (CDCl₃, 298K) and **C1** registered at 600 MHz (CDCl₃, 298K).[16]

Even if the synthesis of the **L**, **HL·Cl**, **C1**, **C2**, **N1** and **N2** were previously synthesized by Dr. Fernando Gómez Villarraga, these compounds have been synthesized again in this work, in order to perform all the catalytic experiments.

4.4.2 Catalytic Experiments with Pd molecular or colloidal systems

Pd complexes **C1** and **C2** (with **L** and **HL·Cl** ligands, respectively) as well as Pd nanoparticles **N1** and **N2** (with **L** and **HL·Cl** at [ligand]/[Pd]=0.5, respectively) have been evaluated as catalysts for the Suzuki-Miyaura reaction (Scheme 2, Table 1).[20,21]



Scheme 2. Suzuki-Miyaura, homocoupling and dehalogenation reactions performed in the presence of Pd complexes **C1** and **C2** and Pd NPs **N1** and **N2**.

Table 1. Suzuki-Miyaura reactions with palladium catalysts.^a

Entry	Catalyst	X	[PhB(OH) ₂]/[Pd]	Conv. ^b (%)	BT ^c (%)	TT ^c (%)	PhMe ^c (%)	Yield BT (%)	Yield TT (%)
1	C1	I	3125	100	51	0	49	51	0
2	C2	I	3125	82	41	0	59	34	0
3	C1	Br	3125	28	71	0	29	20	0
4	C2	Br	3125	46	93	0	7	43	0
5	N1	I	3125	100	81	0	19	81	0
6	N2	I	3125	100	47	0	53	47	0
7	N1	I	0	100	0	0	100	0	0
8	N2	I	0	56	0	0	56	0	0
9	N1	Br	3125	66	5	51	44	3	34
10	N2	Br	3125	36	7	37	56	3	13
11	N1	Br	0	72	0	83	17	0	60
12	N2	Br	0	36	0	72	28	0	26

^a Reaction conditions: $1 \cdot 10^{-3}$ mmol of Pd, 2.5 mmol of 4-halogenotoluene, 5.0 mmol ^tBuOK and 0.5 mmol naphthalene as internal standard in 8.0 mL of DMF and 2.0 mL of H₂O. Temperature 100° C.

^b Conversion after 6 h reaction.

^c Chemoselectivity in 4-methylbiphenyl (BT), 4,4'-dimethylbiphenyl (TT) and toluene (PhMe), respectively.

4-halogenotoluene derivatives (4-chlorotoluene, 4-bromotoluene or 4-iodotoluene) and an excess of phenylboronic acid were chosen as substrates to easily distinguish between cross-coupling and homocoupling products. Under the catalytic reaction conditions applied (Scheme 2)[20], two different by-products can be formed besides the expected cross-coupled product (4-methylbiphenyl; BT) as follows: i) toluene (PhMe) arising from the dehalogenation of the substrates and ii) 4,4'-dimethylbiphenyl (TT), resulting from the 4-bromotoluene homocoupling.

Once optimized,[15] 4-halogenotoluene (substrate/Pd = 2500), phenylboronic acid ($\text{PhB(OH)}_2/\text{Pd} = 3125$ or 0), $^t\text{BuOK}$ (base/Pd = 5000) were employed in a DMF/water mixture (4/1) as solvent.

The dehalogenation of the employed halogenotoluene derivatives is a collateral reaction that takes place in the Suzuki-Miyaura coupling.[22] As shown in Figure 3, when a primary or secondary alcohol is used as solvent in the presence of a base a Pd(II) alkoxide is formed, followed by β -elimination to a Pd(II) hydride and formation of the dehalogenated product after a final step of reductive elimination.

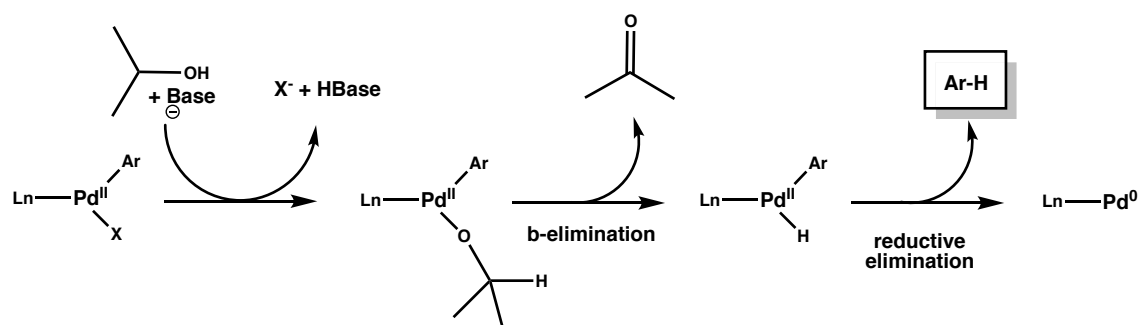


Figure 3. Dehalogenation mechanism for secondary alcohols as solvent.[22]

In this work DMF is used as solvent but its role as hydrogen source has also been reported,[23] as shown in Figure 4.

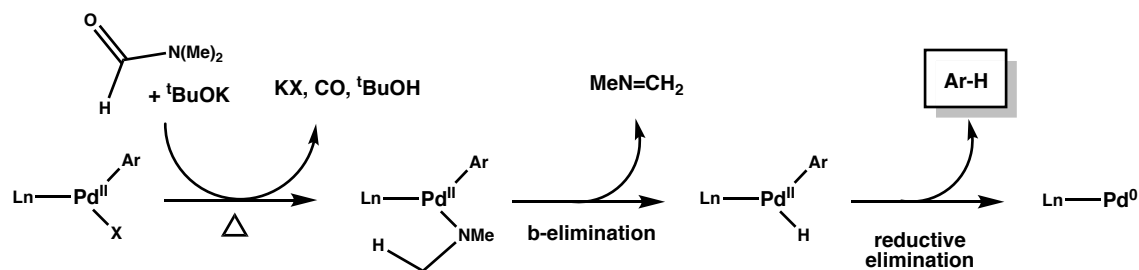


Figure 4. Proposed dehalogenation mechanism for DMF as solvent.[23]

The partial decomposition of DMF in basic media and at high temperature releases carbon monoxide and Pd(II) dimethylamine. Then, the latter intermediate can be transformed into a Pd(II) hydride that finally releases the dehalogenated product through reductive elimination. Proposed catalytic cycles for the Suzuki-Miyaura coupling and the dehalogenation reaction are shown in Figure 5.[22,23,24]

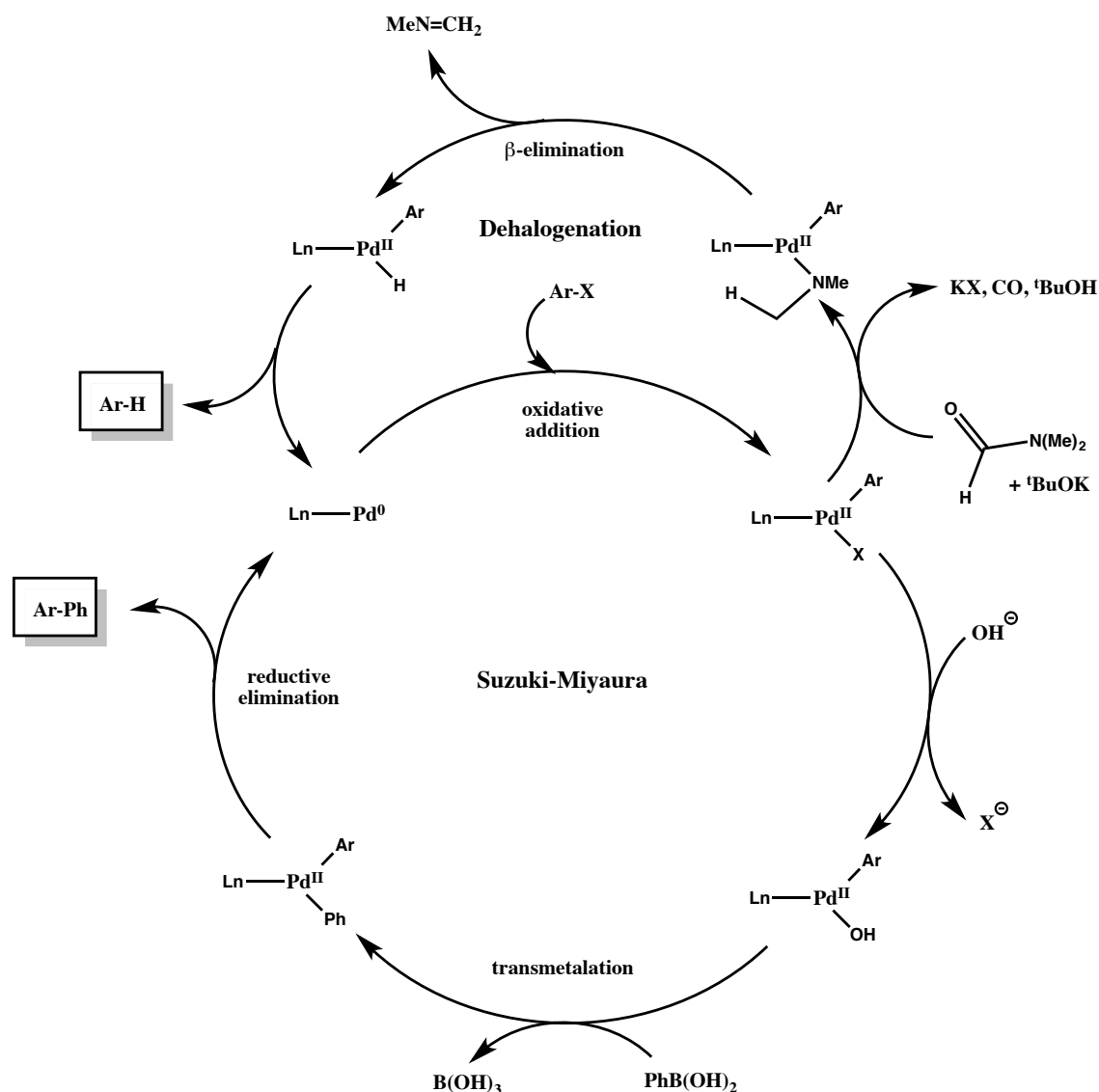


Figure 5. Proposed catalytic cycles for the Suzuki-Miyaura coupling and the dehalogenation reaction.[22,23,24]

As a general trend for the molecular/colloidal catalytic systems here studied, higher conversions were obtained with 4-iodotoluene compared to 4-bromotoluene (Table 1), as expected from the respective C(Ph)-X bond energies (X=Br, 84 kcal/mol; X=I, 67 kcal/mol).[25] Unfortunately 4-chlorotoluene could not be activated probably due to the higher C(Ph)-Cl bond energy value (97.1 kcal/mol)[25] and the Suzuki-Miyaura coupling reaction was unsuccessful.

Interestingly, in the presence of the molecular catalysts C1 and C2, besides the Suzuki-Miyaura expected product (BT), toluene was the only side product observed in a

significant amount using both 4-bromotoluene and 4-iodotoluene as substrates (Table 1, entries 1-4). Homocoupling reaction does not take place, as otherwise predictable according to the literature on Pd molecular complexes.[20] Also, 4-bromotoluene yields BT as the major product, while the amount of the dehalogenation product (toluene) significantly rises when 4-iodotoluene is used.

Recently, V. P. Ananikov *et al.* have demonstrated the formation of Pd NPs when molecular Pd complexes with NHC ligands are used in the Mizoroki-Heck reaction.[26] In our case, even if it is not a definitive proof, TEM control analyses of the solutions after catalysis with C1 or C2 did not show the presence of Pd nanoparticles. In any case, Hg poisoning tests carried out to these systems (*vide infra*) confirm the molecular nature of the real catalyst when C1 or C2 are used.

When 4-iodotoluene was used as substrate with nanocatalysts N1 and N2, complete conversions were achieved in 6 h in both cases. In the case of N1, formation of the cross-coupling product (4-methylbiphenyl; BT) was mainly observed together with a small amount of toluene (Table 1, entry 5). Formation of toluene rises to 53% in the case of N2 (Table 1, entry 6). On the contrary, N1 and N2 behave similarly against 4-bromotoluene, with the formation of 4,4'-dimethylbiphenyl (TT), arising from the homocoupling reaction, together with toluene and small amounts of BT (Table 1, entries 9 and 10). Furthermore, for the two halogenotoluene substrates, both conversion and chemoselectivities are higher for the Pd NP/L system (N1) than for the Pd NP/HL·Cl system (N2). These differences can be explained by the binding of the carbene group at the Pd NP surface in the case of N1 compared to N2. Indeed, the different coordination mode (by C and N in N1 and only by N in N2) may tune both electronic and steric properties at the surface and consequently the catalytic behavior of N1.

In the last years, different authors have investigated the homocoupling of two halogenotoluene substrates catalyzed by Pd as an alternative to Ullmann reaction, which requires stoichiometric quantities of copper under harsh reaction conditions (Figure 6).[27]

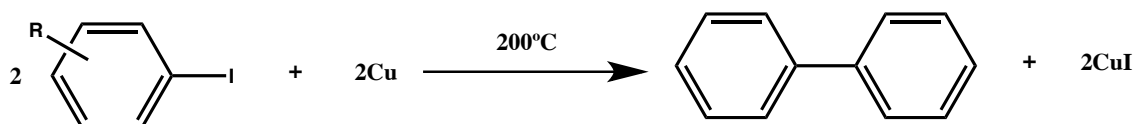


Figure 6. Ullmann reaction

Consequently, palladium complexes[28] and nanoparticles[29] have been tested for this reaction. Nevertheless, these catalysts typically present poor conversions due to their low stability.

Additionally, this homocoupling reaction requires a reducing agent. As explained above, DMF can act as a hydride source[23]. Thus, this solvent can potentially act as a source of electrons for the reduction of Pd(II) to Pd(0) in the homocoupling reaction through a reductive elimination of HX mediated by a base. For this mechanism to take place, a multisite catalyst is required (e.g. the surface of a nanoparticle) in order to avoid the formation of Pd(IV) species arising from two consecutive oxidative additions of ArX on a single Pd(0) site. In a multiple site catalyst, the oxidative addition of ArX onto two vicinal Pd(0) sites (yielding two Pd(I) species) can take place. Consequently, the formation of a hydride onto the surface of a nanoparticle followed by a reductive elimination of HX and a biaryl could be feasible and the Pd(0) sites would be regenerated (Figure 7).

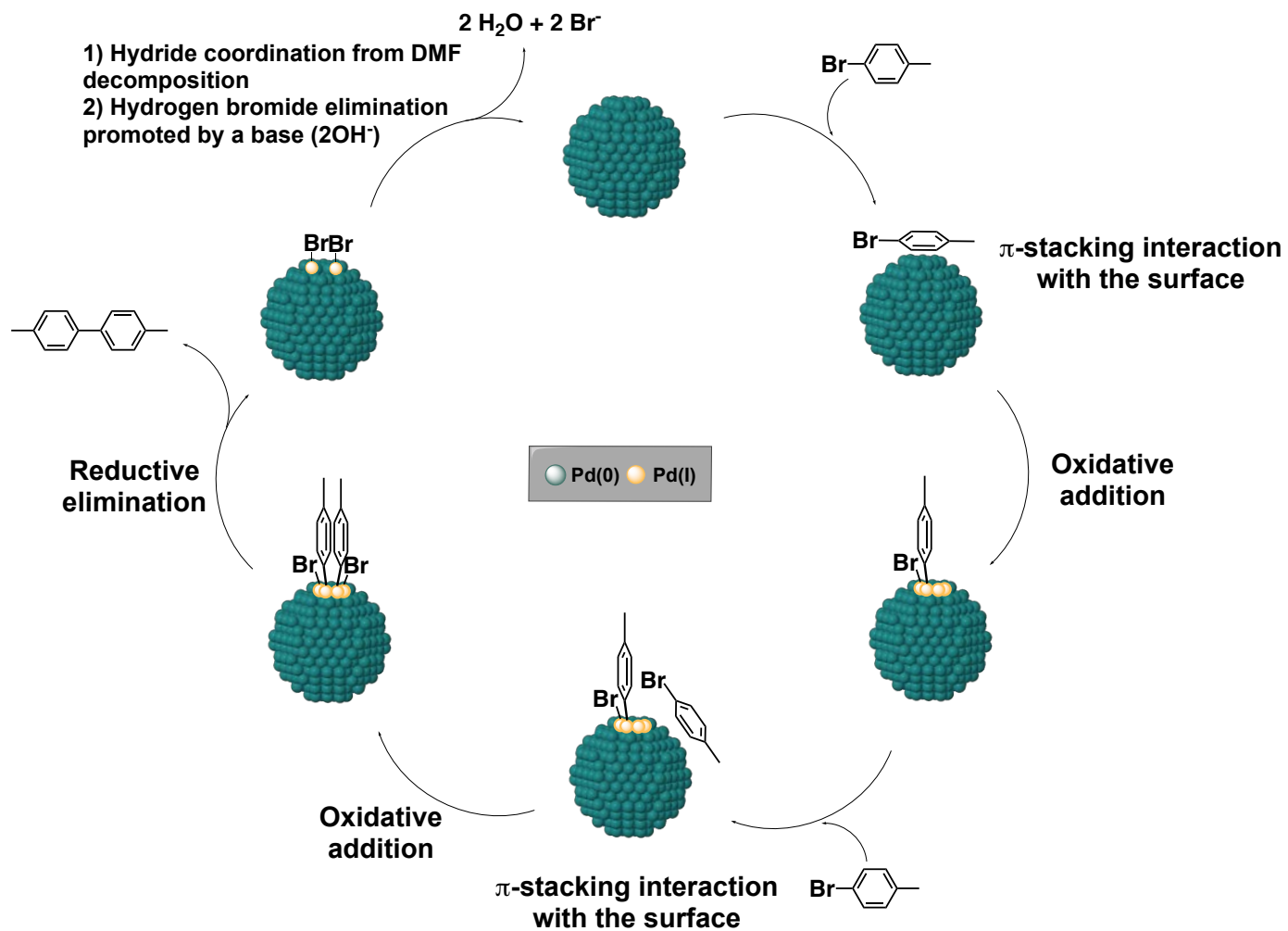


Figure 7. Proposed mechanism for the homocoupling of 4-bromotoluene onto the surface of Pd nanoparticles.

Additionally, the dehalogenation reaction could take place as shown in Figure 8, where a hydride coming from the decomposition of the DMF and present onto the surface of the nanoparticles is able to release the dehalogenated product through a reductive elimination step.

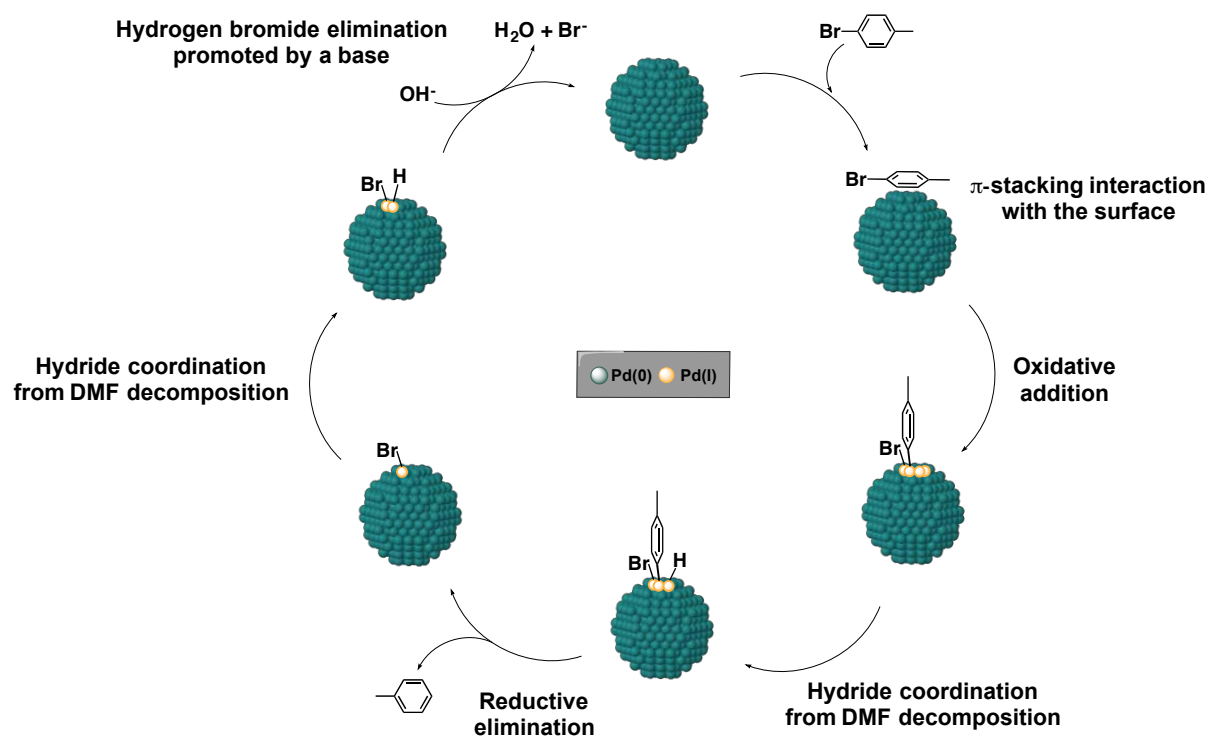


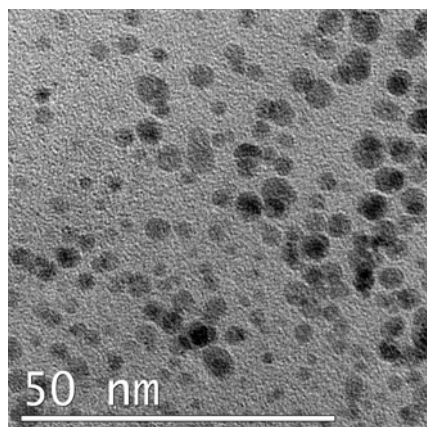
Figure 8. Proposed mechanism for the dehalogenation of 4-bromotoluene onto the surface of Pd nanoparticles.

In order to determine the influence of phenylboronic acid in C-C coupling reactions catalyzed by the colloidal systems, catalytic experiments were also carried out in absence of the boron reagent. Besides that BT was not detected, it is remarkable that full conversion to the dehalogenated product (PhMe) is observed in the case of the reaction carried out with 4-iodotoluene catalyzed by N1 (Table 1, entry 7). However, when 4-bromotoluene is employed a significant increase in the yield of TT homocoupling product is observed for both nanocatalysts (from 34% to 60%; Table 1, entries 9 and 11, respectively, for N1, and from 13% to 26% for N2, entries 10 and 12). When performed with the molecular complexes, the same reaction of 4-halotoluene in the absence of phenylboronic acid reagent did not yield to homocoupling products at all.

A recurrent discussion with Pd NPs as catalysts for C-C coupling reactions is whether the real catalyst are the NPs or molecular Pd species leached from them.[30] There are several publications that support either a surface-based[31] or atom-leaching mechanism.[32] In this context, three different tests have been carried out to assess the nature of the active species during the catalytic process. First of all, in the mercury poisoning test,[33] 100 equivalents of Hg were added to the catalytic mixtures after 10 min of reaction. For molecular systems (C1 and C2) the conversions were not affected, while for the colloidal systems (N1 and N2) the catalytic reactions ceased completely. These data suggest that C1 and C2 act as real molecular catalysts when starting with them whereas Pd NPs are the active species when N1 and N2 are introduced in the catalysis. This is in accordance with the different results observed in catalysis depending on the molecular or colloidal nature of the introduced catalysts. However, the mercury poisoning test is not definitive, since the amalgam of Hg and Pd from the NPs could prevent potential Pd molecular species from leaching. For these reason, two additional experiments have been performed with systems from entries 9 and 10 in Table 1 (Suzuki-Miyaura reaction conditions, p-bromotoluene as the haloderivative and N1 or N2 as the catalyst, respectively). First of all, TEM grids were prepared after the catalytic experiments, observing the existence of Pd NPs (Figure 9). The mean size of these NPs (2.7(0.7) and 3.3(0.6) nm for N1 and N2 after catalysis, respectively) is similar to those found for the same NPs prior to the catalytic tests (2.1(0.9) and 3.2(0.9) nm for N1 or N2, respectively). Even if no restructuring of the NPs seems to

have taken place (which could indicate a leaching / deposition mechanism through the Ostwald ripening process[34]) it is important to note that for N2, the NPs appear isolated after catalysis, in contrast with the aggregation observed prior catalysis.

(a)



(b)

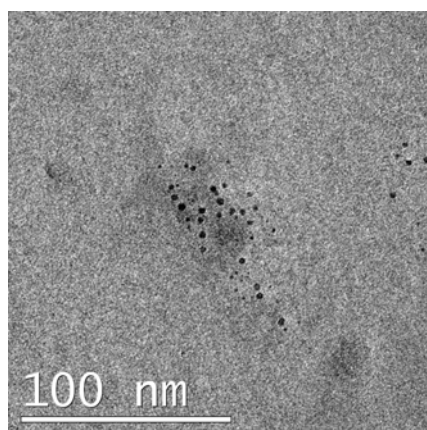


Figure 9. HR-TEM micrographs of Pd nanoparticles (a) N1 and (b) N2 after catalytic experiments.

Secondly, ICP-MS analyses of the solutions after catalysis for entries 9 and 10 in Table 1 have been carried out in order to know the amount of Pd leached from the NPs to the solution. The concentration of Pd in these solutions are 0.17 and 1.8 ppm for N1 or N2, respectively, meaning that 0.7% and 15% of Pd has leached to the solution, for N1 or N2, respectively. The differences on the percentage of leached Pd can be explained by the different coordinative properties of the ligands on each

system. For **N1**, the carbene and pyrazolyl groups from **L** can coordinate to the surface of the NPs, and better stabilize them from Pd leaching than in **N2**, where only the pyrazolyl group from **HL·Cl** can coordinate the surface of the NPs.

The leached molecular Pd species can be responsible of the small amount of C-C heterocoupling reaction observed in entries 9 and 10 of Table 1 (5% and 7%, respectively).

All in all, these experiments would confirm that that **C1** and **C2** act as molecular catalysts in Suzuki-Miyaura C-C heterocoupling and **N1** and **N2** are the real active species for C-C homocoupling reaction.

4.5 Conclusions

A new hybrid pyrazole-imidazol-2-ylidene ligand, 1-[2-(3,5-dimethylpyrazol-1-yl)ethyl]-3-((S)-1-phenylethyl)-3*H*-imidazol-2-ylidene (**L**), has been synthesized for the first time and proved to effectively stabilize small and isolated palladium(0) nanoparticles. A comparison with the counterpart **HL·Cl** as stabilizer led to badly stabilized NPs which evidenced that the coordination of the ylidene group is a key factor in the stabilization process of the colloidal system. The successful preparation and complete characterization of molecular Pd(II) coordination compounds with the same ligands confirmed a chelated coordination mode through the pyrazolic nitrogen and the ylidene group for **L** but a terminal monodentated one through pyrazolic nitrogen for **HL·Cl**. It can be concluded that similar coordination modes of **L** and **HL·Cl** here take place for both the Pd NPs particles and Pd complexes respectively. As a consequence, the coordination of **L** is stronger and leads to nanoparticles with well-controlled size.

All those systems have been tested in catalytic C-C coupling reactions. For colloidal systems (**N1**, **N2**), an improving effect has been observed, in terms of chemoselectivity and yield, of **L** containing NPs (**N1**) with respect to **HL·Cl** containing NPs (**N2**) as the result of the different coordination modes of the carbene group to the surface of the NPs. Interestingly, these systems are the only ones able to achieve the C-C homocoupling reaction between two molecules of bromoarenes or the complete dehalogenation reaction of iodoarenes. The Suzuki-Miyaura reaction is favored with the Pd molecular complexes.

Three different types of reactions have been observed depending on the catalytic system: i) the Suzuki-Miyaura reaction takes place with Pd molecular complexes; ii) a secondary reaction, the dehalogenation of the substrate, is always detected and iii) the C-C homocoupling between two molecules of bromoarenes is observed with colloidal catalysts.

Contribution

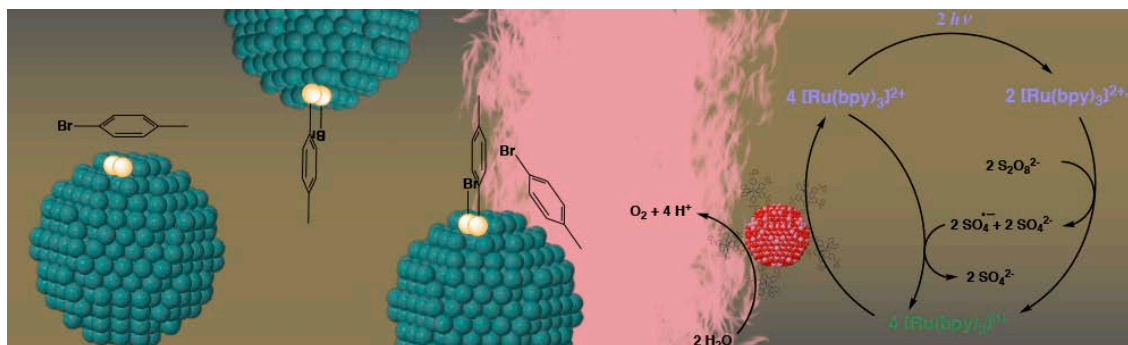
Jonathan De Tovar resynthesized the ligands, complexes and nanoparticles for their testing in the Suzuki-Miyaura catalytic reaction in order to study their dissimilar catalytic behavior.

4.6 References

- [1] Cherney, A. H.; Kadunce, N. T.; Reisman, S. E. *Chem. Rev.* **2015**, *115*, 9587-9652.
- [2] (a) Hopkinson, M. N.; Richter, C.; Schedler, M.; Glorius, F. *Nature* **2014**, *510*, 485-496. (b) Glorius, F. *Top. Organomet. Chem.* **2006**, *21*, 1-20. (c) Lummiss, J. A. M.; Higman, C. S.; Fyson, D. L.; McDonald, R.; Fogg, D. E. *Chem. Sci.* **2015**, *6*, 6739-6746.
- [3] Hadei, N.; Kantchev, E. A. B.; O'Brien, C. J.; Organ, M. G. *Org. Lett.* **2005**, *7*, 1991.
- [4] (a) Frey, G. D.; Lavallo, V.; Donnadiou, B.; Schoeller, W. W.; Bertrand, G. *Science* **2007**, *316*, 439-441. (b) Wang, Y.; Xie, Y.; Wei, P.; King, R. B.; Schaefer, H. F., III; Schleyer, P.; von, R.; Robinson, G. H. *Science* **2008**, *321*, 1069-1071.
- [5] (a) A. V. Zhukhovitskiy, M. J. MacLeod and J. A. Johnson, *Chem. Rev.* **2015**, *115*, 11503. (b) Lara, P.; Rivada-Wheelaghan, O.; Conejero, S.; Philippot, K.; Chaudret, B. *Angew. Chem. Int. Ed.* **2011**, *50*, 12080-12084. (c) Lara, P.; Suarez, A.; Colliere, V.; Philippot, K.; Chaudret, B. *Chem. Cat. Chem.* **2014**, *6*, 87-90. (d) Vignolle, J.; Tilley, T. D. *Chem. Commun.* **2009**, *46*, 7230-7232. (e) Hurst, E. C.; Wilson, K.; Fairlamb, I. J. S.; Chechik, V. *New J. Chem.* **2009**, *33*, 1837-1840. (f) Gonzalez-Galvez, D.; Lara, P.; Rivada-Wheelaghan, O.; Conejero, S.; Chaudret, B.; Philippot, K.; van Leeuwen, P. W. N. M. *Catal. Sci. Technol.* **2013**, *3*, 99-105. (g) Baquero, E. A.; Tricard, S.; Flores, J. C.; de Jesús, E.; Chaudret, B. *Angew. Chem. Int. Ed.* **2014**, *53*, 13220-13224. (h) Ferry, A.; Schaepe, K.; Tegeder, P.; Richter, C.; Chepiga, K. M.; Ravoo, B. J.; Glorius, F. *ACS Catal.* **2015**, *5*, 5414-5420. (i) Martínez-Prieto, L. M.; Ferry, A.; Lara, P.; Richter, C.; Philippot, K.; Glorius, F.; Chaudret, B. *Chem. Eur. J.* **2015**, *21*, 17495-17502. (j) Richter, C.; Schaepe, K.; Glorius, F.; Ravoo, B. J. *Chem. Commun.* **2014**, *50*, 3204-3207. (k) Martínez-Prieto, L. M.; Ferry, A.; Richter, C.; Lecante, P.; Philippot, K.; Glorius, F.; Chaudret, B. *Chem. Commun.* **2016**, *52*, 4768-4771. (l) Martínez-Prieto, L. M.; Urbaneja, C.; Palma, P.; Cámpora, J.; Philippot, K.; Chaudret, B. *Chem. Commun.* **2015**, *51*, 4647-4650.
- [6] Albrecht, M. *Adv. Organomet. Chem.* **2014**, *62*, 111-158.
- [7] (a) Organometallic Nanoparticles, Lara, P.; Philippot, K.; Lacroix, L.-M.; Lachaize, S.; Liakakos, N.; Soulantica, K.; Chaudret, B. in *Advances in Organometallic Chemistry: The Silver / Gold Jubilee International Conference on Organometallic Chemistry Celebratory Book*, A. J. L. Pombeiro (Eds), Wiley VCH, Weinheim, 2013, Chapter 31, 421-436. (b) Organometallic Approach for the Synthesis of Noble Metal Nanoparticles: Towards Application in Colloidal and Supported Nanocatalysis, Kinayyigit, S.; Philippot, K. in *Metal Nanoparticles for Catalysis: Advances and Applications*, T. Tao (Ed.), RSC, 2014, Chapter 4, 47-82. (c) An, K.; Somorjai, G. A. *Chem. Cat. Chem.* **2012**, *4*, 1442. (d) Costa, N. J. S.; Guerrero, M.; Colliere, V.; Teixeira-Neto, E.; Landers, R.; Philippot, K.; Rossi, L. M. *ACS Catal.* **2014**, *4*, 1735-1742.
- [8] Amiens, C.; Ciuculescu-Pradines, D.; Philippot, K. *Coord. Chem. Rev.* **2016**, *38*, 409-432.
- [9] (a) Concepts in Nanocatalysis, Philippot, K.; Serp, P. in *Nanomaterials in Catalysis* P. Serp and K. Philippot (Eds.), Wiley-VCH, Weinheim, 2013, Chapter 1, 1-54 (b) On the use of Organometallic Concepts for the Synthesis of Nanocatalysts, Ayvali, T.; Philippot, K. in *New Materials for Catalytic Applications*, E. Kemnitz and V. Parvulescu (Eds.), Elsevier, 2016, Chapter 3, 41-79 (c) Roucoux, A.; Schulz, J.; Patin, H. *Chem. Rev.* **2002**, *102*, 3757-3778. (d) Guerrero, M.; Chau, N. T. T.; Noel, S.; Denicourt-Nowicki, A.; Hapiot, F.; Roucoux, A.; Montflier, E.; Philippot, K. *Curr. Org. Chem.* **2013**, *17*, 364-399. (e) Chaudret, B.; Gomez, M.; Philippot, K. *Top. Catal.* **2013**, *56*, 1153. (f) Wang, D.; Astruc, D. *Chem. Rev.* **2014**, *114*, 6949-6985.
- [10] (a) Kolmakov, A.; Chen, X.; Moskovits, M. *J. Nanosci. Nanotechnol.* **2008**, *8*, 111-121. (b) Guerrero, M.; Costa, N. J. S.; Vono, L. L. R.; Rossi, L. M.; Gusevskaya, E. V.; Philippot, K. *J. Mater. Chem. A* **2013**, *1*, 1441-1449.
- [11] Bej, A.; Ghosh, K.; Sarkar, A.; Knight, D. W., *RSC Adv.* **2016**, *6*, 11446-11453.
- [12] Kotha, S.; Lahiri, K.; Kashinath, D. *Tetrahedron* **2002**, *58*, 9633-9695.
- [13] Ganesan, A. *Drug Discov. Today* **2001**, *6*, 238.
- [14] Astruc, D.; Ornelas, C.; Diallo, A. K.; Ruiz, *Molecules* **2010**, *15*, 4947-4960.
- [15] Peral, D.; Gómez-Villarraga, F.; Sala, X.; Pons, J.; Bayon, J. C.; Ros, J.; Guerrero, M.; Vendier, L.; Lecante, P.; Garcia-Anton, J.; Philippot, K. *Catal. Sci. Technol.* **2013**, *3*, 475-489.

- [16] Gómez-Villarraga, F.; De Tovar, J.; Guerrero, M.; Nolis, P.; Escriche, L.; Bofill, R.; Ros, J.; Sala, X.; Philippot, K.; García-Antón, J. *Dalton Trans.* **2017**, *46*, 11768-11778.
- [17] Gómez-Villarraga, F. *Síntesis de Complejos y Estabilización de Nanopartículas de Paladio con Ligandos Híbridos Pirazólicos y Carbenos N-Heterocíclicos y su Aplicación en Catálisis* (Tesis Doctoral). Universidad Autónoma de Barcelona, Barcelona, España, 2013.
- [18] Xu, X.; Cheng, D.; Pei, W.; *J. Org. Chem.* **2006**, *71*, 6637-6639.
- [19] Fairlamb, I. J. S.; Kapdi, A. R.; Lee, A. F. *Org. Lett.* **2004**, *6*, 4435-4438.
- [20] Miyaura, N.; Yamada, K.; Suzuki, A. *Tetrahedron Lett.* **1979**, *36*, 3437-3440.
- [21] Miyaura, N.; Suzuki, A. *Chem. Rev.* **1995**, *95*, 2457-2483.
- [22] (a) Lai, R.-Y.; Chen, C.-L.; Liu, S.-T. *J. Chin. Chem. Soc.* **2006**, *53*, 979-985. (b) Navarro, O.; Marion, N.; Oonishi, Y.; Kelly, R. A.; Nolan, S. P. *J. Org. Chem.* **2006**, *71*, 685-692.
- [23] Muzart, J. *Tetrahedron* **2009**, *65*, 8313-8323.
- [24] Phan, N. T. S.; Van Der Sluys, M.; Jones, C. W. *Adv. Synth. Catal.* **2006**, *348*, 609-679.
- [25] Blanksby, S. J.; Ellison, G. B. *Acc. Chem. Res.* **2003**, *36*, 255-263.
- [26] Astakhov, A. V.; Khazipov, O. V.; Chernenko, A. Y.; Pasyukov, D. V.; Kashin, A. S.; Gordeev, E. G.; Khrustalev, V. N.; Chernyshev, V. M.; Ananikov, V. P. *Organometallics* **2017**, *36*, 1981-1992.
- [27] Fanta, P. E. *Synthesis* **1974**, *1*, 9-21.
- [28] (a) Seganish, W. M.; Mowery, M. E.; Riggleman, S.; DeShong, P. *Tetrahedron*, **2005**, *61*, 2117-2121. (b) Nadri, S.; Azadi, E.; Ataei, A.; Joshafhanim, M.; Rafiee, E. *J. Organomet. Chem.* **2011**, *696*, 2966-2970.
- [29] Santra, S.; Ranjan, P.; Mandal, S. K.; Ghorai, P. K. *Inorg. Chim. Acta* **2011**, *372*, 47-52.
- [30] Bej, A.; Ghosh, K.; Sarkar, A.; Knight, D. W. *RSC Adv.* **2016**, *6*, 11446-11453.
- [31] (a) Ellis, P. J.; Fairlamb, I. J. S.; Hackett, S. F. J.; Wilson, K.; Lee, A. F. *Angew. Chem. Int. Ed.* **2010**, *49*, 1820-1824. (b) Narayanan, R.; El-Sayed, M. A. *J. Phys. Chem. B* **2004**, *108*, 8572-8580. (c) Narayanan, R.; El-Sayed, M. A. *J. Am. Chem. Soc.* **2003**, *125*, 8340-8347. (d) Lee, A. F.; Ellis, P. J.; Fairlamb, I. J. S.; Wilson, K. *Dalton Trans.* **2010**, 10473-10482. (e) Sánchez-Sánchez, C.; Orozco, N.; Holgado, J. P.; Beaumont, S. K.; Kyriakou, G.; Watson, D. J.; González-Eripe, A. R.; Feria, L.; Fernández-Sanz, K.; Lambert, R. M. *J. Am. Chem. Soc.* **2014**, *137*, 940-947. (f) Kanuru, V. K.; Kyriakou, G.; Beaumont, S. K.; Papageorgiou, A. C.; Watson, D. J.; Lambert, R. M. *J. Am. Chem. Soc.* **2010**, *132*, 8081-8086. (g) Sánchez-Sánchez, C.; Yubero, F.; González-Elipe, A. R.; Feria, L.; Fernández-Sanz, J.; Lambert, R. M. *J. Phys. Chem. C* **2014**, *118*, 11677-11684. (h) Wang, F.; Li, C.; Sun, L.-D.; Wu, H.; Ming, T.; Wang, J.; Yu, J. C.; Yan, C.-H. *J. Am. Chem. Soc.* **2011**, *133*, 1106-1111. (i) Wang, F.; Li, C.; Chen, H.; Jiang, R.; Sun, L.-D.; Li, Q.; Wang, J.; Yu, J. C.; Yan, C.-H.; *J. Am. Chem. Soc.* **2013**, *135*, 5588-5601.
- [32] (a) Niu, Z.; Peng, Q.; Zhuang, Z.; He, W.; Li, Y. *Chem.-Eur. J.* **2012**, *18*, 9813-9817. (b) Pacardo, D. B.; Slocik, J. M.; Kirk, K. C.; Naik, R. R.; Knecht, M. R. *Nanoscale* **2011**, *3*, 2194-2201. (c) Gaikwad, A. V.; Holuigue, A.; Thathagar, M. B.; ten Elshof, J. E.; Rothenberg, G. *Chem.-Eur. J.* **2007**, *13*, 6908-6913. (d) Reetz, M. T.; Westermann, E.; *Angew. Chem., Int. Ed.* **2000**, *39*, 165-168. (e) de Vries, J. G. *Dalton Trans.* **2006**, 421-429.
- [33] Whitesides, G. M.; Hackett, M.; Brainard, R. L.; Lavalleye, J. P. P. M.; Sowinski, A. F.; Izumi, A. N.; Moore, S. S.; Brown, D. W.; Staud, E. M. *Organometallics* **1985**, *4*, 1819-1830.
- [34] Oliveira, R. L.; He, W.; Klein Gebbink, R. J. M.; de Jong, K. P. *Cat. Sci. Technol.* **2015**, *5*, 1919-1928.

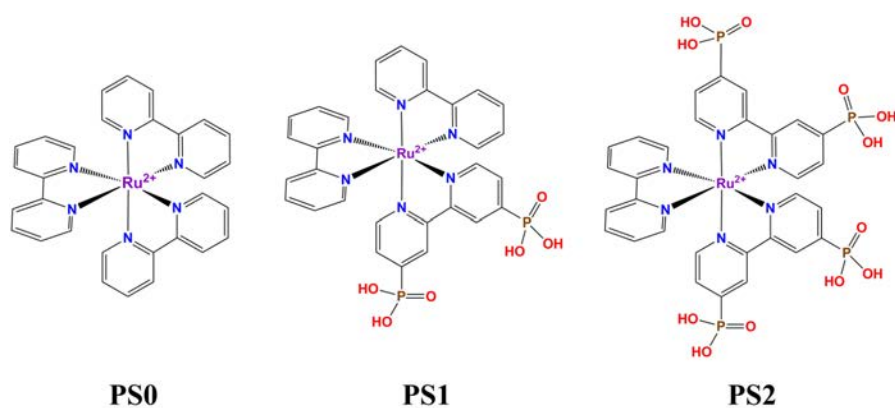
Chapter V. Summary and Conclusions



After exposing the general objectives and the experimental results obtained, the present chapter summarizes the work developed within this thesis.

Chapter III

- ✓ A new synthetic methodology for the easy preparation of Co NPs through the room temperature hydrogenation (3 bar of dihydrogen) of $[\text{Co}(\eta^3\text{-C}_8\text{H}_{13})(\eta^4\text{-C}_8\text{H}_{12})]$ in 1-heptanol is reported. This methodology demonstrates the ability of 1-heptanol to be both a proper solvent and stabilizing agent for the synthesis of isolated and homogeneous in size 3 nm Co(0) NPs. This nanomaterial has been characterized by FT-IR, TEM, WAXS and ICP.
- ✓ Slow (6 days) aerobic oxidation of the obtained Co(0) NPs allows the access to isolated Co_3O_4 NPs of preserved morphology (3.0 nm) and dispersion. These NPs have been characterized by FT-IR, TEM, HREM, XPS and WAXS.
- ✓ When deposited at the surface of a GC-RDE electrode and in 1M NaOH, the ultrafine Co_3O_4 NPs electrocatalytically oxidize water with an onset η of *ca.* 0.29 V and $\eta_{10\text{mA}/\text{cm}^2}$ of 0.486 V, showing ECSA normalized current densities (j_s) of 1.04 mA cm^{-2} at $\eta = 0.35 \text{ V}$, a value that fairly outperforms that of all benchmarked nanostructured metal oxide electrocatalysts deposited onto GC-RDE. Despite stable and showing 95% Faradaic efficiency, the system is less competitive at higher current densities due to its Tafel slope of *ca.* $100 \text{ mV}\cdot\text{dec}^{-1}$.
- ✓ A family of tris(bipyridyl)-based Ru(II) complexes containing phosphonate groups in the bipyridyl rings (PS0, PS1, PS2,) have been prepared as light-harvesting photosensitizers, following previously described procedures.



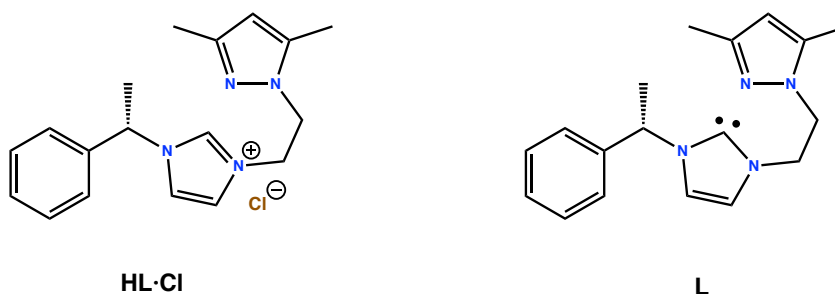
✓ The binding of the Ru(II) photosensitizers to the surface of the Co_3O_4 NPs was afforded by stirring a mixture of the bare Co_3O_4 NPs and the desired photosensitizer in MeOH yielding two new hybrid nanocatalysts of general formula $(\text{PS1})_{0.09}\text{Co}_3\text{O}_4(1\text{-heptanol})_{0.80}$ and $(\text{PS2})_{0.15}\text{Co}_3\text{O}_4(1\text{-heptanol})_{0.97}$. As expected, the mean size of these new hybrid nanomaterials is similar to that of the initial Co_3O_4 NPs. The prepared dyads were characterized by ICP-OES, FT-IR, CV, HREM, STEM-EDX and WAXS.

✓ The $\text{PS1-Co}_3\text{O}_4$ and $\text{PS2-Co}_3\text{O}_4$ dyads and their respective separate analogues under same $\text{Co}_3\text{O}_4/\text{PS}$ ratios have been tested as water oxidation catalysts for the photo-production of O_2 using visible light and $\text{S}_2\text{O}_8^{2-}$ as sacrificial electron acceptor at pH 5.6. The benefits of the dyad approach arise when observing the inactivity of the unbound $\text{Co}_3\text{O}_4/\text{PS}$ systems with regards to the significant TON and TOF values per NP ($5.4 / 0.90 \text{ min}^{-1}$ and $82 / 2.05 \text{ min}^{-1}$) obtained for $\text{PS1-Co}_3\text{O}_4$ and $\text{PS2-Co}_3\text{O}_4$, respectively. The better performance of the latter over the former was attributed to the higher surface functionalization of $\text{PS2-Co}_3\text{O}_4$, that enhance the kinetics of WO and protect better the catalytic entity under catalytic conditions against aggregation. These data stress the important role of the direct connection between the PS and the nanocatalyst by: 1) favoring their efficient electronic communication that allows being kinetically competitive with the typical side deactivation processes of light-driven WO and 2) minimizing catalyst aggregation under turnover conditions by means of the protective/stabilizing PS layer at the surface of the Co_3O_4 NPs.

✓ Both bound and unbound systems have been photo-physically studied observing that no back electron transfer from the dye to the Co_3O_4 NPs was observed in any case, evidencing a good electronic communication in the PS-NP dyad.

Chapter IV

✓ Following a procedure previously described by the research group, the ligands **HL·Cl**, 1-[2-(3,5-dimethylpyrazol-1-yl)ethyl]-3-((S)-1-phenylethyl)-3*H*-imidazol-1-ium chloride and **L**, 1-[2-(3,5-dimethylpyrazol-1-yl)ethyl]-3-((S)-1-phenylethyl)-3*H*-imidazol-2-ylidene, have been synthesized. The latter corresponds to a N-heterocyclic carbene (NHC) ligand with a pending pyrazolyl group, which infers potential chelating properties towards metallic centres. In contrast, **HL·Cl** is a terminal ligand only capable of coordinating through the pyrazolyl group.



✓ These two ligands have been used as stabilizing agents in the synthesis of Pd(0) NPs through the organometallic approach. The better coordinating properties of ligand **L** provokes a good stabilization of the NPs, yielding particles of 2.1 nm of mean size for an initial **L**/Pd ratio of 0.5. On the other hand, when the **HL·Cl** ligand is used to stabilize Pd NPs with the same ligand to palladium ratio, NPs of 3.2 nm were obtained.

✓ For comparative purposes, **L** and **HL·Cl** have been used to synthesize Pd(II) coordination compounds. As expected, **L** chelates the Pd centre through the ylidene and pyrazolyl groups, while **HL·Cl** acts as terminal ligand only coordinating through the pyrazolyl group.

✓ Both colloidal and molecular systems have been tested as catalysts for C-C coupling reactions, under Suzuki-Miyaura conditions (phenylboronic acid and 4-halogenotoluene under basic conditions).

- ✓ As expected, molecular compounds yield the hetero-coupling Suzuki-Miyaura product (4-methylbiphenyl), for iodo- and bromo- 4-halogenotoluene reactions. A secondary reaction has also been observed, the dehalogenation of the 4-halogenotoluene to yield toluene through a palladium hydride species, coming from the partial decomposition of the solvent (DMF) under catalytic conditions.
- ✓ The better coordinating properties of L towards HL·Cl, provokes an improving effect on terms of chemoselectivity (towards 4-methylbiphenyl) and yield.
- ✓ When Pd NPs were used as catalysts under the same reaction conditions, they lead to Suzuki-Miyaura (4-methylbiphenyl) or C-C homocoupling (4,4'-dimethylbiphenyl) reactions depending on the substrate (iodo- or bromo- derivatives, respectively). The dehalogenation of the 4-halogenotoluene to yield toluene has also been observed in all the catalytic tests. In the absence of phenylboronic acid, toluene can even be obtained in quantitative yield.
- ✓ The results obtained in this Chapter, lead us to conclude that the C-C homocoupling reaction takes place on the heterogeneous surface of the Pd Ps, whereas the Suzuki-Miyaura reaction preferentially takes place when coordination compounds are used.

Chapter VI. Annexes



The following papers have been published during this PhD thesis and are closely related with the present work. In the first work, a new chiral family of Ru complexes with the general formula $[\text{RuCl}(-)\text{-L1}(\text{bpy})]^+$ has been synthesized and characterized. DFT calculations of the different isomers have been performed in order to interpret the experimental results in terms of electronic and steric effects. In the second work, both molecular and colloidal Pd systems based both on an ionic liquid or its N-heterocyclic carbene (NHC) are synthesized, characterized and tested in C-C coupling processes. The conversion, yield and the different reactivity are discussed for the set of four systems.

Ruthenium Complexes with Chiral Bis-Pinene Ligands: an Array of Subtle Structural Diversity

Lydia Vaquer,[†] Albert Poater,[‡] Jonathan De Tovar,[§] Jordi García-Antón,[§] Miquel Solà,[‡] Antoni Llobet,^{*,†,§} and Xavier Sala^{*,§}

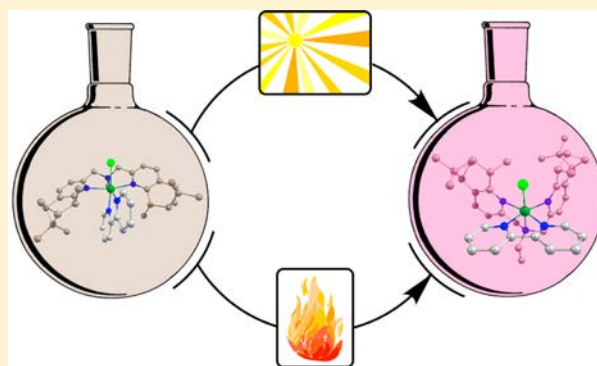
[†]Institute of Chemical Research of Catalonia (ICIQ), Avenida Països Catalans 16, E-43007 Tarragona, Spain

[‡]Departament de Química and Institut de Química Computacional, Universitat de Girona, Campus de Montilivi, E-17071 Girona, Spain

[§]Departament de Química, Universitat Autònoma de Barcelona, Cerdanyola del Vallès, 08193 Barcelona, Spain

S Supporting Information

ABSTRACT: A new chiral derivative of the *N,N*-bis(2-pyridylmethyl)ethylamine (bpea) ligand, Me-pinene[5,6]bpea [(-)-L1], has been prepared from a new aldehyde building block [Me-pinene-aldehyde, (-)-4] arising from the monoterpene chiral pool. The tridentate (-)-L1 ligand has been employed to prepare a new set of Ru–Cl complexes in combination with didentate 2,2'-bipyridine (bpy) with the general formula [RuCl((-)-L1)(bpy)]⁺. These complexes have been characterized in solution by cyclic voltammetry, UV–vis, and 1D and 2D NMR spectroscopy. Isomeric mixtures of *trans, fac*-C1a and *anti, mer*-C1c compounds are formed when (-)-L1 is reacted with a [Ru(bpy)(MeOH)Cl₃] precursor. Density functional theory calculations of all of the potential isomers of this reaction have been performed in order to interpret the experimental results in terms of electronic and steric effects and also to unravel the observed isomerization pathway between *anti, mer*-C1c and *trans, fac*-C1a.



INTRODUCTION

Today, ruthenium complexes have a variety of applications in many fields of science.¹ From a redox catalysis viewpoint, they are excellent because they enjoy a wide range of accessible oxidation states, ranging from 2– to 8+. Thus, they can be applied for both oxidative² and reductive³ transformations. Furthermore, ruthenium complexes bearing enantiopure ligands have already been used as asymmetric catalysts, giving spectacular enantiomeric excess.⁴

Within the asymmetric catalysis field, the nature of the chiral ligand plays a crucial role in the performance of the catalyst, in terms of efficiency and especially stereospecificity. However, despite the wide variety of enantiopure ligands reported so far, just a few of them have been shown to create effective asymmetric environments to a broad range of reactions and substrates.⁵ Therefore, the development of new chiral ligands that could generate “privileged” scaffolds is one of the most important issues in enantioselective catalysis by transition-metal complexes. In addition, the unraveling of the basic principles that make them “privileged” is also of paramount importance. With all this in mind, we have undertaken a project aimed at developing new chiral polypyridylic ligands with different geometries and denticities based on the monoterpene chiral pool.⁶ Their combination with metals such as manganese, iron,

and ruthenium has already led to interesting catalysts for diverse asymmetric oxidative transformations.⁷

Together with the nature of the ligands, their coordination arrangement around a given metal ion is also crucial for the final outcome of a catalytic reaction.⁸ For chiral ligands in an octahedral environment, the formation of metal complexes can lead to a large variety of isomers, especially for second-row transition metals such as ruthenium. This generates an additional challenge from a synthetic perspective in order to be able to separate and isolate individual pure isomers. Therefore, the rational ligand and complex design should be combined with appropriate synthetic methodologies in order to be successful in this type of endeavor.⁹

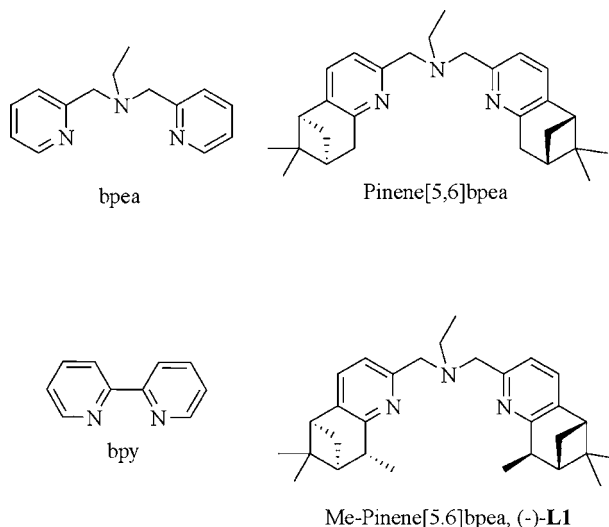
In 2008, we showed how both steric and electronic factors are key to explaining the isomeric ratios obtained when combining the *N,N*-bis(2-pyridylmethyl)ethylamine (bpea) ligand and its chiral derivative pinene[5,6]bpea (Chart 1) with *N*- and *P*-donor didentate ligands in an octahedral ruthenium(II) environment.¹⁰

Here, we further analyze this excellent platform by preparing a new diastereoselectively alkylated Me-pinene[5,6]bpea ligand [(-)-L1; Chart 1] with increased bulkiness and two new

Received: December 6, 2012

Published: April 25, 2013

Chart 1. Drawings of the Ligands Used in This Work



stereogenic centers. Ru–Cl complexes containing this ligand combined with 2,2'-bipyridine (bpy) have been prepared, thoroughly characterized, and stereoisomerically analyzed in comparison with their achiral and chiral analogues previously reported by our group.^{10,11}

EXPERIMENTAL SECTION

Materials. All reagents used in the present work were obtained from Aldrich Chemical Co. and were used without further purification. Reagent-grade organic solvents were obtained from SDS. RuCl₃·3H₂O was supplied by Alfa Aesar and was used as received.

Preparations. Pinene-furan [(-)-1]¹² and [Ru(bpy)(MeOH)Cl₃]¹³ were prepared following the procedures described in the literature.

Me-pinene-furan [(-)-2]. A solution of *n*-BuLi (26 mL, 1.6 M in hexane, 42.21 mmol) was added dropwise over a solution of diisopropylamine (6.5 mL, 46.4 mmol) in dry tetrahydrofuran (THF; 120 mL) at -40 °C. The solution of the formed LDA was brought to 0 °C in an ice bath, stirred for 30 min, and cooled again to -40 °C. A solution of the pyridine-pinene derivative (-)-1 (4.5 g, 18.8 mmol) in THF (120 mL) was added slowly for 1 h. The resulting red solution was stirred at -40 °C for 2 h. Then, methyl iodide (2.6 mL, 42.21 mmol) was added dropwise for 1 h, and the mixture was stirred overnight at room temperature. Water (310 mL) was added, and the product was extracted with dichloromethane, washed with brine, and dried with magnesium sulfate. The product was purified by column chromatography on silica gel using a mixture of hexane/ethyl acetate (95:5) as the eluent. Compound (-)-2 was obtained as a mixture of (-)-2 and Me-pinene-Me-furan (methylation on both the pinene and furan moieties) in a 10:3 ratio. This product was used without further purification in the next step. Yield: 74% (3.5 g, 13.8 mmol). ¹H NMR (400 MHz, CDCl₃): δ 7.49 (d, *J* = 1.5 Hz, 1H, H₉), 7.37 (d, *J* = 7.8 Hz, 1H, H₃), 7.20 (d, *J* = 8.0 Hz, 1H, H₄), 6.87 (d, *J* = 3.4 Hz, 1H, H₇), 6.5 (dd, *J* = 3.2 and 1.6 Hz, 1H, H₈), 3.23 (m, 1H, H₁₃), 2.75 (t, *J* = 4.8 Hz, 1H, H₁₀), 2.56 (m, 1H, H₁₄), 2.16 (m, 1H, H₁₂), 1.42 (m, 6H, H₁₅, H₁₆), 1.29 (d, *J* = 9.4 Hz, 1H, H_{14'}), 0.67 (s, 3H, H₁₇). ¹³C NMR (100 MHz, CDCl₃): δ 160.8 (C, C₂), 160.6 (C, C₁), 154.4 (C, C₆), 142.5 (CH, C₉), 140.3 (C, C₅), 133.1 (CH, C₃), 115.4 (CH, C₄), 111.8 (CH, C₈), 107.2 (CH, C₇), 47.1 (CH, C₁₀), 46.8 (CH, C₁₂), 41.4 (C, C₁₁), 38.8 (CH, C₁₃), 28.6 (CH₂, C₁₄), 26.3 (CH₃, C₁₆), 20.9 (CH₃, C₁₇), 18.3 (CH₃, C₁₅). [α]_D: -7.2 (c 1.5, CH₂Cl₂). ESI-MS: *m/z* 254.1 ([M + H]⁺), 276.1 ([M + Na]⁺).

Me-pinene-COOEt [(-)-3]. (-)-2 (23 g, 90.0 mmol) and ammonium metavanadate (1.5 g, 13.0 mmol) were mixed in water (400 mL). The mixture was heated to 65 °C, and fuming nitric acid (190 mL) was added slowly. The evolved gases were trapped by

connecting the reflux condenser to a solution of water and a mixture of aqueous NaOH (5 M) and H₂O₂ (2–3%). The solution was heated to reflux for 5 h. After distillation of the solvent under vacuum, ethanol (175 mL) and 96% sulfuric acid (64 mL) were added. The resulting solution was heated to reflux overnight. Water (800 mL) was added, and the solution was neutralized with a saturated aqueous solution of sodium carbonate. The black solid was filtered and extracted through a Soxhlet with hexane. The solvent was evaporated to obtain 14 g of (-)-3 as a yellow oil. Yield: 60% (14 g, 54 mmol). ¹H NMR (400 MHz, CDCl₃): δ 7.82 (d, *J* = 7.9 Hz, 1H, H₄), 7.29 (d, *J* = 7.9 Hz, 1H, H₃), 4.46 (m, 2H, H₁₅), 3.32 (m, 1H, H₆), 2.83 (t, *J* = 5.6 Hz, 1H, H₉), 2.58 (m, 1H, H₁₀), 2.18 (m, 1H, H₇), 1.44 (m, 9H, H₁₂, H₁₁, H₁₆), 1.30 (d, *J* = 9.1 Hz, 1H, H_{10'}), 0.63 (s, 3H, H₁₃). ¹³C NMR (100 MHz, CDCl₃): δ 165.7 (C, C₄), 157.6 (C, C₁), 146.2 (C, C₅), 145.5 (C, C₂), 133.4 (CH, C₃), 122.5 (CH, C₄), 61.6 (CH₂, C₁₅), 46.8 (CH, C₉), 40.0 (CH, C₇), 39.4 (C, C₈), 36.7 (CH, C₆), 31.5 (CH₂, C₁₀), 25.9 (CH₃, C₁₂), 21.3 (CH₃, C₁₃), 18.1 (CH₃, C₁₁), 14.4 (CH, C₁₆). [α]_D: -25.4 (c 0.94, CH₂Cl₂). ESI-MS: *m/z* 260.1 ([M + H]⁺).

Me-pinene-aldehyde [(-)-4]. (-)-3 (13.7 g, 52.8 mmol) was dissolved in anhydrous THF (200 mL), and the solution was cooled to -78 °C. LiAlH₄ (1 M in hexane, 63.4 mL) was added for a period of 20 min with a syringe pump. The resulting solution was stirred for 1 h at the same temperature. Glacial acetic acid (27 mL) was added, and the solution was left at room temperature. Hexane (400 mL) was added, and the solution was poured over water (400 mL). The solution was neutralized with a saturated solution of sodium bicarbonate, extracted with hexane, washed with water, and dried with magnesium sulfate. After collection and evaporation of the organic phases, a mixture of aldehyde (-)-4 and alcohol (-)-5 was obtained. This mixture was purified by column chromatography on silica gel. Using dichloromethane as the mobile phase, 6.8 g of (-)-4 was eluted. Yield: 60% (6.8 g, 31.6 mmol). ¹H NMR (400 MHz, CDCl₃): δ 10.04 (s, 1H, H₁₄), 7.68 (d, *J* = 7.5 Hz, 1H, H₄), 7.34 (d, *J* = 7.5 Hz, 1H, H₃), 3.27 (m, 1H, H₆), 2.86 (t, *J* = 5.3 Hz, 1H, H₉), 2.60 (m, 1H, H₁₀), 2.20 (m, 1H, H₇), 1.44 (m, 6H, H₁₁, H₁₂), 1.31 (d, *J* = 10.0 Hz, 1H, H_{10'}), 0.64 (s, 3H, H₁₃). ¹³C NMR (100 MHz, CDCl₃): δ 193.6 (COH, H₁₄), 161.8 (C, C₁), 150.8 (C, C₂), 147.4 (C, C₅), 133.3 (CH, C₃), 119.5 (CH, C₄), 47.6 (CH, C₉), 46.5 (CH, C₇), 41.4 (C, C₈), 38.7 (CH, C₆), 28.2 (CH₂, C₁₀), 26.2 (CH₃, C₁₂), 20.8 (CH₃, C₁₃), 18.1 (CH₃, C₁₁). [α]_D: -19.4 (c 0.98, CH₂Cl₂). ESI-MS: *m/z* 216.1 ([M + H]⁺), 238.1 ([M + Na]⁺).

Me-pinene-OH [(-)-5]. (-)-4 (3 g, 13.9 mmol) was dissolved in dry methanol (34 mL), and then sodium borohydride (1 g, 26.5 mmol) was added slowly. The solution was left at room temperature, and stirring was continued for 4 h. After evaporation of the solvent, dichloromethane (34 mL) and water (26 mL) were added. The product was extracted to the dichloromethane layer, washed with water, and dried with magnesium sulfate. After evaporation, 2.8 g of pure (-)-5 as a yellow solid was obtained. Yield: 92% (2.8 g, 12.9 mmol). ¹H NMR (400 MHz, CDCl₃): δ 7.17 (d, *J* = 7.5 Hz, 1H, H₃), 6.87 (d, *J* = 7.5 Hz, 1H, H₄), 4.70 (b s, 2H, H₁₄), 4.00 (b s, 1H, OH), 3.17 (m, 1H, H₆), 2.75 (t, *J* = 5.4 Hz, 1H, H₉), 2.55 (m, 1H, H₁₀), 2.15 (m, 1H, H₇), 1.43 (s, 3H, H₁₂), 1.38 (d, *J* = 7.2 Hz, 3H, H₁₁), 1.30 (d, *J* = 9.8 Hz, 1H, H_{10'}), 0.63 (s, 3H, H₁₃). ¹³C NMR (100 MHz, CDCl₃): δ 159.6 (C, C₁), 155.3 (C, C₂), 140.4 (C, C₅), 133.4 (CH, C₃), 117.0 (CH, C₄), 63.8 (CH₂, C₁₄), 46.9 (CH, C₉), 46.8 (CH, C₇), 41.3 (C, C₈), 38.6 (CH, C₆), 28.7 (CH₂, C₁₀), 26.3 (CH₃, C₁₂), 20.8 (CH₃, C₁₃), 18.1 (CH₃, C₁₁). [α]_D: -22.9 (c 1.2, CH₂Cl₂). ESI-MS: *m/z* 218.1 ([M + H]⁺), 240.1 ([M + Na]⁺).

Me-pinene-Cl [(-)-6]. (-)-5 (5.15 g, 23.7 mmol) was dissolved in dry dichloromethane (55 mL). A solution of SOCl₂ (5 mL, 71 mmol) in dry dichloromethane (44 mL) was added dropwise. The solution was kept stirring overnight. The solvent was carefully evaporated. Dichloromethane (350 mL) and an aqueous solution of sodium hydroxide (0.4 M, 666 mL) were added. The product was extracted to the dichloromethane layer, washed with water, and dried with magnesium sulfate. After evaporation, (-)-6 was obtained as a yellow oil. Yield: 88% (4.9 g, 21 mmol). ¹H NMR (400 MHz, CDCl₃): δ 7.23 (d, *J* = 7.5 Hz, 1H, H₃), 7.16 (d, *J* = 7.4 Hz, 1H, H₄), 4.68 (s, 2H,

H14), 3.20 (m, 1H, H6), 3.78 (t, $J = 5.7$ Hz, 1H, H9), 2.57 (m, 1H, H10), 2.17 (m, 1H, H7), 1.44 (s, 3H, H12), 1.40 (d, $J = 7.1$ Hz, 3H, H11), 1.32 (d, $J = 9.7$ Hz, 1H, H10'), 0.65 (s, 3H, H13). ^{13}C NMR (100 MHz, CDCl_3): δ 160.4 (C, C1), 153.1 (C, C2), 141.6 (C, C5), 134.1 (CH, C3), 119.9 (CH, C4), 47.0 (CH, C9), 46.7 (CH, C7), 46.6 (CH₂, C14), 41.3 (C, C8), 38.5 (CH, C6), 28.5 (CH₂, C10), 26.2 (CH₃, C12), 20.8 (CH₃, C13), 18.3 (CH₃, C11). $[\alpha]_{\text{D}}^{25}$: -16.4 (c 1.3, CH_2Cl_2). ESI-MS: m/z 236.1 ($[\text{M} + \text{H}]^+$).

Me-pinene[5,6]bpea [(-)-L1]. (-)-6 (2.29 mg, 9.7 mmol) was dissolved in a mixture of acetonitrile/water [1:1 (v/v), 10 mL], and 70% aqueous ethylamine (172 μL , 4.8 mmol) was added. The solution was heated to 60 °C for 5 min. Then, an aqueous solution of sodium hydroxide (10 M, 850 μL , 10.7 mmol) was added slowly. The solution was heated at 60 °C for 1 h. The product was extracted with chloroform and dried with anhydrous magnesium sulfate. The crude was purified by column chromatography of neutral alumina. Using a mixture of dichloromethane/acetone [9:1 (v/v)], (-)-L1 was eluted. Yield: 54% (1.17 g, 2.6 mmol). ^1H NMR (400 MHz, CDCl_3): δ 7.23 (d, $J = 7.7$ Hz, 2H, H2), 7.12 (d, $J = 7.7$ Hz, 2H, H3), 3.80 (s, 4H, H14), 3.15 (m, 2H, H12), 2.70 (t, $J = 5.6$ Hz, 2H, H6), 2.65 (q, $J = 7.1$ Hz, 2H, H15), 2.51 (m, 2H, H7), 2.12 (m, 2H, H8), 1.39 (s, 6H, H10), 1.35 (d, $J = 7.1$ Hz, 6H, H13), 1.28 (d, $J = 9.6$ Hz, 2H, H7'), 1.11 (t, $J = 7.1$ Hz, 3H, H16), 0.61 (s, 6H, H11). ^{13}C NMR (100 MHz, CDCl_3 , 25 °C): δ 159.8 (C, C5), 157.1 (C, C1), 139.4 (C, C4), 133.1 (CH, C3), 119.3 (CH, C2), 59.9 (CH₂, C14), 48.2 (CH₂, C15), 47.0 (2CH, C6, C8), 41.3 (C, C9), 38.7 (CH, C12), 28.7 (CH₂, C7), 26.3 (CH₃, C10), 20.9 (CH₃, C11), 18.5 (CH₃, C13), 12.3 (CH₃, C16). $[\alpha]_{\text{D}}^{25}$: -18.2 (c 1.4, CH_2Cl_2). ESI⁺-HRMS ($[\text{M} + \text{H}]^+$). Anal. Calcd for $\text{C}_{30}\text{H}_{43}\text{N}_2$: m/z 444.3373. Found: m/z 444.3398.

trans,trans-fac-[Ru(-)-L1](bpy)ClCl (C1a) and anti,mer-[Ru(-)-L1](bpy)ClCl (C1c). To a solution of $[\text{Ru}(\text{bpy})(\text{MeOH})\text{Cl}_2]$ (53 mg, 0.134 mmol) and triethylamine (28 μL , 0.20 mmol) in dry ethanol (20 mL) was added (-)-L1 (56 mg, 0.134 mmol). The mixture was heated to reflux for 24 h in the dark. To the resulting red solution was added dry diethyl ether (50 mL). The red solution was filtered and separated from a green solid. The solution was evaporated, and the obtained solid was purified by column chromatography of alumina. Starting with dichloromethane, the polarity of the mobile phase was increased with methanol. With a mixture of dichloromethane/methanol [100:2 (v/v)], a red band was eluted. The first fractions of this band, which had a darker color and contained a mixture of C1a and C1c (11 mg), were separated. The next fractions contained pure C1a (37 mg; yield 36%). Anal. Calcd for $\text{C}_{40}\text{H}_{49}\text{ClF}_6\text{N}_3\text{PRu}$: C, 54.51; H, 5.60; N, 7.95. Found: C, 54.31; H, 5.82; N, 7.68. C1c was isolated by purification of the mixture of C1a and C1c with an alumina semipreparative thin layer chromatograph using a mixture of dichloromethane/methanol [100:2 (v/v)] as the mobile phase, obtaining 5 mg of pure C1c (yield 5%). Anal. Calcd for $\text{C}_{40}\text{H}_{49}\text{ClF}_6\text{N}_3\text{PRu}$: C, 54.51; H, 5.60; N, 7.95. Found: C, 54.42; H, 5.75; N, 7.73. C1a. ^1H NMR (500 MHz, CD_2Cl_2): δ 8.28 (d, $J = 8.0$ Hz, 1H, H4), 8.25 (d, $J = 7.8$ Hz, 1H, H5), 7.98 (d, $J = 5.5$ Hz, 1H, H1), 7.87 (t, $J = 7.3$ Hz, 1H, H3), 7.80 (t, $J = 7.3$ Hz, 1H, H6), 7.50–7.40 (4H, H9, H10, H18, H19), 7.30 (t, $J = 6.4$ Hz, 1H, H2), 7.18 (t, $J = 6.2$ Hz, 1H, H7), 6.68 (d, $J = 5.2$ Hz, 1H, H8), 5.34 (m, 1H, H21), 4.59 (d, $J = 15.6$ Hz, 1H, 28a), 4.26 (2H, H27a, H12), 4.14 (d, $J = 15.7$ Hz, 1H, H27b), 3.78 (d, $J = 15.7$ Hz, 1H, H28b), 2.95 (dt, $J = 10.3$ and 5.4 Hz, 2H, H15, H24), 2.67–2.58 (m, 1H, 29a), 2.58–2.51 (m, 2H, H14a, H23a), 2.48 (dd, $J = 13.7$ and 7.0 Hz, 1H, H29b), 2.23–2.15 (m, 4H, H13, H22, H14b, H23b), 1.76–1.68 (m, 3H, H30), 1.47 (s, 3H, H26), 1.44 (s, 3H, H16), 1.37–1.26 (m, 6H, H11, H20), 0.87 (s, 3H, H25), 0.59 (s, 3H, H17). CV (CH_2Cl_2 vs SSCE): 0.79 V. ESI⁺-HRMS ($[\text{M} - 2\text{Cl}]^{2+}$, $z = 2$). Calcd for $\text{C}_{40}\text{H}_{49}\text{N}_3\text{Ru}$: m/z 347.6532. Found: m/z 347.6518. C1c. ^1H NMR (500 MHz, CD_2Cl_2): δ 10.63 (d, $J = 5.0$ Hz, 1H, H1), 8.65 (d, $J = 7.9$ Hz, 1H, H4), 8.61 (d, $J = 6.9$ Hz, 1H, H5), 8.50 (d, $J = 5.7$ Hz, 1H, H8), 8.02–7.95 (m, 1H, H3), 7.80 (dd, $J = 11.3$ and 4.3 Hz, 1H, H6), 7.51 (ddd, $J = 7.4$, 6.0, and 1.4 Hz, 1H, H2), 7.38–7.32 (m, 1H, H7), 7.08–6.87 (m, 4H, H9, H10, H18, H19), 6.31 (d, $J = 16.6$ Hz, 1H, H28a), 5.63 (d, $J = 13.3$ Hz, 1H, H27a), 4.60 (d, $J = 16.7$ Hz, 1H, H28b), 4.52 (d, $J = 13.4$ Hz, 1H, H27b), 3.89 (dq, $J = 13.3$ and 6.6 Hz, 1H, H29a), 3.24 (dq, $J = 14.5$ and 7.3 Hz, 1H, H29b), 2.61–2.54 (m,

2H, H14a, H23a), 2.53 (dd, $J = 6.4$ and 5.5 Hz, 1H, H15), 2.49 (dd, $J = 6.4$ and 5.5 Hz, 1H, H24), 2.27–2.19 (m, 4H, H13, H22, H14b, H23b), 1.46 (s, 3H, H16), 1.42 (s, 3H, H25), 1.24 (m, 1H, H21), 1.15–1.05 (m, 3H, H30), 0.75 (d, $J = 6.9$ Hz, 3H, H20), 0.65–0.58 (m, 1H, H12), 0.59 (s, 3H, H26), 0.55 (s, 3H, H17), -0.17 (d, $J = 7.0$ Hz, 3H, H11). CV (CH_2Cl_2 , V vs SSCE): 0.83 V. The NMR assignment for C1a and C1c has been carried out in accordance with the labeling shown in Figure S15 in the Supporting Information.

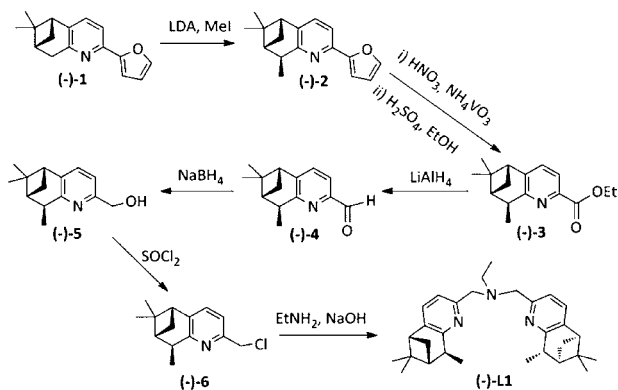
Instrumentation and Measurements. The NMR spectroscopy experiments were performed on Bruker Avance 400 and 500 Ultrashield NMR spectrometers. Samples were run in CD_2Cl_2 and CDCl_3 . Cyclic voltammetry (CV) experiments were performed on an IJ-Cambria HI-660 potentiostat using a three-electrode cell. Typical CV experiments were carried out at a scan rate of 100 mV/s. A glassy carbon electrode (2 mm diameter) was used as the working electrode, a platinum wire as the auxiliary electrode, and a saturated calomel electrode as the reference electrode. Working electrodes were polished with 0.05 μm alumina paste and washed with distilled water and acetone before each measurement. The complexes were dissolved in CH_2Cl_2 containing the necessary amount of *n*-Bu₄NPF₆ (TBAPF₆) as the supporting electrolyte to yield a 0.1 M ionic strength solution. $E_{1/2}$ values reported in this work were estimated from CV experiments as the average of the oxidative and reductive peak potentials ($E_{\text{pa}} + E_{\text{pc}}$)/2. UV–vis spectroscopy was performed on a Cary 50 (Varian) UV–vis spectrophotometer in 1 cm quartz cuvettes. Mass spectrometry analysis were performed in a mass spectrometer with time-of-flight matrix-assisted laser desorption ionization (Bruker Autoflex). Elemental analyses were performed on an EA-1108 CHNS-O elemental analyzer from Fisons Instruments (Universidad de Santiago). $[\alpha]_{\text{D}}$ was measured in a Jasco P-1030 polarimeter with symmetric angular oscillation for the sodium D line and a photomultiplier tube detector. Angular range: ± 90 °C. A Jasco spectropolarimeter (model J-715; Jasco Inc., Easton, MD) interfaced to a computer (J700 software) was used for circular dichroism (CD) measurements at a constant temperature of 25 °C, maintained by a Peltier PTC-351S apparatus (TE Technology Inc., Traverse City, MI), in CH_2Cl_2 . All spectra were recorded with 0.2 cm capped quartz cuvettes.

Computational Details. The density functional theory (DFT) calculations have been carried out with the hybrid B3PW91 functional,¹⁴ as implemented in the Gaussian 03 package.¹⁵ The Ru atoms have been represented with the quasi-relativistic effective core pseudopotentials of the Stuttgart group and the associated basis sets augmented with an f polarization function ($\alpha = 1.235$).¹⁶ The remaining atoms (C, N, P, Cl, and H) have been represented with 6-31G(d,p) basis sets.¹⁷ The B3PW91 geometry optimizations were performed without any symmetry constraints, and the nature of minima was checked by analytical frequency calculations. The energies given throughout the paper are electronic energies without zero-point-energy (ZPE) corrections (inclusion of the ZPE corrections does not significantly modify the results). These energies contain also solvent effects calculated with the polarizable continuum solvation model using ethanol as the solvent.¹⁸ These solvent effects include contributions of nonelectrostatic terms and have been estimated in single-point-energy calculations on the gas-phase-optimized structures.

RESULTS AND DISCUSSION

Synthesis and Characterization. The synthetic strategy that we have followed for preparation of the (-)-L1 ligand is outlined in Scheme 1. This strategy is based on the diastereoselective alkylation of the pyridyl-pinene-aldehyde [(-)-4; Scheme 1]. The latter is a very convenient chiral building block intermediate for the synthesis of a wide variety of polypyridylic ligands via simple Schiff-base chemistry, as we have previously shown with related (nonalkylated) aldehyde scaffolds.^{7b–d} The synthetic pathway followed started with the furan derivative (-)-I developed by Bernhard and co-workers¹² (Scheme 1). Methylation of (-)-I at the methylene group

Scheme 1. Synthetic Pathway for the (–)-L1 Ligand



adjacent to the pyridine ring employing LDA and methyl iodide took place in a diastereoselective manner to form (–)-2 in good yield (74%).¹⁹

The next step consisted of the oxidative degradation of the furan substituent by employing a mixture of nitric acid and ammonium metavanadate. The carboxylic acid formed is esterified in situ with sulfuric acid in ethanol, and compound (–)-3 is obtained in 60% yield. Reduction of the obtained ester (–)-3 with LiAlH₄ resulted in formation of the desired (–)-4 and (–)-5 as minor byproducts. The two products were separated by column chromatography on silica gel (see the Experimental Section for further details), obtaining (–)-4 in 60% yield. The slow and careful addition of NaBH₄ was then employed for the almost quantitative reduction of (–)-4 to alcohol (–)-5 (92% yield). The subsequent formation of (–)-6 in quantitative yield was obtained by the slow addition of SOCl₂ to (–)-5. Finally, a double nucleophilic attack of ethylamine over (–)-6 led to formation of the desired (–)-L1 ligand (54% yield).

(–)-L1 was characterized by NMR (1D and 2D), ESI-MS, and optical polarimetry (see the Experimental Section and Figures S16–S21 in the Supporting Information). The ¹H NMR spectrum of (–)-L1 is presented in Figure 1, together

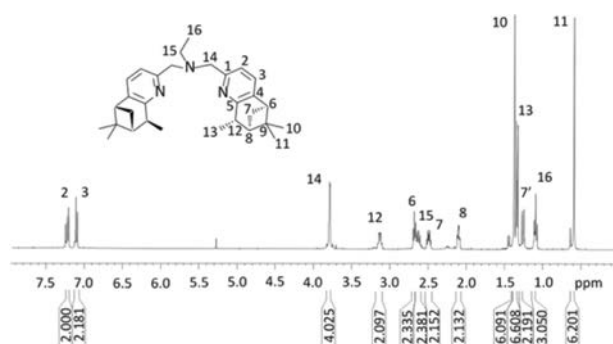


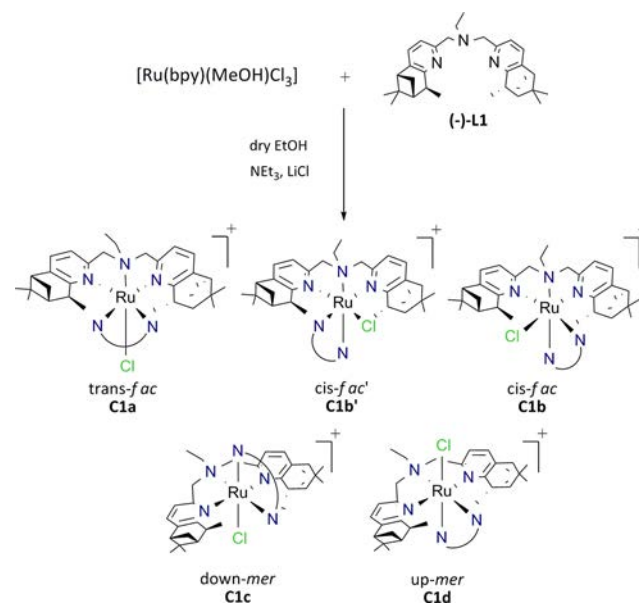
Figure 1. ¹H NMR spectrum of (–)-L1 and its corresponding labeling scheme.

with its corresponding labeling scheme. C₂ symmetry is observed in solution, and thus the two pyridine-pinene moieties are equivalent. This leads to 16 resonances that were unequivocally assigned to the corresponding protons after analysis of the homo- and heteronuclei bidimensional spectra.

Ru–Cl complexes were then prepared by employing [Ru(bpy)(MeOH)Cl₃] as the metal precursor. The sequence of ligand addition to the Ru metal center is reversed here with

regard to the previously related complexes containing the pinene[5,6]bpea and bpea ligands reported earlier,^{10,11} and actually this turns out to be essential in this particular case for preparation of the desired compounds. Attempts to coordinate the bpy ligand to a typical [Ru((–)-L1)Cl₃] intermediate were always unfruitful because of the increased bulkiness of the (–)-L1 ligand. Therefore, we used a solution of [Ru(bpy)(MeOH)Cl₃] in dry ethanol and added (–)-L1 and triethylamine to generate the corresponding complexes (Scheme 2).

Scheme 2. Synthetic Procedure and Potential Isomers of C1



The substitution of one methanol (MeOH) and two chlorido ligands by a flexible^{10,20} C₂-symmetric tridentate N-donor ligand such as (–)-L1 can potentially lead to a wide range of stereoisomers, as shown in Scheme 2. The flexibility of the mentioned ligands will allow them to coordinate in a facial or meridional manner around the octahedral Ru^{II} d⁶ metal center.

When the tridentate ligands act in a facial manner, then *cis* and *trans* isomers can be obtained depending on whether the Ru–Cl bond is *cis* or *trans* to the Ru–N_{aliphatic} bond, respectively. In the particular case of a *cis*/*fac* configuration, two possible isomers can be obtained and are depicted in Scheme 2 as C1b and C1b'. When the tridentate ligands act in a meridional fashion, two possibly isomers can be obtained depending on the relative orientation of the Ru–Cl bond with regard to the ethyl group of the aliphatic amine. These isomers are thus named *anti*,*mer*-C1c and *syn*,*mer*-C1d (Scheme 2).

Reaction of the [Ru(bpy)(MeOH)Cl₃] complex with (–)-L1 in dry ethanol at reflux for 24 h generates a mixture of complexes. A careful ¹H NMR analysis of the crude revealed the presence of two major complexes: *trans*,*fac*-C1a and *anti*,*mer*-C1c in a 84:16 ratio. Additionally, the NMR also showed the presence of small amounts of a third complex that could not be identified but that, on the basis of DFT, could be potentially assigned to C1d (*vide infra*). Overall we managed to account for 78% yield.

It is worth mentioning here that the introduction of two extra methyl groups to the pinene[5,6]bpea ligand [Chart 1; (–)-L1] produces an enhancement of the steric effects close to the metal center in such a way that the number of isomers obtained is now substantially lower.¹⁰ For this reason, in the present case,

we manage to obtain *trans, fac*-**C1a** as the major product. This was also the case for the achiral bpea ligand (Chart 1), where the main isomer obtained was *trans, fac*-[Ru(bpea)(bpy)Cl]⁺ (**C3a**).¹¹ Isolation of both **C1a** and **C1c** (Scheme 2) as pure isomers was accomplished by combining column chromatography and semipreparative thin layer chromatography (TLC), both having alumina as the solid phase. Elution of the former with 50:1 dichloromethane/methanol allowed us to obtain pure **C1a** (36% yield) and a mixture of **C1a** and **C1c**. Semipreparative TLC using the same elution conditions finally allowed us to isolate pure **C1c** (5% yield). In Figure S15 in the Supporting Information, the ¹H NMR of the reaction crude is plotted together with the ¹H NMR of the isolated isomers **C1a** and **C1c**. For these types of complexes, 1D and 2D NMR has been shown to be an extremely powerful tool to unambiguously identify and characterize the isolated isomers (Scheme 2). In particular, the chemical shift of the CH₂-N moieties is indicative of the presence of a facial or meridional disposition of (–)-**L1**. A chemical shift for the CH₂-N unit of around 6 ppm is indicative of meridional geometry, whereas a shift of more than 1 ppm to higher fields indicates facial coordination.²⁰ For **C1a**, this chemical shift is 4 ppm and thus is a clear indication of the facial geometry of (–)-**L1** in this compound. This is further corroborated by the absence of shifted bpy protons because of the fact that the bpy ligand is situated perpendicular to the Ru–Cl bond (see Figures S15 and S22 in the Supporting Information). 2D NOESY experiments allowed us to distinguish between the three potential facial isomers (**C1a**, **C1b**, and **C1b'**; Scheme 2). Two interactions between bpy and (–)-**L1** protons, H8 with H15 and H1 with H20, allow identification of the *trans, fac*-**C1a** isomer (Figure S22 in the Supporting Information). The assignment of the *anti, mer*-**C1c** isomer is based on three key observations. First, the chemical shift of CH₂-N at around 6 ppm suggests a meridional conformation.²⁰ Second, a deshielded doublet shifted to low fields (H1 of the bpy ligand in Figure S27 in the Supporting Information) reveals the presence of the Ru–Cl bond parallel to the bpy plane. Finally, a NOE interaction between H26a of (–)-**L1** and H8 of the bpy ligand (Figure S27 in the Supporting Information) clearly supports the presence of the *anti, mer*-**C1c** isomer.

The electrochemical properties of **C1a** and **C1c** were investigated by means of CV in dichloromethane (Figure S32 in the Supporting Information). *trans, fac*-**C1a** and *anti, mer*-**C1c** isomers exhibit chemically reversible and electrochemically quasi-reversible waves centered at $E_{1/2} = 0.79$ V ($\Delta E_p = 90$ mV) and 0.83 V ($\Delta E_p = 110$ mV), respectively. Therefore, σ donation of the tertiary amine of the (–)-**L1** ligand seems to be more effective when the N_{aliphatic}-Ru bond is *trans* to the Ru–Cl bond, decreasing the Ru^{III/II} redox potential by roughly 40 mV. A similar cathodic shift in the redox potentials is observed in a comparison of related meridional versus facial isomers of achiral bpea complexes, as has been previously reported.^{20a}

In the presence of light and in a CH₂Cl₂ solution, **C1c** is not stable and isomerizes toward the *trans, fac* isomer **C1a**. This transformation has been followed by ¹H NMR and is shown in Figure 2. After 24 h of irradiation, the *anti, mer* isomer **C1c** is no longer present in solution. The isomerization kinetics has also been followed by UV–vis spectroscopy (Figure S33 in the Supporting Information). A decrease in the absorbance at 395, 480, and 500 nm and the appearance of a new band at 530 nm are observed together with clean isosbestic points, indicating a neat interconversion between the two species. Under the same

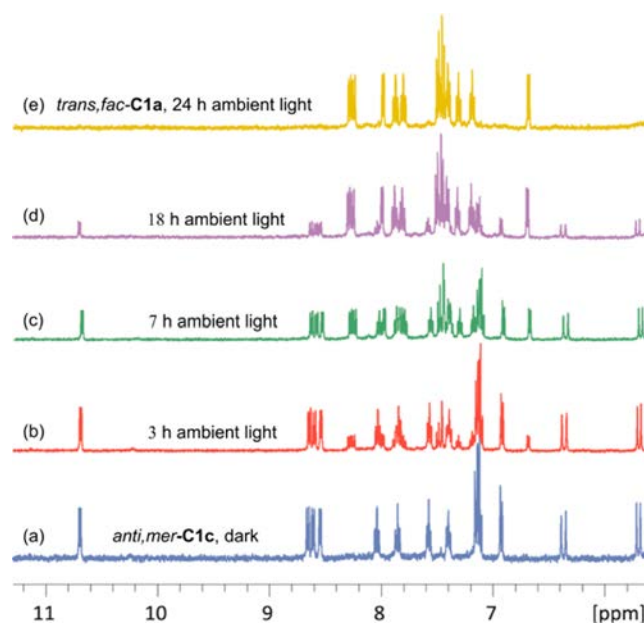


Figure 2. ¹H NMR spectra (aromatic region, CD₂Cl₂) monitoring the isomerization process of *anti, mer*-**C1c** to *trans, fac*-**C1a** triggered by ambient light irradiation.

conditions, but in the absence of light, there is no transformation at all, as indicated by UV–vis and ¹H NMR spectroscopy.

The isomerization of **C1c** → **C1a** can also be thermally promoted in the dark, by refluxing a solution of the former complex in 1,2-dichloroethane. In this case, the reaction is much slower, taking 168 h to proceed (Figure S35 in the Supporting Information).

The thermal *mer/fac* isomerization of a bpea ligand bound to a Ru^{II} metal ion was already described by us for the [Ru(Cl)₂(bpea)(DMSO)] complex.^{20b} In this case, a dissociative mechanism was proposed, in which one of the chlorido ligands was removed as the initial step. In order to gain a deeper understanding of this kind of process and assess the influence of the steric and electronic effects imposed by the ligands over the isomerization mechanism, DFT calculations were carried out for the **C1c** → **C1a** thermal process, where the facial isomer **C1a** is slightly more stable (1.3 kcal/mol) than the meridional isomer **C1c**. Two possible dissociative mechanisms were proposed as the initial hypothesis: a first one based on the dissociation of a pyridylic arm of the (–)-**L1** ligand (pathway a, Figure 3) and a second one based on the removal of the chlorido ligand (pathway b, Figure 3). The energies of the different calculated species involved in both mechanisms are represented in Figure 3. Following pathway a, one pyridyl ring of (–)-**L1** is first decoordinates to reach the transition state **TSI** by means of 34.4 kcal/mol. On the other hand, release of a chlorido ligand from **C1c** (pathway b) leads first to the formation of intermediate **II** and subsequently to pentacoordinated transition state **TSIII** through a highly energetically demanding reorganization process (44.1 kcal/mol). Further ligand reorganization allows the gathering of species **III** with the already facial coordination of (–)-**L1**. In general, decoordination of an “arm” of a chelating ligand is disfavored with regard to decoordination of a monodentate ligand.^{20b} In this case, the steric hindrance exerted by the pinene moieties precludes reorganization of the pentacoordinated species up to

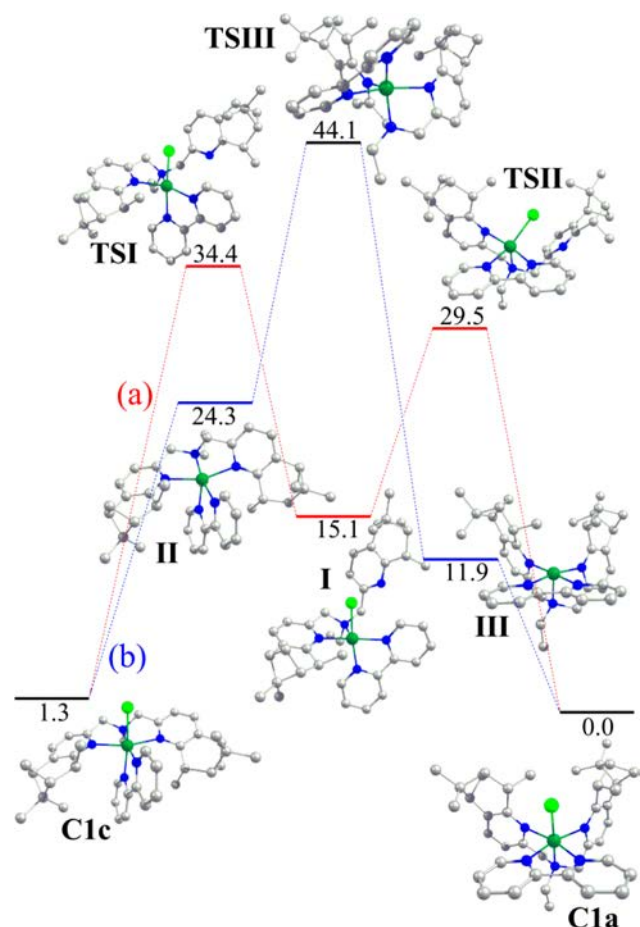


Figure 3. Relative energy diagram for the B3PW91 C1c → C1a isomerization.

44.1 kcal/mol, hampering the viability of this mechanism. However, decooordination of one pyridyl ring gives rise to a much more flexible intermediate, less sterically hindered and easier to reorganize to its facial form. These steric arguments would also explain why in the case of the previously reported [Ru(Cl)₂(bpea)(DMSO)] complex, in which no bulky ligands are used, the proposed *mer*-to-*fac* isomerization mechanism was based on the initial removal of a chlorido ligand.^{20b}

Stereoisomeric Analysis. DFT calculations were performed for the five potential isomers of C1, and their relative energy diagram is shown in Figure 4a. In the same figure, the relative energy diagram is compared with the ones reported recently for the two analogous complexes [Ru(pinene[5,6]-bpea)(bpy)Cl]⁺ (C2; Figure 4b) and ([Ru(bpea)(bpy)Cl]⁺ (C3; Figure 4c), containing respectively nonalkylated and achiral bpea scaffolds.¹⁰ Selected bond distances and angles are collected in Table S1 in the Supporting Information for all of the optimized structures of C1 together with reported data for C2 and C3, for purposes of comparison. To simplify the structural discussion for these complexes, the plane nearly perpendicular to the Ru–X bond (X = monodentate ligand) will be considered to be the equatorial plane.

For the C3 complexes containing the achiral bpea ligand, only the C3a isomer is obtained experimentally. This is due to the absence of a strong steric interaction and the presence of hydrogen bonding between the chlorido ligand and the CH groups situated in the α position with regard to the N atoms of the bpea pyridyl rings (see Figure 4c).¹⁰ Introduction of a

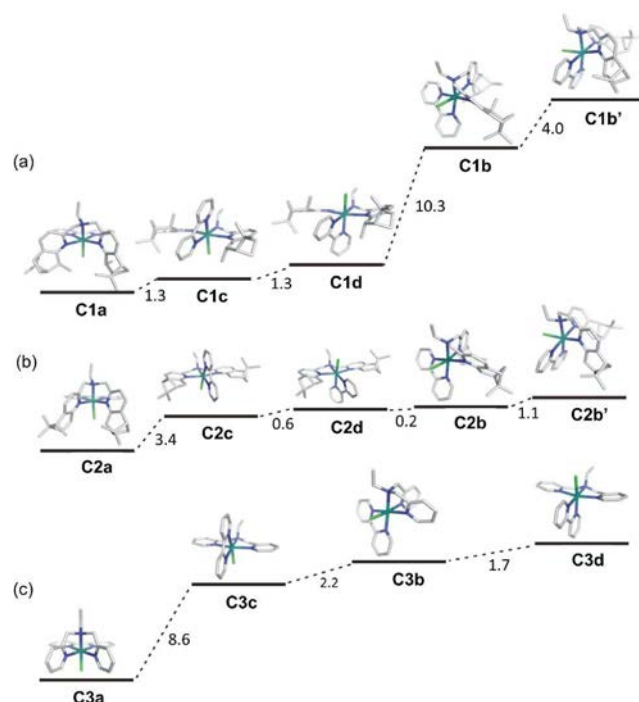


Figure 4. Relative energy diagram for the B3PW91-optimized geometries of the cationic moieties of (a) C1a–C1d, (b) C2a–C2d, and (c) C3a–C3d. Energies are given in kcal/mol. Color codes: ruthenium, light blue; chlorine, green; nitrogen, blue; carbon, gray.

pinene moiety in the 5 and 6 positions of the pyridylic bpea rings (pinene[5,6]bpea, Chart 1) produces large steric interactions and removes the potential hydrogen bonding mentioned above. As a consequence of this, the relative energies of the potential isomers are relatively similar and thus synthetically we obtain a mixture of isomers: *trans, fac*-C2a, *cis, fac*-C2b/C2b', and *syn, mer*-C2d (Figure 4b).¹⁰ Finally, the double alkylation of the pinene moieties in (–)-L1 provokes a further increase of the steric hindrance, clearly destabilizing the *cis, fac* isomers C1b and C1b' by 12.9 and 16.9 kcal/mol over *trans, fac*-C1a, respectively (Figure 4a), which is the more stable isomer in the present case. Strong repulsive steric interactions between the bpy ligand and one of the bulky Me-pinene groups of (–)-L1, both occupying the equatorial plane, are responsible for this energy increase. As a consequence of this, C1b/C1b' isomers present a large distortion of the octahedral geometry (see Figure 4a and Table S1 in the Supporting Information). An indication of the degree of this octahedral distortion is offered by the dihedral angles between the two pyridyl rings of (–)-L1. For C1b, this angle is 68.4°, whereas for C1b', it is 71.4°, while for an ideal geometry, these rings should be almost coplanar. This highly disfavored steric situation explains why these *cis, fac* isomers are not observed experimentally. In sharp contrast, the steric constraints clearly decrease when (–)-L1 coordinates meridionally to the Ru metal center. Now *anti, mer*-C1c and *syn, mer*-C1d are only 1.3 and 2.6 kcal/mol above the more stable *trans, fac*-C1a isomer. This enhanced stability of the *mer* isomers with regard to the *cis, fac* ones is due to the reduced steric hindrance between the bpy ligand and the pinene groups in this new geometry, as can be clearly observed in Figure 4. Nevertheless, there is still some remaining hindrance between the bpy pyridyl group *trans* to the chlorido ligand and (–)-L1, as can be inferred from the increased Ru–N_{bpy} distance from the typical 2.05 Å up to the 2.10 Å calculated for this isomer

(see, for instance, Ru–N4/N5 in Table S1 in the Supporting Information). Finally, the *trans,trans* disposition of (–)-L1 has the lowest steric hindrance between the bpy and pinene groups and thus becomes the most stable isomer. This is in total agreement with the fact that it is by far the major isomer obtained experimentally.

In conclusion, we have prepared a new chiral dialkylated pyridyl-pineno-fused aldehyde building block, (–)-4, which has been employed in the preparation of a new enantiopure derivative of the bpea ligand, (–)-L1. The combination of the latter with a [RuCl(bpy)]⁺ subunit afforded *trans,trans*-C1a as the major product together with *anti,mer*-C1c in much lesser amounts. The reduced isomeric mixture obtained here (when compared with the one previously reported for Ru–Cl complexes bearing a nonalkylated pineno-fused bpea ligand, C2) arises from the strong destabilization of *cis,trans*-C1b/C1b' isomers. As shown by their highly distorted DFT-calculated structures, the large steric repulsions between one of the bulky Me-pinene groups and a bpy pyridyl moiety occupying the equatorial plane produce the observed energy increase. Furthermore, the calculated thermodynamic instability of the *anti,mer* isomer versus its *trans,trans* counterpart is experimentally confirmed by the C1c → C1a thermo- and photoisomerization processes observed. Here again, for the thermal case, steric arguments (lower ligand reorganization energies) support the initial dissociation of a bpea pyridylic arm, as described by DFT, instead of a Ru–Cl decoordination pathway.

■ ASSOCIATED CONTENT

■ Supporting Information

Computational details and spectroscopic (1D and 2D NMR) and electrochemical measurements for the reported complexes, UV–vis spectra of the C1c → C1a isomerization process, and CD spectrum of C1a. This material is available free of charge via the Internet at <http://pubs.acs.org>.

■ AUTHOR INFORMATION

■ Corresponding Author

*E-mail: allobet@icqi.es (A.L.), xavier.sala@uab.cat (X.S.).

■ Notes

The authors declare no competing financial interest.

■ ACKNOWLEDGMENTS

Support from MINECO (Grants CTQ2011-26440, CTQ2010-21497, and CTQ2011-23156/BQU) is gratefully acknowledged. Financial help from the DIUE of the Generalitat de Catalunya (Projects 2009SGR637 and XRQTC) and the FEDER fund (European Fund for Regional Development) for Grant UNGI08-4E-003 is acknowledged. L.V. is grateful for the award of a FI doctoral grant from AGAUR. A.P. is grateful to the European Commission (Grant CIG09-GA-2011-293900), Spanish MICINN (Ramón y Cajal Contract RYC-2009-05226), and Generalitat de Catalunya (Grant 2011BE100793). Support for the research of M.S. was received through the ICREA Academia 2009 prize for excellence in research funded by the DIUE of the Generalitat de Catalunya.

■ REFERENCES

(1) (a) Baranoff, E.; Collin, J.-P.; Furusho, J.; Furusho, Y.; Laemmel, A.-C.; Sauvage, J.-P. *Inorg. Chem.* **2002**, *41*, 1215–1222. (b) Kelley, S. O.; Barton, J. K. *Science* **1999**, *283*, 375–381. (c) Schuster, G. B. *Acc. Chem. Res.* **2000**, *33*, 253–260. (d) Venturi, M.; Balzani, V.; Ballardini, R.; Credi, A.; Gandolfi, M. T. *Int. J. Photoenergy* **2004**, *6*, 1–10.

(e) Weatherly, S. C.; Yang, I. V.; Thorp, H. H. *J. Am. Chem. Soc.* **2001**, *123*, 1236–1237.

(2) (a) Keene, F. R. *Coord. Chem. Rev.* **1999**, *187*, 121–149. (b) Csajnyik, G.; Ell, A. H.; Fadini, L.; Pugin, B.; Bäckvall, J.-E. *J. Org. Chem.* **2002**, *67*, 1657–1662. (c) Bäckvall, J.-E., Ed. *Modern Oxidation Methods*, 2nd Completely Revised; Wiley-VCH Verlag GmbH & Co. KGaA: Berlin, 2010. (d) Stultz, L. K.; Binstead, R. A.; Reynolds, M. S.; Meyer, T. J. *J. Am. Chem. Soc.* **1995**, *117*, 2520–2532. (e) Sala, X.; Romero, I.; Rodríguez, M.; Escriche, L.; Llobet, A. *Angew. Chem., Int. Ed.* **2009**, *48*, 2842–2852. (f) Concepcion, J. J.; Jurss, J. W.; Templeton, J. L.; Meyer, T. J. *J. Am. Chem. Soc.* **2008**, *130*, 16462–16463. (g) Sala, X.; Poater, A.; Romero, I.; Rodríguez, M.; Llobet, A.; Solans, X.; Parella, T.; Santos, T. M. *Eur. J. Inorg. Chem.* **2004**, 612–618. (h) Duan, L.; Bozoglian, F.; Mandal, S.; Stewart, B.; Privalov, T.; Llobet, A.; Sun, L. *Nat. Chem.* **2012**, *4*, 418–423.

(3) (a) Mashima, K.; Kusano, K.-h.; Sato, N.; Matsumura, Y.-i.; Nozaki, K.; Kumobayashi, H.; Sayo, N.; Hori, Y.; Ishizaki, T. *J. Org. Chem.* **1994**, *59*, 3064–3076. (b) Ohta, T.; Miyake, T.; Seido, N.; Kumobayashi, H.; Takaya, H. *J. Org. Chem.* **1995**, *60*, 357–363. (c) Arai, N.; Azuma, K.; Nii, N.; Ohkuma, T. *Angew. Chem., Int. Ed.* **2008**, *47*, 7457–7460. (d) Federsel, C.; Jackstell, R.; Beller, M. *Angew. Chem., Int. Ed.* **2010**, *49*, 6254–6257. (e) Jessop, P. G. *Handb. Homogeneous Hydrogenation* **2007**, *1*, 489–511. (f) Jessop, P. G.; Joo, F.; Tai, C. C. *Coord. Chem. Rev.* **2004**, *248*, 2425–2442. (g) Planas, N.; Ono, T.; Vaquer, L.; Miro, P.; Benet-Buchholz, J.; Gagliardi, L.; Cramer, C. J.; Llobet, A. *Phys. Chem. Chem. Phys.* **2011**, *13*, 19480–19484.

(4) (a) Tse, M. K.; Bhor, S.; Klawonn, M.; Anikumar, G.; Haijun, J.; Doebler, C.; Spannenbert, A.; Maegerlein, W.; Hugl, H.; Beller, M. *Chem.—Eur. J.* **2006**, *12*, 1855–1874. (b) Tse, M.; Bhor, S.; Klawonn, M.; Anikumar, G.; Haijun, J.; Anke, S.; Doebler, C.; Maegerlein, W.; Hugl, H.; Beller, M. *Chem.—Eur. J.* **2006**, *12*, 1875–1888. (c) Serrano, I.; Rodríguez, M.; Romero, I.; Llobet, A.; Parella, T.; Campelo, J. M.; Luna, D.; Marinas, J. M.; Benet-Buchholz, J. *Inorg. Chem.* **2006**, *45*, 2644–2651. (d) Sala, X.; Plantalech, E.; Romero, I.; Rodríguez, M.; Llobet, A.; Poater, A.; Duran, M.; Solà, M.; Jansat, S.; Gómez, M.; Parella, T.; Stoeckli-Evans, H.; Benet-Buchholz, J. *Chem.—Eur. J.* **2006**, *12*, 2798–2807. (e) Sala, X.; Serrano, I.; Rodríguez, M.; Romero, I.; Llobet, A.; van Leeuwen, P. W. N. M. *Catal. Commun.* **2009**, *9*, 117–119. (f) Chatterjee, D. *Coord. Chem. Rev.* **2008**, *252*, 176–198.

(5) (a) Pfaltz, A.; Drury, W. J., III. *Proc. Natl. Acad. Sci. U.S.A.* **2004**, *101*, 5723–5726. (b) Yoon, T. P.; Jacobsen, E. N. *Science* **2003**, *299*, 1699–1693.

(6) Sala, X.; Rodríguez, A. M.; Rodríguez, M.; Romero, I.; Parella, T.; von Zelewsky, A.; Llobet, A.; Benet-Buchholz, J. *J. Org. Chem.* **2006**, *71*, 9283–9290.

(7) (a) Rich, J.; Rodríguez, M.; Romero, I.; Vaquer, L.; Sala, X.; Llobet, A.; Corbella, M.; Collomb, M.-N.; Fontrodona, X. *Dalton Trans.* **2009**, 8117–8126. (b) Gómez, L.; García-Bosch, I.; Company, A.; Sala, X.; Fontrodona, X.; Ribas, X.; Costas, M. *Dalton Trans.* **2007**, 5539–5545. (c) Gómez, L.; García-Bosch, I.; Company, A.; Benet-Buchholz, J.; Polo, A.; Sala, X.; Ribas, X.; Costas, M. *Angew. Chem., Int. Ed.* **2009**, *48*, 5720–5723. (d) Rich, J.; Rodríguez, M.; Romero, I.; Fontrodona, X.; van Leeuwen, P. W. N. M.; Freixa, Z.; Sala, X.; Poater, A.; Solà, M. *Eur. J. Inorg. Chem.* **2013**, 1213–1224.

(8) For instance, see: (a) Aharoni, A.; Vidavsky, Y.; Diesendruck, C. E.; Ben-Asuly, A.; Goldberg, I.; Lemcoff, N. G. *Organometallics* **2011**, *30*, 1607–1615. (b) Fachetti, G.; Cesarotti, E.; Pellizzoni, M.; Zerla, D.; Rimoldi, I. *Eur. J. Inorg. Chem.* **2012**, 4365–4370. (c) Ciancaleoni, G.; Fraldi, N.; Cipullo, R.; Busico, V.; Maccioni, A.; Budzelaar, P. H. M. *Macromolecules* **2012**, *45*, 4046–4053. (d) Roeser, S.; Farras, P.; Bozoglian, F.; Martínez-Belmonte, M.; Benet-Buchholz, J.; Llobet, A. *ChemSusChem* **2011**, *4*, 197–207. (e) Sens, C.; Rodríguez, M.; Romero, I.; Llobet, A.; Parella, T.; Sullivan, B. P.; Benet-Buchholz, J. *Inorg. Chem.* **2003**, *42*, 2040–2048. (f) Serrano, I.; López, M. I.; Ferrer, I.; Poater, A.; Parella, T.; Fontrodona, X.; Solà, M.; Llobet, A.; Rodríguez, M.; Romero, I. *Inorg. Chem.* **2011**, *50*, 6044–6054.

(9) (a) von Zelewsky, A. *Stereochemistry of Coordination Compounds*; Wiley: New York, 1998. (b) von Zelewsky, A. *Coord. Chem. Rev.* **1999**, *190–192*, 811–825.

(10) Sala, X.; Poater, A.; von Zelewsky, A.; Parella, T.; Fontrodona, X.; Romero, I.; Solà, M.; Rodríguez, M.; Llobet, A. *Inorg. Chem.* **2008**, *47*, 8016–8024.

(11) Rodríguez, M.; Llobet, A.; Romero, I.; Deronzier, A.; Biner, M.; Parella, T.; Stoeckli-Evans, H. *Inorg. Chem.* **2001**, *40*, 4150–4156.

(12) Sauer, A. L.; Ho, D. M.; Bernhard, S. *J. Org. Chem.* **2004**, *69*, 8910–8915.

(13) Eskelinen, E.; Da Costa, P.; Haukka, M. *J. Electroanal. Chem.* **2005**, *579*, 257–265.

(14) (a) Becke, A. D. *J. Chem. Phys.* **1993**, *98*, 5648–5652.

(b) Perdew, J. P.; Wang, Y. *Phys. Rev. B* **1992**, *45*, 13244–13249.

(15) Frisch, M. J.; Trucks, G. W.; Schlegel, H. B.; Scuseria, G. E.; Robb, M. A.; Cheeseman, J. R.; Montgomery, J. A., Jr.; Vreven, T.; Kudin, K. N.; Burant, J. C.; Millam, J. M.; Iyengar, S. S.; Tomasi, J.; Barone, V.; Mennucci, B.; Cossi, M.; Scalmani, G.; Rega, N.; Petersson, G. A.; Nakatsuji, H.; Hada, M.; Ehara, M.; Toyota, K.; Fukuda, R.; Hasegawa, J.; Ishida, M.; Nakajima, T.; Honda, Y.; Kitao, O.; Nakai, H.; Klene, M.; Li, X.; Knox, J. E.; Hratchian, H. P.; Cross, J. B.; Bakken, V.; Adamo, C.; Jaramillo, J.; Gomperts, R.; Stratmann, R. E.; Yazyev, O.; Austin, A. J.; Cammi, R.; Pomelli, C.; Ochterski, J. W.; Ayala, P. Y.; Morokuma, K.; Voth, G. A.; Salvador, P.; Dannenberg, J. J.; Zakrzewski, V. G.; Dapprich, S.; Daniels, A. D.; Strain, M. C.; Farkas, O.; Malick, D. K.; Rabuck, A. D.; Raghavachari, K.; Foresman, J. B.; Ortiz, J. V.; Cui, Q.; Baboul, A. G.; Clifford, S.; Cioslowski, J.; Stefanov, B. B.; Liu, G.; Liashenko, A.; Piskorz, P.; Komaromi, I.; Martin, R. L.; Fox, D. J.; Keith, T.; Al-Laham, M. A.; Peng, C. Y.; Nanayakkara, A.; Challacombe, M.; Gill, P. M. W.; Johnson, B.; Chen, W.; Wong, M. W.; Gonzalez, C.; Pople, J. A. *Gaussian 03*, revision C.02; Gaussian, Inc.: Wallingford, CT, 2004.

(16) (a) Andrae, D.; Haussermann, U.; Dolg, M.; Stoll, H.; Preuss, H. *Theor. Chim. Acta* **1990**, *77*, 123–141. (b) Bergner, A.; Dolg, M.; Kuchle, W.; Stoll, H.; Preuss, H. *Mol. Phys.* **1993**, *80*, 1431–1444.

(17) (a) Hehre, W. J.; Ditchfield, R.; Pople, J. A. *J. Chem. Phys.* **1972**, *56*, 2257–2261. (b) Hariharan, P. C.; Pople, J. A. *Theor. Chim. Acta* **1973**, *28*, 213–222.

(18) (a) Barone, V.; Cossi, M. *J. Phys. Chem. A* **1998**, *102*, 1995–2001. (b) Tomasi, J.; Persico, M. *Chem. Rev.* **1994**, *94*, 2027–2094.

(19) (a) Loetscher, D.; Rupprecht, S.; Collomb, P.; Belsler, P.; Viebrock, H.; von Zelewsky, A.; Burger, P. *Inorg. Chem.* **2001**, *40*, 5675–5681. (b) Malkov, A. V.; Bell, M.; Castelluzzo, F.; Kocovski, P. *Org. Lett.* **2005**, *7*, 3219–3222.

(20) (a) Mola, J.; Rodríguez, M.; Romero, I.; Llobet, A.; Parella, T.; Poater, A.; Duran, M.; Solà, M.; Benet-Buchholz, J. *Inorg. Chem.* **2006**, *45*, 10520–10529. (b) Poater, A.; Mola, J.; Gallegos Saliner, A.; Romero, I.; Rodríguez, M.; Llobet, A.; Solà, M. *Chem. Phys. Lett.* **2008**, *458*, 200–204. (c) Mola, J.; Romero, I.; Rodríguez, M.; Bozoglian, F.; Poater, A.; Solà, M.; Parella, T.; Benet-Buchholz, J.; Fontrodona, X.; Llobet, A. *Inorg. Chem.* **2007**, *46*, 10707–10716.

Cite this: *Dalton Trans.*, 2017, **46**, 11768

Dissimilar catalytic behavior of molecular or colloidal palladium systems with a new NHC ligand†

Fernando Gómez-Villarraga,^{‡a} Jonathan De Tovar,^{‡a} Miguel Guerrero,^{‡b,c} Pau Nolis,^{‡d} Teodor Parella,^d Pierre Lecante,^e Nuria Romero,^a Lluís Escriche,^a Roger Bofill,^a Josep Ros,^a Xavier Sala,^a Karine Philippot,^{*b,c} and Jordi García-Antón^{‡*a}

In this work, we describe the synthesis of a new N-heterocyclic carbene (NHC) ligand, derived from a hybrid pyrazole-imidazolium scaffold, namely 1-[2-(3,5-dimethylpyrazol-1-yl)ethyl]-3-((S)-1-phenylethyl)-3H-imidazol-2-ylidene (**L**). This ligand has been used as a stabilizer for the organometallic synthesis of palladium(0) nanoparticles (Pd NPs). **L** presents a better stabilizing effect than its pre-carbenic **HLCl** counterpart, allowing the formation of isolated Pd NPs while **HLCl** yields aggregated ones. Additionally, molecular Pd(II) coordination compounds of **L** and **HLCl** were synthesized and characterized to better understand the coordination modes of these ligands. Both molecular and colloidal Pd systems have been further tested in catalytic C–C coupling processes. Three different types of reactions have been observed depending on the catalytic system: (i) the Suzuki–Miyaura reaction takes place with Pd molecular complexes; (ii) a secondary reaction, the dehalogenation of the substrate, is always detected and (iii) the C–C homocoupling between two molecules of bromoarenes is observed with colloidal catalysts.

Received 26th July 2017,
Accepted 7th August 2017

DOI: 10.1039/c7dt02729j

rsc.li/dalton

Introduction

During the last few years, the use of N-heterocyclic carbenes (NHCs) as primary ligands has emerged in catalysis and beyond. Amongst other catalytic processes, organometallic compounds containing these ligands have been applied in the cross-coupling reactions of un-activated substrates.¹ This can be explained not only by their remarkably strong σ -binding and steric tunability,² but also by their ability to stabilize highly unusual and hitherto elusive reactive species such as metal nanoparticles (MNPs) thanks to their stability under

oxidative conditions once coordinated.³ Thus, NHCs have become ligands of paramount importance in nanochemistry given their advantageous behavior for the stabilization and functionalization of MNPs.⁴ Although different families of NHCs have been largely explored in various important organic transformations when combined with metal pre-catalysts, imidazolium salts are the most frequently employed as the core structures for NHCs given their straightforward syntheses and feasible tuning properties.⁵

Different methodologies can be followed to obtain and stabilize NPs in different media while controlling their size, shape and composition, which, in turn, can tune their unique properties.⁶ The use of coordinating ligands is of particular interest to prepare MNPs because it gives the possibility of modulating their surface properties as known for the synthesis of molecular complexes.⁷ As a consequence, ligand-stabilized MNPs became very attractive for applications in catalysis.⁸ MNPs are able to catalyze not only reactions that can also be catalyzed by molecular complexes (*i.e.* C–C coupling or hydrogenation of olefins) but also reactions that cannot be catalyzed by molecular complexes (*i.e.* hydrogenation of arenes).

Furthermore, palladium is the most versatile transition metal in chemical catalytic reactions since many of these processes cannot be catalyzed by other transition metals.⁹ Thus, Pd(0) NPs have shown large catalytic efficiency in C–C coupling

^aDepartament de Química, Unitat de Química Inorgànica, Facultat de Ciències, Universitat Autònoma de Barcelona, 08193-Bellaterra, Barcelona, Spain.

E-mail: Jordi.GarciaAnton@uab.es; Fax: (+34) 93 581 3101

^bCNRS, LCC (Laboratoire de Chimie de Coordination du CNRS), 205, route de Narbonne, F-31077 Toulouse, France. E-mail: Karine.Philippot@lcc-toulouse.fr; Fax: (+33) 5 61553003

^cUniversité de Toulouse, UPS, INPT, LCC, F-31077 Toulouse, France

^dServei de Ressonància Magnètica Nuclear, Facultat de Ciències, Universitat Autònoma de Barcelona, 08193 Cerdanyola del Vallès, Barcelona, Catalonia, Spain

^eCNRS, CEMES (Centre d'Elaboration de Matériaux et d'Etudes Structurales), 29 rue J. Marvig, F-31055 Toulouse, France

†Electronic supplementary information (ESI) available. CCDC 1432563. For ESI and crystallographic data in CIF or other electronic format see DOI: 10.1039/c7dt02729j

‡These authors equally contributed to this work.



reactions specially when non-aggregated homogeneous NPs of 1–4 nm size are used as catalysts.¹⁰

The Suzuki–Miyaura reaction is one of the most important cross-coupling processes from an industrial point of view.¹¹ It allows to easily obtain biaryl products, important intermediates in the organic syntheses of various target products ranging from performance materials to pharmaceuticals.¹² Although noble metal complexes are usually employed as catalysts for this reaction, MNPs merit study since playing with stabilizing ligands may tune their catalytic performance.¹³

Our research group has focused on discerning the catalytic behavior of colloidal and molecular palladium systems in C–C coupling reactions. For example, we have recently studied Pd molecular/colloidal systems containing new hybrid pyrazole derived ligands with alkylether, alkylthioether or alkylamino moieties leading to different catalytic outputs depending on the system.¹⁴ Here we present improved Pd systems based on a new NHC–pyrazole hybrid ligand. Interestingly, as it will be described hereafter, different behaviors were observed in C–C coupling catalysis that illustrates the possibility of optimizing the catalytic system according to the final aim.

Results and discussion

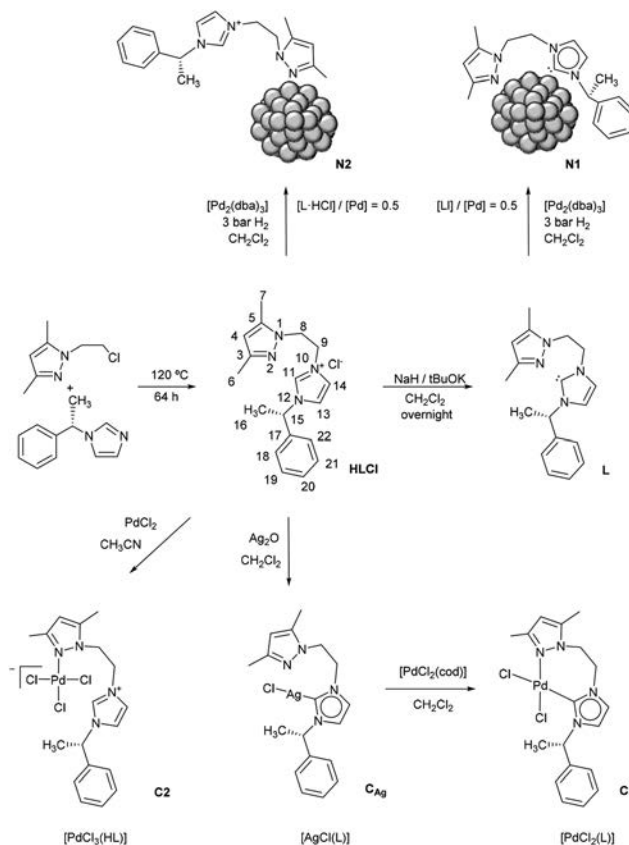
Synthesis of the ligand (L)

For the synthesis of 1-[2-(3,5-dimethylpyrazol-1-yl)ethyl]-3-((*S*)-1-phenylethyl)-3*H*-imidazol-1-ium chloride (**HLCl**), 1-(2-chloroethyl)-3,5-dimethyl-1*H*-pyrazole and 1-(*S*)-(phenylethyl)imidazole were heated solventless at 120 °C for 64 h. The deprotonation of **HLCl** to yield 1-[2-(3,5-dimethylpyrazol-1-yl)ethyl]-3-((*S*)-1-phenylethyl)-3*H*-imidazol-2-ylidene (**L**) was achieved by reacting **HLCl** with NaH and a catalytic amount of *t*BuOK in anhydrous dichloromethane (Scheme 1). Both **L** and **HLCl** have been fully characterized by NMR and IR spectroscopies as well as by ESI-MS (Fig. S1–S6 in the ESI†).

Synthesis of Pd(0) nanoparticles (Pd NPs)

Ligand **L** has been used to prepare Pd NPs according to the organometallic approach under mild reaction conditions.¹⁵ The syntheses have been carried out by reacting [Pd₂(dba)₃] (dba = dibenzylideneacetone) and **L** ([**L**]/[Pd]) molar ratios varying from 0.1 to 1.0) in anhydrous dichloromethane for 18 h in a Fisher-Porter reactor, under 3 bar of dihydrogen at room temperature. Finally, Pd NPs were precipitated and washed with cold pentane and dried under reduced pressure.

TEM (transmission electron microscopy) and SEM (scanning electron microscopy) analyses (after deposition/drying of a drop of crude colloidal solutions onto a holey carbon-covered copper grid) were performed with all the obtained samples. The results showed that the Pd NPs are aggregated into superstructures when a **L**/Pd ratio of 0.1 is used (HR-TEM images are shown in Fig. 1a and SEM-FEG images are shown in ESI, Fig. S7a†). The single NPs are spherical and have a mean size of 3.6(0.9) nm but the superstructures do not have a preferential shape and their size varies from 50 to 250 nm. For



Scheme 1 Synthetic preparation of **L** and **HLCl** and their corresponding Ag and Pd molecular complexes (**C_{Ag}**, **C1** and **C2**) and Pd nanoparticulate systems (**N1** and **N2**).

L/Pd ratios of 0.3, 0.5 and 1.0, only isolated NPs were observed (Fig. 1b–d). In all these cases, NPs are spherical and present similar mean sizes in the range of 2.1–2.4 nm. These similar sizes indicate that a minimum **L**/Pd molar ratio of 0.3 is needed to have stable isolated NPs, but the addition of a higher ligand/metal ratio does not have a significant effect on the size of the NPs.

For comparative purposes, the stabilization of the NPs has also been attempted with the protonated ligand **HLCl** (see HR-TEM images in Fig. 2 and SEM-FEG images in ESI, Fig. S7b–d†). In this case, a molar ratio of 0.1 failed to afford stable NPs. For molar ratios of 0.3 and 0.5 Pd NPs appeared organized into superstructures, and for the molar ratio of 1.0, a mixture of isolated and aggregated NPs was observed. The mean sizes of these NPs are 3.0(0.7), 3.2(0.9) and 2.1(0.9) nm for **HLCl**/Pd molar ratios of 0.3, 0.5 and 1.0, respectively. Therefore, with **HLCl** a higher ratio of ligand is needed to successfully stabilize the NPs. From these results and given the main difference of the two ligands (**L** is a carbene while **HLCl** is not deprotonated), we believe that the stabilization of the Pd NPs takes place by the coordination of **L** through the carbene (M–C) and pyrazolic (M–N) groups to the surface of the Pd NPs whereas **HLCl** would only coordinate through the pyrazolic group (Scheme 1).



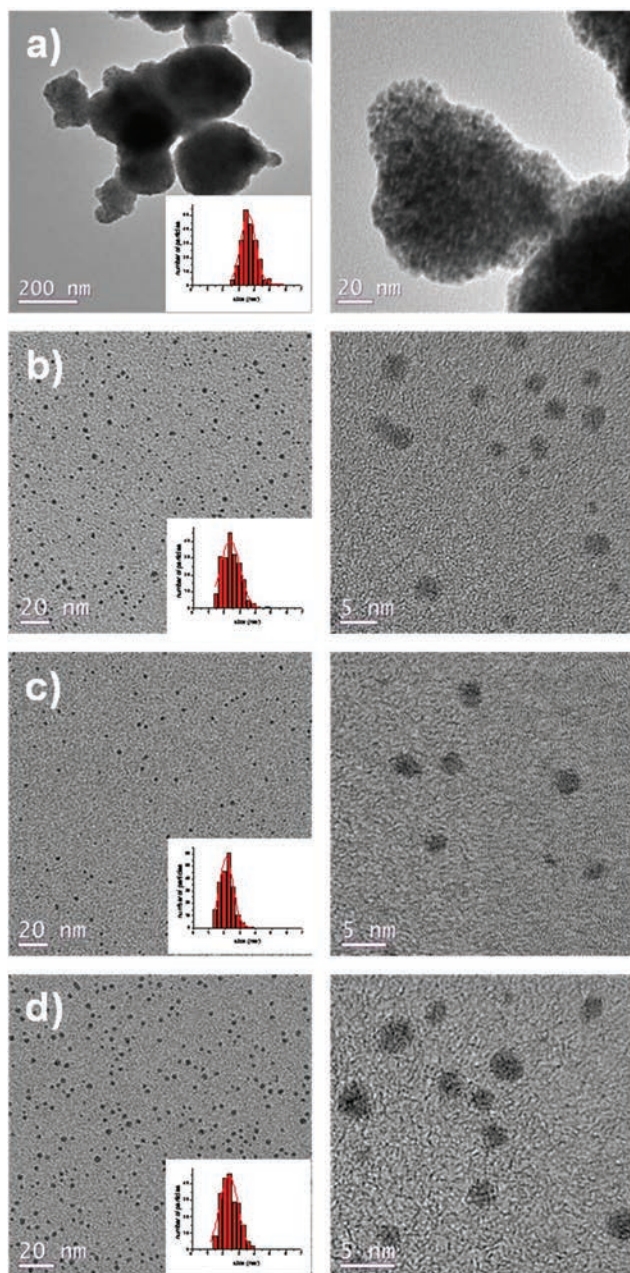


Fig. 1 HR-TEM micrographs and the corresponding size-histograms of Pd nanoparticles stabilized with L synthesized as follows: (a) [L]/[Pd] = 0.1; (b) [L]/[Pd] = 0.3; (c) [L]/[Pd] = 0.5; (d) [L]/[Pd] = 1.0.

The presence of the ligands L or HLCl in N1 or N2 (those prepared with L and HLCl, respectively, in a ligand/Pd molar ratio equal to 0.5) has been demonstrated by IR spectroscopy (Fig. S8† and the Experimental section), and ICP-OES and elemental analyses. The Pd/ligand ratios found are Pd₅₆₁L₃₇ and Pd₁₄₁₅HLCl₉₃ for N1 and N2, respectively.

Wide-angle X-ray scattering (WAXS) measurements have been performed on nanoparticles N1 and N2. The two radial distribution functions (RDFs) (Fig. 3a) are very similar and in good agreement with the fcc structure of bulk Pd. However, significant distances can be observed of at least up to 4 nm,

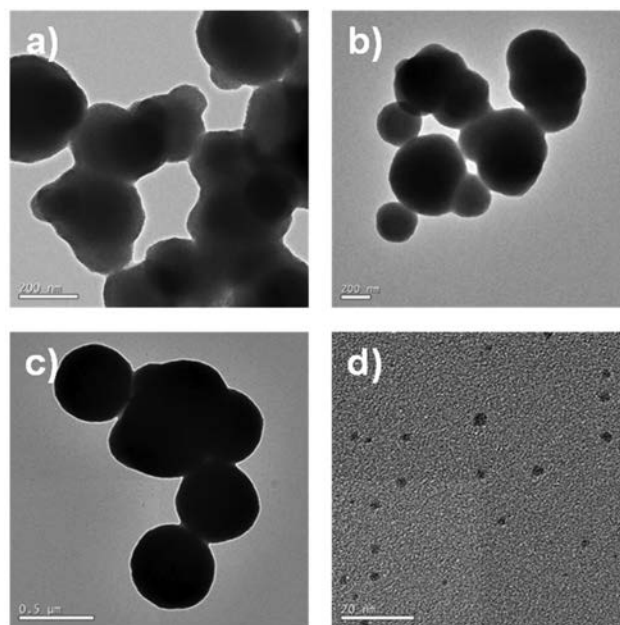


Fig. 2 HR-TEM micrographs and the corresponding size-histograms of Pd nanoparticles stabilized with HLCl synthesized as follows: (a) [HLCl]/[Pd] = 0.3; (b) [HLCl]/[Pd] = 0.5; (c) and (d) [HLCl]/[Pd] = 1.0.

thus being in disagreement with the sizes obtained from HR-TEM (2.1(0.9) and 3.2(0.9) for N1 and N2, respectively). Indeed, when compared with the RDF computed (Fig. 3b) from a spherical model 2.0 nm in diameter, the agreement does not go beyond 1.5 nm. A much better result can be obtained with a dual size model, including a small amount (10%) of much bigger spherical particles (5 nm in diameter). Actually, this dual size model is likely itself oversimplified and different combinations including a large majority of 2 nm particles and a minority of bigger ones should probably lead to the same level of agreement. This result, however, is not in contradiction with the TEM results taking into account not only the mean sizes but also the relatively large tail on the bigger size side.

Synthesis and characterization of Pd(II) molecular complexes (C1–C2)

Pd(II) molecular complexes of L and HLCl have been synthesized in order to better understand the coordination properties of these ligands (Scheme 1).

The silver carbene transmetalation reaction is a general procedure for the preparation of palladium–carbene complexes¹⁶ and was considered to obtain the Pd complex with L. The silver complex of L (C_{Ag}) was prepared by reacting silver dioxide and HLCl in anhydrous dichloromethane. The ¹H NMR spectrum of this complex shows that the pre-carbene proton of the imidazolium salt is no longer present, thus confirming the deprotonation of the imidazolium group and formation of the Ag–NHC bond (Fig. 4 and Fig. S9†). Also, the formation of C_{Ag} has been confirmed by ESI-MS and IR spectroscopy (Fig. S10 and S11,† respectively). The next step consisted of the reaction of C_{Ag} with [PdCl₂(cod)] in anhydrous



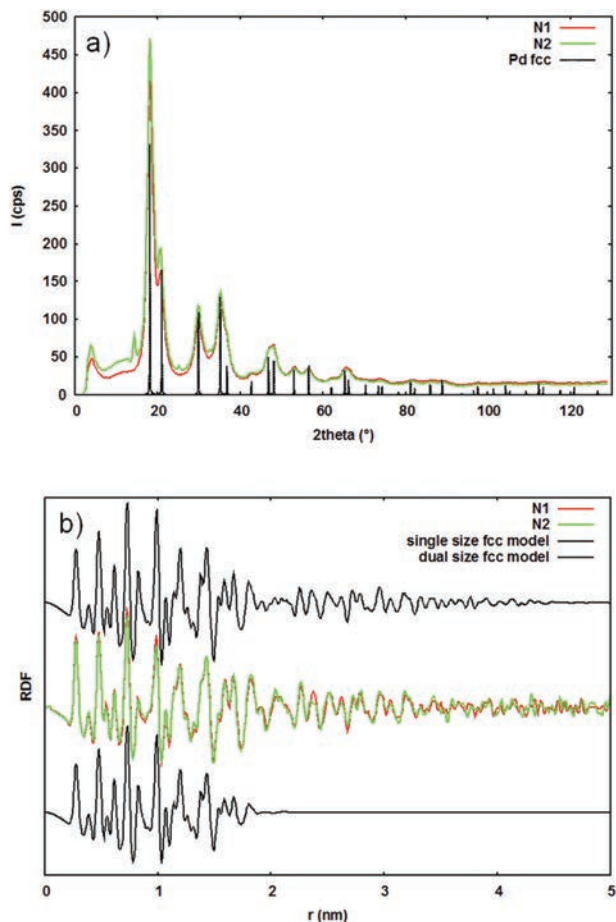


Fig. 3 WAXS measurements on Pd nanoparticles for N1 and N2 and comparison with Pd fcc in reciprocal space (a) and real space including simulated from a model including only 2 nm particles based on the Pd fcc structure (lower) and simulated from a model including 2 nm particles plus 10% of 5 nm particles (upper) (b).

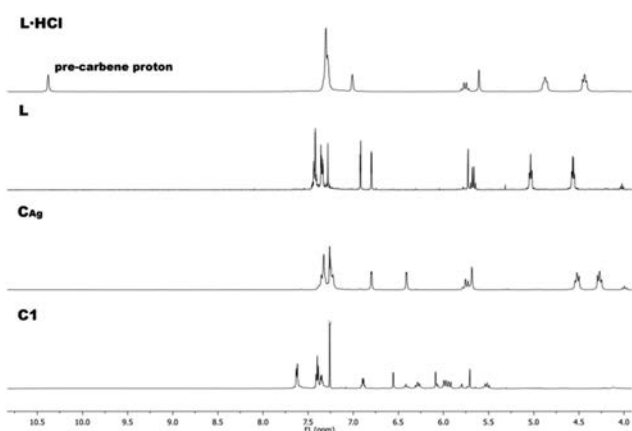


Fig. 4 ^1H -NMR of HLCl, L and C_{Ag} registered at 360 MHz (CDCl_3 , 298 K) and C1 registered at 600 MHz (CDCl_3 , 298 K).

dichloromethane (Scheme 1) to obtain the carbenic Pd complex $[\text{PdCl}_2\text{L}]$ (C1). The absence of the pre-carbene proton in the ^1H -NMR spectrum of C1 confirms the formation of the

Pd-NHC bond (Fig. 4 and Fig. S12 \dagger). The formation of the complex has been attested by HR-ESI-MS and IR spectroscopy (Fig. S13 and S14, \dagger respectively). Moreover, the NMR data also evidence the chelation of the ligand to the metallic centre through the NHC and pyrazolic groups. The rigidity imposed by this coordination mode causes the two protons of each CH_2 in the $\text{N-CH}_2\text{CH}_2\text{-N}$ moiety (H_8 and H_9) to become diastereotopic, resulting in four visible signals assigned to a single hydrogen atom each (see high-resolution NMR spectra of C1 including ^1H and ^{13}C NMR spectroscopy chemical shift assignments in Fig. S12a and b \dagger). It is also noticeable that some proton signals split, which is a single quote labeled in Fig. S12a. \dagger This splitting is due to conformational exchange between a major and a minor component with a ratio of approximately 70/30, as deduced from signal integration.

In order to study further this chemical exchange process, a 2D ROESY (Rotating Frame Overhauser Effect Spectroscopy) spectrum was recorded. 17 Briefly explained, in this NMR experiment ROE and occasionally chemical exchange cross peaks are observed. 18 The former are indicative of through space distance proximity, and the latter are detected when protons experience distinct chemical environments, which is commonly the case when a conformational equilibrium is present. The distinction of the above mentioned different cross peaks families is possible from the opposite signal phase in the ROESY spectrum. Fig. 5 and S12d \dagger show the 2D ROESY spectrum of C1, where chemical exchange cross peaks are detected in the negative phase (blue color), while ROE cross peaks are positive phased (red color). Thus, protons H_8 and H_9 in the ethyl chain undergo a pronounced chemical environment exchange, with cross peaks situated notably separated from the spectrum diagonal. This conformational exchange

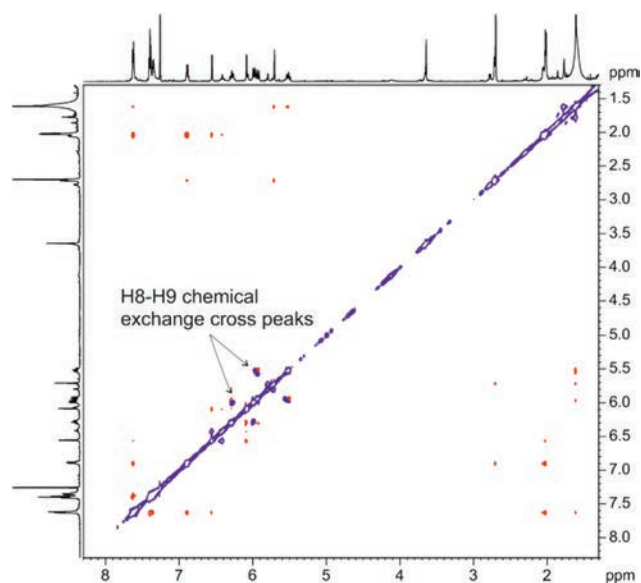


Fig. 5 2D ROESY spectrum of C1 registered at 600 MHz (CDCl_3 , 298 K). Arrows pointing negative cross peaks (blue color) indicate chemical exchange between H_8 and H_9 protons.



might be explained on the basis of a slow conformational equilibrium of the new seven-membered ring formed. Other protons (H_4 , H_6 , H_7 , H_{13} , H_{14} and H_{16}) also exhibit chemical exchange cross peaks, which are closer to the spectrum diagonal, indicating that chemical exchange is taking place between less differentiated chemical environments. This latter effect could be explained as a side-effect from the mentioned seven ring conformational exchange. On the other side, neither benzyl ring protons H_{18} – H_{22} nor H_{15} show any chemical exchange cross peaks, suggesting that these protons are situated far enough from the conformational exchange described.

On the other hand, the direct reaction of **HLCl** with PdCl_2 in acetonitrile yielded the complex $[\text{PdCl}_3(\text{HL})]$ (**C2**, Scheme 1), which has been characterized by NMR and IR spectroscopies and ESI-MS (Fig. S15–S17[†]), thus confirming its stoichiometry. Interestingly, the existence of the protonated ligand HL^+ is confirmed by the singlet ^1H NMR spectroscopy resonance appearing at 9.03 ppm for the H_{11} pre-carbene proton (Fig. S15[†]).

Crystal and molecular structure of trichloro[(*S*)-3-(2-(3,5-dimethyl-1*H*-pyrazol-1-yl)ethyl)-1-(1-phenylethyl)-1*H*-imidazol-3-ium- $\kappa^1\text{N}$]palladium(II) (**C2**)

Single crystals of **C2** suitable for X-ray diffraction analysis were obtained by slow evaporation of a concentrated acetonitrile solution of the complex at RT. The structure of **C2** consists of monomeric $[\text{PdCl}_3(\text{HL})]$ units (Fig. 6a), linked by van der Waals forces (Fig. 6b). The palladium center is coordinated by three terminal chloride ligands and one pyrazolic nitrogen from a 1-[2-(3,5-dimethylpyrazol-1-yl)ethyl]-3-((*S*)-1-phenylethyl)-3*H*-imidazol-1-ium cation in a slightly distorted square-planar geometry. Crystallographic data are listed in Table S1,[†] and the data on selected bond lengths and angles are gathered in Table S2.[†] The positive charge generated by the imidazolium cation is canceled by the negative charge provided by the third chloride ion coordinated to Pd(II), thus forming a zwitterionic structure.

There are three complexes reported in the literature with a PdCl_3N core (terminal chloride ligands and pyrazolic nitrogen).^{19–21} The Pd–N and Pd–Cl bond lengths here observed are comparable to the values found in the literature, and the N–Pd–Cl and Cl–Pd–Cl bond angles slightly deviate from the square planar angles (Table S2[†]).

In compound **C2**, chlorine atoms (Cl2 and Cl3, Fig. 6b) form three different hydrogen bonds: C3–H3A...Cl2 (2.707 Å, 146.11°) and C15–H15...Cl3 (2.935 Å, 154.30°) interacting with hydrogens from the ethylene group of an adjacent **C2** unit, and C11–H11...Cl2 (2.840 Å, 138.45°) interacting with a hydrogen atom from the imidazole aromatic ring of another adjacent **C2** complex. These interactions are responsible for the expansion in the crystallographic direction.

Catalytic experiments with Pd molecular or colloidal systems

C1 and **C2** Pd complexes (with **L** and **HLCl** ligands, respectively) as well as **N1** and **N2** Pd nanoparticles have been evalu-

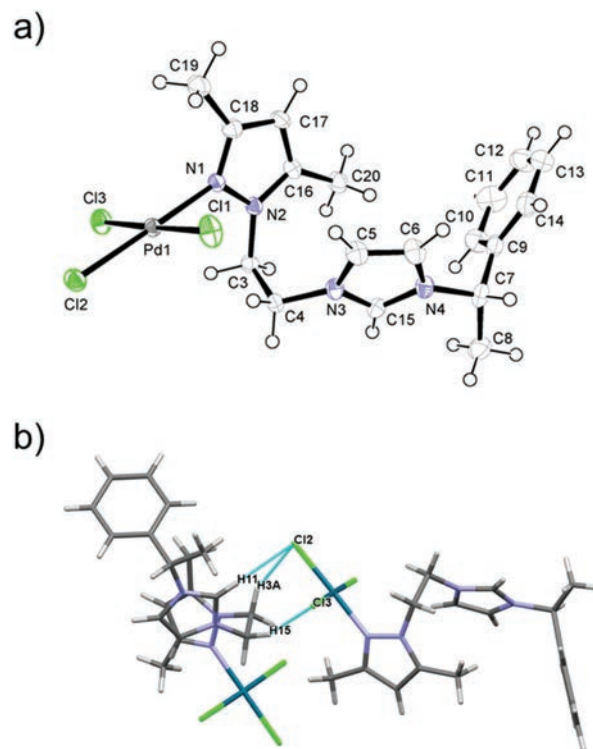
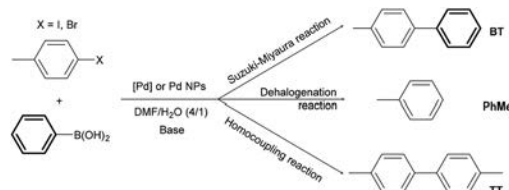


Fig. 6 ORTEP drawing of **C2**, showing the atom-numbering scheme; 50% probability amplitude displacement ellipsoids are shown for all non-hydrogen atoms (a) and hydrogen interactions present in the unit cell of **C2** (b).



Scheme 2 Suzuki–Miyaura, homocoupling and dehalogenation reactions performed in the presence of Pd complexes **C1** and **C2** and Pd NPs **N1** and **N2**.

ated as catalysts for the Suzuki–Miyaura reaction (Scheme 2, Table 1).^{22,23}

4-Halogenotoluene derivatives (4-chlorotoluene, 4-bromotoluene or 4-iodotoluene) and an excess of phenylboronic acid were chosen as substrates in order to easily distinguish between cross-coupling and homocoupling products. Under the catalytic reaction conditions applied (Scheme 2),¹⁴ two different by-products can be formed besides the expected cross-coupled product (4-methylbiphenyl; BT) as follows: (i) toluene (PhMe) arising from the dehalogenation of the substrates and (ii) 4,4'-dimethylbiphenyl (TT), resulting from the 4-bromotoluene homocoupling. Once optimized, 4-halogenotoluene (substrate/Pd = 2500), phenylboronic acid ($\text{PhB}(\text{OH})_2/\text{Pd} = 3125$ or 0), and $t\text{BuOK}$ (base/Pd = 5000) were employed in a DMF/water mixture (4/1) as the solvent. As a general trend,



Table 1 Suzuki–Miyaura reactions with palladium catalysts^a

Entry	Catalyst	X	[PhB(OH) ₂]/[Pd]	Conv. ^b (%)	BT ^c (%)	TT ^c (%)	PhMe ^c (%)	Yield BT (%)	Yield TT (%)
1	C1	I	3125	100	51	0	49	51	0
2	C2	I	3125	82	41	0	59	34	0
3	C1	Br	3125	28	71	0	29	20	0
4	C2	Br	3125	46	93	0	7	43	0
5	N1	I	3125	100	81	0	19	81	0
6	N2	I	3125	100	47	0	53	47	0
7	N1	I	0	100	0	0	100	0	0
8	N2	I	0	56	0	0	56	0	0
9	N1	Br	3125	66	5	51	44	3	34
10	N2	Br	3125	36	7	37	56	3	13
11	N1	Br	0	72	0	83	17	0	60
12	N2	Br	0	36	0	72	28	0	26

^a Reaction conditions: 1×10^{-3} mmol of Pd, 2.5 mmol of 4-halogenotoluene, 5.0 mmol ^tBuOK and 0.5 mmol naphthalene as an internal standard in 8.0 mL of DMF and 2.0 mL of H₂O. Temperature, 100 °C. ^b Conversion after 6 h reaction. ^c Chemoselectivity in 4-methylbiphenyl (BT), 4,4'-dimethylbiphenyl (TT) and toluene (PhMe), respectively.

higher conversions were obtained with 4-iodotoluene compared to 4-bromotoluene in both molecular and colloidal systems (Table 1), as expected from the respective C(Ph)–X bond energies (X = Br, 84 kcal mol⁻¹; X = I, 67 kcal mol⁻¹).²⁴ Unfortunately, 4-chlorotoluene could not be activated probably due to the higher C(Ph)–Cl bond energy value (97.1 kcal mol⁻¹)²⁴ and the Suzuki–Miyaura coupling reaction was unsuccessful.

Interestingly, in the presence of the molecular catalysts C1 and C2, toluene was the only side product observed in a significant amount using both 4-bromotoluene and 4-iodotoluene as substrates (Table 1, entries 1–4). The homocoupling reaction does not take place, as otherwise predictable according to the literature on Pd molecular complexes.¹⁴ Also, 4-bromotoluene yields BT as the major product, while the amount of the dehalogenation product (toluene) significantly increases when 4-iodotoluene is used.

Recently, V. P. Ananikov *et al.* have demonstrated the formation of Pd NPs when molecular Pd complexes with NHC ligands are used in the Mizoroki–Heck reaction.²⁵ In our case, even if it is not a definite proof, TEM control analyses of the solutions after catalysis with C1 or C2 did not show the presence of Pd nanoparticles. In any case, Hg poisoning tests carried out using these systems (*vide infra*) confirm the molecular nature of the real catalyst when C1 or C2 is used.

When 4-iodotoluene was used as a substrate with nanocatalysts N1 and N2, complete conversions were achieved in 6 h in both cases. In the case of N1, the formation of the cross-coupling product (4-methylbiphenyl; BT) was mainly observed together with a small amount of toluene (Table 1, entry 5). The formation of toluene increases to 53% in the case of N2 (Table 1, entry 6). In contrast, N1 and N2 behave similarly against 4-bromotoluene, with the formation of 4,4'-dimethylbiphenyl (TT), arising from the homocoupling reaction, together with toluene and small amounts of BT (Table 1, entries 9 and 10). Furthermore, for the two halogenotoluene substrates, both conversion and chemoselectivities are higher

for the Pd NP/L system (N1) than that for the Pd NP/HCl system (N2). These differences can be explained by the binding of the carbene group at the Pd NP surface in the case of N1 compared to N2. Indeed, the different coordination modes (by C and N in N1 and only by N in N2) may tune both electronic and steric properties at the surface and consequently the catalytic behavior of N1.

In order to determine the influence of phenylboronic acid in C–C coupling reactions catalyzed by the colloidal systems, catalytic experiments were also carried out in the absence of the boron reagent. Besides that BT was not detected, it is remarkable that full conversion to the dehalogenated product (PhMe) is observed in the case of the reaction carried out with 4-iodotoluene catalyzed by N1 (Table 1, entry 7). However, when 4-bromotoluene was employed a significant increase in the yield of the TT homocoupling product is observed for both nanocatalysts (from 34% to 60%; Table 1, entries 9 and 11, respectively, for N1, and from 13% to 26% for N2, entries 10 and 12). When performed with the molecular complexes, the same reaction of 4-halotoluene in the absence of phenylboronic acid reagent did not yield homocoupling products at all.

A recurrent discussion with Pd NPs as catalysts for C–C coupling reactions is whether the real catalysts are the NPs or molecular Pd species leached from them.¹⁰ There are several publications that support either a surface-based²⁶ or atom-leaching mechanism.²⁷ In this context, three different tests have been carried out to assess the nature of the active species during the catalytic process. First of all, in the mercury poisoning test,²⁸ 100 equivalents of Hg were added to the catalytic mixtures after 10 min of reaction. For molecular systems (C1 and C2) the conversions were not affected, while for the colloidal systems (N1 and N2) the catalytic reactions ceased completely. These data suggest that C1 and C2 act as real molecular catalysts when starting with them, whereas Pd NPs are the active species when N1 and N2 are introduced into the catalysis. This is in accordance with the different results observed in catalysis depending on the molecular or colloidal



nature of the introduced catalysts. However, the mercury poisoning test is not definitive, since the amalgam of Hg and Pd from the NPs could prevent potential Pd molecular species from leaching. For this reason, additional experiments have been performed with systems from entries 9 and 10 in Table 1 (Suzuki–Miyaura reaction conditions, *p*-bromotoluene as the haloderivative and **N1** or **N2** as the catalyst, respectively). First of all, TEM grids were prepared after the catalytic experiments, observing the existence of Pd NPs (Fig. S18†). The mean size of these NPs (2.7(0.7) and 3.3(0.6) nm for **N1** and **N2** after catalysis, respectively) is similar to those found for the same NPs prior to the catalytic tests (2.1(0.9) and 3.2(0.9) nm for **N1** or **N2**, respectively). Even if no restructuring of the NPs seems to have taken place (which could indicate a leaching/deposition mechanism through the Ostwald ripening process²⁹), it is important to note that for **N2** the NPs appear isolated after catalysis, in contrast with the aggregation observed prior to catalysis.

Secondly, ICP-MS analyses of the solutions after catalysis for entries 9 and 10 in Table 1 were carried out in order to know the amount of Pd leached from the NPs to the solution. The concentrations of Pd in these solutions are 0.17 and 1.8 ppm for **N1** or **N2**, respectively, meaning that 0.7% and 15% of Pd have leached to the solution for **N1** or **N2**, respectively. The differences on the percentage of leached Pd can be explained by the different coordinative properties of the ligands on each system. For **N1**, the carbene and pyrazolyl groups from **L** can coordinate to the surface of the NPs, and better stabilize them from Pd leaching than in **N2**, where only the pyrazolyl group from **HLCl** can coordinate to the surface of the NPs.

Moreover, the leached molecular Pd species can be responsible for the small amount of C–C heterocoupling reaction observed in entries 9 and 10 of Table 1 (5% and 7%, respectively).

All in all, these experiments indicate that **C1** and **C2** act as molecular catalysts in Suzuki–Miyaura C–C heterocoupling and **N1** and **N2** are the real active species for the C–C homocoupling reaction.

Experimental section

General procedure and reagents

All manipulations were carried out under an argon atmosphere using standard Schlenk tubes or Fisher-Porter reactors and vacuum line techniques, or in a glove-box. [Pd₂(dba)₃] was purchased from Strem Chemicals, and [PdCl₂(CH₃CN)₂]³⁰ and [PdCl₂(cod)]³¹ (cod = 1,5-cyclooctadiene) were prepared as described in the literature. Solvents were purchased from SDS and dried using a purification machine (MBraun MB SPS-800) or distilled prior to use: tetrahydrofuran and diethyl ether over sodium/benzophenone, and pentane, *n*-hexane, acetonitrile and dichloromethane over calcium hydride.

Elemental analyses (C, H, and N) were carried out by the Chemical Analyses Service of the Universitat Autònoma de

Barcelona on a Eurovector 3011 instrument. The Pd weight percentages or concentrations were analyzed by the Chemical Analyses Service of the Universitat Autònoma de Barcelona using an inductively coupled plasma mass spectrometry (ICP-MS) Agilent 7500ce model system or an inductively coupled plasma optical emission spectrometry (ICP-OES) PerkinElmer Optima 4300DV model system. Infrared spectra were recorded on a PerkinElmer FT spectrophotometer, series 2000, as KBr pellets or polyethylene films in the range of 4000–150 cm⁻¹. ¹H NMR, ¹³C {¹H} NMR, HSQC, COSY, DOSY and NOESY spectra for all compounds but **C1** were recorded on Bruker AVANCE 360 and 400 NMR spectrometers in CDCl₃ solutions at room temperature. For **C1**, NMR spectroscopy experiments were performed on a Bruker Avance 600 spectrometer (Bruker Biospin, Rheinstetten, Germany) equipped with TXI HCN z-grad probes. The temperature for all measurements was set to 298 K. The NMR spectroscopy experiments performed for the structural characterization were the standard ¹H, ¹³C, COSY, ROESY, multiplicity-edited HSQC and HMBC experiments (see the ESI†). All chemical shift values (δ) are given in ppm. Electrospray ionization mass spectra (SI-MS) were obtained with an Esquire 3000 ion trap mass spectrometer from Bruker Daltonics.

Specimens for TEM/HR-TEM and SEM-FEG analyses were prepared by slow evaporation of a drop of crude colloidal solution deposited under argon onto holey carbon-covered copper grids. TEM/HR-TEM analyses were performed at the Servei de Microscopia de la UAB with a JEOL JEM 2010 electron microscope working at 200 kV with a resolution point of 2.5 Å. SEM-FEG analyses were performed at the Service Commun de Microscopie Electronique de l'Université Paul Sabatier in Toulouse with an MEB JSM6700F microscope. The size distributions were determined *via* manual analysis of enlarged micrographs by measuring *ca.* 200 particles on a given grid to obtain a statistical size distribution and a mean diameter.

Data collection for WAXS was performed at the CEMES-CNRS (Toulouse) on small amounts of powder. All samples were sealed in 1 mm diameter Lindemann glass capillaries. The measurements of the X-ray intensity scattered by the samples irradiated with graphite monochromatized MoK α (0.071069 nm) radiation were performed using a dedicated two-axis diffractometer. The measurement time was 15 h for each sample. Scattering data were corrected for polarization and absorption effects, then normalized to one Pd atom and Fourier transformed to obtain the RDFs. To make comparisons with the crystalline structure in real space, a model was generated from bulk Pd parameters. The classic Debye's function was then used to compute the intensity values, subsequently Fourier transformed under the same conditions as the experimental ones.

Synthesis and characterization of the ligands

1-[2-(3,5-Dimethylpyrazol-1-yl)ethyl]-3-((*S*)-1-phenylethyl)-3*H*-imidazol-1-ium chloride (**HLCl**). A mixture of 1-(2-chloroethyl)-3,5-dimethyl-1*H*-pyrazole²⁰ (0.942 g, 5.94 mmol) and 1-(*S*)-(phenylethyl)imidazole³² (1.023 g, 5.94 mmol) was heated and stirred at 120 °C for 64 hours. After cooling to room tempera-



ture, the product was dissolved in dichloromethane (5 mL) and precipitated with diethylether (50 mL). For complete precipitation, the system was stored overnight at $-31\text{ }^{\circ}\text{C}$. The product was washed with diethylether ($3 \times 30\text{ mL}$) and dried under vacuum. The product was obtained as a sticky orange solid. Yield: 1.79 g, 91%.

Anal. calcd for $\text{C}_{18}\text{H}_{23}\text{N}_4\text{Cl}\cdot 1.5\text{H}_2\text{O}$: C, 60.41; H, 7.32; N, 15.66. Found: C, 60.54; H, 7.27; N, 16.02. $^1\text{H-NMR}$: (CDCl_3 , 360 MHz, 298 K) δ : 1.89 [s, 3H, H_6 or H_7], 1.92 [br, 3H, H_{16}], 2.06 [s, 3H, H_6 or H_7], 4.44 [br, 2H, H_9], 4.87 [br, 2H, H_8], 5.61 [s, 1H, H_4], 5.76 [q, 1H, $^3J = 7.0\text{ Hz}$, H_{15}], 7.00, 7.23 [2br, 1H each one, H_{13} , H_{14}], 7.30 [br, 5H, $\text{H}_{18}\text{--}\text{H}_{22}$], 10.32 [s, 1H, H_{11}]. (DMSO, 360 MHz, 298 K) δ : 1.81 [d, 3H, $^3J = 7.0\text{ Hz}$, H_{16}], 1.99 [s, 6H, H_6 and H_7], 4.42 [t, 2H, $^3J = 5.0\text{ Hz}$, H_9], 4.58 [t, 2H, $^3J = 5.0\text{ Hz}$, H_8], 5.73 [s, 1H, H_4], 5.83 [q, 1H, $^3J = 7.0\text{ Hz}$, H_{15}], 7.36 [br, 5H, $\text{H}_{18}\text{--}\text{H}_{22}$], 7.72, 7.92 [2br, 1H each one, H_{13} , H_{14}], 9.39 [s, 1H, H_{11}]. $^{13}\text{C}\{^1\text{H}\}$ -NMR: (CDCl_3 , 91 MHz, 298 K) δ : 10.7, 13.4 [C_6 , C_7], 21.1 [C_{16}], 47.9 [C_9], 49.2 [C_8], 59.9 [C_{15}], 105.5 [C_4], 120.4, 123.0 [C_{13} , C_{14}], 126.8, 129.4, 137.8 [$\text{C}_{17}\text{--}\text{C}_{22}$], 136.6 [C_{11}], 140.5, 148.7 [C_3 , C_5]. (DMSO- d_6 , 91 MHz, 298 K) δ : 10.2, 13.3 [C_6 , C_7], 20.6 [C_{16}], 47.2 [C_9], 48.8 [C_8], 58.5 [C_{15}], 105.0 [C_4], 121.3, 123.2 [C_{13} , C_{14}], 126.5, 128.7, 129.0, [$\text{C}_{17}\text{--}\text{C}_{22}$], 136.0 [C_{11}], 139.4, 146.8 [C_3 , C_5]. IR (ATR) cm^{-1} : 3040, 2978 $\nu(\text{C-H})$, 1552 ($\nu(\text{C}=\text{C})$, $\nu(\text{C}=\text{N})$)ar, 1455 ($\delta(\text{C}=\text{C})$, $\delta(\text{C}=\text{N})$)ar, 1160 $\delta(\text{C-H})$ ip, 703 $\delta(\text{C-H})$ oop. MS (ESI): m/z (%) 295.2 (100.0%) [$\text{C}_{18}\text{H}_{23}\text{N}_4\text{Cl} - \text{Cl}^-$].

1-[2-(3,5-Dimethylpyrazol-1-yl)ethyl]-3-((S)-1-phenylethyl)-3H-imidazol-2-ylidene (L). Under an argon atmosphere, sodium hydride (60% dispersion in mineral oil, 124.1 mg, 3.10 mmol) was washed with anhydrous pentane twice ($2 \times 15\text{ mL}$) and the residual solvent was evaporated under reduced pressure. Then, a catalytic amount of potassium *tert*-butoxide (95%, 10 mg, 0.08 mmol) and anhydrous dichloromethane (5 mL) was added. A solution of 1-[2-(3,5-dimethylpyrazol-1-yl)ethyl]-3-((S)-1-phenylethyl)-3H-imidazol-1-ium chloride (**HLCl**, 513.2 mg, 1.55 mmol) in anhydrous dichloromethane (20 mL) was added to the dispersion of NaH/ KO^tBu . The resulting mixture was stirred overnight at room temperature. The reaction crude was then filtered through a small plug of Celite and the solvent was removed under reduced pressure. The product was obtained as a sticky dark orange solid. Yield: 333 mg, 73%.

$^1\text{H-NMR}$: (CDCl_3 , 400 MHz, 298 K) δ : 2.00 [s, 3H, H_6 or H_7], 2.02 [d, 3H, $^3J = 7.0\text{ Hz}$, H_{16}], 2.16 [s, 3H, H_6 or H_7], 4.55 [t, 2H, $^3J = 5.0\text{ Hz}$, H_9], 5.01 [t, 2H, $^3J = 5.0\text{ Hz}$, H_8], 5.65 [q, 1H, $^3J = 7.0\text{ Hz}$, H_{15}], 5.71 [s, 1H, H_4], 6.77, 6.90 [2d, 1H each one, $^3J = 2.0\text{ Hz}$, H_{13} , H_{14}], 7.31–7.42 [2 m, 5H, $\text{H}_{18}\text{--}\text{H}_{22}$]. $^{13}\text{C}\{^1\text{H}\}$ -NMR: (CDCl_3 , 100 MHz, 298 K) δ : 10.7, 13.5 [C_6 , C_7], 21.2 [C_{16}], 48.0 [C_9], 49.2 [C_8], 60.2 [C_{15}], 105.6 [C_4], 120.4, 123.0 [C_{13} , C_{14}], 126.8, 129.5, 137.8 [$\text{C}_{17}\text{--}\text{C}_{22}$], 140.5, 148.8 [C_3 , C_5], signal for [C_{11}] was not observed. IR (ATR) cm^{-1} : 3033, 2960 $\nu(\text{C-H})$, 1552 ($\nu(\text{C}=\text{C})$, $\nu(\text{C}=\text{N})$)ar, 1454 ($\delta(\text{C}=\text{C})$, $\delta(\text{C}=\text{N})$)ar, 1015 $\delta(\text{C-H})$ ip, 700 $\delta(\text{C-H})$ oop.

Synthesis and characterization of the Pd(II) or Ag(I) complexes

Chloro[(S)-3-(2-(3,5-dimethyl-1H-pyrazol-1-yl)ethyl)-1-(1-phenylethyl)-1H-imidazol-2-ylidene]silver(I), (**C_{Ag}**). A mixture of

1-[2-(3,5-dimethylpyrazol-1-yl)ethyl]-3-((S)-1-phenylethyl)-3H-imidazol-1-ium chloride (**HLCl**, 342 mg, 1.03 mmol) and silver (I) oxide (99%, 240 mg, 1.03 mmol) in anhydrous dichloromethane (25 mL) was stirred at room temperature for 24 hours in the dark. Then, the reaction crude was filtered through Celite. The filtrate solvent was removed under vacuum and the product was dried completely. The product was obtained as a sticky grey-brown solid. Yield: 361 mg, 80%.

Anal. calcd for $\text{C}_{18}\text{H}_{22}\text{AgClN}_4$: C, 49.39; H, 5.07; N, 12.80. Found: C, 49.92; H, 5.14; N, 12.47. $^1\text{H-NMR}$: (CDCl_3 , 360 MHz, 298 K) δ : 1.77 [s, 3H, H_6 or H_7], 1.81 [br, 3H, H_{16}], 2.18 [s, 3H, H_6 or H_7], 4.29 [br, 2H, H_9], 4.54 [br, 2H, H_8], 5.68 [s, 1H, H_4], 5.76 [br, 1H, H_{15}], 6.43, 6.80 [2br, 1H each one, H_{13} , H_{14}], 7.23, 7.32 [2br, 5H, $\text{H}_{18}\text{--}\text{H}_{22}$]. $^{13}\text{C}\{^1\text{H}\}$ -NMR: (CDCl_3 , 91 MHz, 298 K) δ : 10.6, 13.7 [C_6 , C_7], 21.4 [C_{16}], 49.3 [C_9], 51.9 [C_8], 60.9 [C_{15}], 105.5 [C_4], 118.5, 122.2 [C_{13} , C_{14}], 126.6, 128.7, 129.2, 139.7 [$\text{C}_{17}\text{--}\text{C}_{22}$], 140.2, 148.9 [C_3 , C_5], signal for [C_{11}] was not observed. IR (ATR) cm^{-1} : 3087, 2977 $\nu(\text{C-H})$, 1551 ($\nu(\text{C}=\text{C})$, $\nu(\text{C}=\text{N})$)ar, 1448 ($\delta(\text{C}=\text{C})$, $\delta(\text{C}=\text{N})$)ar, 1219 $\delta(\text{C-H})$ ip, 700 $\delta(\text{C-H})$ oop. MS (ESI): m/z (%) 401.1 (100.0%) [$\text{C}_{18}\text{H}_{22}\text{N}_4\text{ClAg} - \text{Cl}^-$].

Dichloro[(S)-3-(2-(3,5-dimethyl-1H-pyrazol-1-yl)ethyl)-1-(1-phenylethyl)-1H-imidazol-2-ylidene- $\kappa^1\text{N}$]palladium(II), (**C1**). A mixture of C_{Ag} (242 mg, 0.55 mmol) and dichloro(1,5-cyclooctadiene)palladium(II) (158 mg, 0.55 mmol) in dichloromethane (30 mL) was kept under vigorous stirring for 24 hours at room temperature in the dark. The reaction crude was filtered through Celite. Then, the filtrate solvent was evaporated under vacuum and the resulting solid was washed with hexane (30 mL). The residue was purified by flash column chromatography (silica gel 60 Å) using ethyl acetate:diethyl ether 4:1 as the eluent and then by second column chromatography (silica gel 60 Å) using dichloromethane:hexane 9:1 as the eluent. The product was obtained as a pale yellow powder. Yield: 133 mg, 51%.

$^1\text{H-NMR}$: (CDCl_3 , 600 MHz, 298 K) δ : 1.61 [s, 3H, H_6 or H_7], 2.02 [br, 3H, H_{16}], 2.70 [s, 3H, H_6 or H_7], 5.71 [s, 1H, H_4], 5.87 [br, 2H, H_9], 6.27 [br, 2H, H_8], 6.08, 6.55 [2br, 1H each one, H_{13} , H_{14}], 6.89 [br, H_{15}], 7.39, 7.62 [2br, 5H, $\text{H}_{18}\text{--}\text{H}_{22}$]. $^{13}\text{C}\{^1\text{H}\}$ -NMR: (CDCl_3 , 150 MHz, 298 K) δ : 10.9, 14.5 [C_6 , C_7], 19.5 [C_{16}], 50.1 [C_9], 51.1 [C_8], 59.2 [C_{15}], 106.4 [C_4], 118.5, 123.4 [C_{13} , C_{14}], 127.4, 128.5, 128.8 [$\text{C}_{17}\text{--}\text{C}_{22}$], 139.6, 144.1 [C_3 , C_5], signal for [C_{11}] was not observed. IR (ATR) cm^{-1} : 3097, 2978 $\nu(\text{C-H})$, 1555 ($\nu(\text{C}=\text{C})$, $\nu(\text{C}=\text{N})$)ar, 1452 ($\delta(\text{C}=\text{C})$, $\delta(\text{C}=\text{N})$)ar, 1180 $\delta(\text{C-H})$ ip, 694 $\delta(\text{C-H})$ oop. HRMS (ESI): m/z 399.0808 [$\text{C}_{18}\text{H}_{22}\text{N}_4\text{Cl}_2\text{Pd} - \text{Cl}^- - \text{HCl}$].

Trichloro[(S)-3-(2-(3,5-dimethyl-1H-pyrazol-1-yl)ethyl)-1-(1-phenylethyl)-1H-imidazol-3-ium- $\kappa^1\text{N}$]palladium(II), (**C2**). A mixture of 1-[2-(3,5-dimethylpyrazol-1-yl)ethyl]-3-((S)-1-phenylethyl)-3H-imidazol-1-ium chloride (**HLCl**, 205 mg, 0.62 mmol) and palladium(II) chloride (99.9%, 110 mg, 0.62 mmol) in acetonitrile (20 mL) was kept under vigorous stirring for 24 hours at room temperature. Then, the solution was filtered through Celite. The solvent volume was decreased to *ca.* 2 mL and diethyl ether (30 mL) was added to induce precipitation. The orange powder was filtered and washed with diethyl ether ($3 \times 30\text{ mL}$), and dried under vacuum. The product was obtained as an



orange powder. The single crystals for X-ray diffraction were obtained by slow evaporation of a concentrated acetonitrile solution of the complex at room temperature. Yield: 222 mg, 70%.

Anal. calcd for $C_{18}H_{23}N_4Cl_3Pd$: C, 42.54; H, 4.56; N, 11.02. Found: C, 42.03; H, 4.62; N, 10.76. 1H -NMR: (DMSO- d_6 , 360 MHz, 298 K) δ : 1.80 [d, 3H, $^3J = 7.0$ Hz, H_{16}], 1.98 [s, 3H, H_6 or H_7], 2.01 [s, 3H, H_6 or H_7], 4.38 [t, 2H, $^3J = 5.0$ Hz, H_9], 4.54 [t, 2H, $^3J = 5.0$ Hz, H_8], 5.75 [s, 1H, H_4], 5.79 [br, 1H, H_{15}], 7.32, 7.40 [2 m, 5H, H_{18} – H_{22}], 7.64, 7.83 [2br, 1H each one, H_{13} , H_{14}], 9.03 [s, 1H, H_{11}]. $^{13}C\{^1H\}$ -NMR: (DMSO- d_6 , 91 MHz, 298 K) δ : 10.2, 13.3 [C_6 , C_7], 20.6 [C_{16}], 47.1 [C_9], 48.9 [C_8], 58.5 [C_{15}], 105.0 [C_4], 121.3, 123.2 [C_{13} , C_{14}], 126.4, 128.7, 129.0, 139.4 [C_{17} – C_{22}], 135.8 [C_{11}], 139.4, 146.9 [C_3 , C_5]. IR (ATR) cm^{-1} : 3091, 2984 $\nu(C-H)$, 1555 ($\nu(C=C)$), $\nu(C=N)$ ar, 1453 ($\delta(C=C)$), $\delta(C=N)$ ar, 1152 $\delta(C-H)$ ip, 704 $\delta(C-H)$ oop. MS (ESI): m/z (%) 399.1 (100.0%) [$C_{18}H_{23}N_4Cl_3Pd - Cl^- - 2HCl$], 437.1 (26.5%) [$C_{18}H_{23}N_4Cl_3Pd - Cl^- - HCl$], 473.0 (25.7%) [$C_{18}H_{23}N_4Cl_3Pd - Cl^-$].

Synthesis of Pd/L and Pd/HLCl nanoparticles

The general procedure for the preparation of palladium nanoparticles is detailed through the case of $[L]/[Pd] = 0.5$ (Fig. 2a and Scheme 1). The procedure was similar for all other samples.

$[Pd_2(dba)_3]$ (200 mg, 0.22 mmol) and **L** (28.6 mg, 0.11 mmol) were dissolved in a Fisher-Porter reactor in previously degassed anhydrous dichloromethane (200 mL) under argon at 196 K. The mixture was pressurized under 3 bar of dihydrogen and kept at room temperature under vigorous stirring. The color of the solution turned from purple to black after 1 h. The hydrogen pressure and the temperature were maintained for 18 h. After that period of time, the colloidal solution was black and homogeneous. Hydrogen was evacuated and a drop of the crude colloidal solution was deposited under argon on a holey carbon-covered copper grid using filter paper under the grid for TEM and SEM analysis. Then, the colloidal solution was concentrated to *ca.* 10 mL. The addition of cold pentane (20 mL) allowed the precipitation of the particles as a black solid, which was washed with pentane (3×20 mL) and dried under reduced pressure. The filtered pentane was slightly yellow due to dba elimination. This was corroborated by 1H -NMR experiments of the dried pentane solution. **N1** Anal. found (wt%): Pd, 66.0; N, 5.34 for a stoichiometry of $Pd_{561}L_{37}$. IR (ATR, cm^{-1}): 3026, 2939 $\nu(C-H)$, 1564 ($\nu(C=C)$), $\nu(C=N)$ ar, 1462 ($\delta(C=C)$), $\delta(C=N)$ ar, 700 $\delta(C-H)$ oop. **N2**: anal. found (wt%): Pd, 83.0; N, 2.90 for a stoichiometry of $Pd_{1415}HLCl_{93}$. IR (KBr, cm^{-1}): 3019, 2960 $\nu(C-H)$, 1563 ($\nu(C=C)$), $\nu(C=N)$ ar, 1456 ($\delta(C=C)$), $\delta(C=N)$ ar, 1137 $\delta(C-H)$ ip.

Crystal structure determination of C2

Crystallographic data for compound **C2** were collected at low temperature (180 K) on a Bruker Kappa Apex II diffractometer using graphite-monochromated Mo- $K\alpha$ radiation ($\lambda = 0.71073$ Å) and equipped with an Oxford Cryosystems

Cryostream Cooler device. Crystallographic data for **C2** can be gathered in the ESI, Tables S1 and S2.†

The structures have been solved by Direct Methods using SIR92,³³ and refined by means of least-squares procedures on F^2 with the aid of the program SHELXL97³⁴ included in the software package WinGX version 1.63.³⁵ The atomic scattering factors were taken from International tables for X-ray crystallography.^{36,37} All hydrogen atoms were placed geometrically, and refined by using a riding model. All non-hydrogen atoms were anisotropically refined, and in the last cycles of refinement a weighing scheme was used, where weights are calculated from the following formula: $w = 1/[\sigma^2(F_o^2) + (aP)^2 + bP]$ where $P = (F_o^2 + 2F_c^2)/3$.

Crystallographic data for the structural analyses have been deposited at the Cambridge Crystallographic Data Centre, CCDC, with reference number 1432563 (**C2**).†

Catalytic experiments

The quantification of the catalytic reactions was carried out in an HP5890 Hewlett Packard gas chromatograph equipped with a FID detector and an HP-5 column (5% diphenylpolysiloxane and 95% dimethylpolysiloxane). The products obtained in the catalytic reactions were identified using a G1800A Hewlett Packard gas chromatograph with an electron impact ionization detector and a HP-5 column (5% diphenylpolysiloxane and 95% dimethylpolysiloxane). The mass spectra of the catalytic products are in agreement with those published in the literature.^{38,39}

Suzuki-Miyaura reactions

In a two-neck round-bottom flask fitted with a reflux condenser and a septum, 4-halogenotoluene (2.5 mmol), phenylboronic acid (3.125 mmol), t BuOK (5.0 mmol), and naphthalene (0.5 mmol) as internal standards were dissolved in DMF/ H_2O (10 mL, 4/1). Next, the palladium organometallic complex (1×10^{-3} mmol) or palladium nanoparticles (1×10^{-3} mmol Pd atoms) were added. The solution was vigorously stirred and heated at 100 °C for 6 h under nitrogen. Then, the reaction crude was cooled to room temperature and the products were extracted with a mixture of diethyl ether/brine (20 mL, 1/1). The organic phase was analyzed by GC and GC-MS.

Conclusions

A new hybrid pyrazole-imidazol-2-ylidene ligand, 1-[2-(3,5-dimethylpyrazol-1-yl)ethyl]-3-((S)-1-phenylethyl)-3H-imidazol-2-ylidene (**L**), has been synthesized for the first time and proved to effectively stabilize small and isolated palladium(0) nanoparticles. A comparison with its counterpart **HLCl** as a stabilizer led to badly stabilized NPs which evidenced that the coordination of the ylidene group is a key factor in the stabilization process of the colloidal system. The successful preparation and complete characterization of molecular Pd(II) coordination compounds with the same ligands confirmed a chelated coordination mode through the pyrazolic nitrogen



and the ylidene group for **L** but a terminal monodentate mode through pyrazolic nitrogen for **HLCl**. From our previous research with carbene or pyrazole-containing ligands as stabilizers, we can conclude that similar coordination modes of **L** and **HLCl** here take place for both the Pd NP particles and Pd complexes respectively. As a consequence, the coordination of **L** is stronger and leads to nanoparticles with well-controlled size.

All these systems have been tested in catalytic C–C coupling reactions. For colloidal systems (**N1** and **N2**), we observed an improving effect, in terms of chemoselectivity and yield, of **L** containing NPs (**N1**) with respect to **HLCl** containing NPs (**N2**) as a result of the different coordination modes of the carbene group to the surface of the NPs. Interestingly, these systems are the only ones able to achieve the C–C homocoupling reaction between two molecules of bromoarenes or the complete dehalogenation reaction of iodoarenes. The Suzuki–Miyaura reaction is favored with the Pd molecular complexes.

Taking into account the advantages of the organometallic approach and the different attributes of these catalysts, we believe that these materials could find practical uses in C–C coupling reactions in the future.

Conflicts of interest

There are no conflicts to declare.

Acknowledgements

Support from MINECO (CTQ2015-64261-R and CTQ2015-64436-P) is gratefully acknowledged. F. G. V. and J. DeT. acknowledge the Universitat Autònoma de Barcelona for their pre-doctoral grants. J. G.-A. acknowledges the Serra Hünter Program. The authors thank the Microscopy Service of the Universitat Autònoma de Barcelona for technical assistance with TEM and HR-TEM. CNRS is also thanked through the LTPMM-LEA 368 action.

Notes and references

- (a) M. N. Hopkinson, C. Richter, M. Schedler and F. Glorius, *Nature*, 2014, **510**, 485–496; (b) F. Glorius, *Top. Organomet. Chem.*, 2006, **21**, 1–20; (c) J. A. M. Lummiss, C. S. Higman, D. L. Fyson, R. McDonald and D. E. Fogg, *Chem. Sci.*, 2015, **6**, 6739–6746.
- N. Hadei, E. A. B. Kantchev, C. J. O'Brien and M. G. Organ, *Org. Lett.*, 2005, **7**, 1991.
- (a) G. D. Frey, V. Lavallo, B. Donnadieu, W. W. Schoeller and G. Bertrand, *Science*, 2007, **316**, 439–441; (b) Y. Wang, Y. Xie, P. Wei, R. B. King, H. F. Schaefer III, P. v. R. Schleyer and G. Robinson, *Science*, 2008, **321**, 1069–1071.
- (a) A. V. Zhukhovitskiy, M. J. MacLeod and J. A. Johnson, *Chem. Rev.*, 2015, **115**, 11503–11532; (b) P. Lara, O. Rivada-Wheeler, S. Conejero, K. Philippot and B. Chaudret, *Angew. Chem., Int. Ed.*, 2011, **50**, 12080–12084; (c) P. Lara, A. Suárez, V. Colliere, K. Philippot and B. Chaudret, *ChemCatChem*, 2014, **6**, 87–90; (d) J. Vignolle and T. D. Tilley, *Chem. Commun.*, 2009, **46**, 7230–7232; (e) E. C. Hurst, K. Wilson, I. J. S. Fairlamb and V. Chechik, *New J. Chem.*, 2009, **33**, 1837–1840; (f) D. González-Gálvez, P. Lara, O. Rivada-Wheeler, S. Conejero, B. Chaudret, K. Philippot and P. W. N. M. van Leeuwen, *Catal. Sci. Technol.*, 2013, **3**, 99–105; (g) E. A. Baquero, S. Tricard, J. C. Flores, E. de Jesús and B. Chaudret, *Angew. Chem., Int. Ed.*, 2014, **53**, 13220–13224; (h) A. Ferry, K. Schaepe, P. Tegeder, C. Richter, K. M. Chepiga, B. J. Ravoo and F. Glorius, *ACS Catal.*, 2015, **5**, 5414–5420; (i) L. M. Martínez-Prieto, A. Ferry, P. Lara, C. Richter, K. Philippot, F. Glorius and B. Chaudret, *Chem. – Eur. J.*, 2015, **21**, 17495–17502; (j) C. Richter, K. Schaepe, F. Glorius and B. J. Ravoo, *Chem. Commun.*, 2014, **50**, 3204–3207; (k) L. M. Martínez-Prieto, A. Ferry, C. Richter, P. Lecante, K. Philippot, F. Glorius and B. Chaudret, *Chem. Commun.*, 2016, **52**, 4768–4771; (l) L. M. Martínez-Prieto, C. Urbaneja, P. Palma, J. Cámpora, K. Philippot and B. Chaudret, *Chem. Commun.*, 2015, **51**, 4647–4650.
- M. Albrecht, *Adv. Organomet. Chem.*, 2014, **62**, 111–158.
- (a) P. Lara, K. Philippot, L. M. Lacroix, S. Lachaize, N. Liakakos, K. Soulantica and B. Chaudret, Organometallic Nanoparticles, in *Advances in Organometallic Chemistry: The Silver/Gold Jubilee International Conference on Organometallic Chemistry Celebratory Book*, ed. A. J. L. Pombeiro, Wiley VCH, Weinheim, 2013, ch. 31, pp. 421–436; (b) S. Kinayyigit and K. Philippot, Organometallic Approach for the Synthesis of Noble Metal Nanoparticles: Towards Application in Colloidal and Supported Nanocatalysis, in *Metal Nanoparticles for Catalysis: Advances and Applications*, ed. T. Tao, RSC, 2014, ch. 4, pp. 47–82; (c) K. An and G. A. Somorjai, *ChemCatChem*, 2012, **4**, 1442; (d) N. J. Costa, M. Guerrero, V. Colliere, E. Teixeira-Neto, R. Landers, K. Philippot and L. M. Rossi, *ACS Catal.*, 2014, **4**, 1735–1742.
- C. Amiens, D. Ciuculescu-Pradines and K. Philippot, *Coord. Chem. Rev.*, 2016, **38**, 409–432.
- (a) K. Philippot and P. Serp, Concepts in Nanocatalysis, in *Nanomaterials in Catalysis*, ed. P. Serp and K. Philippot, Wiley-VCH, Weinheim, 2013, ch. 1, pp. 1–54; (b) T. Ayvali and K. Philippot, On the use of Organometallic Concepts for the Synthesis of Nanocatalysts, in *New Materials for Catalytic Applications*, ed. E. Kemnitz and V. Parvulescu, Elsevier, 2016, ch. 3, pp. 41–79; (c) A. Roucoux, J. Schulz and H. Patin, *Chem. Rev.*, 2002, **102**, 3757–3778; (d) M. Guerrero, N. T. T. Chau, S. Noel, A. Denicourt-Nowicki, F. Hapiot, A. Roucoux, E. Montflier and K. Philippot, *Curr. Org. Chem.*, 2013, **17**, 364–399; (e) B. Chaudret, M. Gómez and K. Philippot, *Top. Catal.*, 2013, **56**, 1153; (f) D. Wang and D. Astruc, *Chem. Rev.*, 2014, **114**, 6949–6985.



- 9 (a) A. Kolmakov, X. Chen and M. J. Moskovits, *Nanosci. Nanotechnol.*, 2008, **8**, 111–121; (b) M. Guerrero, N. J. S. Costa, L. L. R. Vono, L. M. Rossi, E. V. Gusevskaya and K. Philippot, *J. Mater. Chem. A*, 2013, **1**, 1441–1449.
- 10 A. Bej, K. Ghosh, A. Sarkar and D. W. Knight, *RSC Adv.*, 2016, **6**, 11446–11453.
- 11 S. Kotha, K. Lahiri and D. Kashinath, *Tetrahedron*, 2002, **58**, 9633–9695.
- 12 A. Ganesan, *Drug Discovery Today*, 2001, **6**, 238.
- 13 D. Astruc, C. Ornelas, A. K. Diallo and J. Ruiz, *Molecules*, 2010, **15**, 4947–4960.
- 14 D. Peral, F. Gómez-Villarraga, X. Sala, J. Pons, J. C. Bayon, J. Ros, M. Guerrero, L. Vendier, P. Lecante, J. García-Antón and K. Philippot, *Catal. Sci. Technol.*, 2013, **3**, 475–489.
- 15 C. Amiens, B. Chaudret, D. Ciuculescu-Pradines, V. Collière, K. Fajerweg, P. Fau, M. Kahn, A. Maisonnat, K. Soulantica and K. Philippot, *New J. Chem.*, 2013, **37**, 3374–3401.
- 16 J. Deng, H. Gao, F. Zhu and Q. Wu, *Organometallics*, 2013, **32**, 4507–4515.
- 17 T. L. Hwang and A. J. Shaka, *J. Am. Chem. Soc.*, 1992, **114**, 3157–3159.
- 18 A. D. Bain, *Prog. Nucl. Magn. Reson. Spectrosc.*, 2003, **43**, 63–103.
- 19 Z. A. Savel'eva, L. A. Glinskaya, S. A. Popov, R. F. Klevtsova, A. V. Tkachev and S. V. Larionov, *Russ. J. Coord. Chem.*, 2009, **35**, 668–673.
- 20 H. M. Lee, P. L. Chiu, C.-H. Hu, C.-L. Lai and Y.-C. Chou, *J. Organomet. Chem.*, 2005, **690**, 403–414.
- 21 G. Aragay, J. Pons, J. García-Antón, X. Solans, M. Font-Bardia and J. Ros, *J. Organomet. Chem.*, 2008, **693**, 3396–3404.
- 22 N. Miyaura, K. Yamada and A. Suzuki, *Tetrahedron Lett.*, 1979, **36**, 3437–3440.
- 23 N. Miyaura and A. Suzuki, *Chem. Rev.*, 1995, **95**, 2457–2483.
- 24 S. J. Blanksby and G. B. Ellison, *Acc. Chem. Res.*, 2003, **36**, 255–263.
- 25 A. V. Astakhov, O. V. Khazipov, A. Y. Chernenko, D. V. Pasyukov, A. S. Kashin, E. G. Gordeev, V. N. Khrustalev, V. M. Chernyshev and V. P. Ananikov, *Organometallics*, 2017, **36**, 1981–1992.
- 26 (a) P. J. Ellis, I. J. S. Fairlamb, S. F. J. Hackett, K. Wilson and A. F. Lee, *Angew. Chem., Int. Ed.*, 2010, **49**, 1820–1824; (b) R. Narayanan and M. A. El-Sayed, *J. Phys. Chem. B*, 2004, **108**, 8572–8580; (c) R. Narayanan and M. A. El-Sayed, *J. Am. Chem. Soc.*, 2003, **125**, 8340–8347; (d) A. F. Lee, P. J. Ellis, I. J. S. Fairlamb and K. Wilson, *Dalton Trans.*, 2010, 10473–10482; (e) C. Sánchez-Sánchez, N. Orozco, J. P. Holgado, S. K. Beaumont, G. Kyriakou, D. J. Watson, A. R. González-Eripe, L. Feria, J. Fernández-Sanz and R. M. Lambert, *J. Am. Chem. Soc.*, 2014, **137**, 940–947; (f) V. K. Kanuru, G. Kyriakou, S. K. Beaumont, A. C. Papageorgiou, D. J. Watson and R. M. Lambert, *J. Am. Chem. Soc.*, 2010, **132**, 8081–8086; (g) C. Sánchez-Sánchez, F. Yubero, A. R. González-Elipe, L. Feria, J. Fernández-Sanz and R. M. Lambert, *J. Phys. Chem. C*, 2014, **118**, 11677–11684; (h) F. Wang, C. Li, L.-D. Sun, H. Wu, T. Ming, J. Wang, J. C. Yu and C.-H. Yan, *J. Am. Chem. Soc.*, 2011, **133**, 1106–1111; (i) F. Wang, C. Li, H. Chen, R. Jiang, L.-D. Sun, Q. Li, J. Wang, J. C. Yu and C.-H. Yan, *J. Am. Chem. Soc.*, 2013, **135**, 5588–5601.
- 27 (a) Z. Niu, Q. Peng, Z. Zhuang, W. He and Y. Li, *Chem. – Eur. J.*, 2012, **18**, 9813–9817; (b) D. B. Pacardo, J. M. Slocik, K. C. Kirk, R. R. Naik and M. R. Knecht, *Nanoscale*, 2011, **3**, 2194–2201; (c) A. V. Gaikwad, A. Holuigue, M. B. Thathagar, J. E. ten Elshof and G. Rothenberg, *Chem. – Eur. J.*, 2007, **13**, 6908–6913; (d) M. T. Reetz and E. Westermann, *Angew. Chem., Int. Ed.*, 2000, **39**, 165–168; (e) J. G. de Vries, *Dalton Trans.*, 2006, 421–429.
- 28 G. M. Whitesides, M. Hackett, R. L. Brainard, J. P. P. M. Lavalleye, A. F. Sowinski, A. N. Izumi, S. S. Moore, D. W. Brown and E. M. Staud, *Organometallics*, 1985, **4**, 1819–1830.
- 29 R. L. Oliveira, W. He, R. J. M. Klein Gebbink and K. P. de Jong, *Catal. Sci. Technol.*, 2015, **5**, 1919–1928.
- 30 S. Komiyama, in *Synthesis of Organometallic Compounds: A Practice Guide*, Board, New York, 1997.
- 31 D. Drew and J. R. Doyle, in *Inorganic Syntheses, 28 (Reagents Transition Met. Complex Organomet. Synth.)*, 1990, pp. 346–349.
- 32 H. Konishi, T. Ueda, T. Muto and K. Manabe, *Org. Lett.*, 2012, **14**, 4722–4725.
- 33 A. Altomare, G. Cascarano, C. Giacovazzo and A. Guagliardi, *J. Appl. Crystallogr.*, 1993, **26**, 343–350.
- 34 G. M. Sheldrick, *Acta Crystallogr., Sect. A: Fundam. Crystallogr.*, 2008, **64**, 112–122.
- 35 L. J. Farrugia, *Appl. Crystallogr.*, 1999, **32**, 837–838.
- 36 T. Hahn, in *International Tables for Crystallography, Volume A*, Kluwer Academic Publishers, Dordrecht, The Netherlands, 1995.
- 37 A. J. C. Wilson, in *International Tables for Crystallography, Volume C*, Kluwer Academic Publishers, Dordrecht, The Netherlands, 1995.
- 38 X. Xu, D. Cheng and W. Pei, *J. Org. Chem.*, 2006, **71**, 6637–6639.
- 39 I. J. S. Fairlamb, A. R. Kapdi and A. F. Lee, *Org. Lett.*, 2004, **6**, 4435–4438.

